NEUTRON COMPTON SCATTERING FROM HYDROGEN AND PEROVSKITE OXIDE INTERFACES

by

CHRISTOPHER P. LEMON

A thesis submitted to
The University of Birmingham
for the degree of
DOCTOR OF PHILOSOPHY

School of Physics and Astronomy
The University of Birmingham

September 2009

Abstract

In this thesis we investigate two independent topics: neutron Compton scattering from hydrogen and perovskite oxide interfaces.

Part one is an investigation of the scattering of high energy neutrons from hydrogen compounds. The motivation for this investigation stems from neutron Compton scattering experiments, performed with the VESUVIO neutron spectrometer at the ISIS pulsed neutron source, which report an anomalously reduced cross section for hydrogen. We explore the possibility that electronic excitation is responsible for the discrepancy between conventional theory and experiment. We conclude that the effect of electronic excitation on the scattering is small, at the energies relevant to the experiments, and therefore cannot account for the anomalies.

Part two is an investigation of two perovskite oxide interfaces: a cuprate-manganite interface, and the interface between $SrTiO_3$ and $LaAlO_3$. Both interfaces are investigated using the techniques of impurity theory. Firstly, a simple model of a cuprate-manganite interface is proposed to explain several recent experiments. By applying the idea that the metallicity of the manganite spills out into the cuprate, we provide a theoretical interpretation of the unusual electronic and magnetic properties observed at the interface. Finally, a simple model of the $SrTiO_3$-$LaAlO_3$ interface is investigated. Two ingredients are contained within this model: the orbital physics of the titanates, and the long range coulomb interactions produced by the polar discontinuity at the interface. From this model, we predict a two dimensional layer of charge confined to the interface, which is consistent with experimental observations.

Acknowledgements

I would like to thank my supervisors: Martin Long and Nikitas Gidopoulos. Martin has played an important role, throughout my PhD, by keeping me motivated with interesting ideas, and by always being available and willing to answer my questions. I have learnt a great deal from Martin, yet it still seems that I have only scratched the surface of his knowledge. I have also benefitted considerably from the teaching and advice that Nikitas has provided. Nikitas has enriched my research experience by involving me in developments at ISIS and by encouraging me to view my work from a broader perspective. It also helps to be working in a motivated group of students, which the theory group at Birmingham has certainly provided.

The going has at times been difficult, but the encouragement and reassurance provided by family has kept me going throughout. Their unwavering support of all my decisions has really allowed me to make the most of my time at Birmingham. This was especially true during my final year, which I couldn't have completed without their help. Fortunately, they also remembered to feed Toby and Cashmere whilst I was preoccupied with writing my thesis!

Last, but certainly not least, I would like to thank Tina, who has stuck by me through everything. With Tina, the time has passed by much quicker than I had anticipated. She has kept me feeling positive throughout and has encouraged me to look forward to the future – I don't know what I would have done without her.

Contents

List of Figures

Part I

Neutron Compton scattering from hydrogen

Chapter 1

Neutron Compton scattering from hydrogen

Neutron Compton scattering, also referred to as deep inelastic neutron scattering, is differentiated from other branches of neutron scattering by the high energies involved. In this high energy regime, which often involves neutron energies in the region of 100eV, the scattering process is so rapid that interatomic forces acting on the struck nucleus can be neglected during the collision. This is the *impulse* limit; in this limit, the relationship between the measured response and the nuclear momentum distributions becomes remarkably simple. In addition, the scattering from the different nuclei can be separated, which enables detailed investigations of the individual atomic species within a sample.

In analogy with x-ray Compton scattering, which provides information of the momentum distribution of electrons, neutron Compton scattering provides information about the momentum distributions of different nuclei. This idea has been applied to extract the condensate fraction in superfluid ^{4}He[1, 2], and to reconstruct the nuclear wavefunctions and potentials of hydrogen in ferroelectric KH_2PO_4[3]. A comprehensive review of the theoretical background for neutron Compton scattering has been given by Watson[4].

In the following four chapters we investigate the application of the neutron Compton scattering technique to hydrogen systems, and determine the reliability of the approximations used to analyse the results. The motivation behind such an investigation originates from several experiments, performed on the VESUVIO neutron spectrometer at the ISIS pulsed neutron source, each reporting an anomalously reduced measurement of the neutron cross section for hydrogen[5, 6, 7, 8, 9, 10, 11]. These anomalies have prompted several investigations: into the theoretical description of scattering high energy neutrons from a variety of different systems[12], and into possible experimental or data analysis problems[13, 14, 15].

This investigation focuses on the theoretical possibility that electronic excitation,

which becomes more significant as the energy of incident neutrons increases, is responsible for the anomalous measurements. Previous investigations[16] into the significance of electronic excitations have reported small modifications to the neutron response. However, due to the more recent influx of experimental data, we re-examine the possibility that electronic excitations may be responsible for the anomalous measurements of hydrogen cross sections. The simple systems which we examine allow for a detailed investigation, of the two different mechanisms responsible for electronic excitation: the centre of mass recoil (CMR) effect, which is caused by the mixing of electronic and nuclear coordinates in the centre of mass frame, and the non-adiabatic coupling (NAC) between the electrons and the nuclei, which is a consequence of the electronic response to the dynamical motion of the nuclei.

Chapter 1 serves as an introduction to the neutron Compton scattering technique, and contains the background material necessary to interpret the experiments which report anomalous measurements of hydrogen cross sections. The impulse approximation is introduced and its application to high energy neutron scattering is discussed, together with the corrections which can be expanded in powers of $1/q$, where q is the transferred momentum. In particular, the effect of the environment on the scattering of the struck nucleus, which is not included in the impulse approximation, is discussed. The possibility of electronic excitation is then introduced, and it is shown that accurate calculations of the response function for hydrogen systems are required to quantify this effect.

In chapter 2, the methods required to analyse the response function of a simple model, which in this case is a four body problem, are introduced. The analysis of the four body problem illustrates how a separation of energy scales, of different modes of excitation, leads to a convolution of the associated excitation probabilities.

The electronic excitation of the hydrogen atom is the topic of chapter 3. The probabilities of electronic excitation are analysed and the energy scales for electronic excitation and dissociation are determined. This analysis enables us to rule out one of the mechanisms of excitation, the CMR effect, as a significant source of electronic excitation at the energy scales considered relevant to the experiments.

Chapter 4 concludes the investigation with an analysis of the NAC effect in the molecular hydrogen system H_2^+. The NAC effect is shown to be synonymous with the breakdown of the Born-Oppenheimer approximation, which assumes the adiabatic separability of the nuclear motion from the electronic motion. To investigate these effects it is necessary to incorporate the non-adiabatic corrections in the calculation of the molecular wavefunctions. The wavefunctions of H_2^+ are calculated using two independent methods: from an approximate numerical solution of the exact Hamiltonian, and by expanding in the basis of electronic states. These two methods reveal the errors which are implicit in applying

the Born-Oppenheimer approximation to the calculation of highly energetic dissociated states, which represent the final states in a high energy neutron scattering experiment, but these errors are found to be small for the momentum transfers actually realised. Finally, it is concluded that a reduction in the scattered intensity of neutrons in the main hydrogen peak would only be observable at momentum transfers approximately an order of magnitude higher than is currently obtainable.

Finally, the results of this work are summarised at the end of chapter 4, where it is concluded that electronic excitation cannot lead to a significant reduction in the measured Compton profile, and therefore cannot be responsible for the reported anomalous hydrogen cross sections.

1.1 The time of flight method

The neutron Compton scattering technique relies on the time of flight method. This method involves measuring the intensity of neutrons scattered through a fixed angle α, as a function of the *time of flight* of the neutron between the accelerator target and the detector. In these experiments, the energy transferred to the struck nucleus typically varies from about 5eV to 150eV, implying that we are close to the high energy limit where the impulse approximation is valid. In this case, the time scale of the scattering event is much shorter than the time scale of atomic motions within the sample, and the nuclei may be regarded as free particles. This means that the response function peaks at the classical *recoil energy* $E_r = \hbar^2 q^2/2M$, which is the energy imparted to a stationary nucleus in a collision with a neutron.

To understand the scattering we therefore consider the classical 'billiard ball' scattering of a neutron, as illustrated in Fig. 1.1(a): an incoming neutron, with momentum $\mathbf{p}$ and mass m, collides with a stationary nucleus of mass M. Conservation of energy and momentum requires:

$$p' \cos(\alpha) + k' \cos(\theta) = k \tag{1.1}$$

$$k' \sin(\theta) = p' \sin(\alpha) \tag{1.2}$$

$$\frac{k^2}{2m} = \frac{p'^2}{2M} + \frac{k'^2}{2m}. \tag{1.3}$$

The relative velocities of the incoming and outgoing neutrons are dependent on the scattering angle α,

$$\frac{k'}{k} = \frac{v'}{v} = \frac{\cos(\theta) + \sqrt{(M/m)^2 - \sin^2(\theta)}}{M/m + 1}. \tag{1.4}$$

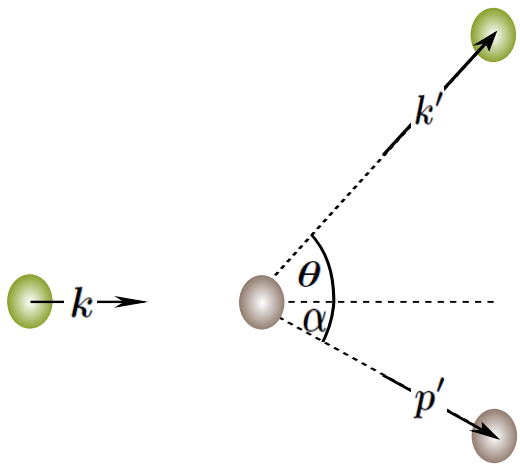

(a) The peak in the time of flight spectrum occurs at E_r, and may be interpreted classically; a neutron of momentum $\mathbf{k}$ scatters of a nucleus which is initially at rest. After the interaction, the neutron recoils at an angle θ and the nucleus recoils at an angle α.

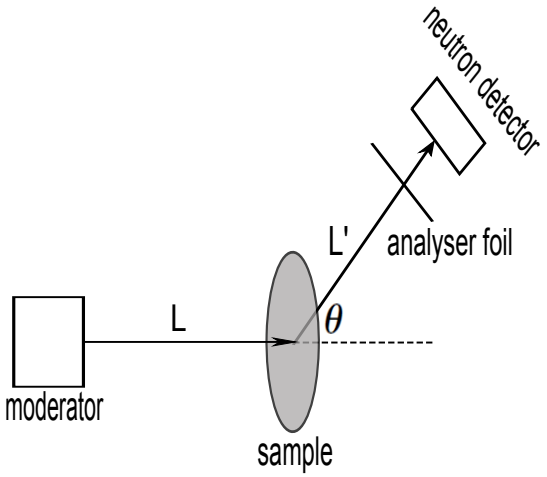

(b) A schematic illustration of the time of flight experiment. The neutron travels a distance L from from the moderator to the sample, where it scatters at an angle θ, before traveling a distance L' through the analyser foil to the neutron detector. The analyser foil absorbs neutrons of a specified energy

Figure 1.1: The time of flight experiment

For hydrogen $M \approx m$ and we obtain the expression $k'/k = \cos(\theta)$, which implies that $\theta \leq \pi/2$, and consequentially there is no backwards scattering from hydrogen. The transferred momentum is simply

$$q^2 = k^2 + k'^2 - 2kk'\cos(\theta) \tag{1.5}$$

and energy transferred to the nucleus is

$$E_r = \frac{k^2}{2m} - \frac{k'^2}{2m} = \frac{q^2}{2M}. \tag{1.6}$$

The time of flight method is performed on the 'inverse geometry' instrument VESUVIO. For an inverse geometry instrument, the energy of the *scattered* neutrons is analysed[1] by placing an analyser foil between the target and the detector to absorb neutrons at a particular resonant energy E_{foil}[2]. By subtracting the 'foil in' spectra from the 'foil out' spectra, the remaining spectra corresponds to the scattering of neutrons with final energy $E' \approx E_{foil}$ and final momentum $k' \approx \sqrt{2ME'}$. It is then possible to express the momentum transfer in terms of the scattering angle, which for hydrogen is simply $q = k'\tan(\theta)$.

[1] In a more conventional 'direct geometry' instrument, the energy of the *incident* neutrons is analysed with a 'chopper', which selects the velocity of the incoming neutrons.

[2] The energy resolution of the detector is therefore dependent upon the resonance width of the analyser foil.

Therefore a large scattering angle corresponds to a large momentum transfer. The time at which the neutron reaches the detector is given by

$$t = t_0 + \frac{L}{v} + \frac{L'}{v'}. \tag{1.7}$$

Where L is the distance from the accelerator target to the sample and L' is the distance from the sample to the detector. Because of the relationship between k and k', the time at which the neutrons reach the detector is dependent on the mass of the struck nucleus, with neutrons scattered from lighter nuclei arriving first. This idea is used in section 1.3 to separate the hydrogen peak, which is the first to be observed, from the peaks associated with heavier nuclei. By estimating the area under the observed peaks it is possible to extract the relative neutron cross sections for the constitutive materials. It is here that an anomaly arises; for large scattering angles (high momentum transfers) the scattering from hydrogen is significantly reduced and the measured cross section for hydrogen is therefore less than expected.

There are several complications that arise when performing these experiments, and these should be considered as possible causes of the anomalous results. The incident flux of neutrons, which varies with the incident neutron energy E_0, has a distribution $N(E_0)dE_0$; for epithermal neutrons from a pulsed source $N(E)$ is approximately equal to c/E, where c is a constant. The number of detected neutrons is dependent on the factor $N(E)$, and the corrections to the data are quite large. The possibility that the energy dependent detector efficiency deviates from the expected intensity has also been considered[15]. It has been shown that this could, in principle, lead to anomalous measurements at large scattering angles.

When performing theoretical calculations it is natural to determine the response, as a function of transferred energy, in a constant-$\mathbf{q}$ scan. As the time of flight varies for a particular detector, in a constant scattering angle scan, both the transferred energy and momentum vary. This presents complications when comparing experiment with theory because we have to convert between a constant scattering angle time of flight scan and a constant-$\mathbf{q}$ scan. This can be achieved with a suitable transformation[14], but again, the corrections are quite large and the validity of the impulse approximation must be assumed. Ideally, the response function would be measured directly, as a function of transferred energy and transferred momentum $\mathbf{q}$, using many closely spaced detectors and without resorting to the impulse approximation.

To understand how the possibility of electron excitation arises in experiments using the time of flight method, it is necessary to understand the theory behind the quantum mechanical scattering of neutrons from nuclei. The more detailed analysis involved for the quantum mechanical problem allows us to justify the simple classical picture. It also

establishes the relationship between the observed scattering and the detailed properties of the sample, via the response function, which allows information, such as the momentum distribution of the struck nucleus, to be extracted.

1.2 The theory behind neutron Compton scattering

To understand the relationship between the properties of the sample and the observed neutron Compton scattering, one starts with the *neutron cross section*, which is an observable quantity. Three approximations must be invoked to arrive at the form which is appropriate to high energy neutron scattering: i) The Born approximation, which is applicable when the scattering is *weak* and the wavelength of the incident neutron is much larger than the range of the scattering potential. ii) The incoherent approximation, which is applicable when the spatial scale of the scattering event is much shorter than the inter-nuclear separation. iii) The impulse approximation, which is applicable when the scattering event occurs on a very short timescale. Once these approximations have been invoked, the neutron cross section simplifies considerably.

1.2.1 The neutron cross section

The most fundamental quantity in any neutron scattering experiment is the neutron cross section. This quantity can be understood by considering the probability of an interaction, P_{int}, between an incident neutron and a sample of thickness Δx with a density of particles N,

$$P_{int} = \frac{W}{J} \propto N\Delta x. \tag{1.8}$$

Where W is the number of interactions per unit time and J is the incident flux of neutrons. The constant of proportionality defines the neutron cross section σ:

$$\frac{W}{J} \equiv \sigma N\Delta x. \tag{1.9}$$

The neutron cross section defines an effective area of a target particle and is measured in units of barn≡bn= $10^{-24}cm^2$. In a neutron scattering experiment an incident neutron with wave vector $\mathbf{k}$ is scattered into a state with wave vector $\mathbf{k}'$, transferring momentum $\hbar\mathbf{q}$ and energy $\hbar\omega$ to the sample in the process. The geometry of this neutron scattering experiment is shown in Fig. 1.2.

The quantity which is measured in an experiment is $Jd^2\sigma$, where $d^2\sigma$ is the double differential cross section: the fraction of neutrons with incident energy E scattered into

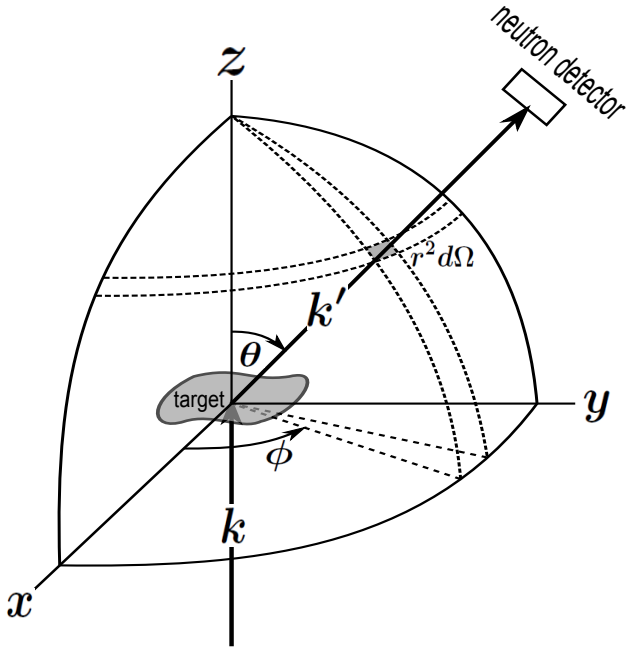

Figure 1.2: The geometry of a neutron scattering experiment. The incident neutron with wave vector $\mathbf{k}$ interacts with the target and is scattered into a state with wave vector $\mathbf{k}'$. The cross section is determined from a measurement of the number of neutrons scattered into the solid angle $d\Omega$ with an energy between E' and $E' + dE'$.

an element of solid angle $d\Omega$ with an energy between E' and $E' + dE'$. From these measurements the cross section per unit solid angle, per unit energy is determined to be

$$\frac{d^2\sigma}{d\Omega dE'}, \tag{1.10}$$

which has the units of (area/energy). To determine the microscopic form of the cross section it is simplest to start with elastic scattering. In this case the differential cross section is

$$d\sigma = \frac{W_{\mathbf{k}\to\mathbf{k}'}}{J}. \tag{1.11}$$

Where $W_{\mathbf{k}\to\mathbf{k}'}$ is the transition rate of the neutron between its initial state, with wavevector $\mathbf{k}$, to its final state, with wavevector $\mathbf{k}'$. This transition rate is determined from Fermi's golden rule,

$$W_{\mathbf{k}\to\mathbf{k}'} = \frac{2\pi}{\hbar}|\int d\mathbf{r}_n \psi^*_{\mathbf{k}}(\mathbf{r}_n)\hat{V}\psi_{\mathbf{k}'}(\mathbf{r}_n)|^2\rho(E'). \tag{1.12}$$

The neutron is represented by a plane wave,

$$\psi_{\mathbf{k}} = \frac{1}{\sqrt{V}}e^{i\mathbf{k}\cdot\mathbf{r}_n} \qquad \text{with} \qquad E = \frac{\hbar^2 k^2}{2m_n}, \tag{1.13}$$

which is normalised in an arbitrary volume V. The density of final states for the scattered neutron satisfies

$$\rho(E')dE' = \frac{V}{(2\pi)^3}d\mathbf{k}' = \frac{V}{(2\pi)^3}k'^2 dk' d\Omega. \tag{1.14}$$

Then, using the relationship $dE' = \hbar^2 k' dk'/m$, the transition rate is

$$W_{\mathbf{k}\to\mathbf{k}'} = \frac{k'\hbar V}{m}\left(\frac{m}{2\pi\hbar^2}\right)^2 |\int d\mathbf{r}_n \psi^*_{\mathbf{k}}(\mathbf{r}_n)\hat{V}\psi_{\mathbf{k}'}(\mathbf{r}_n)|^2 d\Omega. \tag{1.15}$$

We then use the relationship J =velocity of incident neutrons×density of incident neutrons= $\hbar k/mV$ to write the differential cross section as

$$d\sigma = V^2\left(\frac{m}{2\pi\hbar^2}\right)^2 \frac{k'}{k}|\int d\mathbf{r}_n \psi^*_{\mathbf{k}}(\mathbf{r}_n)\hat{V}\psi_{\mathbf{k}'}(\mathbf{r}_n)|^2 d\Omega. \tag{1.16}$$

We then adopt the notation

$$\langle \mathbf{k}'|\hat{V}|\mathbf{k}\rangle = \frac{m}{2\pi\hbar^2}\int d\mathbf{r}_n e^{-i\mathbf{k}'\cdot\mathbf{r}_n}\hat{V}e^{i\mathbf{k}\cdot\mathbf{r}_n} \tag{1.17}$$

to write the cross section per unit solid angle as

$$\frac{d\sigma}{d\Omega} = |\langle \mathbf{k}'|\hat{V}|\mathbf{k}\rangle|^2, \tag{1.18}$$

where we have used the fact that $k' = k$ for elastic scattering. We next need to generalise this to inelastic processes which occur when the neutron transfers some of its energy to the target:

$$E - E' = \frac{\hbar^2 k^2}{2m} - \frac{\hbar^2 k'^2}{2m} = \hbar\omega. \tag{1.19}$$

In this case we introduce the index n to label the internal states of the target. We then define the *microscopic* cross section per unit solid angle, associated with the transition of the target from the initial state $|\Psi_i\rangle$ to the final state $|\Psi_f\rangle$, to be:

$$\left(\frac{d\sigma}{d\Omega}\right)_i^f = \frac{k'}{k}|\langle \Psi_f \mathbf{k}'|\hat{V}|\mathbf{k}\Psi_i\rangle|^2. \tag{1.20}$$

The microscopic cross section per unit solid angle, per unit energy, is then defined such that

$$\left(\frac{d\sigma}{d\Omega}\right)_i^f \equiv \int_0^\infty dE' \left(\frac{d^2\sigma}{d\Omega dE'}\right)_i^f. \tag{1.21}$$

Conservation of energy then dictates that $E_i - E_f = \hbar\omega$, and therefore that

$$\left(\frac{d^2\sigma}{d\Omega dE'}\right)_i^f = \frac{k'}{k}|\langle \Psi_f \mathbf{k}'|\hat{V}|\mathbf{k}\Psi_i\rangle|^2 \delta(\hbar\omega + E_{n'} - E_n). \tag{1.22}$$

This expression contains the transition probabilities between microscopic states: using time-dependent perturbation theory[17], the probability that the system makes a transition from the state $|\mathbf{k}n\rangle$ to the state $|\mathbf{k}'n'\rangle$ is proportional to $|\langle n'\mathbf{k}'|\hat{V}|\mathbf{k}n\rangle|^2\delta(\hbar\omega+E_f-E_i)$. Finally, the experimentally determined quantity is the *macroscopic* cross section per unit solid angle, per unit energy. This is obtained by averaging over all of the microscopic states:

$$\frac{d^2\sigma}{d\Omega dE'} = \frac{k'}{k}\sum_{if} P_i|\langle\Psi_f\mathbf{k}'|\hat{V}|\mathbf{k}\Psi_i\rangle|^2\delta(\hbar\omega + E_f - E_i). \tag{1.23}$$

The probability distribution P_i corresponds to the Boltzmann distribution,

$$P_i = \frac{e^{-\frac{E_i}{kT}}}{\sum_i e^{-\frac{E_i}{kT}}}. \tag{1.24}$$

Additional averaging may also be required to account for the distribution of isotopes and positions of the nuclei. For the hydrides, which are discussed in section 1.3(a), this would involve averaging over the hydrogen occupancy of different interstitial sites.

The cross section, as expressed by Eq. 1.23, can be derived from formal scattering theory[18] in the first Born approximation[3]. This is a consequence of applying Fermi's golden rule, which contains the assumption that the potential is *weak* and each neutron therefore only scatters from the sample once: an assumption which is only valid for a sufficiently thin sample.

1.2.2 The scattering length

When the De Broglie wavelength of the incident neutron is much larger than the range of the scattering potential, the energy of the incident neutron is insufficient to resolve the structure of the target. The scattered wave is then spherically symmetric and may be characterised by a single parameter: the scattering length. This can be understood if we consider an arbitrary central potential $V(r)$, for which the asymptotic wavefunction of the neutron may be expressed in the form[18]

$$\psi_{\mathbf{k}} \sim e^{i\mathbf{k}\cdot\mathbf{r}_n} + f(\theta)\frac{e^{ikr}}{r}. \tag{1.25}$$

The function $f(\theta)$ is the *scattering amplitude* which, for a central potential, can be expanded in terms of Legendre polynomials:

[3]In formal scattering theory we obtain an identical result, but with the potential, $\hat{V}$, replaced by the *transition operator*, or T-matrix, $\hat{T}$. The T-matrix may then be expanded in terms of the potential and the Green function, $\hat{G}$, to obtain $\hat{T} = \hat{V} + \hat{G}\hat{V}\hat{G} + \cdots$. In the first Born approximation we simply apply $\hat{T} = \hat{V}$ to obtain the result, Eq.1.23.

$$f(\theta) = \frac{1}{2ik}\sum_{i=0}^{\infty}(2l+1)[e^{2i\delta_l}-1]P_l(\cos(\theta)), \tag{1.26}$$

which is uniquely defined by the phase shifts δ_l. The scattering amplitude is related to the angular cross section by

$$\frac{d\sigma}{d\Omega} = |f(\theta)|^2. \tag{1.27}$$

If we consider a very simple form for the central potential which corresponds to a *hard sphere* of radius r_0, then the phase shifts are found to be $\delta_l \sim (kr_0)^{2l+1}$. The interaction potential is known to be of very short range, of the order of 5 fm, and the neutron wavelengths that we shall be dealing with in this investigation are typically $k \approx 200\text{Å}^{-1}$. This means that $kr_0 \sim 10^{-2}$ and consequentially $\delta_1/\delta_0 \sim 10^{-4}$, so that to a good approximation we may consider only s-wave ($l = 0$) scattering. The scattering amplitude is then simply

$$f(\theta) = \frac{1}{2ik}[e^{2i\delta_0}-1] = [k\cot(\delta_0) - ik]^{-1}, \tag{1.28}$$

which can be expanded in powers of k^2 so that

$$f(\theta) = -b + ikb^2 + O(k^2). \tag{1.29}$$

The parameter b is the *scattering length*, which is equal to r_0 for the hard sphere potential. The scattering length characterises the purely s-wave scattering, and is in general a complex number $b = b' - ib''$, where the complex part describes absorption of the neutron by a nucleus. The cross section can therefore be represented as the sum of a scattering cross section σ_s and an absorption cross section σ_a. The absorption cross section is inversely proportional to the incident neutron velocity at low energies[19], except in the vicinity of a resonance when the formation of a long lived compound nucleus is likely and σ_a has a pronounced peak. For most nuclei the scattering cross section is much larger than the absorption cross section[4] (for hydrogen $\sigma_s = 81.67$bn and $\sigma_a = 0.3326$bn) and we may write $f(\theta) = -b$. Therefore

$$\sigma = \int |f(\theta)|^2 d\Omega = 4\pi|b|^2 \tag{1.30}$$

and to obtain agreement between Eq. 1.27 and Eq. 1.18, we require that

$$\langle \mathbf{k}'|\hat{V}|\mathbf{k}\rangle = \frac{m}{2\pi\hbar^2}\int d\mathbf{r}_n e^{-i\mathbf{k}'\cdot\mathbf{r}_n}\hat{V}e^{i\mathbf{k}\cdot\mathbf{r}_n} = -b. \tag{1.31}$$

This can only be satisfied by *Fermi's pseudopotential*[21, 22]

[4] Although there are notable exceptions such as ^{3}He[20].

$$\hat{V} = \frac{2\pi\hbar^2}{m} b\delta(\mathbf{r}_n). \tag{1.32}$$

Fermi's pseudopotential is defined to give the correct answer for s-wave scattering in the first Born approximation. The interaction between the neutron and the nucleus is assumed to be *impulsive* and therefore interatomic forces are ignored during the instant of the collision. In addition, the complex part of the scattering length which allows for absorption processes is also neglected. In practice, the scattering length which appears in Fermis's pseudopotential is treated as a phenomenological constant to be determined by experiment.

For an array of nuclei the potential operator is represented as a sum over the independent potentials of each nucleus[5],

$$\hat{V} = \sum_j \hat{V}_j = \frac{2\pi\hbar^2}{m} \sum_j b_j \delta(\mathbf{r}_n - \mathbf{R}_j). \tag{1.33}$$

The observed scattering is then the superposition of the spherical waves emanating from each nucleus. When Fermi's pseudopotential is substituted into the cross section, Eq.1.34, we obtain

$$\frac{d^2\sigma}{d\Omega dE'} = \left(\frac{k'}{k}\right) \sum_{if} P_i |\langle \Psi_f | \sum_j b_j e^{i\mathbf{q}\cdot\mathbf{R}_j} | \Psi_i \rangle|^2 \delta(\hbar\omega + E_f - E_i), \tag{1.34}$$

which is a function of the transferred momentum $\mathbf{q} = \mathbf{k} - \mathbf{k}'$ and the transferred energy $\hbar\omega$.

1.2.3 The bound atom cross section

The *bound* atom cross section characterises the scattering of low energy neutrons from bound atoms in condensed matter systems; it is distinct from the *free* atom cross section which is defined $\sigma_f = \frac{\sigma}{(1+m/M)^2}$. It is the bound atom cross section which is extracted directly from experimental data in the time of flight experiments[6]. The scattering length depends on the relative spins of the incident neutron and the struck nucleus. To describe an interaction between a neutron and a nucleus of spin I we define the scattering lengths b^+ and b^- for the total spin states $I + \frac{1}{2}$ and $I - \frac{1}{2}$ respectively. The cross section can then be expressed as the sum of a coherent part, which arises from the weighted averages of the scattering lengths, and an incoherent part which arises because of the difference in scattering lengths. The simplest example is hydrogen, for which

[5]This representation of the potential operator is valid in the first Born approximation since multiple scattering is assumed to be negligible.

[6]This is despite the fact that a nucleus is completely dissociated from its bound state in a high energy neutron-nucleus collision.

$$b^+ = 1.04 \times 10^{-14} m \qquad b^- = -4.74 \times 10^{-14} m. \tag{1.35}$$

Here, b^+ and b^- correspond to the triplet and singlet spin states respectively. The average is

$$\langle b \rangle = \frac{3}{4} b^+ + \frac{1}{4} b^- = -0.38 \times 10^{-14} m \tag{1.36}$$

and the coherent bound atom cross section is therefore

$$\sigma_c = 4\pi \langle b \rangle^2 = 1.8\text{bn}. \tag{1.37}$$

The total bound atom cross section is

$$\sigma = 4\pi \langle |b|^2 \rangle = 4\pi \left(\frac{3}{4} |b^+|^2 + \frac{1}{4} |b^-|^2 \right) = 81.7\text{bn}. \tag{1.38}$$

For hydrogen the scattering is almost entirely incoherent. This is because the opposite signs of b^+ and b^- result in a small average $\langle b \rangle$. This is not the case for deuterium, for which

$$b^+ = 0.95 \times 10^{-14} m \qquad b^- = 0.10 \times 10^{-14} m. \tag{1.39}$$

In this case the total bound atom cross section is $\sigma = 7.6$bn, which contains a large coherent part $\sigma_c = 5.6$bn. When quantum mechanical exchange forces are negligible and the averaging over spin degrees of freedom is independent of the thermal averaging, the cross section for scattering from N identical nuclei may be written

$$\frac{d^2\sigma}{d\Omega dE'} = \left(\frac{\sigma_c}{4\pi} + \delta_{jj'} \frac{\sigma_i}{4\pi} \right) \left(\frac{k'}{k} \right) S(\mathbf{q}, \omega), \tag{1.40}$$

where the index j refers to the j-th nucleus. The neutron cross section divides into a coherent part and an incoherent part. As a consequence of random spin orientations and isotope distributions, the potential experienced by the neutron varies throughout the sample. The coherent scattering is created by the average potential, experienced by the neutron as it passes through the sample, and leads to strong interference effects. The incoherent scattering is proportional to the mean square deviation of the potential, from its average value, and does not lead to interference effects. The *response function*[7], $S(\mathbf{q}, \omega)$, is defined

$$S(\mathbf{q}, \omega) = \sum_{if} P_i |\langle \Psi_f | \sum_j e^{i\mathbf{q}\cdot\mathbf{R}_j} | \Psi_i \rangle|^2 \delta(\hbar\omega + E_f - E_i). \tag{1.41}$$

[7]The function $S(\mathbf{q}, \omega)$ is more commonly referred to as the *dynamic structure factor*.

The response function contains information about the structure and dynamical properties of the target, including the probabilities of exciting the electronic modes. This investigation is essentially an analysis of the response functions for a variety of different models, with the aim being to extract the electronic excitation probabilities.

1.2.4 The Impulse approximation

In neutron scattering experiments involving sufficiently high momentum transfers we may, to a good approximation, take the limit $q \to \infty$. This is known as the impulse approximation, and it is assumed that it is valid in the time of flight experiments. The impulse approximation is applied by considering the response function, written in the form[8]

$$S(\mathbf{q},\omega) = \frac{1}{2\pi\hbar N}\int_{-\infty}^{\infty} dt e^{-i\omega t}\sum_{jj'} Y_{jj'}(\mathbf{q},t). \tag{1.42}$$

The density-density correlation function $Y_{jj'}$ is defined

$$Y_{jj'}(\mathbf{q},t) = \langle e^{-i\mathbf{q}\cdot\hat{\mathbf{r}}_j} e^{i\mathbf{q}\cdot\hat{\mathbf{r}}_{j'}(t)}\rangle, \tag{1.43}$$

where the angled brackets denote a thermodynamic average. In the Heisenberg representation, the time dependence of the operator $\hat{\mathbf{r}}_j$ is

$$\hat{\mathbf{r}}_j(t) = e^{i\mathcal{H}t}\mathbf{r}_j e^{-i\mathcal{H}t}. \tag{1.44}$$

The angular brackets denote an average over all degrees of freedom, including thermodynamic averaging. This form of the response function shows how the response of the sample is related to the spectrum of spontaneous fluctuations (correlations), a relationship which is formally described by the *fluctuation-dissipation theorem*. This relationship stems from the fact that neutron scattering, because it is a very weak process, measures the properties of the unperturbed system.

For large momentum transfers $q \gg 2\pi/d$ and it is only necessary to consider the incoherent terms, Y_{jj}, of the density-density correlation function. Physically, the spatial scale of the scattering event, which is set by $1/q$, is too small to detect correlations between the positions of different nuclei[9]. The impulse approximation is then applied to the incoherent terms by deriving the short time expansion of $\hat{\mathbf{r}}_j(t)$, which is obtained from the Taylor series:

[8] This form of the response function is obtained by writing the Dirac delta function as a time integral, and working in the Heisenberg representation[23].

[9] This approximation is particularly good for hydrogen since σ_i is much larger than σ_c.

$$\hat{\mathbf{r}}_j(t) = \hat{\mathbf{r}}_j(0) + it[\mathcal{H}, \hat{\mathbf{r}}_j] - \frac{t^2}{2}[\mathcal{H}, [\mathcal{H}, \hat{\mathbf{r}}_j]] + ... \tag{1.45}$$

The Hamiltonian is generally of the form

$$\mathcal{H} = \sum_j \frac{\hat{\mathbf{p}}_j^2}{2m_j} + V(\hat{\mathbf{r}}_j), \tag{1.46}$$

which implies

$$[\mathcal{H}, \hat{\mathbf{r}}_j] = -i\frac{\hat{\mathbf{p}}_j}{m_j}$$

$$[\mathcal{H}, [\mathcal{H}, \hat{\mathbf{r}}_j]] = \left[V, i\frac{\hat{\mathbf{p}}_j}{m_j}\right] = -\frac{1}{m_j}\frac{\partial V}{\partial \hat{\mathbf{r}}_j} = \frac{\hat{\mathbf{f}}_j}{m_j}. \tag{1.47}$$

Putting this together we can write the time dependency of the coordinate as

$$\hat{\mathbf{r}}_j(t) = \hat{\mathbf{r}}_j(0) + \frac{\hat{\mathbf{p}}_j(0)}{m_j}t + \frac{\hat{\mathbf{f}}_j(0)}{2m_j}t^2 + ... \tag{1.48}$$

In this expression $\hat{\mathbf{p}}_j$ is the momentum of the struck particle and $\hat{\mathbf{f}}_j$ is the force acting on it. In the impulse approximation we assume that the time t of the scattering event is so short that we may neglect the forces acting on the particle and consider the particle to be moving freely with initial momentum $\mathbf{p}$. Using the Baker-Campbell-Hausdorff theorem $e^A e^B = e^{A+B+1/2[A,B]+\cdots}$, the correlation function can then be written

$$\begin{aligned} Y_{jj}(\mathbf{q}, t) &\approx \langle e^{i(\mathbf{q}\cdot\hat{\mathbf{p}}_j/m_j + \frac{1}{2}\left[\mathbf{q}\cdot\hat{\mathbf{r}}_j, \mathbf{q}\cdot\hat{\mathbf{p}}_j/m_j\right])t}\rangle = \langle e^{i(\mathbf{q}\cdot\hat{\mathbf{p}}_j/m_j + \hbar q^2/2m_j)t}\rangle \\ \Rightarrow S_\infty(\mathbf{q}, \omega) &= \frac{1}{2\pi\hbar N}\sum_j \int_{-\infty}^{\infty} \langle e^{-i\omega t + \frac{i\hbar q^2 t}{2m_j} + i\mathbf{q}\cdot\hat{\mathbf{p}}_j t/m_j}\rangle dt. \end{aligned} \tag{1.49}$$

If the nucleus can be represented as a single particle state, which is a reasonable assumption if the nucleus sits in a Born-Oppenheimer potential well, then the response function takes a very useful form. The momentum state $|\mathbf{p}\rangle$ is an eigenstate of the momentum operator $\hat{\mathbf{p}}_j$ such that $\hat{\mathbf{p}}_j|\mathbf{p}_j\rangle = \hbar\mathbf{p}_j|\mathbf{p}_j\rangle$. With these single particle states, the expectation value is evaluated by integrating over the momentum and replacing the time integral with a Dirac delta function:

$$\begin{aligned} \int_{-\infty}^{\infty} \langle e^{-i\omega t + \frac{i\hbar q^2 t}{2m_j} + i\mathbf{q}\cdot\hat{\mathbf{p}}_j t/m_j}\rangle dt &= \int_{-\infty}^{\infty} dt \int d\mathbf{p}_j e^{-i\omega t + \frac{i\hbar q^2 t}{2m_j} + i\mathbf{q}\cdot\hbar\mathbf{p}_j/m_j} n(\mathbf{p}_j) \\ &= \int n(\mathbf{p}_j)\delta\left(\omega - \omega_r - \hbar\mathbf{q}\cdot\mathbf{p}_j/m\right) d\mathbf{p}_j. \end{aligned} \tag{1.50}$$

For N identical particles the summation over j contributes a factor of N, which cancels

with the factor of N in the denominator. We may then write the response function, obtained using the impulse approximation, as

$$S_\infty(\mathbf{q},\omega) = \frac{1}{\hbar}\int n(\mathbf{p})\delta\left(\omega - \omega_r - \hbar\mathbf{q}\cdot\mathbf{p}/m\right) d\mathbf{p}, \tag{1.51}$$

where the recoil energy of the struck nucleus is defined $E_r = \hbar\omega_r = \hbar^2q^2/2m$. In the impulse approximation, the response function is related to the momentum distribution of the target by a *Radon transformation*. This simple relationship between the response function and the momentum distribution of the sample is what makes the impulse approximation valuable; by inverting the Radon transformation it is possible to obtain the momentum distribution, and therefore also the spatial wavefunction[10], from measurements of the neutron cross section. This method has been applied to determine the momentum distributions of nuclei in several systems including: hydrogen in KH_2PO_4[3], the Fermi liquid ^{3}He[20], and the Bose condensate ^{4}He[24].

The impulse approximation can also be interpreted classically; if we consider the classical scattering of a neutron, with initial momentum $\mathbf{k}$, by a nucleus, with initial momentum $\mathbf{p}$, then conservation of energy and momentum requires

$$\frac{p^2}{2m} + \frac{k^2}{2M} = \frac{p'^2}{2m} + \frac{k'^2}{2M} \tag{1.52}$$

$$\mathbf{p} + \mathbf{k} = \mathbf{p}' + \mathbf{k}', \tag{1.53}$$

which implies that ω is

$$\omega = \frac{\hbar k^2}{2M} - \frac{\hbar k'^2}{2M} = \omega_r + \frac{\hbar\mathbf{q}\cdot\mathbf{p}}{m}. \tag{1.54}$$

This is exactly the value that the response function assigns to ω in the impulse approximation. In other words, in the impulse approximation the final states correspond to those of a free particle with initial momentum $\mathbf{p}$, scattered into a state with momentum $\mathbf{p}+\mathbf{q}$. Therefore we can obtain detailed information about the momentum distribution of the struck particle, which is created by the surrounding particles, without knowing the details of the interactions between the particles. Although the final state is assumed to be that of a free particle, the impulse approximation is still applicable to bound state problems, such as for a nucleus in a harmonic potential. In the final state, for sufficiently high energies, the forces acting on the nucleus do not change its energy significantly during the time scale of the interaction. In this case, the impulse approximation provides a continuous envelope of the discrete excitation spectra, which is actually observed if the energy resolution of the experiment is insufficient to distinguish between the individual

[10]There is a loss of phase when obtaining the wavefunction since $n(\mathbf{p}) = |\psi(\mathbf{p})|^2$. This loss of phase is only avoided if the wavefunction has the symmetry $\psi(\mathbf{r}) = \psi(-\mathbf{r})$.

peaks.

There is a subtlety involved when applying the impulse approximation to analyse experimental data. In the limit $q \to \infty$ the struck nucleus is completely dissociated, not only from other nuclei within a molecule or solid, but also from all of the electrons. It is shown in section 3.2 that for hydrogen the electron remains in its ground state for the energies considered and therefore it is sensible to refer to the *atomic* impulse approximation, for which the entire atom recoils. However, this does not make a significant difference to the analysis of the experimental data, because the mass of the atom is almost the same as the mass of the nucleus. At high enough energies the electrons can be excited as the atom recoils and, in a time of flight measurement, this would lead to a series of peaks arriving at different times.

For the short time expansion to be valid the correlation function $Y_{jj'}(\mathbf{q}, t)$ must decay to zero on a suitably short time scale τ_s[4]. This time scale is defined $\tau_s = 1/\Delta\omega$, where $\Delta\omega$, is the width of the response function. We therefore obtain

$$\tau_s \sim \frac{m_j}{q\langle p_q^2\rangle^{1/2}}, \tag{1.55}$$

where $\langle p_q^2\rangle^{1/2}$ is the width of the momentum distribution (but projected onto $\mathbf{q}$) of the struck nucleus. The inverse dependence of τ_s on q implies that the short time expansion is indeed valid when the transferred momentum is large.

1.2.5 Y-scaling

It is sometimes convenient to introduce the concept of *y-scaling*, which simplifies Eq. 1.51. By aligning the z axis of the momentum coordinates with $\mathbf{q}$ the response function can be expressed as a function of a single variable[25] $y = (m/\hbar q)(\omega - \omega_r)$:

$$S_\infty(\mathbf{q}, \omega) = \frac{m}{\hbar q} J(\hat{\mathbf{q}}, y). \tag{1.56}$$

Where $J(\hat{\mathbf{q}}, y)$ is the neutron Compton profile,

$$J(\hat{\mathbf{q}}, y) = \int n(\mathbf{p})\delta(\hat{\mathbf{q}} \cdot \mathbf{p} - y)d\mathbf{p}, \tag{1.57}$$

and $\hat{\mathbf{q}}$ is a unit vector in the direction of the momentum transfer $\mathbf{q}$. The Compton profile is therefore the one dimensional projection of the nuclear momentum distribution along the direction of $\mathbf{q}$. The Compton profile can be determined from measurements of the partial differential cross section by performing a constant energy scan through all possible scattering angles[11].

[11]However, for an isotropic system the nuclear momentum distribution can be determined from the

The y-scaling technique demonstrates that the impulse approximation corresponds to the simultaneous limit $q \to \infty$ and $\omega \to \infty$, such that y remains finite. By taking the limit in this way the response function is well approximated for sufficiently high momentum transfers by $S_\infty(\mathbf{q}, \omega)$. The y-scaling technique is used in several of the neutron Compton scattering experiments which are central to this investigation, including the work on the hydrides which is discussed later in this chapter.

In the limit of very high momentum transfers we may assume that the struck particle is initially at rest, and the appropriate limit of the response function is then obtained through *x-scaling*; by introducing the variable $x = \hbar q^2/2M\omega$ into Eq. 1.51, and taking the limit $q \to \infty$, we obtain[25]

$$\lim_{q\to\infty}[S_\infty(\mathbf{q}, \omega)] = \frac{1}{\omega}\delta(1 - x) = \delta(\omega - \omega_r). \tag{1.58}$$

By taking the limit $q \to \infty$ (whilst x remains constant) of $S_\infty(\mathbf{q}, \omega)$, which was obtained by applying the impulse approximation, we obtain a delta function peak in the response function, centred at the recoil energy E_r. Therefore, in the limit of infinite momentum transfer the response function describes scattering from a stationary nucleus. This choice of scaling is analogous to *Bjorken scaling*[26], which was originally used in lepton-nucleon scattering to provide experimental evidence for the existence of the 'point-like' constituents of nucleons, i.e, quarks.

1.2.6 Final state effects

In an experiment involving high energy neutrons it is often necessary to include the corrections to the impulse approximation which arise because q is finite, and consequentially, the final states of the recoiling protons are affected by the interatomic forces. If these corrections are large, then a detailed theory of the interactions in the system under study is required. In general these *final state effects* lead to a broadening of the response function, a shift of the peak to below the recoil frequency ω_r, and an asymmetry such that weight is transferred from the low frequency tail to the high frequency tail. These effects are conveniently captured by expanding the response function in powers of $1/q$, so that the leading order term corresponds to the impulse approximation.

The response function for finite values of q can be represented as the convolution of a *final state resolution function*, $R(\mathbf{q}, \omega')$, with the $q \to \infty$ limit of the response function:

$$S(\mathbf{q}, \omega) = \int_{-\infty}^{\infty} R(\mathbf{q}, \omega')S_\infty(\mathbf{q}, \omega - \omega')d\omega' \tag{1.59}$$

where the resolution function $R(\mathbf{q}, \omega)$ becomes a delta function $\delta(\omega)$ in the limit $q \to \infty$.

data collected at a single scattering angle.

For large values of q the resolution function should be approximately a delta function, which means that an expansion of $S_\infty(\mathbf{q}, \omega - \omega')$ in powers of ω' should give a convergent expression for $S(\mathbf{q}, \omega)$. The expansion takes the form

$$S(\mathbf{q}, \omega) = \frac{m}{\hbar q} \sum_{n=0}^{\infty} (-1)^n A_n(\mathbf{q}) \frac{d^n J(y)}{dy^n} \tag{1.60}$$

where the coefficients of the expansion are defined

$$A_n = \frac{R_n(\mathbf{q})}{n!} \frac{m}{\hbar q} \qquad \text{where} \qquad R_n(\mathbf{q}) = \int_{-\infty}^{\infty} \omega^n R(\mathbf{q}, \omega) d\omega. \tag{1.61}$$

These coefficients have been calculated explicitly[25], and are given by:

$$A_n(\mathbf{q}) = \begin{cases} 1 & n = 0 \\ 0 & n = 1, 2 \\ O(q^{-1}) & n = 3, 5, ... \\ O(q^{-2}) & n = 4, 6, ... \end{cases} \tag{1.62}$$

The antisymmetric corrections are of order q^{-1}, whilst the symmetric corrections are of order q^{-2}. For many neutron scattering experiments these final state corrections play a significant role in the analysis of the data. A notable example of the application of this procedure is in the determination of the condensate fraction[1, 2] in liquid ^{4}He[12]. However, when the energy transfer is of the order of 100eV the final state effects are expected to be small.

1.3 Neutron Compton scattering from hydrogen compounds

The motivation for studying the neutron response from systems containing hydrogen stems from several experiments. Anomalous measurements, of the atomic cross section for hydrogen, have been reported in neutron Compton scattering experiments involving hydrogen compounds[5, 6, 7, 8, 9, 10, 11]. We will examine a particularly clear example involving neutron Compton scattering from niobium and palladium hydrides[8].

[12]When the momentum transfer is sufficiently large the final state effects have been shown to be small[27].

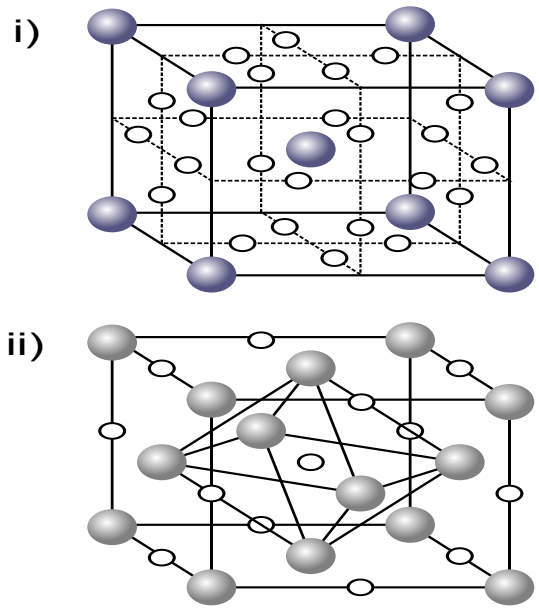

(a) i) The body centred cubic crystal structure of niobium with interstitial tetrahedral sites ii) The face centred cubic crystal structure of palladium with octahedral interstital sites

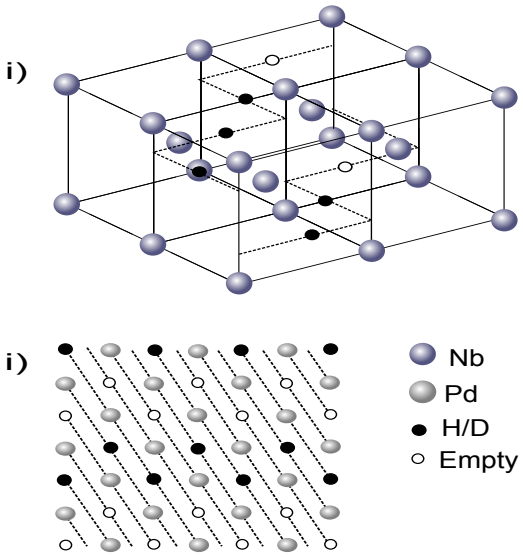

(b) i) NbH_x (NbD_x) at temperatures below $200K$, for which the hydrogen (deuterium) forms ordered chains. ii) Top view of PdH_x (PdD_x), for which hydrogen (deuterium) pairs occupy the 420 planes, alternating with pairs of empty sites.

Figure 1.3: Crystal structures of palladium and niobium hydrides.

1.3.1 Niobium and palladium hydrides

Niobium hydride (NbH_x) forms in the body centred cubic structure with the hydrogen atoms occupying tetrahedral interstitial sites illustrated in Fig. 1.3(a). There are six as many hydrogen sites as niobium atoms, allowing a maximum hydrogen capacity for NbH_6. In the doping range $0.73 < x < 1.00$ and the temperature range $200K < T < 370K$ the β-phase is stable, and in this phase the body centred cubic structure experiences a slight tetragonal distortion. Below about $200K$ the energetically favourable H sites form chains, as illustrated in Fig. 1.3(b).

Palladium hydride forms in the face centred cubic structure with the hydrogen atoms occupying octahedral interstitial sites. There are equal numbers of hydrogen sites and Palladium atoms, allowing a maximum hydrogen capacity for PdH. At room temperature the α-phase is saturated at about $x \approx 0.02$, where a β-phase starts to form, and is fully developed at $x \approx 0.60$. The hydrogen or deuterium atoms exhibit partial ordering, as illustrated in Fig. 1.3(b).

1.3.2 Anomalous neutron Compton cross sections

We will briefly summarise some results obtained, by Karlsson et al, from neutron Compton scattering measurements of the neutron cross sections of hydrogen in niobium and palladium hydrides[8]. The quantities of interest are the cross section ratios σ_H/σ_{Pd} and σ_H/σ_{Nb}, where σ_H, σ_{Nb} and σ_{Pd} are the neutron cross sections of hydrogen, niobium and palladium respectively. These values are determined directly from the time of flight spectra of niobium and palladium hydrides, and are compared with the conventionally expected values. It is found that in both compounds there is an anomalous reduction in σ_H/σ_{Nb} and σ_H/σ_{Pd}.

The double differential cross section for N identical nuclei is[28]

$$\frac{d^2\sigma}{d\Omega dE'} = Nb^2\frac{k'}{k}S(\mathbf{q},\omega). \tag{1.63}$$

The impulse approximation is then applied to represent the response function in terms of the Compton profile:

$$S(\mathbf{q},\omega) = \frac{M}{q}J(\hat{\mathbf{q}},y). \tag{1.64}$$

In a sample containing several distinct nuclei with different masses M_i, the number of neutrons measured in a time interval Δt is[29]

$$C(t)\Delta t = \left(N(E)\frac{dE}{dt}\Delta t\right)(\eta(E')\Delta\Omega f(E'))\sum_j N_j\frac{d^2\sigma_j}{d\Omega dE'}, \tag{1.65}$$

where $N(E)$ is the number of incident neutrons of energy E per cm^{2}s, $\eta(E')$ is the detector efficiency, $\Delta\Omega$ is the element of solid angle covered by the detector and $f(E')$ is the energy resolution associated with the analyser foil. The count rate can then be related to the Compton profile by

$$C(t) = \frac{k'}{k}\left(N(E)\frac{dE}{dt}\right)(\eta(E')\Delta\Omega f(E'))\sum_j \sigma_j N_j\frac{M_j}{4\pi q}J(\hat{\mathbf{q}},y)\otimes R(y). \tag{1.66}$$

The term $J(\hat{\mathbf{q}},y)\otimes R(y)$ represents a convolution of the Compton profile with the momentum space instrument resolution function. The cross section of a particular element, which is defined to be $\sigma_j = 4\pi|b_j|^2$, has a simple relationship with the area under the relevant peak in the time of flight spectrum,

$$A_j \propto \sigma_j N_j. \tag{1.67}$$

Where A_j is the area under the peak associated with the nuclei j, N_j is the number of nuclei in the sample, and Σ_j is the cross section. The constant of proportionality is

eliminated if we take the ratio of two such areas,

$$\frac{A_j}{A_{j'}} = \frac{\sigma_j N_j}{\sigma_{j'} N_{j'}}. \tag{1.68}$$

The ratio of two cross sections can therefore be obtained directly from the time of flight spectra, and can be compared with the expected value.

The time of flight spectrum for $NbH_{0.16}D_{0.70}$, measured at an angle $\theta = 65°$, is shown in Fig. 1.4(b). The experimental energy resolution is achieved by determining both the foil in and foil out spectra, as is illustrated in Fig. 1.4(a), using a gold analyser foil with a Lorentzian shaped absorption resonance centred at 4908 meV. The energy of the scattered neutron is therefore $E' \approx 4.9$ eV, which corresponds to a momentum $k' \approx 48.6\text{Å}^{-1}$, and a momentum transfer of $q \approx k' \tan(\theta)$. The difference spectrum is illustrated in Fig. 1.4(b) and has three peaks corresponding to hydrogen, deuterium and niobium, in order of increasing mass. The cross section ratios σ_H/σ_{Nb} and σ_H/σ_{Pd} determined from the areas of the peaks in the difference spectra are illustrated, as a function of the scattering angle, in Fig. 1.4(c) and Fig. 1.4(d). The ratio σ_H/σ_{Nb} starts to decrease significantly from the conventionally expected value for angles $\theta \geq 60°$ and for the highest scattering angles (and momentum transfers) is reduced by approximately 40%. Similar measurements of the ratio σ_H/σ_{Pd} show a substantial reduction from the conventionally expected value for angles $\theta \geq 50°$ and for the largest scattering angles is reduced by approximately 60%. On the contrary, measurements of the ratio σ_D/σ_{Nb}, which are shown in Fig. 1.4(e) do not show a significant deviation from the conventionally expected value, and show no angular dependence. However, this is to be expected for deuterium because the relationship between the transferred momentum and the scattering angle is $q \approx 2k'\sqrt{3 - z\cos(\theta)}/z$, with $z = \cos(\theta) + \sqrt{3 + \cos^2(\theta)}$. Therefore, whilst in hydrogenated samples a momentum transfer $q \approx 58\text{Å}^{-1}$ corresponds to a scattering angle $\theta \approx 60°$, in deuterated samples it corresponds to a much larger scattering angle, $\theta \approx 90°$. The data therefore indicates a shortfall, in the measured intensity of scattered neutrons, when the momentum transferred from the neutrons to the nuclei is large.

The scattering angle is also related to the scattering time (Eq. 1.55), whereby large scattering angles are associated with short scattering times. The cross section ratios σ_H/σ_{Nb} and σ_H/σ_{Pd} are shown in Fig. 1.4(f) and clearly decrease rapidly from the expected values for scattering times $\tau_s \leq 0.6$ fs.

Several possible sources of error have been ruled out in these experiments including the problem of separating the overlapping peaks in the time of flight spectrum. For large scattering angles, for which the anomalies are observed to be most significant, the overlap between the different peaks is actually small. The problem of multiple scattering has also been investigated using monte carlo simulations and has been found to lead to very small

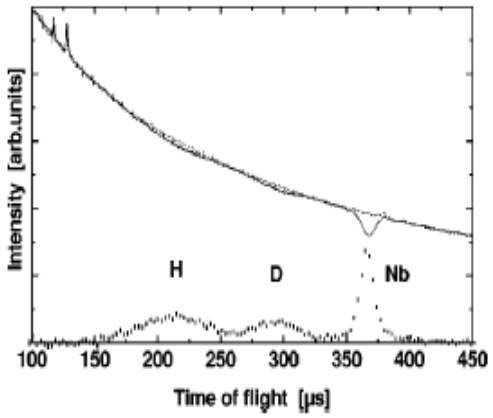

(a) The time of flight spectra for both the foil in, and foil out measurements at an angle $\theta \approx 65°$.

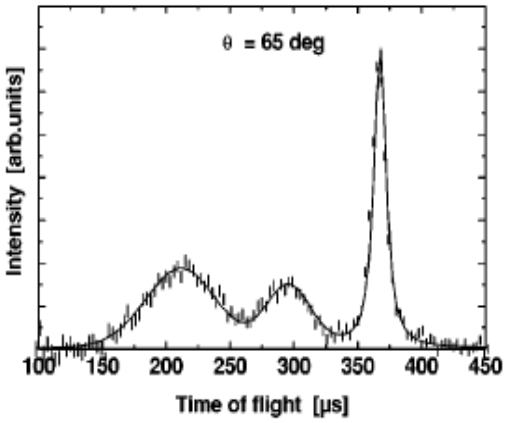

(b) The difference between the foil in and foil out measurements at an angle $\theta \approx 65°$.

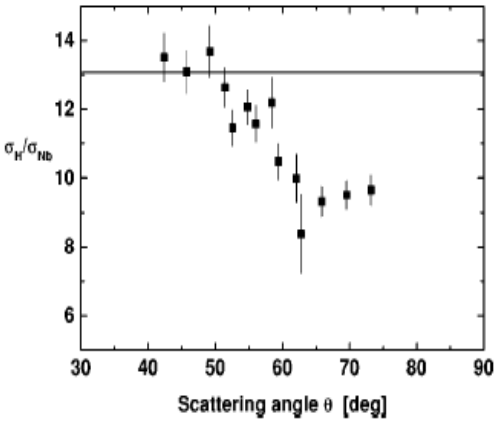

(c) The measured cross section ratio $\sigma_H/\sigma_{Nb} = 81.67/6.25 = 13.1$ in $NbH_{0.78}$. The conventionally expected value is indicated by the horizontal line, and is obtained, within experimental error, below an angle of $\theta \approx 60°$.

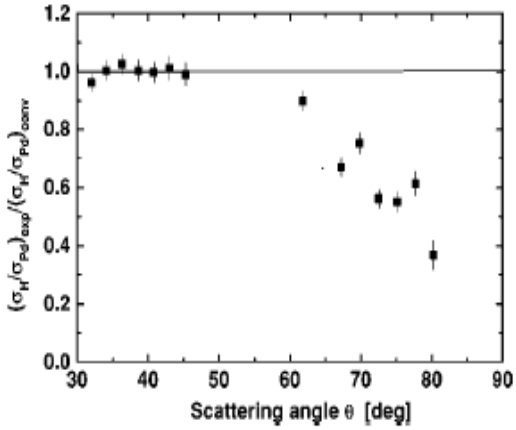

(d) The measured cross section ratio σ_H/σ_{Pd} in $NbH_{0.54}$, normalised to unity. The conventionally expected value is indicated by the horizontal line, and is obtained, within experimental error, below an angle of $\theta \approx 60°$.

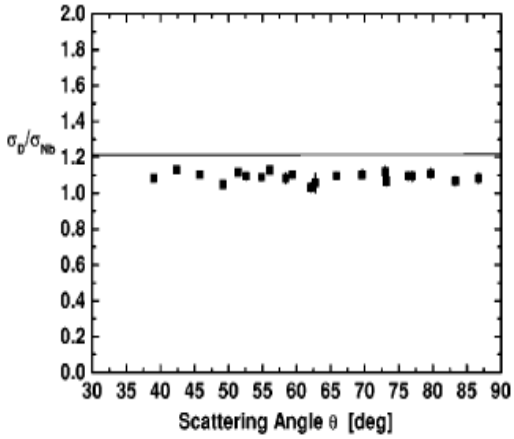

(e) The measured cross section ratio σ_D/σ_{Nb} in $NbH_{0.16}D_{0.70}$. The conventionally expected value $\sigma_D/\sigma_{Nb} = 7.63/6.25 = 1.22$ is indicated by the horizontal line.

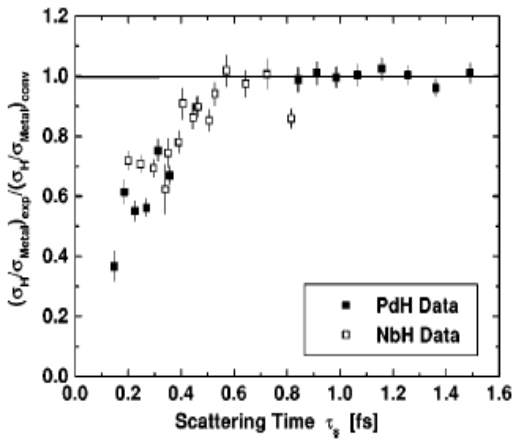

(f) The measured ratio of cross sections σ_H/σ_{Nb} and σ_H/σ_{Pd}, as a function of the scattering time Eq. 1.55. The ratios are found to be anomalously reduced below $\tau_s \approx 0.6$fs.

corrections.

1.4 Interpretation of the anomalous measurements

The departure of the measured hydrogen cross section from the expected value, for short scattering times, has prompted several investigations into possible quantum coherence between the protons in the sample[12]. It has been suggested that, for scattering times on the scale of 1fs, entangled states between the protons may be expected to survive. To support this idea a calculation of the scattering from an entangled pair of identical protons was performed, and the scattering was reported to be proportional to the spin dependent *incoherent* cross section, and was therefore less than the expected *total* cross section. However, Several problems with this result have been pointed out; it is inconsistent with observations of scattering from the highly entangled superfluid ^{4}He, which has a negligible incoherent cross section but produces observable scattering[14]. Furthermore, a more thorough treatment of the entangled protons reported that the reduced cross section was a consequence of unnecessary approximations[30, 31].

Apart from the possible theoretical causes of the anomalies, there are also several possible experimental causes, which are also being investigated[14, 15]. One possibility, which has been considered, is that the energy dependent detector efficiency deviates from the expected distribution at high energies. Another possibility is that the anomalies are related to the transformation from the constant scattering angle time of flight scan, to the constant $\mathbf{q}$ scan. It has been suggested that it would be better to determine the response function, $S(\mathbf{q}, \omega)$, directly by combining data from many detectors. The integrated intensity could then be obtained by integrating the response function over a constant $\mathbf{q}$ scan[15], rather than integrating over a constant scattering[13] angle.

We choose an alternative line of investigation: the possibility that electronic excitations may be responsible for the appearance of a reduced cross section. This idea is particularly relevant to hydrogen because the mass ratio of the electron to the nucleus m_e/M, which is an important parameter in the calculation of electronic excitations, is largest for hydrogen. The basic idea is as follows; if the electrons are excited in the collision, then the time of flight spectrum will contain additional peaks associated with the recoiling nuclei in excited electronic states, and these peaks would appear before the main hydrogen peak. The temporal separation of the peaks depends on the energetic separation of the electronic energy levels of the target. In the bulk material the electronic states form bands with a characteristic bandwidth t, and with a continuous set of energy levels. The resulting time of flight spectrum would therefore contain a shallow peak smeared out across all of the electronic states, and would be difficult to separate from the background.

The experimental investigations of high energy neutron scattering from hydrogen, such as the investigation of niobium and palladium hydrides discussed in the previous section, provide an incentive to explore the scattering process in more detail. In particular, we have discussed how the presence of peaks associated with electronic excitations may appear, and how they may not show up clearly in a time of flight spectrum.

The theoretical techniques introduced in this chapter will be used in the following three chapters to undertake a detailed investigation of the role of electronic excitations in high energy neutron scattering events. The response function as defined by Eq 1.41 provides the detailed information which we require to understand how the different modes are excited in the neutron-nucleus interactions, and the energy scales for which each mode becomes important.

To perform satisfactorily detailed calculations of neutron-nucleus scattering in bulk materials, such as for the metal hydrides, is no simple task. Several complications must be overcome, including: the accurate determination of the electronic structure, together with a good description of the coupling between the nuclear and electronic degrees of freedom which is valid for rapid nuclear motion, and the problem of treating the hydrogen order/disorder in the interstitial lattice sites. It is perhaps more reasonable to focus on the coupling between the electronic and nuclear motion which is a central part of this investigation. This involves the idea that a hydrogen nucleus sits in a potential well created by the surrounding electrons, and that the coupling between the electronic motion and the recoiling nucleus leads to electronic excitation. To quantify the size of this effect it is sufficient to study much simpler systems including hydrogen atoms and molecules.

The following two chapters involve calculating the response function for exactly solvable systems, to interpret the different mechanisms through which the systems are excited. In chapter 4, the focus turns to molecular hydrogen. The validity of the adiabatic approximation is analysed and the amount of electronic excitation, at the energy scale of the experiments, is determined. Finally, the investigation is rounded off by showing that the adiabatic approximation is valid up to very high energies, and therefore it can be shown that the probabilities associated with electronic excitation remain small even at the high energies considered. This conclusion supports the view that the anomalies may be related to the difficulties associated with the data analysis[14, 15].

Chapter 2

Electronic excitation in separable systems

The interaction between a simple atom or molecule and a neutron leads to a complicated response function, capable of describing the excitation probabilities associated with every excitation mode of the system, for the entire range of transferred energies and transferred momenta. Although the details of the response function depend intimately on the Hamiltonian of the target system, it is nevertheless possible to elucidate some of the most relevant features by studying the response functions of some exactly solvable models. In this chapter we focus on a particular class of Hamiltonian which is *separable* and we show how the response functions of such models can be interpreted. We also show that the separability, which makes these models exactly solvable, also means that the probability of electronic excitation is fundamentally limited because of the small mass ratio, m_e/m_p, of the electron mass and the proton mass.

In the first section we show how to interpret the matrix elements appearing in the response function in terms of the excitation probabilities of the system, and show that the matrix elements are all that is required to determine the amount of electronic excitation. We then separate the centre of mass wavefunction from the internal wavefunction and show that the excitation probabilities depend only on the internal wavefunctions. These techniques are very general and are applied to each of the models investigated. Two further techniques are also discussed which apply to particular models: the convolution of probabilities that occurs in separable systems, and the dependence on angular momentum of the response function, which applies to models with spherical symmetry.

The first model is the simple harmonic oscillator which is solved to obtain analytical formulas for both the wavefunctions and the electronic excitation probabilities. The results of this model demonstrate the high energy scales required to excite the electronic degrees of freedom, and the techniques employed to obtain the solution are also used in

the more sophisticated models to follow.

The second model is a four body system consisting of two protons and two electrons which interact via a model potential. The electron-proton interaction is harmonic and is attractive, whilst the electron-electron and proton-proton interactions are repulsive. This model resembles the molecule H_2^+ and, although it does not feature the important dissociation dynamics of a real molecule, it does demonstrate the difference in the energy scales of the electronic and nuclear modes. The wavefunction separates into a product of the nuclear and electronic wavefunctions. Because of this separability, the excitation probabilities of the four body problem are found to be a *convolution* of the excitation probabilities associated with the electronic and nuclear modes.

2.1 The excitation probabilities

In this section we will show how the matrix elements appearing in the response function can be associated with the probabilities of exciting the target system from the initial state Ψ_i to a final state Ψ_f. The response function is

$$S(\mathbf{q},\omega) = \sum_{if} P_i |\langle \Psi_i | \sum_j e^{i\mathbf{q}\cdot\mathbf{r}_j} | \Psi_f \rangle|^2 \delta(\hbar\omega + E_i - E_f). \tag{2.1}$$

We will consider a discrete set of microscopic states for the target system. Because we are interested in excitation probabilities, and not the coherent scattering (which becomes negligible for large momentum transfers anyway), we will focus on the scattering from a single nucleus located at $\mathbf{r}_t$. Then, according to Fermi's Golden rule, the matrix element $|\langle \Psi_i | e^{i\mathbf{q}\cdot\mathbf{r}_t} | \Psi_f \rangle|^2$ is the probability that the target makes a transition from the state Ψ_i to the state Ψ_f, when the momentum transferred from the neutron to the target is $\mathbf{q}$. To see that these probabilities are correctly normalised we use the resolution of the identity,

$$\sum_f |\Psi_f\rangle\langle\Psi_f| = \hat{1}, \tag{2.2}$$

and sum over all such quantities:

$$\sum_f |\langle \Psi_i | e^{i\mathbf{q}\cdot\mathbf{r}} | \Psi_f \rangle|^2 = \sum_f \langle \Psi_i | e^{i\mathbf{q}\cdot\mathbf{r}_t} | \Psi_f \rangle \langle \Psi_f | e^{-i\mathbf{q}\cdot\mathbf{r}_j} | \Psi_i \rangle = \langle \Psi_i | \Psi_i \rangle = 1. \tag{2.3}$$

We can therefore define a probability distribution

$$P_{\mathbf{q}}(E_f; E_i) \equiv |\langle \Psi_i | e^{i\mathbf{q}\cdot\mathbf{r}_t} | \Psi_f \rangle|^2 \tag{2.4}$$

which defines the probability that, if the system is initially in the state Ψ_i and gains

momentum $\mathbf{q}$, the system will be excited into the state Ψ_f. The contribution to the response function from the particle at $\mathbf{r}_t$ may be written

$$S_t(\mathbf{q},\omega) = \sum_{if} P_i P_{\mathbf{q}}(E_f;E_i)\delta(\hbar\omega + E_i - E_f). \tag{2.5}$$

In any calculations of the response function it is useful to verify that the complete set of excitations is included by integrating over the energy:

$$\int dE S_t(\mathbf{q},\omega) = 1. \tag{2.6}$$

Throughout this chapter we shall make the simplifying assumption that the initial state is the ground state Ψ_0, so that the distribution of initial states P_i is omitted. This assumption is is valid at room temperature because the thermal excitations are only of the order of 0.025eV: this is significantly lower in energy than the modes of excitation for the systems we investigate. In this chapter we calculate $P_{\mathbf{q}}(E_f)$ to determine the electronic excitation probabilities of the harmonic oscillator and a four body problem. These probabilities allow us to quantify the amount of electronic excitation occurring in these systems, at the energies we are interested in.

2.2 Conservation of momentum in the centre of mass frame

A simple technique for reducing the number of degrees of freedom of an N particle molecular Hamiltonian from $3N$ to $3N-3$ is to make use of the translational invariance by representing the Hamiltonian in the centre of mass frame. The general Hamiltonian for a system of N particles is

$$\mathcal{H} = \sum_{i=1}^{N} \frac{\hat{p_i}^2}{2m_i} + \frac{1}{2}\sum_{i<j}\hat{V}_{ij}(|\mathbf{r}_i - \mathbf{r}_j|). \tag{2.7}$$

The centre of mass coordinate of the system is defined to be

$$\mathbf{R}_{cm} = \frac{1}{M}\sum_{i=1}^{N} m_i\mathbf{r}_i \qquad M = \sum_{i=1}^{N} m_i. \tag{2.8}$$

The remaining $N-1$ coordinates may be expressed as linear combinations of the original coordinates:

$$\mathbf{R}_i = \sum_{j=1}^{N} T_{ij}\mathbf{r}_j \qquad i = \{1,....,N-1\}. \tag{2.9}$$

The transformation matrix $\hat{T}$ is defined so that the last row contains the components of the centre of mass coordinate, $T_{Nj} = m_j/M$. Then translational invariance implies that the addition of an arbitrary displacement vector $\mathbf{R}_0$ leaves the transformation unchanged:

$$\mathbf{R}_i = \sum_{j=1}^{N-1} T_{ij}\mathbf{r}_j = \sum_{j=1}^{N-1} T_{ij}(\mathbf{r}_j + \mathbf{R}_0) \Rightarrow \sum_{j=1}^{N-1} T_{ij} = 0. \tag{2.10}$$

In the new coordinates the Hamiltonian is[32]

$$\mathcal{H} = \sum_{i=1}^{N-1} P_{ij}\hat{P}_i\hat{P}_j + \frac{\hat{P}_{cm}^2}{2M} + \frac{1}{2}\sum_{i<j}\hat{V}_{ij}(\mathbf{R}_1, ..., \mathbf{R}_{N-1}). \tag{2.11}$$

Therefore, to separate the centre of mass motion from the internal coordinates it is required that the components of the remaining $N-1$ coordinates sum to zero, and there is clearly an element of choice when deciding on the appropriate coordinate system. Furthermore, it is possible to choose from a discrete number of different Jacobi coordinates which diagonalise the transformation matrix P_{ij}, thereby eliminating the cross terms in the momentum operators[33]. Often it is intuitive to group the particles into clusters and to choose the centre of mass coordinates of the various clusters as a set of Jacobi coordinates. Once the centre of mass coordinate has been separated from the internal coordinates it is then a simple matter to obtain the centre of mass wavefunction,

$$\Psi^{cm}(\mathbf{R}_{cm}) = \frac{1}{\sqrt{V}} e^{i\mathbf{k}_{cm}\cdot\mathbf{R}_{cm}}, \tag{2.12}$$

and to write the total wavefunction Ψ^t as the product of the centre of mass wavefunction Ψ^{cm} and an internal wavefunction Ψ^{in}:

$$\Psi^t(\mathbf{R}_{cm}, \mathbf{R}_1, ..., \mathbf{R}_{N-1}) = \Psi^{cm}(\mathbf{R}_{cm})\Psi^{in}(\mathbf{R}_1, ..., \mathbf{R}_{N-1}), \tag{2.13}$$

with energy $E = E_{cm} + E_{in}$. If a neutron scatters from the particle with coordinate $\mathbf{r}_t$, the transition probability is

$$\left|\left\langle \Psi_i^t(\mathbf{r}_1, ..., \mathbf{r}_N) \left| e^{i\mathbf{q}\cdot\mathbf{r}_t} \right| \Psi_f^t(\mathbf{r}_1, ..., \mathbf{r}_N) \right\rangle\right|^2. \tag{2.14}$$

The coordinate of the scattering target can be written as

$$\mathbf{r}_t = \mathbf{R}_{cm} + \sum_{j=1}^{N-1} \alpha_j \mathbf{R}_j, \tag{2.15}$$

where the components α_j are obtained from the matrix $\hat{T}$. The matrix element may then be written as the product

$$\left|\left\langle \Psi_i^{cm}(\mathbf{R}_{cm}) \left| e^{i\mathbf{q}\cdot\mathbf{R}_{cm}} \right| \Psi_f^{cm}(\mathbf{R}_{cm}) \right\rangle\right|^2$$
$$\times \left|\left\langle \Psi_i^{in}(\mathbf{R}_1, ..., \mathbf{R}_{N-1}) \left| e^{i\sum_{j=1}^{n-1}\alpha_j \mathbf{q}\cdot\mathbf{R}_j} \right| \Psi_f^{in}(\mathbf{R}_1, ..., \mathbf{R}_{N-1}) \right\rangle\right|^2. \quad (2.16)$$

The first term can be easily evaluated:

$$\left\langle \Psi_i^{cm}(\mathbf{R}_{cm}) \left| e^{i\mathbf{q}\cdot\mathbf{R}_{cm}} \right| \Psi_f^{cm}(\mathbf{R}_{cm}) \right\rangle = \frac{1}{V}\int e^{-i\mathbf{k}_{cm}\cdot\mathbf{R}_{cm}} e^{i\mathbf{q}\cdot\mathbf{R}_{cm}} e^{i\mathbf{k}'_{cm}\cdot\mathbf{R}_{cm}} d\mathbf{R}_{cm} = \delta_{\mathbf{k}'-\mathbf{k},\mathbf{q}}. \quad (2.17)$$

Finally, the response function can then be represented in terms of the internal wavefunctions by summing over the final states with momentum $\mathbf{k}'$, with the only contribution arising when $\mathbf{k}' - \mathbf{k} = \mathbf{q}$

$$S_t(\mathbf{q}, \omega) = \sum_{if} P_i \left|\left\langle \Psi_i^{in} \left| e^{i\sum_{j=1}^{N-1}\alpha_j \mathbf{q}\cdot\mathbf{R}_j} \right| \Psi_f^{in} \right\rangle\right|^2 \delta(\hbar\omega - \Delta E_{in} - \Delta E_{cm}), \quad (2.18)$$

where the energy transferred to the centre of mass frame is

$$\Delta E_{cm} = \frac{k^2}{2M} + \frac{\mathbf{k}\cdot\mathbf{q}}{M} \quad (2.19)$$

and the energy transferred to the internal wavefunction is denoted ΔE_{in}. The total momentum is transferred to the centre of mass frame, reflecting the fact that in the centre of mass frame the total momentum must be equal to zero. The energy is transferred to both the centre of mass wavefunction, and to the internal wavefunction, thereby exciting the internal modes of the system. By transforming to the centre of mass frame we can see that the electronic excitations probabilities that we are interested in are completely contained in the matrix elements of the internal wavefunctions. This method is used in each of the models in this chapter, and in the investigation of molecular hydrogen in chapter 4.

2.3 The convolution of probabilities in separable models

The excitation probabilities associated with the different modes of a system can occasionally be decomposed into a convolution of the excitation probabilities associated with each of the modes. For this simplification to work, it must be possible to separate the Hamiltonian using a linear transformation of the coordinates. This is the case in section 2.6 where

a four body wavefunction is expressed as a product involving the centre of mass motion, and the electronic and nuclear motion. In this case it is possible to describe the four body excitation probabilities in terms of a convolution of the electronic and nuclear excitation probabilities. One could also imagine more complicated systems where the excitations of independent modes may lead to a similar convolution of the excitation probabilities.

In a separable system the wavefunction may be expressed as the product

$$\Psi(\mathbf{r}_1, ..., \mathbf{r}_n) = \prod_{j=1}^{n} \Psi^j(\mathbf{r}_j). \tag{2.20}$$

The coordinate of the scattering target can be written as

$$\mathbf{r}_t = \sum_{j=1}^{n} \alpha_j \mathbf{r}_j \tag{2.21}$$

and the matrix element is

$$\left\langle \Psi_i(\mathbf{r}_1, ..., \mathbf{r}_n) \left| e^{i\mathbf{q}\cdot\mathbf{r}_t} \right| \Psi^f(\mathbf{r}_1, ..., \mathbf{r}_n) \right\rangle = \prod_{j=1}^{n} \left\langle \Psi_i^j(\mathbf{r}_j) \left| e^{i\alpha_j\mathbf{q}\cdot\mathbf{r}_j} \right| \Psi_f^j(\mathbf{r}_j) \right\rangle . \tag{2.22}$$

The probability of exciting the target is

$$P_{\mathbf{q}}(E_f; E_i) = \prod_{j=1}^{n} \left| \left\langle \Psi_j^i(\mathbf{r}_j) \left| e^{i\alpha_j\mathbf{q}\cdot\mathbf{r}_j} \right| \Psi_j^f(\mathbf{r}_j) \right\rangle \right|^2 = \prod_{j=1}^{n} P_{\mathbf{q}}^j(E_f^j; E_i^j), \tag{2.23}$$

where the total energy is $E = \sum_{j=1}^{n} E^j$ and the probabilities associated with the coordinates $\mathbf{r}_j$ are denoted $P_{\mathbf{q}}^j$. The response function can then be expressed as a convolution of the probabilities associated with exciting each mode:

$$S_t(\mathbf{q}, \omega) = \sum_{if} P_i \delta(\hbar\omega + E_i - E_f) \prod_{j=1}^{n} P_{\mathbf{q}}^j(E_f^j; E_i^j). \tag{2.24}$$

Associated with each mode of excitation is a momentum scale, T_{ij}, and an energy scale, E^j. These scales determine the characteristics of the response function for a separable model, and when the energy scales are different, it is a simple matter to distinguish between the different modes of excitation in the observed response function.

2.4 Separating the rotational symmetry

When determining the response of a simple one body problem it is often the case that the system can be well described by a spherically symmetric potential; this is true for the hydrogen atom, and is often assumed to be true in simple atomic calculations. In these cases it is always possible to calculate the excitation probabilities as a one dimensional

integral over the radial coordinate. The single particle Hamiltonian for a spherically symmetric system is

$$\mathcal{H} = -\frac{\hbar^2}{2m}\nabla^2_{\mathbf{r}} + V(|\mathbf{r}|). \tag{2.25}$$

The solution is represented as a product of a spherical harmonic Y_l^m and a term depending on $r = |\mathbf{r}|$:

$$\Psi(\mathbf{r}) = Y_l^m(\theta,\phi)X_{nl}(r). \tag{2.26}$$

If we assume that the system is initially in the ground state the transition matrix element is

$$\left\langle \Psi_0 \left| e^{i\mathbf{q}\cdot\mathbf{r}} \right| \Psi_f \right\rangle = \frac{1}{\sqrt{4\pi}} \int_{\phi=0}^{2\pi}\int_{\theta=0}^{\pi}\int_{r=0}^{\infty} X_{00}^*(r)e^{i\mathbf{q}\cdot\mathbf{r}}Y_l^m(\theta,\phi)X_{nl}(r)r^2\sin(\theta)drd\theta d\phi. \tag{2.27}$$

The exponential can be expanded as an infinite sum involving spherical Bessel functions J_l:

$$e^{i\mathbf{q}\cdot\mathbf{r}} = 4\pi\sum_{l'=0}^{\infty} i^{l'}J_{l'}(qr)\sum_{m'=-l'}^{l'}(Y_{l'}^{m'})^*(\theta,\phi)Y_{l'}^{m'}(\theta',\phi'), \tag{2.28}$$

where θ,ϕ are the angular coordinates of $\mathbf{r}$ and θ',ϕ' are the angular coordinates of $\mathbf{q}$. Then substituting this into Eq. 2.27 and using the orthogonality of the spherical harmonics we obtain

$$\left\langle \Psi_0 \left| e^{i\mathbf{q}\cdot\mathbf{r}} \right| \Psi_f \right\rangle = \sqrt{4\pi}Y_l^m(\theta',\phi')\int_{r=0}^{\infty} r^2X_{00}^*(r)J_l(qr)X_{nl}(r)dr, \tag{2.29}$$

and the probability of exciting the system into the state with quantum numbers (n,l,m) is therefore

$$P_{\mathbf{q}}(n,l,m) = 4\pi(Y_l^m)^*(\theta',\phi')Y_l^m(\theta',\phi')\left|\int_{r=0}^{\infty} r^2X_{00}^*(r)J_l(qr)X_{nl}(r)dr\right|^2. \tag{2.30}$$

This expression can be simplified further by applying the addition theorem for spherical harmonics:

$$P_l(\cos(\gamma)) = \frac{4\pi}{2l+1}\sum_{m=-l}^{l}(Y_l^m)^*(\theta,\phi)Y_l^m(\theta',\phi'), \tag{2.31}$$

where P_l is a Legendre polynomial and γ is the angle between the coordinates of the spherical harmonics. In Eq. 2.30 γ equals zero and therefore $P_l(\gamma) = 1$. Finally, after

summing over the quantum number m we obtain

$$P_{\mathbf{q}}(n,l) = \sum_{m=-l}^{l} P_{\mathbf{q}}(n,l,m) = (2l+1)\left|\int_{r=0}^{\infty} r^2 X_{00}^*(r) J_l(qr) X_{nl}(r) dr\right|^2. \tag{2.32}$$

This result is used for a four body problem later in this chapter, and for the hydrogen atom in chapter 3.

2.5 The harmonic oscillator

To introduce the mathematical techniques and theoretical concepts encountered in real physical systems, it is best to start with the simplest possible model: the harmonic oscillator. The wavefunctions and their respective energies can be easily found using standard techniques for solving ordinary differential equations, but we choose instead to use a slightly less conventional approach involving integral representations (appendix A). This approach has the advantage that it can be generalised to the more complicated problem of calculating the dissociated states of hydrogen, which is encountered in the next chapter. In this section we calculate the response function of the harmonic oscillator in three simple steps: i) we transform the Hamiltonian to the centre of mass frame, ii) we calculate the harmonic wavefunctions, and iii) we calculate the harmonic response function. These steps are the same, albeit less complicated, as those used to solve all the systems in this investigation, and so the harmonic oscillator is a useful model to study.

The harmonic potential is often encountered in physical systems and leads to a discrete set of vibrational modes, such as the phonons in a lattice, and the vibrational modes of nuclei in molecules. We are interested in electronic excitations, so we employ a toy Hamiltonian for an electron and a proton with an attractive harmonic interaction:

$$\mathcal{H} = -\frac{\hbar^2}{2m_p}\nabla^2_{\mathbf{R}_1} - \frac{\hbar^2}{2m_e}\nabla^2_{\mathbf{r}_1} + \frac{k_1}{2}(\mathbf{R}_1 - \mathbf{r}_1)^2. \tag{2.33}$$

2.5.1 Tranformation into the centre of mass frame

We employ the centre of mass coordinate, $\mathbf{R}_{cm}$, and the relative coordinate, $\mathbf{R}$, between the electron and the proton:

$$\mathbf{R}_{cm} = \frac{m_p\mathbf{R}_1 + m_e\mathbf{r}_1}{m_e + m_p} \qquad \mathbf{R} = \mathbf{R}_1 - \mathbf{r}_1. \tag{2.34}$$

In the centre of mass frame the Hamiltonian is

$$\mathcal{H} = -\frac{\hbar^2}{2M}\nabla^2_{\mathbf{R}_{cm}} - \frac{\hbar^2}{2\mu}\nabla^2_{\mathbf{R}} + \frac{k_1}{2}\mathbf{R}^2, \tag{2.35}$$

for which the effective masses are defined

$$M = m_e + m_p \qquad \mu = \frac{m_e m_p}{m_e + m_p}. \tag{2.36}$$

The first term in the Hamiltonian controls the translational motion of the centre of mass frame, whilst the remaining terms control the relative motion of the two particles in the centre of mass frame. The Hamiltonian separates in these coordinates, resulting in a solution of the form

$$\Psi^{ho}(\mathbf{R}_{cm}, \mathbf{R}) = \frac{1}{\sqrt{V}} e^{i\mathbf{k}_{cm}\cdot\mathbf{R}_{cm}} \Psi(\mathbf{R}). \tag{2.37}$$

The total energy is the sum of the centre of mass energy and the internal energy: $E = E_{cm} + E_{in}$.

2.5.2 The internal wavefunctions

The wavefunction representing the relative motion of the two particles in the centre of mass frame satisfies

$$\left[-\frac{\hbar^2}{2\mu}\nabla^2_{\mathbf{R}} + \frac{k_1}{2}\mathbf{R}^2\right]\Psi(\mathbf{R}) = E_{in}\Psi(\mathbf{R}). \tag{2.38}$$

The coefficients can be removed with a suitable scaling of the coordinate $\mathbf{R}$ and the energy E_{in}:

$$\mathbf{r} = \left(\frac{\mu k_1}{\hbar^2}\right)^{\frac{1}{4}}\mathbf{R} \qquad \varepsilon_{in} = \left(\frac{\mu}{\hbar^2 k_1}\right)^{\frac{1}{2}} E_{in}, \tag{2.39}$$

which gives

$$\left[-\nabla^2_{\mathbf{r}} + \mathbf{r}^2\right]\Psi(\mathbf{r}) = 2\varepsilon_{in}\Psi(\mathbf{r}). \tag{2.40}$$

The equation is again separable and the internal wavefunction factorises into the product state $\Psi(\mathbf{r}) = \psi_x(x)\psi_y(y)\psi_z(z)$ with energy $\varepsilon_{in} = \varepsilon_x + \varepsilon_y + \varepsilon_z$, where each function ψ satisfies an equation of the form

$$\left[-\frac{d^2}{dx} + x^2\right]\psi(x) = 2\varepsilon\psi(x). \tag{2.41}$$

The asymptotic behaviour of this equation as $x \to \infty$ is found using the WKB approximation. Then the ansatz $\psi(x) = e^{-\frac{x^2}{2}}\phi(x)$ results in a simple equation for $\phi(x)$,

$$\left[\frac{d^2}{dx^2} - 2x\frac{d}{dx} + (2\varepsilon - 1)\right]\phi(x) = 0. \tag{2.42}$$

The coefficients of the above equation are linear in the dependent variable: a situation which is encountered in each of the three systems described in this chapter. It may therefore be solved using the method of integral representations by introducing the *Laplace kernel* e^{zx}

$$\phi(x) = \int_C e^{zx} f(z) dz. \tag{2.43}$$

This transforms the differential equation into an integral equation,

$$\int_C e^{zx} f(z)(z^2 - 2xz + (2\varepsilon - 1))dz = 0. \tag{2.44}$$

Then integrating by parts we obtain

$$= [-2ze^{zx} f(z)]_{\partial C} + \int_C \left((z^2 + 2\varepsilon + 1)f(z) + 2z\frac{df(z)}{dz}\right) e^{zx} dz. \tag{2.45}$$

The function $f(z)$ is chosen so that both the integrand and the boundary term vanish. The integrand vanishes when

$$\frac{df(z)}{dz} + \left(\frac{z^2 + 2\varepsilon + 1}{2z}\right) f(z) = 0. \tag{2.46}$$

The function $f(z)$ which solves this equation is

$$f(z) = e^{-\frac{z^2}{4}} z^{-\frac{2\varepsilon+1}{2}}, \tag{2.47}$$

which gives the integral representation for $\phi(x)$,

$$\phi(x) \propto \int_C e^{zx} e^{-\frac{z^2}{4}} z^{-\frac{2\varepsilon+1}{2}} dz, \tag{2.48}$$

where the normalisation is to be determined at the end of the calculation. The boundary term can be made to vanish by choosing a closed contour which encircles the pole at the origin. The wave function must be finite which implies that the pole must be of integer order n, where $n > 0$. This quantises the energy spectrum so that the energy levels are given by

$$\frac{2\varepsilon + 1}{2} = n + 1 \Rightarrow \varepsilon = n + \frac{1}{2}. \tag{2.49}$$

Returning to the integral representation and transforming to the new variable $z = 2t$ we find

$$\phi(x) \propto \int_{C(0)} e^{-t^2+2xt} t^{-n-1} dt. \tag{2.50}$$

This integral can be evaluated using Cauchy's integral formula,

$$\left[\frac{d^n}{dz^n} f(z)\right]_{z=z_0} = \frac{n!}{2\pi i} \int_{C(z_0)} \frac{f(z)}{(z-z_0)^{n+1}} dz, \tag{2.51}$$

which gives, when applied to Eq. 2.50

$$\phi(x) \propto \left[\frac{d^n}{dt^n} e^{-t^2+2xt}\right]_{t=0}. \tag{2.52}$$

Making a further substitution $\omega = x - t$, we obtain

$$\phi(x) \propto (-1)^n e^{x^2} \left[\frac{d^n}{d\omega^n} e^{-\omega^2}\right]_{\omega=x} = (-1)^n e^{x^2} \frac{d^n}{dx^n} e^{-x^2} = H_n(x). \tag{2.53}$$

This expression relates $\phi(x)$ to the Rodrigues representation of the Hermite polynomials $H_n(x)$, which can be used to calculate the wavefunctions. The normalisation constant is determined from the integral

$$N^2 = \int_{-\infty}^{\infty} \psi(x)^* \psi(x) dx = 2^n \sqrt{\pi} n! \tag{2.54}$$

The normalised wavefunction is therefore

$$\psi(x) = \frac{1}{\sqrt{2^n n! \pi^{\frac{1}{2}}}} e^{-\frac{x^2}{2}} H_n(x). \tag{2.55}$$

Finally, the internal wave function with quantum numbers $\mathbf{n} = (n_x, n_y, n_z)$ is then

$$\Psi_{\mathbf{n}}(\mathbf{r}) = \frac{1}{\sqrt{2^{n_x+n_y+n_z} n_x! n_y! n_z! \pi^{\frac{3}{2}}}} e^{-\frac{1}{2}(x^2+y^2+z^2)} H_{n_x}(x) H_{n_y}(y) H_{n_z}(z) \tag{2.56}$$

with an energy of

$$E_{\mathbf{n}} = \left(\frac{\hbar^2 k}{\mu}\right)^{\frac{1}{2}} \left(n_x + n_y + n_z + \frac{3}{2}\right). \tag{2.57}$$

2.5.3 The response function

The response function of the harmonic oscillator to an interaction between the neutron and the proton is

$$S(\mathbf{q}, \omega) = \sum_{if} P_i |\langle \Psi_i^{ho} | e^{i\mathbf{q}\cdot\mathbf{R}_1} | \Psi_f^{ho} \rangle|^2 \delta(\hbar\omega + E_i - E_f). \tag{2.58}$$

The coordinate of the proton is

$$\mathbf{R}_1 = \mathbf{R}_{cm} + \alpha \left(\frac{\hbar^2}{\mu k_1} \right)^{\frac{1}{4}} \mathbf{r}, \tag{2.59}$$

where the mass ratio $\alpha = \frac{m_e}{m_e+m_p}$. After integrating out the centre of mass coordinate the response function is

$$S(\mathbf{q}, \omega) = \sum_{\mathbf{n}} P_{\mathbf{q}}(E_{\mathbf{n}}) \delta(\hbar\omega + E_{\mathbf{0}} - E_{\mathbf{n}} - \Delta E_{cm}), \tag{2.60}$$

where the probability of exciting the electron from the ground state to an excited state $\Psi_{\mathbf{n}}$, given a momentum transfer $\mathbf{q}$, is

$$P_{\mathbf{q}}(E_{\mathbf{n}}) = |\langle \Psi_{\mathbf{0}} | e^{i\alpha \mathbf{q}\cdot\mathbf{r}} | \Psi_{\mathbf{n}} \rangle|^2. \tag{2.61}$$

2.5.4 Electronic excitation probabilities

To calculate the transition probabilities we require the matrix element

$$\langle \Psi_{\mathbf{0}} | e^{i\alpha \mathbf{q}\cdot\mathbf{r}} | \Psi_{\mathbf{n}} \rangle = \frac{1}{\sqrt{2^{n_x+n_y+n_z} n_x! n_y! n_z! \pi^3}} \int e^{i\alpha \mathbf{q}\cdot\mathbf{r}} e^{-(x^2+y^2+z^2)} H_{n_x}(x) H_{n_y}(y) H_{n_z}(z) d^3\mathbf{r}. \tag{2.62}$$

The generating function can be deduced from the integral representation of $H_n(x)$:

$$e^{2xt-t^2} = \sum_{n=0}^{\infty} H_n(x) \frac{t^n}{n!}, \tag{2.63}$$

and can be used to evaluate the transition probabilities:

$$\sum_{n=0}^{\infty} \frac{s^n}{n!} \int_{-\infty}^{\infty} e^{-x^2} H_n(x) e^{i\alpha q_x x} dx = e^{i\alpha q_x s} e^{-\frac{\alpha^2 q_x^2}{4}} \int_{-\infty}^{\infty} e^{-\left(x - s - \frac{i\alpha q_x}{2}\right)^2} dx = \sqrt{\pi} e^{i\alpha q_x s} e^{-\frac{\alpha^2 q_x^2}{4}}$$

$$= \sqrt{\pi} 4 \sum_{n=0}^{\infty} \frac{s^n}{n!} (-i\alpha q_x)^n \sqrt{\pi} e^{-\frac{\alpha^2 q_x^2}{4}}. \tag{2.64}$$

Then, comparing the first and last terms, we find the equality

$$\int_{-\infty}^{\infty} e^{-x^2} H_n(x) e^{i\alpha q_x x} dx = (-i\alpha q_x)^n \sqrt{\pi} e^{-\frac{\alpha^2 q_x^2}{4}}. \tag{2.65}$$

Then the scattering probabilities are

$$P_{\mathbf{q}}(E_{\mathbf{n}}) = \left| \frac{1}{\sqrt{2^{n_x+n_y+n_z} n_x! n_y! n_z!}} (-i\alpha q_x)^{n_x} (-i\alpha q_y)^{n_y} (-i\alpha q_z)^{n_z} e^{-\frac{\alpha^2 q_x^2}{4} - \frac{\alpha^2 q_y^2}{4} - \frac{\alpha^2 q_z^2}{4}} \right|^2 . \quad (2.66)$$

The energy depends only on the sum $N = n_x + n_y + n_z$ resulting in degenerate eigenstates. The quantities of interest are the probabilities of exciting the system to particular energy levels. To calculate these probabilities, all of the degenerate states corresponding to a particular energy level must be summed over:

$$P_{\mathbf{q}}(E_N) = \sum_{n_x+n_y+n_z=N} P_{\mathbf{q}}(E_{\mathbf{n}}) = \sum_{n_x=0}^{\infty} \sum_{n_y=0}^{\infty} \sum_{n_z=0}^{\infty} \frac{\alpha^6 q_x^2 q_y^2 q_z^2}{2^{n_x+n_y+n_z} n_x! n_y! n_z!} e^{-\frac{\alpha^2 q^2}{2}} \delta_{N,n_x+n_y+n_z}. \quad (2.67)$$

This can be greatly simplified by using the generalisation of the binomial theorem to three dimensions:

$$(x+y+z)^n = \sum_{i=0}^{\infty} \sum_{j=0}^{\infty} \sum_{k=0}^{\infty} \frac{n!}{i!j!k!} x^i y^j z^k \delta_{i+j+k,n}. \quad (2.68)$$

A comparison of the two formulas results in the following expression for the probability of exciting the system from the ground state to an excited state with energy E_N:

$$P_{\mathbf{q}}(E_N) = \frac{1}{N!} \left(\frac{\alpha^2 q^2}{2} \right)^N e^{-\frac{\alpha^2 q^2}{2}}, \quad (2.69)$$

and the response function is

$$S(\mathbf{q}, \omega) = \sum_N P_{\mathbf{q}}(E_N) \delta(\hbar\omega + E_0 - E_N - \Delta E_{cm}). \quad (2.70)$$

The simple form of the excitation probabilities occurs because, when we calculate the matrix elements, we are essentially performing a Fourier transform of the wavefunctions for the harmonic oscillator. It can be easily verified that these probabilities sum to unity regardless of the magnitude of the transferred momentum. The probability that the electron is excited, in a high energy neutron-nucleus collision, is examined in section 2.7. The response function for the harmonic oscillator also appears in the four body problem, which is the investigated next.

2.6 A four body problem

In a molecule the adiabatic separation of the nuclear motion and the electronic motion results in a separation of the electronic, vibrational and rotational modes, and this in turn results in an excitation spectrum which depends on the associated energy scales E_{el}, E_{vib} and E_{rot}. The interaction of the neutron with a proton can then excite the different modes of the molecule which, depending on the energy transferred from the incident neutron, can leave the molecule in a higher electronic, vibrational or rotational state. The excitation spectrums associated with each of the different modes can therefore be probed with incident neutrons within different energy ranges.

In this section we investigate a model of two electrons and two protons interacting with model force laws[34]; the interaction between the electrons and the protons is attractive and harmonic, whilst the electron-electron and proton-proton interactions are repulsive and are modeled with an inverse square law. With these simple interactions the Hamiltonian is separable and the wavefunctions can be found analytically[1]. The model contains the electronic, vibrational and rotational modes which are present in molecular systems, and the excitation probabilities are a *convolution* of those associated with each of the different modes. Whilst this is only true in a separable system, in a real molecule the different energy scales associated with each mode lead to a similar situation.

The Hamiltonian for this model is

$$\begin{aligned}\mathcal{H} = &-\frac{\hbar^2}{2}\left[\frac{\nabla^2_{\mathbf{R}_1}}{m_p} + \frac{\nabla^2_{\mathbf{R}_2}}{m_p} + \frac{\nabla^2_{\mathbf{r}_1}}{m_e} + \frac{\nabla^2_{\mathbf{r}_2}}{m_e}\right] \\ &+\frac{k_1}{2}\left((\mathbf{R}_1-\mathbf{r}_1)^2 + (\mathbf{R}_1-\mathbf{r}_2)^2 + (\mathbf{R}_2-\mathbf{r}_1)^2 + (\mathbf{R}_2-\mathbf{r}_2)^2\right) \\ &+\frac{k_2}{2}\left(\frac{1}{(\mathbf{R}_1-\mathbf{R}_2)^2} + \frac{1}{(\mathbf{r}_1-\mathbf{r}_2)^2}\right). \end{aligned} \tag{2.71}$$

Where $k_2 \geq 0$.

2.6.1 Transformation into the centre of mass frame

The transformation into the centre of mass frame is performed by representing the Hamiltonian in Jacobi coordinates. The general technique involves grouping the particles into clusters, and defining the coordinates between the centre of mass of each of the clusters. In this case it is convenient to group the electrons into one pair, and the protons into another pair, which gives the following choice of Jacobi coordinates:

[1] Interestingly, this model has been used to study the validity of the Born-Oppenheimer approximation

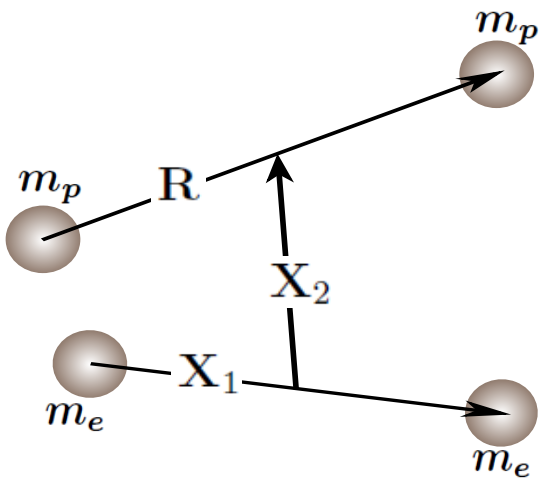

Figure 2.1: The centre of mass frame coordinates for the four body problem.

$$\mathbf{R}_{cm} = \frac{m_p(\mathbf{R}_1 + \mathbf{R}_2) + m_e(\mathbf{r}_1 + \mathbf{r}_2)}{2(m_p + m_e)}$$

$$\mathbf{R} = (\mathbf{R}_1 - \mathbf{R}_2)$$

$$\mathbf{X}_1 = \mathbf{r}_1 - \mathbf{r}_2$$

$$\mathbf{X}_2 = \frac{\mathbf{r}_1 + \mathbf{r}_2}{2} - \frac{\mathbf{R}_1 + \mathbf{R}_2}{2}. \tag{2.72}$$

The total Hamiltonian separates completely in the centre of mass frame, resulting in the following set of four equations governing the motion of the particles:

$$\left[-\frac{\hbar^2}{4M}\nabla^2_{\mathbf{R}_{cm}}\right]\Psi_{cm}(\mathbf{R}_{cm}) = E_{cm}\Psi_{cm}(\mathbf{R}_{cm}) \tag{2.73}$$

$$\left[-\frac{\hbar^2}{m_p}\nabla^2_{\mathbf{R}} + \frac{k_1}{2}\mathbf{R}^2 + \frac{k_2}{2\mathbf{R}^2}\right]\Psi_{nu}(\mathbf{R}) = E_{nu}\Psi_{nu}(\mathbf{R}) \tag{2.74}$$

$$\left[-\frac{\hbar^2}{m_e}\nabla^2_{\mathbf{X}_1} + \frac{k_1}{2}\mathbf{X}_1^2 + \frac{k_2}{2\mathbf{X}_1^2}\right]\Psi_{el}(\mathbf{X}_1) = E_{el}\Psi_{el}(\mathbf{X}_1) \tag{2.75}$$

$$\left[-\frac{\hbar^2}{4\mu}\nabla^2_{\mathbf{X}_2} + 2k_1\mathbf{X}_2^2\right]\Psi_{el-nu}(\mathbf{X}_2) = E_{el-nu}\Psi_{el-nu}(\mathbf{X}_2). \tag{2.76}$$

where the total energy is the sum $E = E_{cm} + E_{nu} + E_{el} + E_{el-nu}$. After the centre of mass motion associated with Eq. 2.73 has been separated, the four body wavefunction can be written as the product

$$\Psi_{fb}(\mathbf{R}_{cm}, \mathbf{R}, \mathbf{X}_1, \mathbf{X}_2) = \frac{1}{\sqrt{V}}e^{i\mathbf{k}_{cm}\cdot\mathbf{R}_{cm}}\Psi_{nu}(\mathbf{R})\Psi_{el}(\mathbf{X}_1)\Psi_{el-nu}(\mathbf{X}_2). \tag{2.77}$$

The wavefunction Ψ_{nu} represents the vibrational motion of the nuclei in the potential well created by the attractive electron-proton interaction, and the repulsive proton-proton interaction. Similarily, the wavefunction Ψ_{el} represents the vibrational motion of the electrons in the potential well created by the attractive electron-proton interaction, and the repulsive electron-electron interaction. Finally, the wavefunction Ψ_{el-nu} represents the relative motion of the electron pair and the proton pair in the potential well created by the attractive electron-proton interaction.

Each of the wavefunctions Ψ_{nu}, Ψ_{el} and Ψ_{el-nu} have a similar functional form to the harmonic wavefunctions calculated in the previous section. In the next section we will calculate each of these wavefunctions and their associated energies.

2.6.2 The electronic-nuclear wavefunctions

The wavefunction Ψ_{el-nu} corresponding to the relative motion of the electron pair and the proton pair is determined from Eq. 2.76. The coordinates and energy are scaled to remove the coefficients:

$$\mathbf{x}_2 = \left(\frac{8k_1\mu}{\hbar^2}\right)^{\frac{1}{4}} \mathbf{X}_2 \qquad \varepsilon_{el-nu} = \left(\frac{\mu}{2\hbar^2 k_1}\right)^{\frac{1}{2}} E_{el-nu}. \tag{2.78}$$

The Hamiltonian corresponds to that of the harmonic oscillator,

$$\left[-\nabla^2_{\mathbf{x}_2} + \mathbf{x}_2^2\right] \Psi_{el-nu}(\mathbf{x}_2) = 2\varepsilon_{el-nu}\Psi_{el-nu}(\mathbf{x}_2). \tag{2.79}$$

The wave functions $\Psi_{el-nu}(\mathbf{x}_2)$ are the harmonic wavefunctions $\Psi_{\mathbf{n}}(\mathbf{x}_2)$ with the corresponding energies E_N.

2.6.3 The nuclear wavefunctions

The nuclear wavefunction Ψ_{nu} represents both the vibrational states and the rotational states of the two nuclei, and is determined from Eq. 2.74 with a suitable scaling of the coordinates and energy:

$$\mathbf{r} = \left(\frac{m_p k_1}{2\hbar^2}\right)^{\frac{1}{4}} \mathbf{R} \qquad \varepsilon_{nu} = \left(\frac{m_p}{2\hbar^2 k_1}\right)^{\frac{1}{2}} E_{nu}. \tag{2.80}$$

Then, after scaling the constant k_2 (which has the units energy×area) appropriately, the Hamiltonian is

$$\left[-\nabla^2_{\mathbf{r}} + \mathbf{r}^2 + \frac{k_2}{\mathbf{r}^2}\right] \Psi_{nu}(\mathbf{r}) = 2\varepsilon_{nu}\Psi_{nu}(\mathbf{r}). \tag{2.81}$$

The above equation is separable in spherical polar coordinates, so that the nuclear wavefunction can be expressed as the product $\Psi_{nu}(\mathbf{r}) = X(r)Y_l^m(\theta,\phi)$. The vibrational states are characterised by $X(r)$ and the rotational states are the spherical harmonics. The function $X(r)$ satisfies

$$\left[r^2\frac{d^2}{dr^2} + 2r\frac{d}{dr} - r^4 + 2\varepsilon_{nu}r^2 - L(L+1)\right]X(r) = 0. \tag{2.82}$$

The repulsive potential has been incorporated into the *centrifugal potential* by defining an angular quantum number that satisfies $L(L+1) = l(l+1) + k_2$, i.e,

$$L = -\frac{1}{2} + \sqrt{\left(l+\frac{1}{2}\right)^2 + k_2}. \tag{2.83}$$

The negative value of L was ignored because it leads to irregular solutions with infinite energy. The regular solutions follow the power law r^L and can be obtained with the ansatz $X(r) = r^L y(r)$. Then we find

$$\left[r^2\frac{d^2}{dr^2} + 2(L+1)r\frac{d}{dr} + (2\varepsilon_{nu}r^2 - r^4)\right]y(r) = 0. \tag{2.84}$$

Then in terms of the variable $x = r^2$ the above equation is

$$\left[4x\frac{d^2}{dx^2} + 2(2L+3)\frac{d}{dx} + (2\varepsilon_{nu} - x)\right]y(x) = 0. \tag{2.85}$$

The coefficients of this equation are all linear functions of x and therefore $y(x)$ may be found by employing the method of integral representations with the Laplace kernel, e^{zx}:

$$y(x) = \int_C e^{zx}f(z)dz. \tag{2.86}$$

The differential equation is transformed into the following integral equation

$$\int_C e^{zx}f(z)(4xz^2 + 2(2L+3)z + (2\varepsilon_{nu} - x))dz = 0. \tag{2.87}$$

Then performing an integration by parts on the terms proportional to x, we obtain

$$\left[(4z^2-1)e^{zx}f(z)\right]_{\partial C} + \int_C e^{zx}\left((2(2L+3)z + 2\varepsilon_{nu})f(z) - \frac{d}{dz}\left(f(z)(4z^2-1)\right)\right)dz = 0. \tag{2.88}$$

The integrand vanishes when

$$\frac{d}{dz}\left(f(z)(4z^2-1)\right) - (2(2L+3)z + 2\varepsilon_{nu})f(z) = 0, \tag{2.89}$$

for which the solution is

$$f(z) = (2z-1)^{\frac{2L+3+2\varepsilon_{nu}}{4}-1}(2z+1)^{\frac{2L+3-2\varepsilon_{nu}}{4}-1}, \tag{2.90}$$

so that the integral representation of $y(x)$ is

$$y(x) \propto \int_C e^{zx}(2z-1)^{\frac{2L+3+2\varepsilon_{nu}}{4}-1}(2z+1)^{\frac{2L+3-2\varepsilon_{nu}}{4}-1}dz. \tag{2.91}$$

For a finite solution we require that there is a pole in the complex plane of order n+1, which quantises the energy:

$$\frac{2L+3-2\varepsilon_{nu}}{4} = -n \Rightarrow \varepsilon_{nu} = 2n + L + \frac{3}{2}, \tag{2.92}$$

where both $n \geq 0$ and $l \geq 0$. It is instructive to compare this quantisation of the energy with that of the quantum harmonic oscillator derived in the previous section, which is the same when $k_2 = 0$. The degenerate states with a particular value of l but different m are all related by simple rotations. In the previous discussion of the harmonic oscillator these rotations are obtained by permuting the quantum numbers n_x, n_y and n_z, which is equivalent to a rotation by $\frac{\pi}{2}$ about one of the coordinate axes. It is also possible to obtain some rather obscure identities between the Hermite polynomials and the associated Laguerre polynomials by comparing the wavefunctions.

The pole in Eq. 2.91 can be shifted to the origin with a translation $t = z + 1$,

$$y(x) \propto e^{-\frac{x}{2}} \int_{C(0)} e^{tx}(t-1)^{n+L+\frac{1}{2}}t^{-n-1}dt. \tag{2.93}$$

The contour can be chosen to enclose the residue at the origin, and although the non-integer value of L will result in a branch cut, it is along the real axis from $z = \frac{1}{2}$ to $z = \infty$ and does not intersect the contour. Then the integral can be evaluated using Cauchy's integral formula to find the residue at $z = 0$:

$$y(x) \propto e^{-\frac{x}{2}} \left[\frac{d^n}{dt^n}\left(e^{tx}(t-1)^{n+L+\frac{1}{2}}\right)\right]_{z=0}. \tag{2.94}$$

Then a general formula for $y(x)$ is found by employing Leibnitz's rule,

$$\frac{d^n}{dz^n}\left(f(z)g(z)\right) = \sum_{j=0}^{n} \frac{n!}{j!(n-j)!}\left(\frac{d^j}{dz^j}f(z)\right)\left(\frac{d^{n-j}}{dz^{m-i}}g(z)\right) \tag{2.95}$$

which gives, when applied to Eq. 2.93,

$$y(x) \propto e^{-\frac{x}{2}} \sum_{j=0}^{n} \frac{(-1)^j(L+\frac{3}{2})_n}{j!(n-j)!(L+\frac{3}{2})_j}x^j = e^{-\frac{x}{2}}L_n^{L+\frac{1}{2}}(x). \tag{2.96}$$

Where $(L+\frac{3}{2})_j$ is the pockhammer symbol and $L_n^{L+\frac{1}{2}}(x)$ is an associated Laguerre poly-

nomial. The normalisation constant is determined by evaluating the following integral

$$N^2 = \int_0^\infty r^2 X^*(r)X(r)dr = \frac{1}{2}\int_0^\infty x^{\frac{1}{2}} X^*(x)X(x)dx = \frac{1}{2n!}\Gamma\left(n + L + \frac{3}{2}\right) \tag{2.97}$$

We therefore find that the vibrational component of the nuclear wavefunction, $\Psi_{nu} = X_{nl}(r)Y_l^m(\theta,\phi)$, is

$$X_{nl}(r) = \sqrt{\frac{2n!}{\Gamma(n + L(l) + \frac{3}{2})}} e^{-\frac{r^2}{2}} r^{L(l)} L_n^{L(l)+\frac{1}{2}}(r^2), \tag{2.98}$$

with an energy of

$$E_{nl} = \left(\frac{2\hbar^2 k_1}{m_p}\right)^{\frac{1}{2}} \left(2n + L(l) + \frac{3}{2}\right). \tag{2.99}$$

2.6.4 The electronic wavefunctions

The electronic wavefunctions are the solutions of Eq. 2.75 and are obviously of the same functional form as the nuclear wavefunctions:

$$\Psi_{el} = X_{n'l'}(x_1)Y_{l'}^{m'}(\theta',\phi'). \tag{2.100}$$

The scaling of the coordinates and the energy is

$$\mathbf{x}_1 = \left(\frac{m_e k_1}{2\hbar^2}\right)^{\frac{1}{4}} \mathbf{X}_1 \qquad \varepsilon_{el} = \left(\frac{m_e}{2\hbar^2 k_1}\right)^{\frac{1}{2}} E_{el}. \tag{2.101}$$

2.6.5 The total internal wavefunctions

Combining all of the wavefunctions we obtain the total internal wavefunction,

$$\Psi_{\mathbf{n}nlm}^{n'l'm'} \equiv \Psi_{nu}\Psi_{el-nu}\Psi_{el} = X_{nl}(r)Y_l^m(\theta,\phi)X_{n'l'}(x_1)Y_{l'}^{m'}(\theta',\phi')\Psi_{\mathbf{n}}(\mathbf{x}_2), \tag{2.102}$$

with an energy

$$E_{Nnl}^{n'l'} \equiv \left(\frac{2\hbar^2 k_1}{m_e}\right)^{\frac{1}{2}} \left[\left(2n' + L(l') + \frac{3}{2}\right) + \sqrt{\frac{1}{1-\alpha}}\left(N + \frac{3}{2}\right) + \sqrt{\frac{\alpha}{1-\alpha}}\left(2n + L(l) + \frac{3}{2}\right)\right]. \tag{2.103}$$

where the first, second and third terms are associated with the electronic, electronic-nuclear and nuclear energies respectively. The contribution to the energy from the electronic excitations and the electronic-nuclear excitations are roughly equal, whilst the contribution from the nuclear excitations are smaller by a factor of approximately $\sqrt{\alpha}$. This leads to a separation of energy scales associated with the different modes of excitation: a feature which will be discussed further in section 2.7.

2.6.6 The excitation probabilities

The scattering from each proton is identical and therefore, to calculate the excitation probabilities, we need only consider the contribution to the response function from the nucleus at $\mathbf{R}_1$:

$$S_1(\mathbf{q},\omega) = \sum_{if} P_i |\langle \Psi_i^{fb}| e^{i\mathbf{q}\cdot\mathbf{R}_1} |\Psi_f^{fb}\rangle|^2 \delta(\hbar\omega + E_i - E_f). \tag{2.104}$$

Where we have assumed that the system is initially in its ground state. The coordinate of the struck proton is

$$\mathbf{R}_1 = \mathbf{R}_{cm} + \frac{1}{2}\left(\frac{2\hbar^2}{m_p k_1}\right)^{\frac{1}{4}} \mathbf{r} - \alpha \left(\frac{\hbar^2}{8k_1\mu}\right)^{\frac{1}{4}} \mathbf{x}_2. \tag{2.105}$$

The next step is to integrate out the centre of mass coordinate to represent the response function in terms of the internal wavefunctions. Initially, the nuclei and the electrons are assumed to be in their vibrational and rotational ground states. After integrating out the centre of mass coordinate the response function is

$$S_1(\mathbf{q},\omega) = \sum_{\substack{n'l'm' \\ \mathbf{n}nlm}} |\langle \Psi_0| e^{i\mathbf{q}\cdot(\frac{1}{2}\mathbf{r} - \alpha\mathbf{x}_2)} |\Psi_{\mathbf{n}nlm}^{n'l'm'}\rangle|^2 \delta(\hbar\omega + E_0 - E_{Nnl}^{n'l'} - \Delta E_{cm}). \tag{2.106}$$

We note that the interaction between the neutron and the proton cannot excite the electronic rotational and vibrational modes of this system. This is because there is no scattering from the electrons and therefore their relative momentum remains unchanged. The electronic states with quantum numbers $(n', l'm')$ are therefore eliminated from consideration.

Because of the separability of the four body wavefunctions and the linearity of the transformation to the centre of mass coordinates, the response function simplifies considerably. The excitation probabilities of the internal states are a convolution of the nuclear excitation probabilities, $P_{\mathbf{q}}^{nu}$, and the electronic-nuclear excitation probabilities $P_{\mathbf{q}}^{el-nu}$:

$$S_1(\mathbf{q},\omega) = \sum_{Nnlm} P_{\mathbf{q}}^{el-nu}(E_N) P_{\mathbf{q}}^{nu}(E_{nl},m)\delta(\hbar\omega + E_0 - E_{Nnl}^{00} - \Delta E_{cm}). \tag{2.107}$$

All remains is to determine $P_{\mathbf{q}}^{nu}$ and $P_{\mathbf{q}}^{el-nu}$. The electronic-nuclear excitation probabilities are exactly equal to the harmonic excitation probabilities of the previous section,

$$P_{\mathbf{q}}^{el-nu}(E_N) = \frac{1}{N!}\left(\frac{\alpha^2 q^2}{2}\right)^N e^{-\frac{\alpha^2 q^2}{2}}, \tag{2.108}$$

with the mass ratio $\alpha = \frac{m_e}{m_e+m_p}$. The nuclear excitation probabilities are

$$P_{\mathbf{q}}^{nu}(E_{nl},m) = \left| \int X_{10}^* (Y_0^0)^* e^{i\frac{\mathbf{q}\cdot\mathbf{r}}{2}} X_{nl} Y_l^m d\mathbf{r} \right|^2. \tag{2.109}$$

Because of the spherical symmetry we can sum over the degenerate states with quantum number m:

$$P_{\mathbf{q}}^{nu}(E_{nl}) \equiv \sum_{l=-m}^{m} P_{\mathbf{q}}^{nu}(E_{nl},m) = (2l+1)\left| \int_0^\infty X_{10}^* J_l\left(\frac{qr}{2}\right) X_{nl} dr \right|^2. \tag{2.110}$$

The response function for the four body problem,

$$S_1(\mathbf{q},\omega) = \sum_{Nnl} P_{\mathbf{q}}^{el-nu}(E_N) P_{\mathbf{q}}^{nu}(E_{nl})\delta(\hbar\omega + E_0 - E_{Nnl}^{00} - \Delta E_{cm}), \tag{2.111}$$

is discussed further in section 2.7.

2.7 The excitation probabilities of separable systems

The two models analysed in this chapter demonstrate the inherent difficulty of exciting the electronic modes of a separable system. This fact is easily verified by examining the excitation probabilities for each of the models as a function of transferred momentum and transferred energy, and is due to the small mass ratio $\alpha = \frac{m_e}{m_e+m_p} \approx 5.441 \times 10^{-4}$. Thus, for each model we will examine the probabilities $P_{\mathbf{q}}(E)$ for constant momentum transfer, and for constant energy transfer. To gain some indication of the ability of each model to be excited we will also evaluate the probability $P_{\mathbf{q}}(E_0)$ of remaining in the ground state for a reasonable value of transferred momentum.

2.7.1 The harmonic oscillator

The excitation probabilities calculated in section 2.5 are

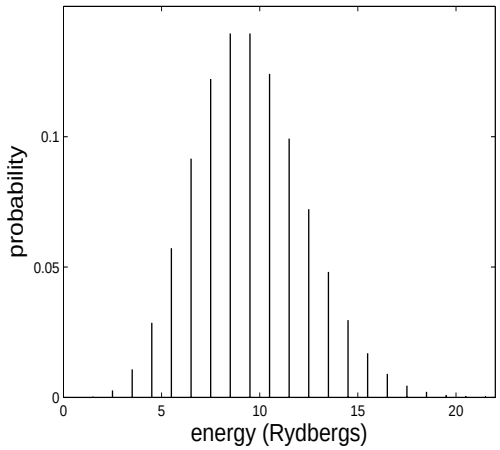

(a) The excitation probabilities for the nuclear-electronic modes, evaluated for $q \approx 8000\text{Å}^{-1}$

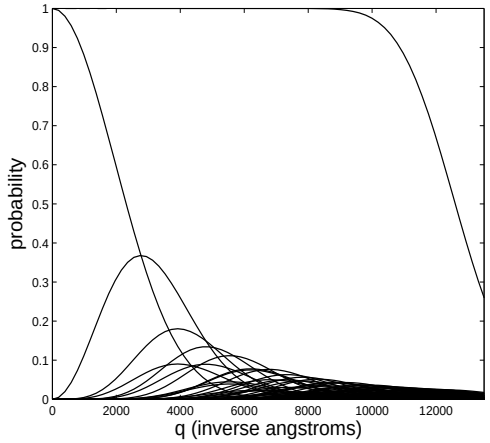

(b) The excitation probabilities for the nuclear-electronic modes, evaluated as a function of transferred momentum q.

Figure 2.2: Excitation probabilities for the harmonic oscillator.

$$P_{\mathbf{q}}(E_N) = \frac{1}{N!}\left(\frac{\alpha^2 q^2}{2}\right)^N e^{-\frac{\alpha^2 q^2}{2}}. \tag{2.112}$$

If we choose the energy scale to be in units of the Bohr energy E_b, i.e, the energy of the hydrogen atom, then we obtain $k_1 \approx 19.7$. This allows us to calculate the excitation probabilities for an energy transfer $E = 100\text{eV}$, which is equivalent to $q = 219.7\text{Å}^{-1}$. At this momentum we obtain the probability, from Eq. 2.112, that the electron remains in its ground state is $P_{\mathbf{q}}(E_0) \approx 0.9823$. The amount of electronic excitation is proportional to $\alpha^2 q^2$, and is consequentially only about 1.2%.

2.7.2 The four body problem

The excitation probabilities for the four body problem were determined in section 2.6 to be

$$P_{\mathbf{q}}(E_{Nnl}) = P^{nu}_{\mathbf{q}}(E_{nl}) P^{el-nu}_{\mathbf{q}}(E_N), \tag{2.113}$$

where the electronic-nuclear probabilities are defined

$$P^{el-nu}_{\mathbf{q}}(E_N) = \frac{1}{N!}\left(\frac{\alpha^2 q^2}{2}\right)^N e^{-\frac{\alpha^2 q^2}{2}}, \tag{2.114}$$

the nuclear probabilities are defined

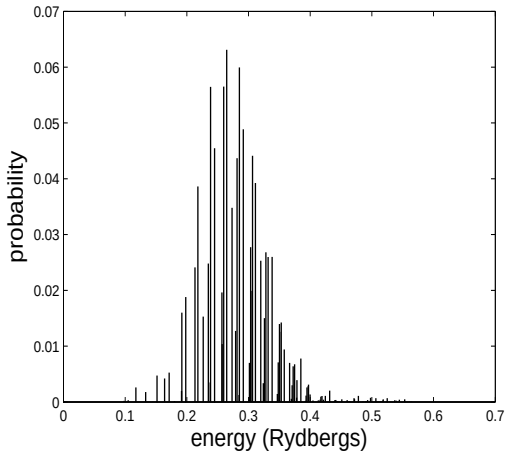

(a) The excitation probabilities of the nuclear modes of the four body problem, evaluated for $q \approx 28\text{Å}^{-1}$, with $k_2 = 10$.

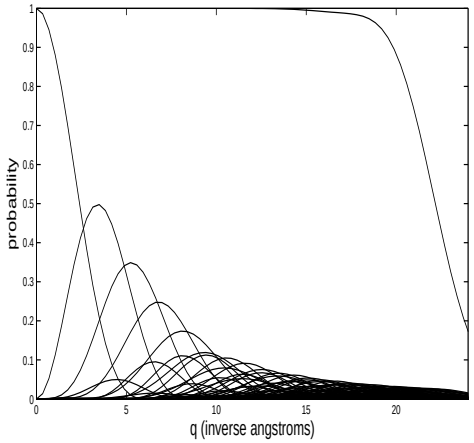

(b) The excitation probabilities of the nuclear modes of the four body problem, evaluated with $k_2 = 10$, as a function of transferred momentum q.

Figure 2.3: Nuclear excitation probabilities for the four body problem.

$$P_{\mathbf{q}}^{nu}(E_{nl}) = (2l+1)\left|\int_0^\infty X_{10}^* J_l\left(\frac{qr}{2}\right) X_{nl} dr\right|^2, \tag{2.115}$$

and the energies of the accessible excited states are

$$E_{Nnl} = \left(\frac{2\hbar^2 k_1}{m_e}\right)^{\frac{1}{2}}\left[\sqrt{\frac{1}{1-\alpha}}\left(N+\frac{3}{2}\right) + \sqrt{\frac{\alpha}{1-\alpha}}\left(2n+L(l)+\frac{3}{2}\right)\right]. \tag{2.116}$$

The dependence of the nuclear-electronic excitation probabilities on the transferred energy and momentum is shown in Fig. 2.2. The results are identical, apart from a slight change of scale, to those of the harmonic oscillator. The probabilities $P_{\mathbf{q}}^{el-nu}(E_N)$ for a fixed value of $q \approx 8000\text{Å}^{-1}$ are illustrated in Fig. 2.2(a), which are calculated for a very high momentum transfer to illustrate the different electronic modes. The probabilities $P_{\mathbf{q}}^{el-nu}(E_N)$ are also calculated as a function of momentum transfer in Fig. 2.2(b), which illustrates that as q increases the higher energy electronic modes are excited with increasing probability. The sum over all probabilities is also evaluated for each value of q, to verify that the complete set of excitations is included.

The nuclear-electronic excitation probabilities obviously resemble those of the harmonic oscillator, whilst the nuclear excitation probabilities have a more complicated structure due to the additional potential parameter k_2 which reduces the symmetry[2]to that of the

[2]The full symmetry of the harmonic oscillator is represented by the group of four dimensional rotations.

rotation group SO(3). Interestingly, the range of values that k_2 may take are $k_2 > -\frac{1}{4}$, with acceptable (finite energy and normalisable) solutions even when the proton-proton and electron-electron interactions become attractive. When $k_2 = -\frac{1}{4}$ the energy of these states is no longer finite and the particles experience a first order transition, collapsing into each other.

The excitation probabilities of the nuclear rotational and vibrational states are illustrated in Fig. 2.3. Also illustrated, in Fig. 2.4, are the convoluted excitation probabilities of the complete four body excitation spectrum. The peaks associated with the nuclear excitations are easily distinguished from those of the nuclear-electronic excitations due to the different energy scales of the two modes. The rotational and vibrational modes of the nuclei are accessible on an energy scale of order $\sqrt{\alpha}$ and can therefore be easily excited in the scattering process. If we scale the nuclear-electronic energy in units of E_b then, for an energy transfer of $E = 100$eV, the nuclear modes are highly excited. However, the probability that the electrons remain in the ground state is $P_{\mathbf{q}}(E_0) \approx 0.993$, and the amount of electronic excitation is therefore less than 1%. A similar situation occurs in molecules, whereby the rotational, vibrational and electronic modes all occur on different energy scales and can therefore distinguished from each other; at low energies the rotational modes are excited, then at slightly higher energies the vibrational modes also become excited, and at even higher energies the electronic modes are excited. This idea is important when we calculate the excitation probabilities for a molecule because, when we investigate the probability that the electron remains in its ground state, we must consider very high energy nuclear vibrational states. In fact, the energies are sufficiently high that the nuclei will dissociate. Dissociation is not a feature of the four body problem studied in this chapter, but it does occur in the hydrogen atom which is investigated in the next chapter.

A similar situation occurs in the hydrogen atom; the 'accidental' degeneracy of the energy levels is related to a hidden symmetry, which is also described by the group of four dimensional rotations[17].

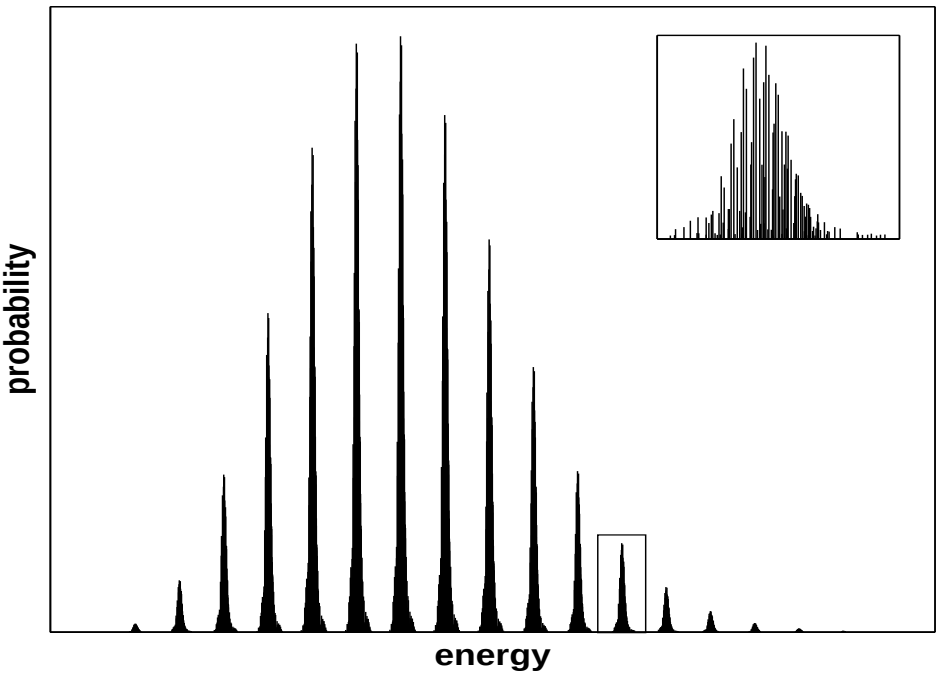

Figure 2.4: An example of the convolution of probabilities, for the nuclear and nuclear-electronic modes, in the four body problem. The excitation of the nuclear-electronic modes occurs on an energy scale E_b. These modes, which display the same excitation probabilities as the harmonic oscillator, are only excited when the momentum transfer is $q \sim 1000\text{Å}^{-1}$. Each electronic peak has a finer structure associated with the nuclear rotational and vibrational modes, which are excited on a smaller energy scale, $\sqrt{\alpha}E_b$. The nuclear modes (which are magnified in the upper right corner) are excited at modest momentum transfers $q \sim 1\text{Å}^{-1}$.

Chapter 3

The hydrogen atom

Dating back to 1913, when Niels Bohr first reproduced the energy spectrum of the hydrogen atom[35] using the *Bohr model*, the hydrogen atom has always been considered to be the prototypical quantum system. The study of the hydrogen atom has often lead to new insights into fundamental physics, including: the calculation of the energy spectrum of hydrogen, obtained from the analytic solutions to the Schrodinger equation in 1926, the theoretical understanding of spin, acquired from the analytic solutions to the Dirac equation in 1928, and the development of quantum electrodynamics, motivated by the observation of the *Lamb shift* in 1947. There is substantial benefit in having analytical solutions to a simple problem such as the hydrogen atom: The concepts developed by studying the solutions to the simplest problem often apply to the more complicated problems one usually encounters.

In this chapter we investigate the response function of the hydrogen atom in detail. The energy spectrum of the hydrogen atom consists of a discrete set of bound states with negative energy, and a continuum of dissociated states with positive energy. In a high energy neutron-nucleus collision the electron is excited, and for very high energy collisions the electron becomes completely dissociated from the proton. This is similar to the situation which occurs in molecules when the struck proton dissociates, although the energy scale for electronic dissociation is considerably higher. The solution to the hydrogen atom illustrates how to quantise the energies of the continuum, and obtain a probability density associated with scattering into the high energy dissociated electronic states. These concepts are useful for the work in the next Chapter on the dissociation of hydrogen molecules.

Finally we make some conclusions regarding the probability of exciting an electron in the hydrogen atom, and in separable systems in general. It is found that the amount of electronic excitation for experimentally obtainable momentum transfers is very small ($< 1\%$). This is a direct consequence of the separable form of the wavefunctions, which

means that the only mechanism available for electronic excitation is centre of mass recoil (CMR).

3.1 Excitation probabilities for dissociated states

In the hydrogen atom we must consider the probability of exciting an electron into the continuum of dissociated states. In this case the final states can be characterised by the continuous energy parameter ε. We then quantise the system by making the system size finite and determine how the intervals $\Delta\varepsilon$ scale with the system size. We can then write $\Psi_\varepsilon = \sqrt{\Delta\varepsilon}\tilde{\Psi}_\varepsilon$, and in the limit that the system size becomes infinite we can take the limit $\Delta\varepsilon \to d\varepsilon$, and then the sum over final states becomes an integral. The resolution of the identity then becomes

$$\int d\varepsilon |\tilde{\Psi}_\varepsilon\rangle\langle\tilde{\Psi}_\varepsilon| = \hat{1}. \tag{3.1}$$

We then calculate

$$\begin{aligned}\sum_f |\langle\Psi_i|e^{i\mathbf{q}\cdot\mathbf{r}}|\Psi_f\rangle|^2 &= \sum_\varepsilon \Delta\varepsilon\langle\Psi_i|e^{i\mathbf{q}\cdot\mathbf{r}}|\tilde{\Psi}_\varepsilon\rangle\langle\tilde{\Psi}_\varepsilon|e^{-i\mathbf{q}\cdot\mathbf{r}}|\Psi_i\rangle \\ &\to \int d\varepsilon\langle\Psi_i|e^{i\mathbf{q}\cdot\mathbf{r}}|\tilde{\Psi}_\varepsilon\rangle\langle\tilde{\Psi}_\varepsilon|e^{-i\mathbf{q}\cdot\mathbf{r}}|\Psi_i\rangle = \langle\Psi_i|\Psi_i\rangle = 1.\end{aligned} \tag{3.2}$$

Therefore the squared matrix element is associated with a probability density

$$\rho_\mathbf{q}(\varepsilon; E_i) \equiv |\langle\Psi_i|e^{i\mathbf{q}\cdot\mathbf{r}}|\tilde{\Psi}_\varepsilon\rangle|^2. \tag{3.3}$$

This method of dealing with a continuous excitation spectrum is used to determine the electronic excitation probabilities for the dissociated states of the hydrogen atom in section 3.2. When there are both discrete and continuous excitation spectrums the most general form of the response function is

$$\begin{aligned}S(\mathbf{q},\omega) &= \sum_{if} P_i P_\mathbf{q}(E_f; E_i)\delta(\hbar\omega + E_i - E_f) + \sum_i P_i \int d\varepsilon \rho_\mathbf{q}(\varepsilon; E_i)\delta(\hbar\omega + E_i - \varepsilon) \\ &= \sum_{if} P_i P_\mathbf{q}(E_f; E_i)\delta(\hbar\omega + E_i - E_f) + \sum_i P_i \rho_\mathbf{q}(\hbar\omega + E_i; E_i).\end{aligned} \tag{3.4}$$

Throughout this chapter we shall again make the simplifying assumption that the initial state is the ground state Ψ_0, and we will then calculate the quantities $P_\mathbf{q}(E_f)$ and $\rho_\mathbf{q}(\varepsilon)$ to determine the electronic excitation probabilities of the hydrogen atom.

3.2 The hydrogen atom

We will now look at the simplest realistic model: the hydrogen atom. This is useful as a first step towards understanding the full range of excitations which occur in more complicated hydrogen systems, such as in a molecule, or in a solid. The important process which is encountered when one investigates the hydrogen atom, which was lacking in the two previous models, is dissociation; in an interaction involving a sufficiently high momentum transfer it is possible for the electron to dissociate from the proton, resulting in a continuum of high energy excitations. Understanding how the electron dissociates from the proton will provide the necessary understanding which is required in the next chapter when one considers the dissociation of two nuclei which occurs in molecules. The Hamiltonian for the hydrogen atom is

$$\mathcal{H} = -\frac{\hbar^2}{2m_p}\nabla^2_{\mathbf{R}_1} - \frac{\hbar^2}{2m_e}\nabla^2_{\mathbf{r}_1} - \frac{e^2}{4\pi\epsilon_0|\mathbf{R}_1 - \mathbf{r}_1|}. \tag{3.5}$$

3.2.1 Transformation into the centre of mass frame

We perform the usual transformation to the centre of mass frame using the following coordinates

$$\mathbf{R}_{cm} = \frac{m_p\mathbf{R}_1 + m_e\mathbf{r}_1}{m_p + m_e} \qquad \mathbf{R} = \mathbf{R}_1 - \mathbf{r}_1. \tag{3.6}$$

Then the Hamiltonian is

$$\hat{H} = -\frac{\hbar^2}{2M}\nabla^2_{\mathbf{R}_{cm}} - \frac{\hbar^2}{2\mu}\nabla^2_{\mathbf{R}} - \frac{e^2}{4\pi\epsilon_0|\mathbf{R}|} = E, \tag{3.7}$$

where the effective masses are again given by

$$M = m_e + m_p \qquad \mu = \frac{m_e m_p}{m_e + m_p}, \tag{3.8}$$

and the wavefunction again factorises into the product of the centre of mass wavefunction and the internal wavefunction:

$$\Psi^h(\mathbf{R}_{cm}, \mathbf{R}) = \frac{1}{\sqrt{V}} e^{i\mathbf{k}_{cm}\cdot\mathbf{R}_{cm}}\Psi(\mathbf{R}). \tag{3.9}$$

3.2.2 The internal wavefunctions

The internal wave function satisfies

$$\left[-\frac{\hbar^2}{2\mu}\nabla^2_{\mathbf{R}} - \frac{e^2}{4\pi\epsilon_0|\mathbf{R}|}\right]\psi(\mathbf{R}) = E_{in}\Psi(\mathbf{R}). \tag{3.10}$$

The appropriate scaling of the coordinates and the energy is

$$\mathbf{r} = \frac{\mu e^2}{4\pi\epsilon_0\hbar^2}\mathbf{R} = \frac{1}{a_0}\mathbf{R} \qquad \varepsilon = \frac{32\pi^2\epsilon_0^2\hbar^2}{e^4\mu}E_{in} = \frac{1}{E_b}E_{in}, \tag{3.11}$$

where we have introduced the *Bohr radius* a_0 and the *Bohr energy* E_b. Then the Hamiltonian is

$$\left[-\nabla^2_{\mathbf{r}} - \frac{2}{|\mathbf{r}|}\right]\psi(\mathbf{r}) = \varepsilon\Psi(\mathbf{r}). \tag{3.12}$$

We again apply separation of variables to represent the wavefunction in the form $\Psi(\mathbf{r}) = X(r)Y_l^m(\theta,\phi)$, which gives the following equation for $X(r)$:

$$\left[r^2\frac{d^2}{dr^2} + 2r\frac{d}{dr} + 2r + \varepsilon r^2 - l(l+1)\right]X(r) = 0. \tag{3.13}$$

The solutions follow a power law close to $r = 0$; the regular solutions follow the power law r^l, whilst the irregular solutions follow the power law r^{-l-1}. The solution which is finite at the origin is be obtained with the ansatz $X(r) = r^l y(r)$:

$$\left[r\frac{d^2}{dr} + (2l+2)\frac{d}{r} + (2+\varepsilon r)\right]y(r) = 0. \tag{3.14}$$

This equation contains coefficient which are linear in r and can therefore be solved with the Laplace Kernel, e^{zr}:

$$y(r) = \int_C e^{zr}f(z)dz, \tag{3.15}$$

which results in the integral equation

$$\int_C e^{zr}f(z)(rz^2 + (2l+2)z + (2+\varepsilon r))dz = 0. \tag{3.16}$$

Performing an integration by parts to remove the r coefficients gives

$$\left[(z^2+\epsilon)e^{zr}f_l(z)\right]_{\partial C} + \int_C\left(2f_l(z) + (2l+2)zf_l(z)\frac{d}{dz}((z^2-\varepsilon)f(z))\right)e^{zr}dz = 0. \tag{3.17}$$

We again demand that the boundary term vanish, and that the integrand be equal to zero:

$$\frac{d}{dz}((z^2-\varepsilon)f(z) - (2+(2l+2)z)f(z) = 0, \tag{3.18}$$

with the solution

$$f(z) = (z + i\sqrt{\varepsilon})^{l+\frac{i}{\sqrt{\varepsilon}}})(z - i\sqrt{\varepsilon})^{l-\frac{i}{\sqrt{\varepsilon}}}). \tag{3.19}$$

The integral representation for $y(r)$ is therefore

$$y(r) \propto \int_C e^{zr}(z + i\sqrt{\varepsilon})^{l+\frac{i}{\sqrt{\varepsilon}}}(z - i\sqrt{\varepsilon})^{l-\frac{i}{\sqrt{\varepsilon}}}dz \tag{3.20}$$

The nature of the solutions which are obtained by solving this integral depends on the choice of the parameterisation of the energy ε_n. If we choose to look for bound states with negative energy, then we find solutions which are of a polynomial form. If however we look for positive energy states for which the electron is completely dissociated from the electron, then we find that the solutions are of a transcendental form. In the next section we find the analytic form of both styles of solution and then discuss how to calculate the excitation probabilities associated with each.

3.2.3 The bound states of the hydrogen atom

To calculate wavefunctions representing the bound state we paramaterise the energy so that $\varepsilon = -\frac{1}{n^2}$. There is then a pole of order n at the point $z = -\frac{1}{n}$, which quantises the energy by requiring that n be a positive integer. In this case the wave function defined by Eq. 3.20 is

$$y(r) \propto \int_C e^{zr}\left(z - \frac{1}{n}\right)^{l+n}\left(z + \frac{1}{n}\right)^{l-n}dz. \tag{3.21}$$

The contour must be chosen to form a closed loop around the residue which ensures that the boundary term will vanish and a non-trivial solution exists. If n had not been a integer there would have been a branch cut which would have prevented this. It is convenient to shift the residue to the origin with the translation $t = z + \frac{1}{n}$:

$$y(r) \propto e^{-\frac{r}{n}}\int_{C(0)} e^{rt}\left(t - \frac{2}{n}\right)^{l+n} t^{l-n}dt. \tag{3.22}$$

This can be evaluated using Cauchys integral formula:

$$y(r) \propto e^{-\frac{r}{n}}\left[\frac{d^{n-l-1}}{dt^{n-l-1}}\left(e^{rt}\left(t - \frac{2}{n}\right)^{l+n}\right)\right]_{t=0}, \tag{3.23}$$

and then using Leibnitz's rule:

$$y(r) \propto e^{-\frac{r}{n}}\sum_{i=0}^{n-l-1}\frac{(l+n)!(-1)^i}{i!(n-l-1-i)!(2l+1+i)!}\left(\frac{2r}{n}\right)^i = e^{-\frac{r}{n}}L_{n-l-1}^{2l+1}\left(\frac{2r}{n}\right). \tag{3.24}$$

To normalise these wavefunctions we simply calculate

$$N^2 = \int_0^\infty r^2 X^*(r) X(r) dr = \left(\frac{n}{2}\right)^3 \left[\frac{2n(n+l)!}{(n-l-1)!}\right]. \tag{3.25}$$

The normalised radial wave functions for the bound states of hydrogen are therefore

$$X_{nl}(r) = \sqrt{\left(\frac{2}{n}\right)^3 \frac{(n-l-1)!}{2n(n+l)!}} \left(\frac{2r}{n}\right)^l e^{-\frac{r}{n}} L_{n-l-1}^{2l+1}\left(\frac{2r}{n}\right), \tag{3.26}$$

with an energy $E_n = -\frac{E_b}{n^2}$.

3.2.4 The dissociated states of the hydrogen atom

To obtain the wavefunctions describing the dissociated states we return to Eq. 3.20, and apply the transformation $z = i\sqrt{\varepsilon}\zeta$:

$$X(r) \propto (i\sqrt{\varepsilon}r)^l \int_C e^{i\sqrt{\varepsilon}\zeta r}(1-\zeta^2)^l \left(\frac{1-\zeta}{1+\zeta}\right)^{\frac{1}{i\sqrt{\varepsilon}}} d\zeta, \tag{3.27}$$

with the boundary condition

$$\left[e^{i\sqrt{\varepsilon}\zeta r}(1-\zeta^2)^{l+1}\left(\frac{1-\zeta}{1+\zeta}\right)^{\frac{1}{i\sqrt{\varepsilon}}}\right]_{\partial C} = 0. \tag{3.28}$$

To analyse the positive energy dissociated states it is convenient to parameterise the energy so that $\varepsilon = \frac{1}{\eta^2}$:

$$X(r) \propto \left(\frac{r}{\eta}\right)^l \int_C (1-\zeta^2)^l e^{i\left(\frac{\zeta r}{\eta} + \eta \ln\left(\frac{1+\zeta}{1-\zeta}\right)\right)} d\zeta. \tag{3.29}$$

For these choices of ε the integrand has become multi-valued, requiring branch cuts in the ranges $\zeta < -1$ and $\zeta > 1$ in the complex plane. A contour must now be chosen which satisfies the boundary condition

$$\left[(1-\zeta^2)^{l+1} e^{i\left(\frac{\zeta r}{\eta} + \eta \ln\left(\frac{1+\zeta}{1-\zeta}\right)\right)}\right]_{\partial C} = 0. \tag{3.30}$$

There is no longer a pole in the complex plane so we cannot choose a closed contour as we did previously. Instead, we must choose the contour such that the contribution from the boundary is zero at both ends, which leaves just three possibilities: we can place the ends of the contour at the two branch points at $\zeta = \pm 1$, or the in the asymptotic region $\zeta \to i\infty$. The latter choice $\zeta \to i\infty$ diverges[1] close to $r = 0$. This only leaves the contour

[1] if we scale the coordinate such that $\tilde{\zeta} = \frac{\eta}{r}\zeta$, it can be shown that $X(r)$ follows the power law r^{-l-1} close to the origin

which connects the two branch points at $\zeta = \pm 1$:

$$X(r) \propto \left(\frac{r}{\eta}\right)^l \int_{-1}^{1} (1-\zeta^2)^l e^{i\left(\frac{\zeta r}{\eta} + \eta \ln\left(\frac{1+\zeta}{1-\zeta}\right)\right)} d\zeta. \tag{3.31}$$

If we write $e^{if(\zeta)} = \cos(f(\zeta)) + i\sin(f(\zeta))$ we find that the complex part is antisymmetric in ζ, and therefore does not contribute to the integral. We can then write

$$X(r) \propto \left(\frac{r}{\eta}\right)^l \int_{0}^{1} (1-\zeta^2)^l \cos\left(\frac{\zeta r}{\eta} + \eta \ln\left(\frac{1+\zeta}{1-\zeta}\right)\right) d\zeta. \tag{3.32}$$

This integral representation of the wave functions can be transformed into a form more useful for numerical calculations by introducing the variable $\zeta = \tanh(x)$:

$$X(r) \propto \left(\frac{r}{\eta}\right)^l \int_{0}^{\infty} \frac{dx}{\cosh^{2l+2}(x)} \cos\left(\frac{r}{\eta}\tanh(x) + 2\eta x\right). \tag{3.33}$$

Normalising the dissociated states is much more difficult than normalising the bound states. To normalise the dissociated states we require the asymptotic behaviour of the radial probability density $r^2 X(r)$ as $r \to \infty$, which can be seen in Fig. 3.44. The energy levels can be quantised by normalising the radial wavefunctions in a finite sphere of radius L, which results in a normalisation constant proportional to L. To determine the constant of proportionality we must evaluate Eq. 3.32 in the limit $r \to \infty$. For this calculation it is convenient to introduce a variable x, which is defined by the expression $1 - \zeta = \frac{\eta x}{r}$. We then find

$$X(r) \propto \left(\frac{r}{\eta}\right)^{l-1} \int_{0}^{\frac{r}{\eta}} dx \left(\frac{\eta x}{r}\right)^l \left(2 - \frac{\eta x}{r}\right)^l \cos\left(\frac{r}{\eta} - \eta \ln\frac{\eta x}{r} - x + \eta \ln\left(2 - \frac{\eta x}{r}\right)\right)$$

$$= \frac{\eta}{r} 2^l \int_{0}^{\frac{r}{\eta}} dx x^l \left(1 - \frac{\eta x}{2r}\right)^l \cos\left(\frac{r}{\eta} + \eta \ln\frac{2r}{\eta} - x - \eta \ln x + \eta \ln\left(1 - \frac{\eta x}{2r}\right)\right). \tag{3.34}$$

In the limit $r \to \infty$ the last term vanishes and we obtain

$$\lim_{r\to\infty}[X(r)] = \frac{\eta}{r} 2^l \int_{0}^{\infty} dx x^l \cos\left(\frac{r}{\eta} + \eta \ln\frac{2r}{\eta} - x - \eta \ln x\right)$$

$$= \frac{\eta}{r} 2^l \int_{0}^{\infty} dx x^l \mathrm{Re}\left(e^{i\left(\frac{r}{\eta} + \eta \ln\frac{2r}{\eta} - x - \eta \ln x\right)}\right)$$

$$= \frac{\eta}{r} 2^l \mathrm{Re}\left(\int_{0}^{\infty} dx x^{l-i\eta} e^{-ix} e^{i\left(\frac{r}{\eta} + \eta \ln\frac{2r}{\eta}\right)}\right). \tag{3.35}$$

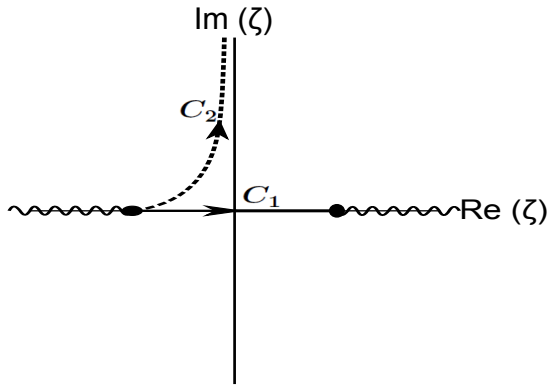

(a) The contours used to calculate the dissociated electronic states. The contours C_1 and C_2 are associated with the regular and irregular solutions respectively.

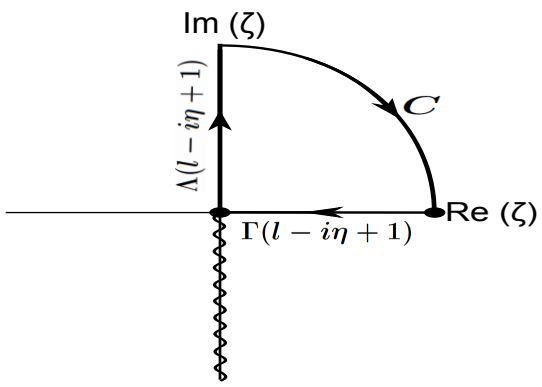

(b) The relationship between $\Gamma(l - i\eta + 1)$ and $\Lambda(l - i\eta + 1)$. Regularisation is required to make the integral over C vanish.

Figure 3.1: Contours of integration for dissociated states of hydrogen.

To perform the integral over x is convenient to rotate x in the complex plane by introducing the variable $y = ix$:

$$\int_0^\infty dx x^{l-i\eta} e^{-ix} = (i)^{i\eta-l-1} \int_0^{i\infty} dy y^{l-i\eta} e^{-y} = (i)^{i\eta-l-1} \Lambda(l - i\eta + 1). \tag{3.36}$$

This integral is related to the Gamma function $\Gamma(l - i\eta + 1)$, which can be seen by performing the contour integral illustrated in Fig. 3.1(b). To obtain the identity $\Lambda(l - i\eta+1) = \Gamma(l-i\eta+1)$, the integral must be regularised so that the integral over C vanishes. The regularised wave functions therefore have the asymptotic form

$$\lim_{r\to\infty} [X(r)] = \frac{\eta}{r} 2^l \mathrm{Re}\left(i^{i\eta-l-1} \Gamma(l - i\eta + 1) e^{i\left(\frac{r}{\eta} + \eta \ln \frac{2r}{\eta}\right)} \right)$$

$$= \frac{\eta}{r} 2^l \mathrm{Re}\left(e^{-\frac{\eta\pi}{2} - \frac{il\pi}{2} - \frac{i\pi}{2}} \Gamma(l - i\eta + 1) e^{i\left(\frac{r}{\eta} + \eta \ln \frac{2r}{\eta}\right)} \right). \tag{3.37}$$

We can now define the phase shift[2] of the wavefunction,

$$\delta_l = \arg(\Gamma(l - i\eta + 1)). \tag{3.38}$$

The asymptotic wave functions may then be written

$$\lim_{r\to\infty} [X(r)] = 2^l \frac{\eta}{r} e^{-\frac{\eta\pi}{2}} |\Gamma(l - i\eta + 1)| \sin\left(\frac{r}{\eta} + \eta \ln \frac{2r}{\eta} + \delta_l \right), \tag{3.39}$$

and the normalisation constant is therefore

[2]This is the phase shift of the l-th partial wave of the dissociated electronic wavefunction.

$$N^2 = \int_0^L r^2 R_{\eta l}(r) R^*_{\eta l}(r) dr$$
$$= 2^{2l} e^{-\eta\pi} |\Gamma(l - i\eta + 1)|^2 \eta^2 \int_0^L \sin^2\left(\frac{r}{\eta} + \eta \ln\frac{2r}{\eta} + \delta_l\right) dr. \quad (3.40)$$

The term involving the Gamma function can be simplified by using the identity

$$|\Gamma(l - i\eta + 1)|^2 = \frac{\pi\eta}{\sinh(\pi\eta)} \prod_{p=1}^{l} (p^2 + \eta^2). \quad (3.41)$$

Apart from the logarithm, the asymptotic form of the wavefunction corresponds to the l-th partial wave component of the scattered wave for the dissociated electron. The logarithm arises because of the long ranged nature of the coulomb potential. However, in the limit $r \to \infty$ this logarithm changes very slowly compared to r and can be safely ignored. The integral required for the normalisation is therefore

$$\lim_{L\to\infty}\left[\int_0^L \sin^2\left(\frac{r}{\eta} + \eta \ln\frac{2r}{\eta} + \delta_l\right) dr\right] = \lim_{L\to\infty}\left[\int_0^L \sin^2\left(\frac{r}{\eta} + \delta_l\right) dr\right] = \frac{L}{2}, \quad (3.42)$$

and the normalisation constant is found to be

$$N^2 = 2^{2l-1} e^{-\pi\eta} \frac{L\pi\eta^3}{\sinh(\pi\eta)} \left[\prod_{p=1}^{l} \left(p^2 + \eta^2\right)\right]. \quad (3.43)$$

The normalised dissociated wave functions with energy $E = \frac{E_b}{\eta^2}$ are

$$X_{\eta l}(r) = \sqrt{\frac{\sinh(\pi\eta)}{L 2^{2l-1}\eta^3 \pi e^{-\pi\eta} \prod_{p=1}^{l}(p^2 + \eta^2)}} \left(\frac{r}{\eta}\right)^l \int_0^\infty \left(\frac{\cos(\frac{r}{\eta}\tanh(x) + 2\eta x)}{\cosh^{2l+2}(x)}\right) dx. \quad (3.44)$$

The radial probability distribution, $r^2|X(r)|^2$, for several bound states and a dissociated state, are illustrated in Fig. 3.2.

3.2.5 Electronic excitation probabilities

To calculate the electronic excitation probabilities we start from the response function for the hydrogen atom,

$$S(\mathbf{q}, \omega) = \sum_{if} P_i |\langle \Psi_i^h | e^{i\mathbf{q}\cdot\mathbf{R}_1} | \Psi_f^h \rangle|^2 \delta(\hbar\omega + E_i - E_f). \quad (3.45)$$

The coordinate of the proton is $\mathbf{R}_1 = \mathbf{R}_{cm} + \alpha a_0 \mathbf{r}$. We assume that the electron is initially

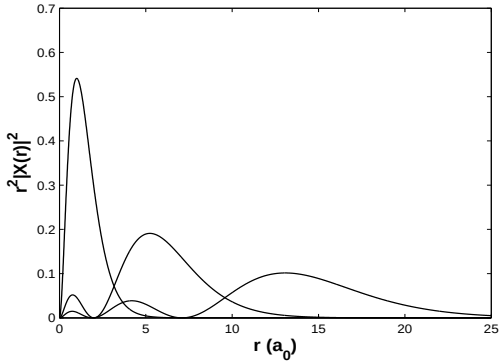

(a) The first three $l = 0$ states for the bound states of hydrogen.

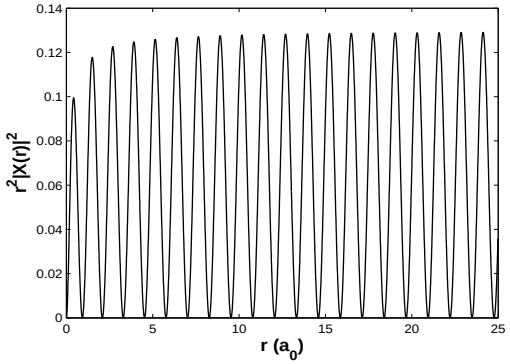

(b) The $l = 0$ dissociated state of hydrogen with energy $E = 6$.

Figure 3.2: The radial charge distributions $(r^2|X(r)|^2)$ of states belonging to the discrete spectrum of bound states, and the continuous spectrum of dissociated states.

in the ground state configuration, and then represent the response function in terms of the internal wavefunctions,

$$S(\mathbf{q},\omega) = \sum_{\varepsilon lm} |\langle \Psi_0 | e^{i\alpha \mathbf{q}\cdot\mathbf{r}} | \Psi^m_{\varepsilon l}\rangle|^2 \delta(\hbar\omega + E_0 - E_{el} - \Delta E_{cm}). \tag{3.46}$$

At this point we need to distinguish between the excitation probabilities of the bound states and those of the dissociated states, since each case is interpreted differently. For the bound states we have the discrete excitation probabilities

$$P_{\mathbf{q}}(E_n, l, m) = |\langle \Psi_0 | e^{i\mathbf{q}\cdot\mathbf{R}_1} | \Psi^m_{nl}\rangle|^2, \tag{3.47}$$

whilst for the dissociated states we have the excitation probability density

$$\rho_{\mathbf{q}}(E_\eta, l, m) dE_\eta = |\langle \Psi_0 | e^{i\mathbf{q}\cdot\mathbf{R}_1} | \Psi^m_{\eta l}\rangle|^2. \tag{3.48}$$

The contribution from the bound states is simply

$$P_{\mathbf{q}}(E_n, m) = \left| \int X_{10} (Y^0_0)^* e^{i\alpha\mathbf{q}\cdot\mathbf{r}} X_{nl} Y^m_l d\mathbf{r} \right|^2. \tag{3.49}$$

Then due to the spherical symmetry

$$P_{\mathbf{q}}(E_n, l) = \sum_{m=-l}^{l} P_{\mathbf{q}}(E_n, l, m) = (2l+1) \left| \int_0^\infty X_{10} J_l(\alpha q r) X_{nl} dr \right|^2. \tag{3.50}$$

To calculate probability density for the contribution from the dissociated states we first quantise the wavefunctions in a finite sphere of radius L, and then take the limit $L \to \infty$ to obtain the continuum limit. In this limit the interval ΔE_η between neighbouring energy

becomes the measure dE_η for the energy. To confine the wavefunctions (Eq. 3.44) to a sphere of radius L, the wavefunction must vanish at the boundary of the sphere. This quantises the energy by imposing the condition

$$\frac{L}{\eta} + \eta \ln \frac{2L}{\eta} + \delta_l = m\pi. \tag{3.51}$$

If we examine the quantity $\frac{L}{m\pi}$ and take the limit $L \to \infty$, then we find

$$\lim_{L\to\infty} \left[\frac{L}{m\pi}\right] = \lim_{L\to\infty} \left[\frac{L}{\left(\frac{L}{\eta} + \eta \ln \frac{2L}{\eta} + \delta_l\right)}\right] = \eta. \tag{3.52}$$

The interval between neighbouring energy levels is therefore

$$\Delta E_\eta = \Delta\left(\frac{1}{\eta^2}\right) = \frac{2}{\eta}\Delta\left(\frac{1}{\eta}\right) = \frac{2\pi}{\eta L}. \tag{3.53}$$

This term must be incorporated into the normalisation of the wavefunctions in Eq. 3.44:

$$X_{\eta l}(r) = \sqrt{\frac{\Delta E_\eta \sinh(\pi\eta)}{2^{2l}\eta^2\pi^2 e^{-\pi\eta}\prod_{p=1}^{l}(p^2+\eta^2)}} \left(\frac{r}{\eta}\right)^l \int_0^\infty \left(\frac{\cos(\frac{r}{\eta}\tanh(x) + 2\eta x)}{\cosh^{2l+2}(x)}\right) dx. \tag{3.54}$$

If we define $X_{\eta l} = \sqrt{\Delta E_\eta}\tilde{X}_{\eta l}$, then in the continuum limit $\Delta E_\eta \to dE_\eta$ and the probability density takes the form

$$\rho_{\mathbf{q}}(E_\eta, l, m) = |\langle\Psi_0|e^{i\mathbf{q}\cdot\mathbf{R}_1}|\tilde{\Psi}^m_{\eta l}\rangle|^2 = \left|\int X_{10}(Y^0_0)^* e^{i\alpha\mathbf{q}\cdot\mathbf{r}}\tilde{X}_{\eta l}Y^m_l d\mathbf{r}\right|^2. \tag{3.55}$$

Then, using the spherical symmetry,

$$\rho_{\mathbf{q}}(E_\eta, l) = \sum_{m=-l}^{l}\rho_{\mathbf{q}}(E_\eta, l, m) = (2l+1)\left|\int_0^\infty X_{10}J_l(\alpha q r)\tilde{X}_{\eta l}dr\right|^2. \tag{3.56}$$

The integral over the continuum of dissociated states gives

$$\begin{aligned}&\int_0^\infty \rho_{\mathbf{q}}(E_\eta, l)\delta(\hbar\omega + E_0 - E_\eta - \Delta E_{cm})dE_\eta \\ &= \rho_{\mathbf{q}}(\hbar\omega + E_0 - \Delta E_{cm}, l)\Theta(\hbar\omega + E_0 - \Delta E_{cm}).\end{aligned} \tag{3.57}$$

Finally, the complete hydrogen response function is

$$\begin{aligned}S(\mathbf{q},\omega) &= \sum_{nl} P_{\mathbf{q}}(E_n, l)\delta(\hbar\omega + E_0 - E_n - \Delta E_{cm}) \\ &+ \sum_l \rho_{\mathbf{q}}(\hbar\omega + E_0 - \Delta E_{cm}, l)\Theta(\hbar\omega + E_0 - \Delta E_{cm})\end{aligned} \tag{3.58}$$

3.2.6 The excitation probabilities for the hydrogen atom

The probability of exciting an electron in the hydrogen atom is found from the probability distributions:

$$P_{\mathbf{q}}(E_n, l) = (2l+1)\left|\int_0^\infty r^2 X_{10}^*(r) J_l(\alpha q r) X_{nl}(r) dr\right|^2 \tag{3.59}$$

$$\rho_{\mathbf{q}}(E_\eta, l) = (2l+1)\left|\int_0^\infty r^2 X_{10}^*(r) J_l(\alpha r q) \tilde{X}_{\eta l}(r) dr\right|^2. \tag{3.60}$$

The natural calculation to begin with is the probability that the electron remains in its ground state,

$$P_{\mathbf{q}}(E_0, 0) = 16\left|\int_0^\infty r^2 e^{-2r} \frac{\sin(\alpha r q)}{\alpha r q} dr\right|^2 = \frac{1}{\left(1+\frac{\alpha^2 q^2}{4}\right)^4}. \tag{3.61}$$

We are essentially calculating the momentum distribution of the electron relative to the proton, i.e, $n(\alpha q)$. If we consider an incident neutron with an energy of $E = 100$eV, which is experimentally obtainable, then this corresponds to a momentum of 219.7Å^{-1}, or equivalently $116.2a_0^{-1}$. Then using this value for the transferred momentum q the probability that the electron remains in its ground state is $P_{\mathbf{q}}(E_0, 0) \approx 0.996$, which corresponds to the excitation of only 0.4% of the electrons. Similar conclusions have been made in previous works such as [16, 36]. For the hydrogen atom this quantity is all that we require and we could stop here. Nevertheless, it is instructive to calculate the probabilities associated with electronic dissociation, which occurs at much higher energies than neutron Compton scattering experiments are currently able to probe.

The excitation probabilities $P_{\mathbf{q}}(E_n, l)$ for the bound states, and the excitation probability densities $\rho_{\mathbf{q}}(E_{\eta,l})$ for the dissociated states are illustrated in Fig. 3.3. The momentum transfer q is chosen to be large so that both the bound states and the dissociated states are excited. An examination of these probabilities shows that when the momentum transfer is increased, the dissociated states with high angular momentum are more likely to be excited.

The excitation probabilities as a function of transferred momentum are illustrated in Fig. 3.4, where all the states with angular momentum $l \leq 10$ and energy $E \leq 20$ are included. To verify that the entire excitation spectrum is included in the calculation of the excitation probabilities we sum over all of the energies, for each value of q. For large values of q this summation starts to drop below one, indicating that some of the states are not accounted for. This is because high energy states, and states with high angular momentum are excited for high values of q. There is a significant probability ($\sim 10\%$) that the electron becomes excited above 1000Å^{-1}, at which point there are transitions to

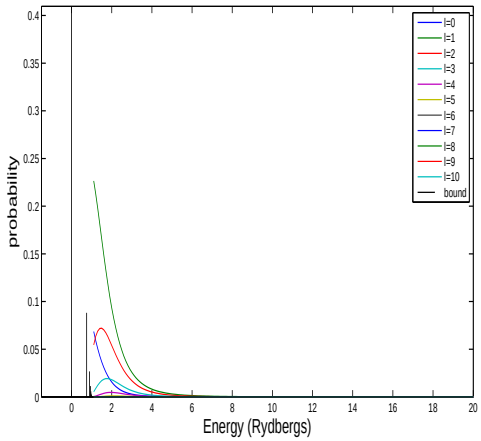

(a) The excitation probabilities of the electronic modes of the hydrogen atom, evaluated at $q \approx 3500\text{Å}^{-1}$.

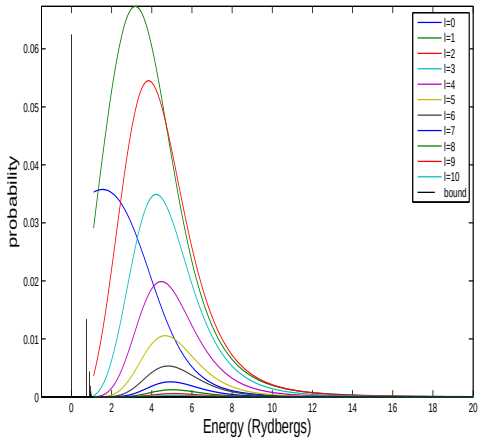

(b) The excitation probabilities of the electronic modes of the hydrogen atom, evaluated at $q \approx 7000\text{Å}^{-1}$.

Figure 3.3: Excitation probabilities for the hydrogen atom.

higher energy bound states and to the dissociated state with angular momentum $l = 1$. This fact can be understood if we expand the exponent of the transition operator in powers of $\alpha\mathbf{q}$. The first order correction is $\sim \mathbf{q}\cdot\mathbf{r}$ which has the form of a dipole operator, and consequentially satisfies the selection rule $\Delta l = \pm 1$. As the momentum transfer is increased, higher order terms become significant which are capable of exciting the higher angular momentum dissociated states.

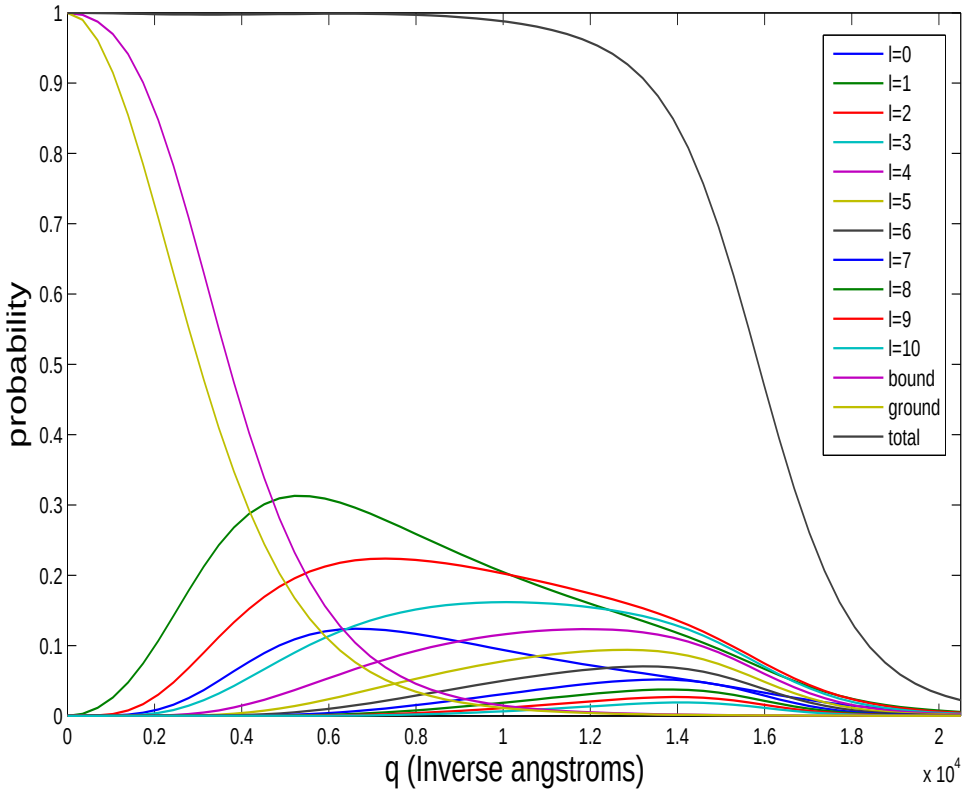

Figure 3.4: The complete excitation probabilities of the hydrogen atom, evaluated as a function of q. The total probability is indicated by the black line running along the top of the graph, indicating that all of the low energy states are accounted for.

Chapter 4

Non-adiabatic effects in molecular hydrogen

In a molecular system containing several nuclei it is convenient to assume that, because the light electrons travel much faster than the heavy nuclei, we can adiabatically separate the electronic and nuclear degrees of freedom by applying the Born-Oppenheimer approximation[37]. However, if we employ the basic Born-Oppenheimer style molecular wavefunctions, then the electron is only excited through the CMR effect. The resulting electronic excitation probabilities would then be expected to be of the same order of magnitude as in the hydrogen atom, i.e, less than one percent. However, in a sufficiently high energy neutron-nucleus collision the recoiling nucleus can travel at speeds which are comparable to that of an electron, and the logic behind an adiabatic separation obviously breaks down. We would then anticipate large non-adiabatic corrections to the final state wavefunctions, which opens up the possibility of electronic excitation through non-adiabatic processes. Understanding the nature of the break down of the adiabatic approximation is therefore the main goal of this chapter.

In this chapter we investigate non-adiabatic effects arising in H_2^+, and assess the accuracy of the adiabatic approximation as a function of the mass ratio $\alpha \approx m_e/m_p$ and the transferred momentum q. The H_2^+ molecule has obviously been subjected to many detailed investigations and, consequently, the methods that we employ are not wholly original. However, the non-adiabatic properties of high energy dissociated states are rather less well studied and it is therefore necessary to perform accurate calculations for these states. Previous studies[16] have looked at the non-adiabatic effects in simple molecules, but we employ a slightly different, non-perturbative, approach to investigate the non-adiabatic effects. We utilise two different methods to obtain the molecular wavefunctions, and the results are compared so that we may understand the strengths and weaknesses of each method.

In the first approach we perform a *Born-Huang* expansion[38] of the exact wavefunction. This technique uses the electronic states, obtained from applying the Born-Oppenheimer approximation, as a basis in which to recover the exact solution. This leads to the *Born-Huang* matrix equation for the nuclear wavefunctions which contains non-adiabatic coupling (NAC) between the electronic states. This approach is particularly intuitive, and clearly illustrates the mechanism by which NAC leads to electronic excitation.

The second approach is to obtain an approximate numerical solution to the exact molecular Hamiltonian. To simplify the molecular Hamiltonian it is necessary to make a distinction between two styles of coordinates: the Euler angles, which specify the orientation of the molecule, and the shape coordinates, which specify the relative positions of the particles. We rigourously separate the three Euler angles from the internal shape coordinates to obtain a much simpler form of the Hamiltonian which can be solved numerically to obtain the zero angular momentum eigenstates. This approach is non-perturbative and does not rely on the use of a particular basis set to obtain the molecular wavefunctions: it is therefore of use when investigating situations where the adiabatic approximation is known to break down.

By comparing the solutions obtained using both techniques we show that the results are consistent, but highlight specific points where the adiabatic separation of nuclear and electronic coordinates breaks down. From this analysis we conclude that for realistic values of α and q NAC leads to less electronic excitation than CMR, and therefore the adiabatic approximation remains valid.

Finally, we look at the implications of this work for experiments involving neutron Compton scattering from systems such as NbH_2 and PdH_2, and conclude that electronic excitations cannot be responsible for the anomalous measurements of hydrogenic cross sections.

4.1 The Born-Oppenheimer approximation

The Born-Oppenheimer (or adiabatic) approximation greatly simplifies the investigation of molecular systems. The approximation relies upon one simple assumption; the motion of the light electrons follows the motion of the heavy nuclei. Basically, because the electrons are much lighter and move much faster than the heavy nuclei, it is assumed that the electrons arrange themselves around the *instantaneous* positions of the nuclei. The nuclei, however, only feel the *average* potential created by the charge cloud of the electrons. Therefore, the electronic distribution can be studied for a fixed nuclear configuration and the resulting electronic energies, which depend upon the nuclear configuration, form

potential energy surfaces which govern the motion of the nuclei.

To derive the Born-Oppenheimer approximation we start with the molecular Hamiltonian, which may be written

$$\mathcal{H}_{mol} = \mathcal{H}_e + \mathcal{T}_n, \tag{4.1}$$

where the electronic kinetic energy and the potential energy terms are contained in the electronic Hamiltonian,

$$\mathcal{H}_e = \sum_{i=1}^{N_e} \frac{\hbar^2 \nabla^2_{\mathbf{r}_i}}{2m_e} + \sum_{i>j=1}^{N_e} \frac{1}{|\mathbf{r}_i - \mathbf{r}_j|} + \sum_{\alpha>\beta=1}^{N} \frac{Z_\alpha Z_\beta}{|\mathbf{R}_\alpha - \mathbf{R}_\beta|} - \sum_{i=1}^{N_e}\sum_{\alpha=1}^{N} \frac{Z_\alpha}{|\mathbf{R}_\alpha - \mathbf{r}_i|}, \tag{4.2}$$

and the kinetic energy of the nuclei is

$$\mathcal{T}_n = -\sum_{\alpha=1}^{N} \frac{\hbar^2 \nabla^2_\alpha}{2M_\alpha}. \tag{4.3}$$

We will adopt the compact notation $\mathbf{R} = (\mathbf{R}_1, ..., \mathbf{R}_N)$ and $\mathbf{r} = (\mathbf{r}_1, ..., \mathbf{r}_{N_e})$ for the nuclear and electronic coordinates respectively. The electronic Hamiltonian depends *parametrically* on the nuclear coordinates $\mathbf{R}$. We may therefore solve it for each nuclear configuration, so that both the electronic wavefunction and the electronic energy depend parametrically on $\mathbf{R}$:

$$\mathcal{H}_e \Phi_n(\mathbf{r}; \mathbf{R}) = \varepsilon_n(\mathbf{R}) \Phi_n(\mathbf{r}; \mathbf{R}). \tag{4.4}$$

The energy eigenvalues map out the potential energy surfaces for the nuclei:

$$\left[\mathcal{T}_n + \varepsilon_n(\mathbf{R})\right] X_n^m(\mathbf{R}) = E_n^m X_n^m(\mathbf{R}), \tag{4.5}$$

where the wavefunction X_n^m correpsonds to the m-th vibrational mode of the nuclei in the n-th potential energy surface. In the Born-Oppenheimer approximation we express the molecular wavefunction as

$$\Psi_n^m(\mathbf{R}, \mathbf{r}) = X_n^m(\mathbf{R}) \Phi_n(\mathbf{r}; \mathbf{R}). \tag{4.6}$$

This result was originally derived by Born and Oppenheimer using Taylor series expansions in the small parameter $\lambda = (m_e/M)^{\frac{1}{4}}$. They expanded the molecular Schrödinger equation in powers of λ and solved the electronic eigenvalue problem in powers of the internuclear displacements, assuming the latter to be small. It was systematically showed that, when there is no degeneracy in the electronic energy, the Born-Oppenheimer molecular wavefunction (Eq 4.6) has an error of order λ^3.

For high energy states, for which the oscillations of the nuclei can no longer be regarded as being small, the original treatment by Born and Oppenheimer is not valid. Other approaches, which circumvent this problem by using variational methods to derive a wavefunction of the same form Eq 4.6, do not give a good indication of the size of the errors involved. For high energy dissociated states the situation is even less clear and quantifying the errors is a difficult task. It has also been demonstrated[39], using the model four body problem discussed in chapter 2, that in addition to the customary expansion parameter λ, other non-analytic terms may appear in the expansion of the wavefunction in the large M limit. In this chapter we investigate, as thoroughly as possible, the reliability of the adiabatic approximation for high energy dissociated states.

4.2 Going beyond the Born-Oppenheimer approximation

To acquire accurate molecular wavefunctions it is necessary to go beyond the Born-Oppenheimer approximation. There are many schemes which allow us to do this, usually involving a insightfully chosen basis set, but the simplest is probably the *Born-Huang* expansion. This expansion exploits the completeness of the electronic wavefunctions, which are used as a basis for the exact solution. The exact wavefunction is expanded as

$$\Psi_n^m(\mathbf{R},\mathbf{r}) = \sum_{n'} X_{nn'}^m(\mathbf{R})\Phi_{n'}(\mathbf{r};\mathbf{R}) \tag{4.7}$$

with an energy

$$E_n^m = \sum_{n'n''} \langle X_{nn'}^m \Phi_n | \varepsilon_n(\mathbf{R}) + \mathcal{T}_n | X_{nn''}^m \Phi_n \rangle. \tag{4.8}$$

To obtain the exact equations for the vector $\boldsymbol{X}_n^m = (X_{n1}^m, X_{n2}^m, ...)$ we require the Hamiltonian matrix elements

$$\hat{\boldsymbol{\mathcal{H}}}_{n'n''} = \widehat{\langle \Phi_{n'} | \mathcal{T}_n | \Phi_{n''} \rangle} + \delta_{n'n''}\varepsilon_{n'}. \tag{4.9}$$

The first term is in fact an operator which acts on the vector $\boldsymbol{X}_n^m$. This operator, when fully expanded, is

$$\widehat{\langle \Phi_{n'} | \mathcal{T}_n | \Phi_{n''} \rangle} = \delta_{n'n''}\mathcal{T}_n - \sum_{\alpha=1}^{N} \frac{\hbar^2 \langle \Phi_{n'} | \nabla_\alpha | \Phi_{n''} \rangle}{M_\alpha} \nabla_\alpha + \langle \Phi_{n'} | \mathcal{T}_n | \Phi_{n''} \rangle. \tag{4.10}$$

This results in a set of coupled differential equations which, in matrix notation, may be written

$$\hat{\boldsymbol{\mathcal{H}}}\boldsymbol{X}_n^m = E_n^m \boldsymbol{X}_n^m. \tag{4.11}$$

The matrix Hamiltonian defined by Eq. 4.11 contains the small coupling terms between different electronic Born-Oppenheimer states. When two electronic states become degenerate for some nuclear configuration the concept of a distinct energy surface breaks down. In this case one can perform a *diabatic* transformation[40] which eliminates the off-diagonal coupling terms from the Hamiltonian matrix and removes the degeneracy. Degeneracy of the electronic energy surfaces also leads to a geometric *Berry phase*[41], which appears when the nuclei are transported along a path in configuration space which encloses a degenerate point.

It is usually impractical to use a large number of electronic states as a basis and we are forced to truncate the expansion of the wavefunction to just a few terms. In this chapter the non-adiabatic matrix equations are solved for the H_2^+ molecule, using a basis of just two electronic states.

4.3 The failure of the Born-Oppenheimer approximation

A straightforward application of the adiabatic approximation to molecular systems reveals that it is insufficient for describing the electronic excitation that occurs in very high energy neutron-nucleus scattering. This is because the separation of the molecular wavefunction, into a nuclear part and an electronic part, eliminates the coupling, between different electronic states, which leads to electronic excitation upon nuclear dissociation. This can be demonstrated by calculating the excitation probabilities for an interaction between the neutron and the nucleus at $\mathbf{R}_t$:

$$P_{\mathbf{q}}(E_f; E_i) = |\langle \Psi_i | e^{i\mathbf{q}\cdot\mathbf{R}_t} | \Psi_f \rangle|^2. \tag{4.12}$$

In the adiabatic approximation the molecular wavefunction is decomposed into nuclear and electronic parts, i.e,

$$\Psi_n^m(\mathbf{R}, \mathbf{r}) = X_n^m(\mathbf{R})\Phi_n(\mathbf{r}; \mathbf{R}). \tag{4.13}$$

If we substitute this into Eq. 4.12, we find that

$$P_{\mathbf{q}}(E_{n'm'}; E_{nm}) = \left| \int d\mathbf{R} X_n^m(\mathbf{R}) e^{i\mathbf{q}\cdot\mathbf{R}_t} X_{n'}^{m'}(\mathbf{R}) \right|^2 \delta_{nn'}, \tag{4.14}$$

where we have made use of the orthogonality condition,

$$\int d\mathbf{r}\Phi_n(\mathbf{r};\mathbf{R})\Phi_{n'}(\mathbf{r};\mathbf{R}) = \delta_{nn'}, \tag{4.15}$$

for the electronic wavefunctions. We therefore find that the adiabatic approximation does not allow electronic excitation[1]. The non-adiabatic contributions to electronic excitation arise from the coupling between different electronic states that appears in the Born-Huang expansion of the molecular wavefunction:

$$\Psi_n^m(\mathbf{R},\mathbf{r}) = \sum_{n'} X_{nn'}^m(\mathbf{R})\Phi_{n'}(\mathbf{r};\mathbf{R}). \tag{4.16}$$

We then find the excitation probabilities,

$$P_{\mathbf{q}}(E_{n'm'};E_{nm}) = \left|\sum_{n''}\int d\mathbf{R}X_{nn''}^m(\mathbf{R})e^{i\mathbf{q}\cdot\mathbf{R}_t}X_{n'n''}^{m'}(\mathbf{R})\right|^2. \tag{4.17}$$

In this chapter we will make use of a Born-Huang expansion of the molecular wavefunction to determine the probability that the H_2^+ molecule is electronically excited during molecular dissociation. However, the drawback of this technique is that we can only use a finite basis of electronic states, and we cannot be certain of the relative errors. Therefore, to fully capture the non-adiabatic effects, we also solve the molecular Hamiltonian directly to incorporate the contributions from all of the electronic states.

4.4 The molecular Hamiltonian of H_2^+

In this section we will focus on the simplest realistic system, the hydrogen molecular ion H_2^+, which can be solved with a high degree of accuracy. To obtain the desired level of accuracy we work with the exact Hamiltonian for as long as possible, which requires us to carefully consider the symmetries of the molecule. We make use of known techniques to separate the translational and rotational symmetries of the molecule. This reduces the number of coordinates from nine, to just three for the zero angular momentum states. The eigenstates of the simplified three dimensional Hamiltonian are then be obtained using numerical techniques. We start from the Hamiltonian for the general three-body problem,

$$\mathcal{H} = -\frac{\hbar^2}{2}\left[\frac{\nabla_{\mathbf{R}_1}^2}{m_1}+\frac{\nabla_{\mathbf{R}_2}^2}{m_2}+\frac{\nabla_{\mathbf{R}_3}^2}{m_3}\right]+\frac{e^2}{4\pi\epsilon_0}\left[\frac{Z_1Z_2}{|\mathbf{R}_1-\mathbf{R}_2|}+\frac{Z_2Z_3}{|\mathbf{R}_2-\mathbf{R}_3|}+\frac{Z_1Z_3}{|\mathbf{R}_1-\mathbf{R}_3|}\right]. \tag{4.18}$$

[1]If the adiabatic approximation is applied in the centre of mass frame, as it often is, we are then able to determine the contribution to electronic excitation from the CMR effect. Unfortunately, the contribution to electronic excitation from the NAC is always excluded when the Born Oppenheimer expansion is applied.

The first step is to transform to the centre of mass frame, which is accomplished with the following choice of Jacobi coordinates[2]:

$$\mathbf{R}_{cm} = \frac{m_1\mathbf{R}_1 + m_2\mathbf{R}_2 + m_3\mathbf{R}_3}{m_1 + m_2 + m_3} \tag{4.19}$$

$$\mathbf{r}_1 = \mathbf{R}_3 - \frac{m_1\mathbf{R}_1 + m_2\mathbf{R}_2}{m_1 + m_2} \tag{4.20}$$

$$\mathbf{r}_2 = \mathbf{R}_1 - \mathbf{R}_2. \tag{4.21}$$

In these coordinates the centre of mass can be separated, and the molecular wavefunction is

$$\Psi_{mol} = \frac{1}{\sqrt{V}} e^{i\mathbf{k}_{cm}\cdot\mathbf{R}_{cm}} \Psi(\boldsymbol{r}_1, \boldsymbol{r}_2). \tag{4.22}$$

The six dimensional wavefunctions $\Psi(\boldsymbol{r}_1, \boldsymbol{r}_2)$, which represent the motion of the nuclei and the electron in the centre of mass frame, are the eigenstates of the Hamiltonian

$$\mathcal{H} = -\frac{\hbar^2\nabla^2_{\mathbf{r}_1}}{2\mu_1} - \frac{\hbar^2\nabla^2_{\mathbf{r}_2}}{2\mu_2} + \frac{e^2}{4\pi\epsilon_0}\left[\frac{Z_1Z_2}{\left|\mathbf{r}_1 + \frac{m_1}{m_1+m_2}\mathbf{r}_2\right|} + \frac{Z_2Z_3}{\left|\mathbf{r}_1 + \frac{m_2}{m_1+m_2}\mathbf{r}_2\right|} + \frac{Z_1Z_3}{|\mathbf{r}_2|}\right]. \tag{4.23}$$

The reduced masses are defined

$$\mu_1 = \frac{(m_1 + m_2)m_3}{m_1 + m_2 + m_3} \qquad \mu_2 = \frac{m_1m_2}{m_1 + m_2}. \tag{4.24}$$

4.4.1 Separating the rotational symmetry

After separating the centre of mass motion of a molecule containing N particles there are $3N-3$ remaining degrees of freedom. It is then useful to think in terms of the *shapes* which are created from all the possible configurations of the particles in the centre of mass frame. Since every possible orientation of these shapes can be obtained by successive rotations through the three *Euler angles*, we only require $3N-6$ shape coordinates to define every possible shape[32]. A common example is the *Eckart frame*[42], which is often used to study polyatomic molecules. In this case, the $3N-6$ coordinates represent the vibrational modes of the N nuclei about their equilibrium configurations.

By applying this idea to the three body problem it is possible to reduce the number of degrees of freedom to just three for $\boldsymbol{L} = 0$ states, or just four for $\boldsymbol{L} \neq 0$ states[3]. In the

[2]There are obviously other choices, but this choice is appropriate because it treats the two nuclei symmetrically and simplifies the treatment of nuclear dissociation. In general, different Jacobi coordinates are appropriate for describing different entrance and exit channels in scattering processes.

[3]The group SO(3) (the group of proper three dimensional rotations) is a symmetry of the general

latter case three of the coordinates describe the evolution of shape of the system, and the fourth describes the evolution of the angular momentum vector in a body fixed frame. To utilise the rotational symmetry and reduce the number of degrees of freedom, we represent the Hamiltonian in a suitable body-fixed frame of reference, where the coordinate axes rotate with the molecule. The choice of body fixed frame is not unique, but is equivalent to choosing a particular gauge. We will make a choice (Very similar choices have previously been used in, e.g, [43]) which defines the body fixed frame illustrated in Fig. 4.1, for which $\boldsymbol{r}_2$ lies along the body fixed z-axis and $\boldsymbol{r}_1$ is in the x-z plane: $\boldsymbol{r}_1 = r_1(0,0,1)$ and $\boldsymbol{r}_2 = r_2(\sin(\gamma),0,\cos(\gamma))$, where γ is the angle between $\boldsymbol{r}_1$ and $\boldsymbol{r}_2$. The transformation to the body fixed frame is accomplished by representing the Hamiltonian in bi-spherical coordinates:

$$\mathbf{r}_1(x_1,y_1,z_1) \mapsto \mathbf{r}_1(\theta_1,\phi_1,r_1) \qquad \mathbf{r}_2(x_2,y_2,z_2) \mapsto \mathbf{r}_2(\theta_2,\phi_2,r_2) \tag{4.25}$$

$$x_1 = r_1\cos(\phi_1)\sin(\theta_1) \qquad x_2 = r_2\cos(\phi_2)\sin(\theta_2) \tag{4.26}$$

$$y_1 = r_1\sin(\phi_1)\sin(\theta_1) \qquad y_2 = r_2\sin(\phi_2)\sin(\theta_2) \tag{4.27}$$

$$z_1 = r_1\cos(\theta_1) \qquad z_2 = r_2\cos(\theta_2). \tag{4.28}$$

The Hamiltonian becomes may then be written

$$\mathcal{H} = -\frac{1}{2\mu_1 r_1^2}\left(\hbar^2\frac{\partial}{\partial r_1}\left(r_1^2\frac{\partial}{\partial r_2}\right) - \hat{\boldsymbol{L}}_1^{\,2}\right) - \frac{1}{2\mu_2 r_2^2}\left(\hbar^2\frac{\partial}{\partial r_2}\left(r_2^2\frac{\partial}{\partial r_2}\right) - \hat{\boldsymbol{L}}_2^{\,2}\right) + \frac{e^2}{4\pi\epsilon_0}\hat{V}, \tag{4.29}$$

where $\hat{V}$ is the potential energy, and the single particle angular momentum operators are

$$\hat{\boldsymbol{L}}_i^{\,2} = (\hat{L}_i)_x^2 + (\hat{L}_i)_y^2 + (\hat{L}_i)_z^2 = -\hbar^2\left(\frac{1}{r_i^2\sin(\theta_i)}\frac{\partial}{\partial\theta_i}\left(\sin(\theta_i)\frac{\partial}{\partial\theta_i}\right) + \frac{1}{r_i^2\sin^2(\theta_i)}\frac{\partial^2}{\partial\phi_i^2}\right). \tag{4.30}$$

Then to define the body-fixed frame we rotate the first set of coordinates so that the z-axis lies along $\boldsymbol{r}_2$ (i.e $\hat{\mathbf{z}}_1 = \hat{\mathbf{r}}_2$). We therefore apply a rotation of the coordinates, $\mathbf{r}_1' = \boldsymbol{R}(\phi_2,\theta_2,0)\mathbf{r}_1$:

N-body molecular Hamiltonian. However, due to the non-Abelian character of SO(3) it is only possible to eliminate two degrees of freedom, except in the special case where $\boldsymbol{L} = 0$.

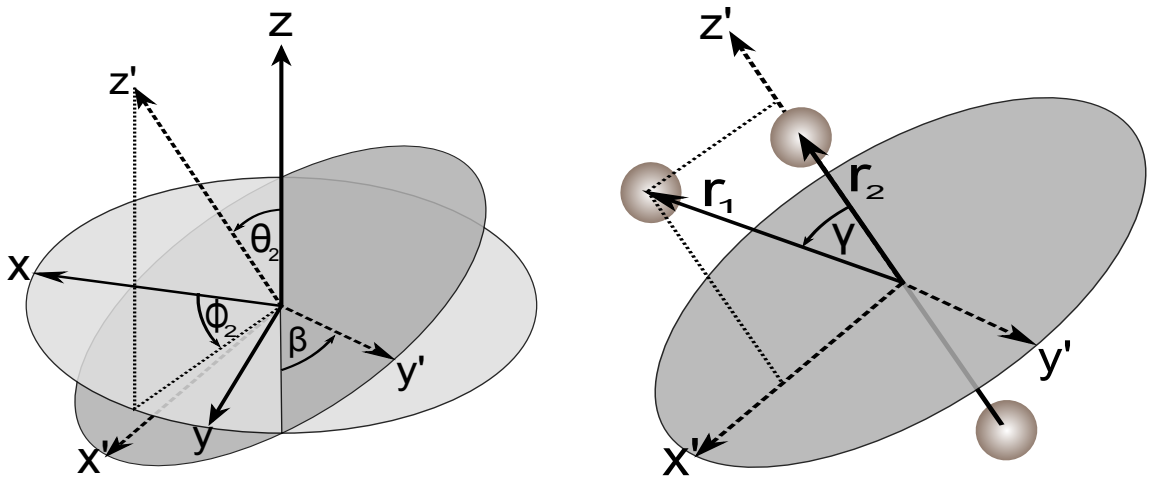

(a) The body fixed frame is defined relative to the space fixed frame by the Euler angles θ_2, ϕ_2 and β.

(b) The shape of the particles is defined in terms of the shape coordinates r_1, r_2 and γ in the body fixed frame.

Figure 4.1: Separation of the Euler angles from the shape coordinates.

$$\begin{pmatrix} (\mathbf{r}_1')_x \\ (\mathbf{r}_1')_y \\ (\mathbf{r}_1')_z \end{pmatrix} = \begin{pmatrix} \cos(\theta_2)\cos(\phi_2) & \cos(\theta_2)\sin(\phi_2) & -\sin(\theta_2) \\ -\sin(\phi_2) & \cos(\phi_2) & 0 \\ \sin(\theta_2)\cos(\phi_2) & \sin(\theta_2)\sin(\phi_2) & \cos(\theta_2) \end{pmatrix} \begin{pmatrix} (\mathbf{r}_1)_x \\ (\mathbf{r}_1)_y \\ (\mathbf{r}_1)_z \end{pmatrix}. \quad (4.31)$$

We then define the body fixed coordinates illustrated in Fig. 4.1 in terms of the angles γ and β:

$$\begin{pmatrix} r_1\cos(\beta)\sin(\gamma) \\ r_1\sin(\beta)\sin(\gamma) \\ r_1\cos(\gamma) \end{pmatrix} \equiv \begin{pmatrix} (\mathbf{r}_1')_x \\ (\mathbf{r}_1')_y \\ (\mathbf{r}_1')_z \end{pmatrix}. \quad (4.32)$$

After employing the above identities, the transformed Hamiltonian may be written

$$\cos(\beta)\sin(\gamma) = \sin(\theta_1)\sin(\theta_2)\cos(\phi_1-\phi_2) - \cos(\theta_1)\cos(\theta_2) \quad (4.33)$$

$$\sin(\beta)\sin(\gamma) = \sin(\theta_1)\sin(\phi_1-\phi_2) \quad (4.34)$$

$$\cos(\gamma) = \sin(\theta_1)\sin(\theta_2)\cos(\phi_1-\phi_2) + \cos(\theta_1)\sin(\theta_2). \quad (4.35)$$

The wave function depends on the body fixed coordinates $\Phi(r_1,\gamma,\beta,r_2,\theta_2,\phi_2)$, and the differential operators must also be represented in the body fixed frame:

$$\frac{\partial}{\partial\theta_1} = \frac{\partial\gamma}{\partial\theta_1}\frac{\partial}{\partial\gamma} + \frac{\partial\beta}{\partial\theta_1}\frac{\partial}{\partial\beta} \quad (4.36)$$

$$\frac{\partial}{\partial\phi_1} = \frac{\partial\gamma}{\partial\phi_1}\frac{\partial}{\partial\gamma} + \frac{\partial\beta}{\partial\phi_1}\frac{\partial}{\partial\beta} \tag{4.37}$$

$$\left[\frac{\partial}{\partial\theta_2}\right]_1 = \left[\frac{\partial}{\partial\theta_2}\right]_2 + \frac{\partial\gamma}{\partial\theta_2}\frac{\partial}{\partial\gamma} + \frac{\partial\beta}{\partial\theta_2}\frac{\partial}{\partial\beta} \tag{4.38}$$

$$\left[\frac{\partial}{\partial\phi_2}\right]_1 = \left[\frac{\partial}{\partial\phi_2}\right]_2 + \frac{\partial\gamma}{\partial\phi_2}\frac{\partial}{\partial\gamma} + \frac{\partial\beta}{\partial\phi_2}\frac{\partial}{\partial\beta}, \tag{4.39}$$

where the indices 1 and 2 refer to the operator acting in the $(r_1, \theta_1, \phi_1, r_2, \theta_2, \phi_2)$ and $(r_1, \gamma, \beta, r_2, \theta_2, \phi_2)$ coordinate spaces respectively. After calculating the derivatives in the body fixed frame we find that

$$\frac{1}{\hbar^2}\hat{\boldsymbol{L}}_1^2 = -\frac{1}{r_1^2\sin(\gamma)}\frac{\partial}{\partial\gamma}\left(\sin(\gamma)\frac{\partial}{\partial\gamma}\right) - \frac{1}{r_1^2\sin^2(\gamma)}\frac{\partial^2}{\partial\beta^2} \tag{4.40}$$

$$\begin{aligned}\frac{1}{\hbar^2}\hat{\boldsymbol{L}}_2^2 = &-\frac{1}{r_2^2\sin(\gamma)}\frac{\partial}{\partial\gamma}\left(\sin(\gamma)\frac{\partial}{\partial\gamma}\right)\\ &-\frac{1}{r_2^2}\left(\frac{\cos^2(\gamma)}{\sin^2(\gamma)} + \frac{\cos^2(\theta_2)}{\sin^2(\theta_2)} + \frac{2\cos(\theta_2)\cos(\gamma)\cos(\beta)}{\sin(\theta_2)\sin(\gamma)}\right)\frac{\partial^2}{\partial\beta^2}\\ &-\frac{2\sin(\beta)\cos(\theta_2)}{r_2^2\sin(\theta_2)}\frac{\partial^2}{\partial\gamma\partial\beta} - \frac{1}{r_2^2\sin(\theta_2)}\frac{\partial}{\partial\theta_2}\left(\sin(\theta_2)\frac{\partial}{\partial\theta_2}\right) - \frac{1}{r_2^2\sin^2(\theta_2)}\frac{\partial^2}{\partial\phi_2^2} + \frac{2\cos(\beta)}{r_2^2}\frac{\partial^2}{\partial\gamma\partial\theta_2}\\ &-\frac{2\cos(\gamma)\sin(\beta)}{r_2^2\sin(\gamma)}\frac{\partial^2}{\partial\beta\partial\theta_2} + \frac{2\sin(\beta)}{r_2^2\sin(\theta_2)}\frac{\partial^2}{\partial\gamma\partial\phi_2} + \frac{1}{r_2^2}\left(\frac{2\cos(\theta_2)}{\sin^2(\theta_2)} + \frac{2\cos(\gamma)\cos(\beta)}{\sin(\theta_2)\sin(\gamma)}\right)\frac{\partial^2}{\partial\beta\partial\phi_2}.\end{aligned} \tag{4.41}$$

The first operator $\hat{L}_1^2$ retains its original form in the body fixed frame because it does not affect θ_2 and ϕ_2, but $\hat{L}_2^2$ becomes much more complicated. The reason for using these coordinates will become clear in the next section where we will see that the solution of the Hamiltonian can be greatly simplified by using the correct angular momentum eigenfunctions.

4.4.2 The angular momentum operators

The eigenfunctions of the Hamiltonian are not eigenfunctions of the single particle angular momentum operators $\hat{\boldsymbol{L}}_1$ and $\hat{\boldsymbol{L}}_2$. Instead, we must use the total angular momentum operator $\hat{\boldsymbol{L}} = \hat{\boldsymbol{L}}_1 + \hat{\boldsymbol{L}}_2$, which we will now calculate in the body fixed frame. In the centre of mass frame the components of the total angular momentum are

$$\frac{i}{\hbar}\hat{L}_x = -\sin(\phi_1)\frac{\partial}{\partial\theta_1} - \frac{\cos(\phi_1)\cos(\theta_1)}{\sin(\theta_1)}\frac{\partial}{\partial\phi_1} - \sin(\phi_2)\frac{\partial}{\partial\theta_2} - \frac{\cos(\phi_2)\cos(\theta_2)}{\sin(\theta_2)}\frac{\partial}{\partial\phi_2} \tag{4.42}$$

$$\frac{i}{\hbar}\hat{L}_y = \cos(\phi_1)\frac{\partial}{\partial\theta_1} - \frac{\sin(\phi_1)\cos(\theta_1)}{\sin(\theta_1)}\frac{\partial}{\partial\phi_1} + \cos(\phi_2)\frac{\partial}{\partial\theta_2} - \frac{\sin(\phi_2)\cos(\theta_2)}{\sin(\theta_2)}\frac{\partial}{\partial\phi_2} \tag{4.43}$$

$$\frac{i}{\hbar}\hat{L}_z = \frac{\partial}{\partial\phi_1} + \frac{\partial}{\partial\phi_2}, \tag{4.44}$$

which are represented in the body fixed frame as

$$\frac{i}{\hbar}\hat{L}_x = -\frac{\cos(\phi_2)\cos(\theta_2)}{\sin(\theta_2)}\frac{\partial}{\partial\phi_2} + \frac{\cos(\phi_2)}{\sin(\theta_2)}\frac{\partial}{\partial\beta} - \sin(\phi_2)\frac{\partial}{\partial\theta_2} \tag{4.45}$$

$$\frac{i}{\hbar}\hat{L}_y = -\frac{\sin(\phi_2)\cos(\theta_2)}{\sin(\theta_2)}\frac{\partial}{\partial\phi_2} + \frac{\sin(\phi_2)}{\sin(\theta_2)}\frac{\partial}{\partial\beta} + \cos(\phi_2)\frac{\partial}{\partial\theta_2} \tag{4.46}$$

$$\frac{i}{\hbar}\hat{L}_z = \frac{\partial}{\partial\phi_2}, \tag{4.47}$$

from which we obtain

$$\frac{1}{\hbar^2}\hat{\boldsymbol{L}}^2 = -\frac{1}{\sin(\theta_2)}\frac{\partial}{\partial\theta_2}\left(\sin(\theta_2)\frac{\partial}{\partial\theta_2}\right) - \frac{1}{\sin^2(\theta_2)}\frac{\partial^2}{\partial\phi_2^2} - \frac{1}{\sin^2(\theta_2)}\frac{\partial^2}{\partial\beta_2^2} + \frac{2\cos(\theta_2)}{\sin^2(\theta_2)}\frac{\partial^2}{\partial\beta\partial\phi_2}. \tag{4.48}$$

It can be verified that these angular momentum operators commute with the Hamiltonian and obey the necessary commutation relations,

$$\left[\hat{\boldsymbol{L}}^2, \hat{L}_z\right] = 0 \qquad \left[\hat{L}_a, \hat{L}_b\right] = i\hbar\epsilon^{abc}\hat{L}_c. \tag{4.49}$$

It turns out that the Hamiltonian is conveniently expressed in terms of the body fixed angular momentum operators. If the angles ϕ_2 and β are exchanged, then we obtain a set of operators for which the z-axis is the vector $\hat{\mathbf{r}}_2$:

$$\frac{i}{\hbar}\hat{J}_x = -\frac{\cos(\beta)\cos(\theta_2)}{\sin(\theta_2)}\frac{\partial}{\partial\beta} + \frac{\cos(\beta)}{\sin(\theta_2)}\frac{\partial}{\partial\phi_2} - \sin(\beta)\frac{\partial}{\partial\theta_2} \tag{4.50}$$

$$\frac{i}{\hbar}\hat{J}_y = -\frac{\sin(\beta)\cos(\theta_2)}{\sin(\theta_2)}\frac{\partial}{\partial\beta} + \frac{\sin(\beta)}{\sin(\theta_2)}\frac{\partial}{\partial\phi_2} + \cos(\beta)\frac{\partial}{\partial\theta_2} \tag{4.51}$$

$$\frac{i}{\hbar}\hat{J}_z = \frac{\partial}{\partial\beta}. \tag{4.52}$$

These body fixed angular momentum operators satisfy the same commutation relations as the original operators:

$$\left[\hat{\boldsymbol{J}}^2, \hat{J}_z\right] = 0 \qquad \left[\hat{J}_a, \hat{J}_b\right] = i\hbar\epsilon^{abc}\hat{J}_c. \tag{4.53}$$

It must be emphasised however that the components of the body fixed angular momentum operators do *not* commute with the Hamiltonian. It is also apparent that $\hat{\boldsymbol{J}}^2 = \hat{\boldsymbol{L}}^2$, and

therefore $\hat{\boldsymbol{J}}^2$ *does* commute with the Hamiltonian. The angular momentum eigenfunctions are solutions to the differential equation

$$\left(\hat{\boldsymbol{J}}^2 - \hbar^2 l(l+1)\right) \mathcal{D}^{(j)}_{k_z m_z}(\theta_2, \phi_2, \beta) = 0. \tag{4.54}$$

The solutions are the $2j+1$ dimensional Wigner-D matrices, otherwise known as the symmetric-top eigenfunctions. Because the operators $\hat{\boldsymbol{L}}^2/\hat{\boldsymbol{J}}^2$, $\hat{L}_z$ and $\hat{J}_z$ mutually commute, they can be simultaneously diagonalised. The general form of the Wigner-D matrices is

$$\mathcal{D}^{(j)}_{k_z m_z}(\theta_2, \phi_2, \beta) = e^{ik_z\phi_2} d^{(j)}(\theta_2) e^{im_z\beta}, \tag{4.55}$$

where the quantum numbers k_z and m_z correspond to the z-component of the angular momentum in the centre of mass and the body fixed frames respectively. The Wigner-d matrices $d^{(j)}(\theta_2)$ satisfy the differential equation

$$\left(\frac{d^2}{d\theta_2^2} + \frac{\cos(\theta_2)}{\sin(\theta_2)}\frac{d}{d\theta_2} - \frac{m_z^2 + k_z^2 - 2m_z k_z\cos(\theta_2)}{\sin^2(\theta_2)} + j(j+1)\right) d^{(j)}_{m_z k_z}(\theta_2) = 0 \tag{4.56}$$

and may be expressed in terms of the Jacobi polynomials,

$$d^{(j)}_{k_z m_z}(\theta_2) = \left(\frac{(j+k_z)!(j-k_z)!}{(j+m_z)!(j-m_z)!}\right)^{\frac{1}{2}} \cos^{k_z+m_z}\left(\frac{\theta_2}{2}\right) \sin^{k_z-m_z}\left(\frac{\theta_2}{2}\right) P^{(k_z-m_z, k_z+m_z)}_{j-k_z}(\cos(\theta_2)). \tag{4.57}$$

Finally, the Hamiltonian may be rewritten in terms of the body fixed coordinates and the angular momentum operators,

$$\begin{aligned}\mathcal{H} = &-\frac{1}{2\mu_1 r_1^2}\left(\hbar^2\frac{\partial}{\partial r_1}\left(r_1^2\frac{\partial}{\partial r_2}\right) + \frac{\hbar^2}{\sin(\gamma)}\frac{\partial}{\partial\gamma}\left(\sin(\gamma)\frac{\partial}{\partial\gamma}\right) - \frac{1}{\sin^2(\gamma)}\hat{J}_z^2\right) \\ &-\frac{1}{2\mu_2 r_2^2}\left(\hbar^2\frac{\partial}{\partial r_2}\left(r_2^2\frac{\partial}{\partial r_2}\right) + \frac{\hbar^2}{\sin(\gamma)}\frac{\partial}{\partial\gamma}\left(\sin(\gamma)\frac{\partial}{\partial\gamma}\right)\right) \\ -\frac{1}{2\mu_2 r_2^2}&\left(-\hat{J}_x^2 - \hat{J}_y^2 - \frac{\cos^2(\gamma)}{\sin^2(\gamma)}\hat{J}_z^2 - 2i\hbar\hat{J}_y\frac{\partial}{\partial\gamma} + \frac{2\cos(\gamma)}{\sin(\gamma)}\hat{J}_x\hat{J}_z\right) + \frac{e^2}{4\pi\epsilon_0}V.\end{aligned} \tag{4.58}$$

The solutions to this equation are linear combinations of the $2j+1$ angular momentum eigenfunctions,

$$\Psi^{lk_z}_n(r_1, \gamma, \beta, r_2, \theta_2, \phi_2) = \sum_{m_z} \psi^{lm_z}_n(r_1, r_2, \gamma)\mathcal{D}^{(l)}_{k_z m_z}(\theta_2, \phi_2, \beta). \tag{4.59}$$

We have now completed the partial separation of the angular momentum eigenfunctions.

The coordinates of the three dimensional functions $\psi_n^{jm_z}$ can be chosen independently of the angular coordinates which greatly simplifies the problem.

4.4.3 Shape space

In the previous sections we have shown that the eigenstates of the three body Hamiltonian may be represented, in the body fixed frame of reference, in terms of the Wigner D-matrices. There is then only the problem of determining the three dimensional functions $\psi_n^{jm_z}(r_1, r_2, \gamma)$ which control the *shape* of the three particles in the body fixed frame. For $N = 3$ the particles all lie in a single plane and the shape is simply a triangle, as illustrated in Fig. 4.2.

To carry out an investigation of non-adiabatic effects it is appropriate to work in the spheroidal coordinate system. This is a very natural choice of coordinates for a diatomic molecule because, as will be explained later in this chapter, the electronic Born-Oppenheimer Hamiltonian becomes clearly separable and can be solved analytically. To perform this transformation it is convenient to make use of an intermediate coordinate system which is defined by the inter-particle distances:

$$s_1^2 = |\mathbf{R}_2 - \mathbf{R}_3|^2 \qquad s_2^2 = |\mathbf{R}_1 - \mathbf{R}_3|^2 \qquad s_3^2 = |\mathbf{R}_2 - \mathbf{R}_1|^2 . \tag{4.60}$$

These coordinates are illustrated in Fig. 4.2(b). These can be expressed in terms of the body fixed coordinates:

$$s_1^2 = \left|\mathbf{r}_1 + \frac{m_1}{m_1+m_2}\mathbf{r}_2\right|^2 = r_1^2 + \frac{2m_1 r_1 r_2 \cos(\gamma)}{m_1+m_2} + \frac{m_1^2 r_2^2}{(m_1+m_2)^2} \tag{4.61}$$

$$s_2^2 = \left|\mathbf{r}_1 - \frac{m_2}{m_1+m_2}\mathbf{r}_2\right|^2 = r_1^2 - \frac{2m_2 r_1 r_2 \cos(\gamma)}{m_1+m_2} + \frac{m_2^2 r_2^2}{(m_1+m_2)^2} \tag{4.62}$$

$$s_3 = r_2. \tag{4.63}$$

When the derivatives have been transformed the Hamiltonian becomes

$$\begin{aligned}\mathcal{H} = &-\frac{\hbar^2}{2m_1}\left[\frac{1}{s_2^2}\frac{\partial}{\partial s_2}s_2^2\frac{\partial}{\partial s_2} + \frac{1}{s_3^2}\frac{\partial}{\partial s_3}s_3^2\frac{\partial}{\partial s_3} + \frac{p^3}{s_1}\frac{\partial p}{\partial s_1}\frac{1}{s_2 s_3}\frac{\partial^2}{\partial s_2 \partial s_3}\right] \\ &-\frac{\hbar^2}{2m_2}\left[\frac{1}{s_1^2}\frac{\partial}{\partial s_1}s_1^2\frac{\partial}{\partial s_1} + \frac{1}{s_3^2}\frac{\partial}{\partial s_3}s_3^2\frac{\partial}{\partial s_3} + \frac{p^3}{s_2}\frac{\partial p}{\partial s_2}\frac{1}{s_1 s_3}\frac{\partial^2}{\partial s_1 \partial s_3}\right] \\ &-\frac{\hbar^2}{2m_3}\left[\frac{1}{s_1^2}\frac{\partial}{\partial s_1}s_1^2\frac{\partial}{\partial s_1} + \frac{1}{s_2^2}\frac{\partial}{\partial s_2}s_2^2\frac{\partial}{\partial s_2} + \frac{p^3}{s_3}\frac{\partial p}{\partial s_3}\frac{1}{s_1 s_2}\frac{\partial^2}{\partial s_1 \partial s_2}\right]\end{aligned}$$

$$+\frac{2\hbar^2}{p^4}\left[\frac{s_1^2}{m_1}+\frac{s_2^2}{m_2}+\frac{s_3^2}{m_3}\right]\hat{J}_z^2$$
$$+\frac{\hbar^2}{2m_1s_3^2}\left[\hat{J}_x^2+\hat{J}_y^2-2\hat{J}_z^2+i\hat{J}_y\frac{p^2}{s_2}\frac{\partial}{\partial s_2}-2\hat{J}_x\hat{J}_z\frac{p}{s_2}\frac{\partial p}{\partial s_2}\right]$$
$$+\frac{\hbar^2}{2m_2s_3^2}\left[\hat{J}_x^2+\hat{J}_y^2-2\hat{J}_z^2-i\hat{J}_y\frac{p^2}{s_1}\frac{\partial}{\partial s_1}+2\hat{J}_x\hat{J}_z\frac{p}{s_1}\frac{\partial p}{\partial s_1}\right]$$
$$+\frac{e^2}{4\pi\epsilon_0}\left(\frac{Z_2Z_3}{s_1}+\frac{Z_1Z_3}{s_2}+\frac{Z_1Z_2}{s_3}\right). \tag{4.64}$$

As would be expected, this choice of coordinates treats the particles in a highly symmetric manner. The term p is symmetric in s_1, s_2 and s_3, and is defined

$$p^4=((s_1+s_2)^2-s_3^2)(s_3^2-(s_1-s_2)^2)=((s_2+s_3)^2-s_1^2)(s_1^2-(s_2-s_3)^2)$$

$$=((s_1+s_3)^2-s_2^2)(s_2^2-(s_1-s_3)^2). \tag{4.65}$$

The transformation to spheroidal coordinates is performed using the relationships

$$u=\frac{s_1+s_2}{s_3}\qquad v=\frac{s_1-s_2}{s_3}\qquad w=s_3. \tag{4.66}$$

The spheroidal coordinates are illustrated in Fig. 4.2(c). These expressions are easily inverted to give the inter-particle separations in terms of the spheroidal coordinates,

$$s_1=\frac{(u+v)w}{2}\qquad s_2=\frac{(u-v)w}{2}\qquad s_3=w. \tag{4.67}$$

When performing this transformation we will make the simplification $m_1=m_2$ and choose the values of Z_1, Z_2 and Z_3 which are appropriate for studying H_2^+. We then obtain

$$\mathcal{H}=-\frac{\hbar^2}{2}\left(\frac{1}{m_1}+\frac{1}{m_3}\right)\mathcal{A}-\frac{\hbar^2}{2m_3}\mathcal{B}+\frac{e^2}{4\pi\epsilon_0}V, \tag{4.68}$$

where the operators $\mathcal{A}$ and $\mathcal{B}$ are defined to be

$$\mathcal{A}=\frac{4}{w^2(u^2-v^2)}\left(\frac{\partial}{\partial u}\left((u^2-1)\frac{\partial}{\partial u}\right)+\frac{\partial}{\partial v}\left((1-v^2)\frac{\partial}{\partial v}\right)\right)-\frac{4w^2}{p^4}\hat{J}_z^2 \tag{4.69}$$

$$\mathcal{B}=\frac{2}{w^2}\frac{\partial}{\partial w}\left(w^2\frac{\partial}{\partial w}\right)-\frac{4}{w^2(u^2-v^2)}\left(w\frac{\partial}{\partial w}+1\right)\left(-u(u^2-1)\frac{\partial}{\partial u}+v(1-v^2)\frac{\partial}{\partial v}\right)$$

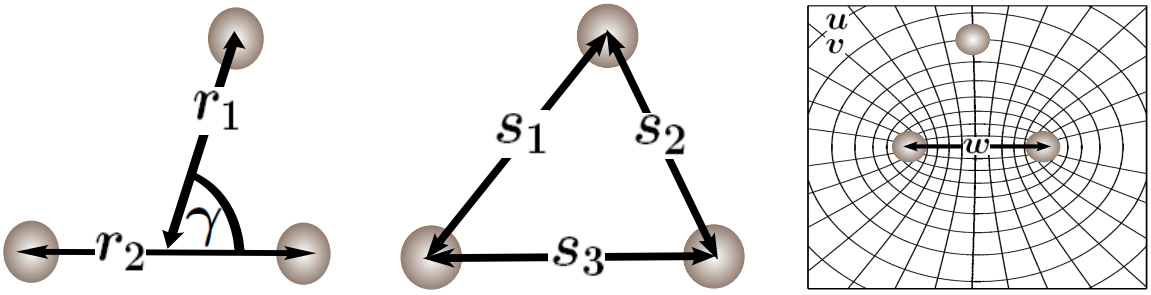

(a) The shape coordinates in the original body-fixed frame: $r_1 = |\mathbf{r}_1|$ and $r_2 = |\mathbf{r}_2|$

(b) The symmetric shape coordinates s_1, s_2 and s_3

(c) Spheroidal coordinates: contours of constant u and v are displayed

Figure 4.2: Three different choices of shape coordinates for the three body problem.

$$+\frac{2(u^2+v^2)}{w^2(u^2-v^2)}\left(\frac{\partial}{\partial u}\left((u^2-1)\frac{\partial}{\partial u}\right)+\frac{\partial}{\partial v}\left((1-v^2)\frac{\partial}{\partial v}\right)\right)$$
$$-\frac{4p^2 i\hat{J}_y}{(u^2-v^2)w^4}\left(v\frac{\partial}{\partial u}-u\frac{\partial}{\partial v}\right)-\frac{8p\hat{J}_x\hat{J}_z}{(u^2-v^2)w^4}\left(u\frac{\partial p}{\partial v}-v\frac{\partial p}{\partial u}\right)-\frac{2(u^2+v^2)w^2}{p^4}\hat{J}_z^2$$
$$-2\hat{J}_x^2-2\hat{J}_y^2+4\hat{J}_z^2 \tag{4.70}$$

$$V=\left(\frac{2}{w}-\frac{8u}{(u^2-v^2)w}\right), \tag{4.71}$$

with $p^4 = w^4(u^2-1)(1-v^2)$ in the spheroidal coordinate system. The coefficients can be removed by scaling the internuclear separation w and the energy E,

$$\omega=\frac{4\pi\epsilon_0\hbar^2(m_1+m_3)}{e^2m_1m_3}w=\frac{a_0}{1-\alpha}w \qquad \varepsilon=\frac{e^4m_1m_3}{32\pi^2\epsilon_0^2\hbar^2(m_1+m_3)}E=(1-\alpha)E_bE. \tag{4.72}$$

Then the Hamiltonian can be expressed in terms of the mass ratio, $\alpha=\frac{m_1}{m_1+m_3}$,

$$\mathcal{H}=-\mathcal{A}-\alpha\mathcal{B}+V. \tag{4.73}$$

This is the most convenient representation of the Hamiltonian for our investigation of the H_2^+ molecule. The separation of the centre of mass coordinates, and the partial separation of the rotational coordinates, from the internal shape coordinates has resulted in a drastic simplification of the Hamiltonian. In particular, the $L = 0$ states can now be studied by solving a relatively simple three dimensional problem.

4.5 Non-adiabatic wavefunctions for H_2^+

To obtain non-adiabatic wavefunctions for H_2^+ we use two independent methods. The first method is a Born-Huang expansion of the wavefunction into the basis of electronic states. The second method is to solve numerically, without resorting to any particular basis set, the exact Hamiltonian for the $L = 0$ states. By comparing the solutions of both of these methods we are able to carefully analyse the accuracy of the adiabatic approximation.

4.5.1 Application of the Born-Oppenheimer approximation to H_2^+

We will now apply the Born-Oppenheimer approximation to the H_2^+ molecular ion, using the equations derived in the previous section. The analysis for this problem is well known and can be found in, e.g, [44]. The only difference being that, because we are working in the body fixed centre of mass frame, we use the reduced masses: as opposed to the nuclear masses which are relevant to the laboratory frame. To obtain the electronic Hamiltonian we set the mass ratio α (≈ 0.00054) equal to zero, and we then only have to consider the operator $\mathcal{A}$. The first step involves finding the solutions of the electronic Hamiltonian,

$$\mathcal{H}_e \Phi_n^{m_z}(\mathbf{r}) = \left[\mathcal{A} + V\right] \Phi_n^{m_z}(\mathbf{r}) = \varepsilon_n^{m_z}(w) \Phi_n^{m_z}(\mathbf{r}), \tag{4.74}$$

where the index m_z specifies the angular momentum in the body-fixed frame and n specifies an electronic energy level. The electronic Hamiltonian is clearly separable using the ansatz $\phi = L(u)M(v)e^{im_z\beta}$ and the equations satisfied by $L(u)$ and $M(v)$ are

$$\frac{d}{du}\left((u^2-1)\frac{dL}{du}\right) + \left(A + 2wu - g^2u^2 - \frac{m^2}{u^2-1}\right)L = 0 \tag{4.75}$$

$$\frac{d}{dv}\left((1-v^2)\frac{dM}{dv}\right) + \left(-A + g^2v^2 - \frac{m^2}{1-v^2}\right)M = 0, \tag{4.76}$$

where A is a separation constant and $g^2 = -w^2\epsilon/4$. The function $M(v)$ is known as a spheroidal harmonic and can be expanded in terms of the associated Legendre polynomials, whilst the function $L(u)$ has a more complicated series expansion. These functions are not convenient to work with analytically, so it is better to seek a numerical solution of Eq. 4.74 to determine the electronic wavefunctions and their eigenvalues. To obtain numerical solutions it is convenient to parameterise the coordinates so that $u = \cosh(\theta)$ and $v = \cos(\phi)$, and to change the measure by defining a new wavefunction $\tilde{X}(w) = w^2X(w)$. These steps change the form of the operators and simplify the boundary conditions considerably (see appendix G).

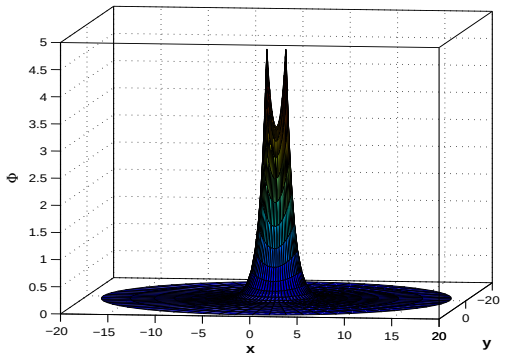

(a) Electronic wavefunction for the $1\sigma_g$ state, at the equilibrium inter-nuclear separation $w \approx 2$. The amplitude is maximal above the two nuclei at $x \approx \pm 1$.

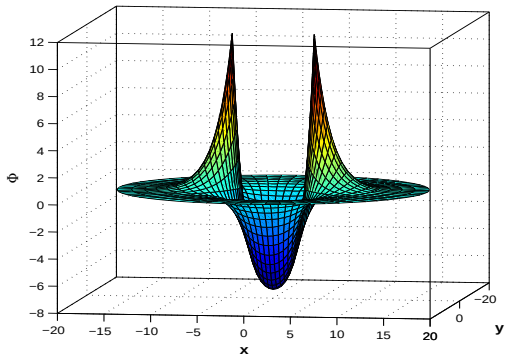

(b) Electronic wavefunction for the $2\sigma_g$ state, at the equilibrium inter-nuclear separation $w \approx 8.8$. The amplitude is maximal above the two nuclei at $x \approx \pm 4.4$.

Figure 4.3: Electronic Born-Oppenheimer wavefunctions for H_2^+.

States with different values of $|m_z|$ have different energies and are labeled σ, π, δ, $\cdots$ for $m_z = 0, \pm 1, \pm 2, \cdots$ respectively. States which are even under inversion symmetry (bonding states) are labeled with the subscript g, whilst states which are odd under inversion symmetry (anti-bonding states) are labeled with the subscript u. Illustrated in Fig. 4.3 are the bonding states $1\sigma_g$ and $2\sigma_g$. In our investigation we will only require the set of bonding, zero-angular momentum, σ_g states.

In the limits $w \to 0$ and $w \to \infty$ the molecular states have simple forms. As $w \to 0$ the two nuclei become equivalent to a single nucleus with twice the charge, and correspondingly the molecular orbitals become the eigenstates of the helium ion. The $1\sigma_g$ state corresponds to the helium 1s state with energy $E = -4 + 1/w$, whilst the $2\sigma_g$ and $3\sigma_g$ states are those of the helium 2s and 2p states respectively, with energy $E = -1 + 1/w$. At infinite nuclear separation the $1\sigma_g$ becomes the superposition of two hydrogenic $1s$ states centered on the two nuclei, and becomes degenerate with the $1\sigma_u$ state with energy $E = -1$. The $2\sigma_g$ and $3\sigma_g$ states become the superposition of the 2s and 2p hydrogenic states respectively, with energy $E = -1/4$.

The adiabatic energy surfaces, obtained from the eigenvalues of the electronic Hamiltonian, are illustrated in Fig. 4.4. The final step of the Born-Oppenheimer approximation is to determine the nuclear wavefunctions from the nuclear Hamiltonian,

$$[-\alpha\mathcal{B} + \varepsilon_m(w)]\,\tilde{X}_n^m(w) = E_n^m \tilde{X}_n^m(w). \tag{4.77}$$

The ground state energy surface, which forms the potential well for the two nuclei, has a potential minimum close to $w \approx 2$, where the potential is roughly harmonic. In their

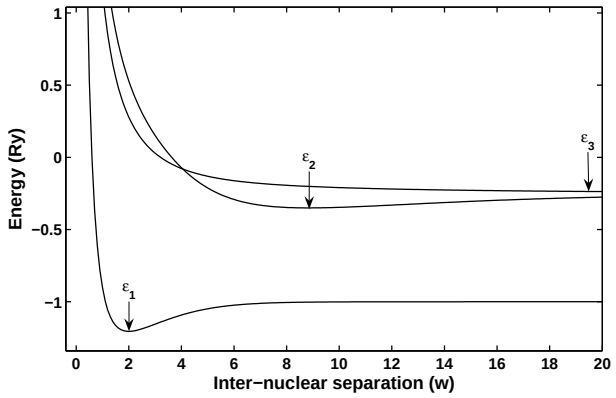

Figure 4.4: The adiabatic energy surfaces of the symmetric σ_g electronic wavefunctions of H_2^+. The ϵ_1 energy surface forms a potential well centred at $w \approx 2$, whilst the ϵ_2 energy surface forms a potential well centred at $w \approx 8.8$. At $w \approx 4$ the ϵ_2 and ϵ_3 energy surfaces become degenerate.

ground state, the nuclei oscillate about the equilibrium separation, where their low energy wavefunctions are similar to those of the harmonic oscillator.

4.5.2 Application of the Born-Huang expansion to H_2^+

The Born-Oppenheimer approximation is usually reliable for accurate solutions of the molecular Hamiltonian, but there are some special cases where it can give poor results. This can happen when two energy surfaces come close together or become degenerate, as is the case for the $2\sigma_g$ and $3\sigma_g$ states in H_2^+ at $w \approx 4$. The error depends on the difference in energy between the two states and can become large when this difference is very small. It is also questionable how accurate the adiabatic approximation is when the derivatives of the nuclear coordinates are large, which is relevant when the nuclei are moving fast. For our purposes it is therefore necessary to expand in the basis of electronic states.

We will again restrict attention to the zero angular momentum states. In addition, it is only necessary to include those states with even symmetry because the Hamiltonian does not mix odd and even states. The expansion of the wavefunction, performed in the basis of σ_g states, is then

$$\Psi_n^m(\theta, \phi, w) = \sum_{n'} \tilde{X}_{nn'}^m(w) \Phi_{n'}(\theta, \phi; w). \tag{4.78}$$

The expectation value of the energy is

$$E_n^m = \sum_{n'n''} \langle \tilde{X}_{nn'}^m \Phi_{n'} | (-\alpha \mathcal{B}_0 + \varepsilon_n(w)) | \tilde{X}_{nn''}^m \Phi_{n''} \rangle, \tag{4.79}$$

and the Hamiltonian matrix is then constructed from the matrix elements,

$$\hat{\boldsymbol{\mathcal{H}}}_{n'n''} = -\widehat{\langle \Phi_{n'} | \alpha \mathcal{B}_0 | \Phi_{n''} \rangle} + \delta_{n'n''} \varepsilon_{n'}(w). \tag{4.80}$$

The components of the wavefunction can be expressed in terms of the vector $\tilde{\boldsymbol{X}}_n^m =$

$(\tilde{X}^m_{n1}, \tilde{X}^m_{n2}, ...)$, which satisfies the matrix equation

$$\hat{\boldsymbol{\mathcal{H}}}\tilde{\boldsymbol{X}}^m_n = E^m_n \tilde{\boldsymbol{X}}^m_n. \tag{4.81}$$

Later in this chapter we perform a simple calculation, which involves an expansion in the $1\sigma_g$ and $2\sigma_g$ electronic states, of the non-adiabatic molecular wavefunction. The details of the calculation are outlined in appendix H, and the results are discussed in section 4.6.

4.5.3 Numerical solution of the exact Hamiltonian

To obtain information about the non-adiabatic effects in the most direct way we will solve the exact Hamiltonian (Eq. 4.73), for the states with zero angular momentum, numerically. By solving the Hamiltonian directly it is guaranteed that any non-adiabatic effects, with contributions from *all* electronic Born-Oppenheimer states, will be captured. This approach is non-perturbative, i.e, it does rely on an expansion in the usual parameter αq[16], and is not biased towards any particular basis set; the price we pay for using this approach is increased numerical difficulty. The solutions are represented on a three dimensional grid using a finite difference technique so that the ground state is obtained first and subsequent states of higher energy are found using orthogonality. The number of bound states increases dramatically for small values of α, and all of these states must be calculated before the dissociated states are reached. Since we are interested in the high energy dissociated states of the molecule, which requires the calculation of a large number of excitations, we are forced to restrict the value of the mass ratio to $\alpha = 0.005$. This value is an order of magnitude larger than the actual value ($\alpha \approx 0.00054$), but we are still able to make some general deductions which are relevant to realistic systems. For the zero angular momentum states we need only consider the Hamiltonian

$$\left[-\mathcal{A}_0 - \alpha\mathcal{B}_0 + V\right]\Psi^{00}_n(u,v,w) = E^{00}_n \Psi^{00}_n(u,v,w), \tag{4.82}$$

where the $L = 0$ operators are defined

$$\mathcal{A}_0 = \frac{4}{w^2(u^2-v^2)}\left(\frac{\partial}{\partial u}\left((u^2-1)\frac{\partial}{\partial u}\right) + \frac{\partial}{\partial v}\left((1-v^2)\frac{\partial}{\partial v}\right)\right) \tag{4.83}$$

$$\begin{aligned}\mathcal{B}_0 = {} & \frac{2}{w^2}\frac{\partial}{\partial w}\left(w^2\frac{\partial}{\partial w}\right) - \frac{4}{w^2(u^2-v^2)}\left(w\frac{\partial}{\partial w}+1\right)\left(-u(u^2-1)\frac{\partial}{\partial u} + v(1-v^2)\frac{\partial}{\partial v}\right) \\ & + \frac{2(u^2+v^2)}{w^2(u^2-v^2)}\left(\frac{\partial}{\partial u}\left((u^2-1)\frac{\partial}{\partial u}\right) + \frac{\partial}{\partial v}\left((1-v^2)\frac{\partial}{\partial v}\right)\right).\end{aligned} \tag{4.84}$$

The solution technique is outlined in appendix G, and the results are discussed in the

next section.

4.6 Non-adiabatic effects in H_2^+

In this section we will analyse the non-adiabatic effects in H_2^+ and show that the Born-Oppenheimer approximation is robust for realistic values of transferred momentum. The adiabatic approximation is however found to be less accurate in the vicinity of the nodes of the nuclear wavefunction, but this effect is dependent on the mass ratio α and is extremely small.

An instructive way of characterising the non-adiabatic effects is to compare the numerical solutions obtained from directly solving the exact Hamiltonian with those obtained from the expansion in the electronic basis. We therefore calculate the high energy dissociated states of the molecule using both methods and show that there is agreement (within numerical error) between the solutions. Using these solutions we can then determine the matrix elements which lead to the largest transition probabilities, and we find that the probability of electronic excitation is of the order α^2.

We begin with the calculation of the final states in the basis of adiabatic electronic states for $\alpha = 0.005$. The two degenerate solutions with $E > -0.25$, calculated in the $1\sigma_g$ and $2\sigma_g$ basis, are illustrated in Fig. 4.5. We can express the final solution in the form

$$\Psi_f^{\varepsilon_m}(\theta, \phi, w) = \sum_n X_n^{\varepsilon_m}(w)\Phi_n(\theta, \phi; w). \tag{4.85}$$

The solution in Fig. 4.5(a) corresponds to the nuclei moving in the potential well created by the $1\sigma_g$ state, with a correspondingly large nuclear amplitude $X_1^{\varepsilon_1}$ associated with the $1\sigma_g$ state, but only a small admixture of $X_2^{\varepsilon_2}$ associated with the $2\sigma_g$ potential well. Conversely, the degenerate solution in Fig. 4.5(b) corresponds to the nuclei moving in the $2\sigma_g$ state and has a large nuclear amplitude $X_2^{\varepsilon_2}$ associated with the $2\sigma_g$ state.

We next consider the wavefunctions obtained from attempting a numerical solution of the exact Hamiltonian (Eq. 4.73), using a finite difference method on a three dimensional grid (appendix G). A particular high energy dissociated state of the molecule, with $\boldsymbol{L} = 0$, is illustrated in Fig. 4.6. To allow a direct comparison with the nuclear amplitudes obtained in the electronic expansion, we have integrated out the electronic coordinates to obtain the nuclear amplitudes X_1 and X_2 associated with the $1\sigma_g$ and $2\sigma_g$ states. We represent the wavefunction of the final state in the form

$$\Psi_f(\theta, \phi, w) = \sum_n X_n(w)\Phi_n(\theta, \phi; w), \tag{4.86}$$

and calculate the nuclear amplitudes numerically using the expression

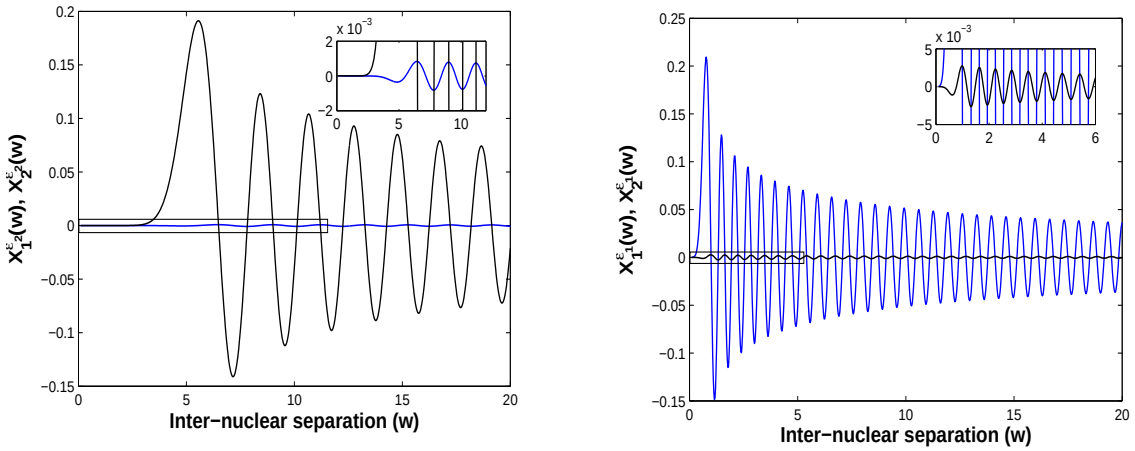

(a) Nuclear amplitudes $X_1^{\varepsilon_2}$ and $X_2^{\varepsilon_2}$ of the nuclei in the potential ε_2.

(b) Nuclear amplitudes $X_1^{\varepsilon_1}$ and $X_2^{\varepsilon_1}$ of the nuclei in the potential ε_1.

Figure 4.5: Nuclear amplitudes obtained from the Born-Huang expansion. The amplitudes $X_1^{\varepsilon_1}$ (blue line) and $X_2^{\varepsilon_2}$ (black line) are associated with the $1\sigma_g$ and $2\sigma_g$ electronic states respectively.

$$X_n(w) = \langle \Psi_f(\theta, \phi, w) | \Phi_n(\theta, \phi; w) \rangle. \tag{4.87}$$

It is also useful to define the overlaps O_1 and O_2 with the $1\sigma_g$ and $2\sigma_g$ states, i.e,

$$O_n(w) = \frac{|X_n(w)|^2}{\sum_{n'} |X_{n'}(w)|^2}. \tag{4.88}$$

The state illustrated in Fig. 4.6 is calculated with $\alpha = 0.005$, for an energy $E > -0.25$, which lies just above the dissociation energy of the $2\sigma_g$ state. This wavefunction has been obtained without any bias towards a particular basis set and there are two points that are noteworthy.

The first point is that the overlaps, $O_1(w)$ and $O_2(w)$, in Fig. 4.6 illustrate how the adiabatic approximation breaks down close to the nodes in the nuclear amplitude. Within a region of order α of these nodes the overlap with the $1\sigma_g$ state dips sharply, and higher electronic states such as $2\sigma_g$ and $3\sigma_g$ appear. This issue is well known[45] and is a general feature of exact molecular wavefunctions. The affected regions correspond to low probability nuclear configurations for which the electronic and nuclear coordinates can no longer be decoupled adiabatically. The nature of the wavefunctions in these regions is not entirely clear but the effect this has on the matrix elements is very small and can be safely ignored.

The second point is that the overlap O_1 with the electronic $1\sigma_g$ state is unity until $w \approx 4$, where it rapidly falls to zero and the overlap O_2 with the $2\sigma_g$ state rises equally rapidly

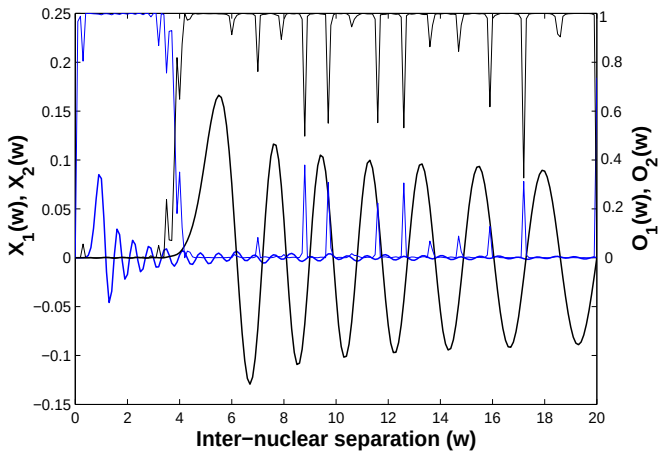

Figure 4.6: Nuclear amplitudes obtained from the approximate numerical solution of the exact Hamiltonian. The nuclear amplitudes X_1 (blue line) and X_2 (black line) of high energy ($E > -0.25$) states are illustrated. The overlap O_1 with the $1\sigma_g$ state (blue line) and the overlap O_2 (black line) with the $2\sigma_g$ state (black dotted line state) is also illustrated. The wavefunction is a linear combination of the nuclear amplitudes $X_1^{\varepsilon_1}$ and $X_2^{\varepsilon_2}$ associated with the potentials ε_1 and ε_2 respectively.

from zero to unity. The main electronic component of the exact solution is therefore $1\sigma_g$ close to $w = 0$, but changes to $2\sigma_g$ as the nuclear wavefunction passes through a node, where it remains out to infinite inter-nuclear separation. At first sight this feature is rather surprising and appears to resemble an electronic transition as the nuclei dissociate. However, further analysis reveals that this behaviour is actually just a consequence of the degeneracy of the final molecular state. It is clear that the wavefunction illustrated in Fig. 4.6 is simply a linear combination of the degenerate solutions shown in Fig. 4.5:

$$\Psi_f = c_1 \Psi_f^{\varepsilon_1} + c_2 \Psi_f^{\varepsilon_2}. \tag{4.89}$$

The rapid change in the overlaps O_1 and O_2, observed in Fig. 4.6, is caused by the different exponential behaviour of $\Psi_f^{\varepsilon_1}$ and $\Psi_f^{\varepsilon_2}$ close to $w = 0$. We will now consider how the matrix elements for electronic excitations are calculated.

There are two processes which facilitate the excitation of electrons, namely the centre of mass recoil (CMR) and non-adiabatic corrections (NAC), and it is necessary to distinguish between these. The CMR mechanism for electronic excitation appears in both atoms and molecules, and occurs due to mixing of the electronic and the nuclear coordinates in the centre of mass frame. The NAC mechanism only occurs in molecules and is caused by the response of the electrons to the dynamic motion of the nuclei.

To calculate the transition probabilities we require the matrix elements associated with transferring momentum $\boldsymbol{q}$ and energy $\hbar\omega$ to the molecule, which we assume is initially in its ground state Ψ_0 (no angular momentum and lowest vibronic state). We need only consider the interaction of the neutron with the proton at $\boldsymbol{R}_1$ because the two nuclei are identical and the two contributions average to the same result. The probability of exciting the molecule from the ground state to Ψ_f is

$$P_{\boldsymbol{q}}(E_f) = |\langle \Psi_0(\theta,\phi,w)| e^{i\boldsymbol{q}\cdot(\frac{1}{2}\boldsymbol{r}_2 - \frac{m}{2M+m}\boldsymbol{r}_1)} |\Psi_f(\theta,\phi,w)\rangle|^2. \tag{4.90}$$

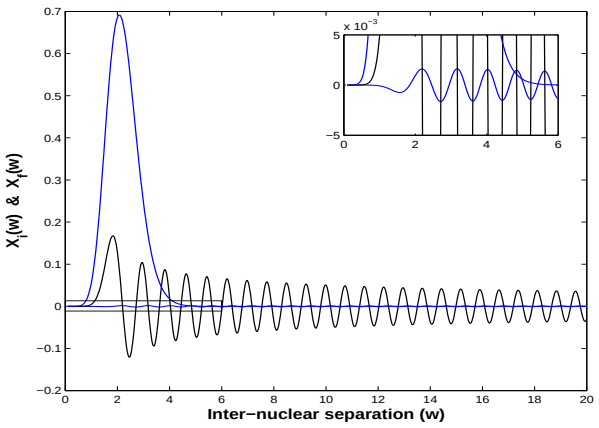

Figure 4.7: The nuclear amplitudes, X_i and X_f, associated with the initial and final states in a high energy scattering process. In this case the realistic value of $\alpha = 0.00054$ has been used. The final state illustrated corresponds to the two nuclei dissociating in the potential well ε_2. Then the electronic transition $1\sigma_g \rightarrow 2\sigma_g$ is related to the overlap of the ground state with the small $1\sigma_g$ component $X_1^{\varepsilon_2}(w)$ of the final state (top right figure).

The CMR contribution arises from the term $\frac{m}{2M+m}\boldsymbol{q}\cdot\boldsymbol{r}_1$. The amount of electronic excitation resulting from CMR in H_2^+ should be similar to that found in the hydrogen atom and we will neglect this term. The NAC contribution arises from the term $\frac{\boldsymbol{q}}{2}\cdot\boldsymbol{r}_2$, which is expressed in the spheroidal coordinate system as $\frac{q}{2}w\cos(\gamma)$, where γ is the angle between $\boldsymbol{q}$ and $\boldsymbol{r}_2$. We are therefore only interested in the matrix element

$$\langle\Psi_0(\theta,\phi,w)|e^{i\frac{q}{2}w\cos(\gamma)}|\Psi_f(\theta,\phi,w)\rangle. \tag{4.91}$$

To obtain a large transition amplitude we require that the final state oscillates with a frequency roughly equal to $\frac{q}{2}w$ and has a significant overlap with the ground state, which resembles a Gaussian centred at $w \approx 2$. When an electronic transition occurs the nuclei simultaneously begin to vibrate in the potential well associated with the excited state. Because the time scale of the neutron-nucleus interaction is too short for the nuclear configuration too change appreciably, only transitions between nuclear states with a sizeable overlap are possible (Franck-Condon principle).

In Fig. 4.7 a realistic value of $\alpha = 0.00054$ has been used to calculate the initial and final state in a high energy scattering process. The final state is a high energy dissociated state associated with the potential well ε_2. The overlap with the nuclear ground state is large but, because of the orthogonality of the electronic states, only the very small $X_1^{\varepsilon_2}$ component associated with the $2\sigma_g$ state contributes to the matrix element. In fact, the probability of electronic excitation via CMR and NAC are of the same order of magnitude, and are roughly proportional to[4] $(\alpha q/\Delta)^2$.

[4]This can be derived from perturbation theory, by expanding in the parameter αq.[16, 46]

4.7 Breakdown of the adiabatic approximation in H_2^+

From the calculation of high energy dissociated molecular states, we can observe the gradual breakdown of the adiabatic approximation. The magnitude of the non-adiabatic corrections can be characterised in terms of the mass ratio, α, and the transferred momentum, q. The non-adiabatic corrections to the molecular wavefunctions are proportional to the hybridisation between the different electronic modes, which is of the order $\alpha q/\Delta$. By comparing the adiabatic separation of the molecular wavefunctions, with an *exact* separation of the molecular wavefunctions (see appendix B), we can see explicitly how the adiabatic approximation breaks down

The exact separation of the electronic and nuclear degrees of freedom has a simple interpretation; the molecular wavefunction, $\Psi(\mathbf{R},\mathbf{r})$, is interpreted as a joint probability density amplitude for the nuclear and electronic coordinates. It can therefore be decomposed exactly[5] into the product of a conditional probability amplitude of the electronic coordinates, $\Phi(\mathbf{r};\mathbf{R})$, and a marginal probability amplitude for the nuclear coordinates, $X(\mathbf{R})$.

The exact separation[47] leads to a set of coupled equations which define the probability amplitudes $X(\mathbf{R})$ and $\Phi(\mathbf{r};\mathbf{R})$. We will once again concentrate on the $L=0$ states of H_2^+, and employ the Hamiltonian, Eq. 4.58, which is represented in the bi-spherical polar coordinate system. To simplify matters we define $\tilde{\Psi}\equiv r_2\Psi$ and enforce the parameterisation $\tilde{\Psi}=X(r_2)\Phi(r_1,\gamma;r_2)$. We then obtain the following set of coupled equations for $X(r_2)$ and $\Phi(r_1,\gamma;r_2)$:

$$\left[-\alpha\frac{d^2}{dr_2}+\varepsilon(r_2)-E\right]X(r_2)=0$$

$$\left[-\alpha\frac{\partial^2}{\partial r_2^2}-\frac{\alpha}{X(r_2)}\frac{dX(r_2)}{dr_2}\frac{\partial}{\partial r_2}-\frac{\alpha}{r_2^2\sin(\gamma)}\frac{\partial}{\partial\gamma}\left(\sin(\gamma)\frac{\partial}{\partial\gamma}\right)+\mathcal{H}_{BO}-\varepsilon(r_2)\right]\Phi(r_1,\gamma;r_2)=0. \tag{4.92}$$

For convenience, we can also recast the equation for $X(r_2)$ into a first order *Riccati equation*. We define

$$\chi(r_2)=\frac{1}{X(r_2)}\frac{dX(r_2)}{dr_2}. \tag{4.93}$$

The normalisation condition for the nuclear wavefunction, $X(r_2)$, is then subsumed into the boundary condition for $\chi(r_2)$ at $r_2=0$. The coupled equations for the nuclear and electronic probability amplitudes are

[5] This separation is unique, up to a choice of phase for the electronic and nuclear wavefunctions. A particular choice of phase, which is in general an arbitrary function of the nuclear coordinate, amounts to a choice of gauge.

$$-\alpha\left(\frac{d\chi}{dr_2}+\chi^2\right)+E-\varepsilon(r_2)=0$$

$$\left[-\alpha\frac{\partial^2}{\partial r_2^2}-\alpha\chi\frac{\partial}{\partial r_2}-\frac{\alpha}{r_2^2\sin(\gamma)}\frac{\partial}{\partial\gamma}\left(\sin(\gamma)\frac{\partial}{\partial\gamma}\right)+\mathcal{H}_{BO}-\varepsilon(r_2)\right]\Phi(r_1,\alpha;r_2)=0. \quad (4.94)$$

The nuclear and electronic wavefunctions can be expressed, via the Born-Huang expansion, as

$$X(r_2)=\sqrt{\sum_n |X_n(r_2)|^2}$$

$$\Phi(r_1\gamma;r_2)=\sum_n\frac{X_n(r_2)}{X(r_2)}\Phi_n(r_1,\gamma;r_2). \quad (4.95)$$

Whilst these equations are not necessarily advantageous numerically, they do highlight the non-adiabatic effects which are present in the exact molecular wavefunctions. The nuclear wavefunction, which is the sum of positive definite quantities, is nodeless[6].

Using the solutions obtained from the Born-Huang expansion, we can approximate the exact nuclear wavefunctions. The nuclear probability amplitude, $X(r_2)$, and the nuclear potential, $\varepsilon(r_2)$, are illustrated in Fig. 4.8(a). These approximations are for the expansion in the $1\sigma_g$ and $2\sigma_g$ basis, for $\alpha = 0.005$. The hybridisation between the two electronic states is proportional to $\alpha q/\Delta$, where Δ is the energy gap between the electronic states. The $1\sigma_g$ component of the molecular wavefunction is roughly $X_1(r_2)\sim\sin(qr_2/\sqrt{\alpha})$ and we may therefore approximate the nuclear amplitude to be

$$X(r_2)\sim\sqrt{\sin^2\left(\frac{qr_2}{\sqrt{\alpha}}\right)+O\left(\frac{\alpha^2q^2}{\Delta^2}\right)}. \quad (4.96)$$

When there is a node in $X_1(r_2)$ the nuclear amplitude is $X(r_2)\sim\alpha q/\Delta$. This leads to a sharp peak in $\chi(r_2)$ which results in a spike in the nuclear potential, $\varepsilon(r_2)$, at each of the nodes[45]. Close to these nodes the difference between the adiabatic nuclear potential and the exact nuclear potential is dramatic and the adiabatic approximation breaks down completely, as illustrated in Fig. 4.8(b). In the adiabatic limit, $\alpha\to 0$, the regions where the adiabatic approximation breaks down shrink to zero and the adiabatic approximation becomes exact. However, as α or q are increased, the expansion of these regions is proportional to $\alpha q/\Delta$ and non-adiabatic effects can become large.

At very high energies the potential can be treated as a constant V_0 and the final states are well represented by plane waves of the form $\exp(iqr_2/\sqrt{\alpha})$. In fact, the Compton profile, which is obtained via the impulse approximation, can be recovered in this limit[48].

[6]This is a general feature which occurs because the nuclear amplitudes, $X_n(\mathbf{R})$, cannot all have a node at the same point.

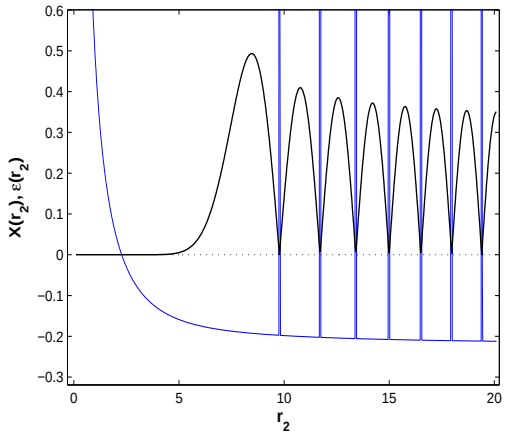

(a) The nuclear amplitude, $X(r_2)$ (black line), and the nuclear potential, $\varepsilon(r_2)$ (blue line), calculated in the basis of $1\sigma_g$ and $2\sigma_g$.

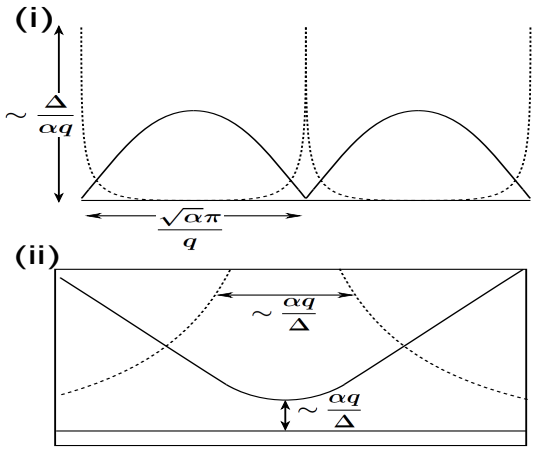

(b) Breakdown of the adiabatic approximation. (i) The nuclear potential (dashed line) and the nuclear amplitude (solid line). (ii) The width of the spike in the nuclear potential is proportional to $\alpha q/\Delta$.

Figure 4.8: Non-adiabatic effects in the exact molecular wavefunctions for H_2^+.

In the case of a molecule the impulse approximation relates the response function to the momentum distribution, in the centre of mass frame, of the struck nucleus.

The conclusion we can make based on the calculations of this chapter is that the expansion of the wavefunction in the basis of adiabatic electronic states gives a reliable measure of the NAC contribution to electronic excitations. This contribution is dependent on the small admixture of $X_1^{\varepsilon_2}$ in the nuclear state associated with the potential well ε_2. The subsequent non-adiabatic correction to the matrix elements can be approximated from perturbation theory, and is therefore proportional to $\alpha^2 q^2/\Delta^2$, which is expected to be small in all cases considered.

4.8 Conclusion

We have performed a detailed investigation of the electronic excitations occurring in high energy neutron scattering events. Starting from the simplest model systems we have explicitly calculated the response functions and determined the amount of electronic excitation which occurs for large values of transferred momentum. We have then investigated the non-adiabatic effects which lead to electronic excitation in hydrogen molecules and concluded that these effects would not be observable, within experimental error, for the energies obtainable in neutron Compton scattering experiments.

This has implications for the neutron Compton scattering experiments performed on

materials such as NbH_2 and PdH_2, which have produced anomalous measurements of the neutron cross sections. In particular, we can rule out the possibility that electronic excitations are responsible for the reduced ratio of cross sections such as σ_H/σ_{Nb} and σ_H/σ_{Pd}. Our conclusion, therefore, is that the origin of the anomalous measurements probably resides in some other aspect of the experiments[14, 15].

Part II

Perovskite oxide interfaces

Chapter 5

Perovskite oxide interfaces

An impressive variety of exotic properties have recently been observed at atomically precise interfaces between perovskite oxides. Many of these properties are not realised at interfaces between conventional semiconducting materials and, therefore, it may prove possible to utilise perovskite oxide interfaces in new technological applications. The exotic properties originate, in part, from the extremely rich phases found in complex oxides, which tend to be dominated by strong interactions among the electrons. At an oxide interface, the close proximity of these different phases can drastically alter the interfacial properties at the nanoscale. Additional complexity is also introduced at an interface because of the artificially broken symmetry, which can result in polar discontinuities, lattice distortions, interdiffusion, and electronic reconstructions. Already, a variety of intriguing properties have been observed at interfaces between perovskite oxides, including: a high mobility two-dimensional electron gas[49, 50] between two band insulators, magnetism[51] between two non-magnetic materials, an electronic reconstruction[52] between a band insulator and a Mott-Hubbard insulator, and an orbital reconstruction[53] between two strongly correlated materials.

Not only is it possible to create new properties at an interface, which are distinct from the bulk phases of either material, but it is also possible to control these properties through electrostatic doping; with an applied field, the charge in the interfacial layers can be tuned to investigate the disorder free[1] phase diagram of the system. These interfaces may therefore advance fundamental research into the phase transitions in oxide materials.

Interfaces with first row transition metal oxides are particularly well studied because the ground state properties of the constituent materials are extremely diverse, and can be very sensitive to changes in doping, strain, and applied magnetic fields. These materials will be the focus of the second part of this thesis where two interfaces will be investi-

[1] In a chemically doped system, the disorder introduced through chemical substitution can distort the phase diagram.

gated: the interface between the ferromagnetic metallic manganite $La_{2/3}Ca_{1/3}MnO_3$ and the cuprate superconductor $YBa_2Cu_3O_7$, and the interface between the band insulators $LaAlO_3$ and $SrTiO_3$.

In this chapter we briefly review the most fundamental concepts that are relevant to the perovskite oxides; these concepts provide the foundations for building detailed models of specific materials.

In chapter 6 we introduce impurity theory techniques, which are later employed to model the two interfaces under investigation. A simple model, involving non-interacting electrons, of the symmetry breaking at an interface is solved. This model highlights the physical ideas which are crucial in the more complicated models, for real interfaces, which are introduced later. The use of models involving non-interacting electrons obviously requires justification: their relevance is discussed in more detail, as the models are developed, in later chapters.

In chapter 7 we introduce the interface between a cuprate and a manganite and discuss some of the properties of these extremely complicated materials. Experimental observations, of an orbital reconstruction and unusual magnetic properties, at the cuprate-manganite interface are also discussed. In chapter 8 we attempt to provide a theoretical interpretation for these experimental observations, using a simple impurity model of the cuprate-manganite interface. The results are then compared, with reasonable success, with experiment.

In chapter 9 we discuss the extraordinary properties of the high mobility interface between the band insulators $LaAlO_3$ and $SrTiO_3$. Finally, in chapter 10 we introduce an impurity model for this interface. The model highlights the effects of the interfacial polar discontinuity, and exhibits interesting charging phenomena.

5.1 First row transition metal oxides

Interest in transition metal oxides has been renewed since the discoveries of high temperature superconductivity (HTSC) in the cuprates[54] in 1986, and the colossal magnetoresistance (CMR) effect in the manganites[55] shortly thereafter. In addition, there are other examples of interesting properties in materials such as the cobaltates, which are potentially useful for their thermoelectric properties[56], the vanadates, which are considered to be the prototypical systems exhibiting the metal-insulator transition[57], and the titanates, which exhibit ferroelectric properties. It is this remarkable variety of physical phenomena[58], the complex interplay between the many competing interactions, and the rich assortment of phases which makes these materials so interesting both theoretically and technologically.

The most important issues which must be considered when modeling the transition metal oxides are: the lifting of the degeneracy of the $3d$ electronic states due to symmetry and Jahn-Teller effects, and the complicated exchange interactions which arise from the strong electronic correlations. These issues will be the main topic of this chapter.

The first row transition metal oxides comprise of the elements from Ti with 22 electrons, to Cu with 29, each of which contains an unfilled $3d$ shell which is five-fold degenerate in a spherically symmetric potential. In many transition metal oxides the transition metal cation is surrounded by six closed shell oxygen neighbours which form an octahedron, such as in the perovskite crystal structure illustrated in Fig. 5.2(a). The five-fold orbital degeneracy of the $3d$ states is lifted by the crystal field of the surrounding negatively charged oxygen ions, which for the perovskite structure results in the triply degenerate t_{2g} and doubly degenerate e_g states illustrated in Fig. 5.1. The energy level splitting can be understood by considering a single $3d$ electron in the potential produced by the six neighbouring oxygen ions of charge Ze. From the oxygen ions located at $\mathbf{r} = \pm a\hat{\mathbf{x}}$ the symmetry breaking potential is

$$\delta V_x = \frac{Ze}{\sqrt{r^2 + a^2 - 2ax}} + \frac{Ze}{\sqrt{r^2 + a^2 + 2ax}} \approx Ze\left(\frac{2}{a} + \frac{35}{4a^5}\left(x^4 - \frac{r^4}{5}\right)\right), \tag{5.1}$$

where we have expanded up to fourth order in powers of r/a. If we also include the potentials from the oxygen ions at $\mathbf{r} = \pm a\hat{\mathbf{y}}$ and $\mathbf{r} = \pm a\hat{\mathbf{z}}$ then the total perturbing potential is

$$\delta V \approx Ze\left(\frac{6}{a} + \frac{35}{4a^5}\left(x^4 + y^4 + z^4 - \frac{3}{5}r^4\right)\right), \tag{5.2}$$

which can be reexpressed in terms of spherical harmonics:

$$\left(x^4 + y^4 + z^4 - \frac{3}{5}r^4\right) = \frac{16}{3}\sqrt{\frac{2\pi}{35}}\frac{r^4}{8}(Y_4^4 + Y_4^{-4}) + \frac{4}{15}\sqrt{\pi}r^4 Y_4^0. \tag{5.3}$$

An effective Hamiltonian can be constructed from the matrix elements for the $3d$ states, $\langle X_{32}(r)Y_2^m|\delta V|X_{32}(r)Y_2^{m\prime}\rangle$, and the eigenfunctions can then be expanded in terms of the five $3d$ spherical harmonics. This requires the following formula which reduces the product of two spherical harmonics to one:

$$Y_{l_1}^{m_1}Y_{l_2}^{m_2} = \sum_l \sqrt{\frac{(2l_1+1)(2l_2+1)}{4\pi(2l+1)}}\langle l_1 l_2 00|l_1 l_2 l0\rangle\langle l_1 l_2 m_1 m_2|l_1 l_2 l(m_1+m_2)\rangle Y_l^{m_1+m_2}, \tag{5.4}$$

where we have used the Clebsch-Gordan coefficients associated with the coupling of two

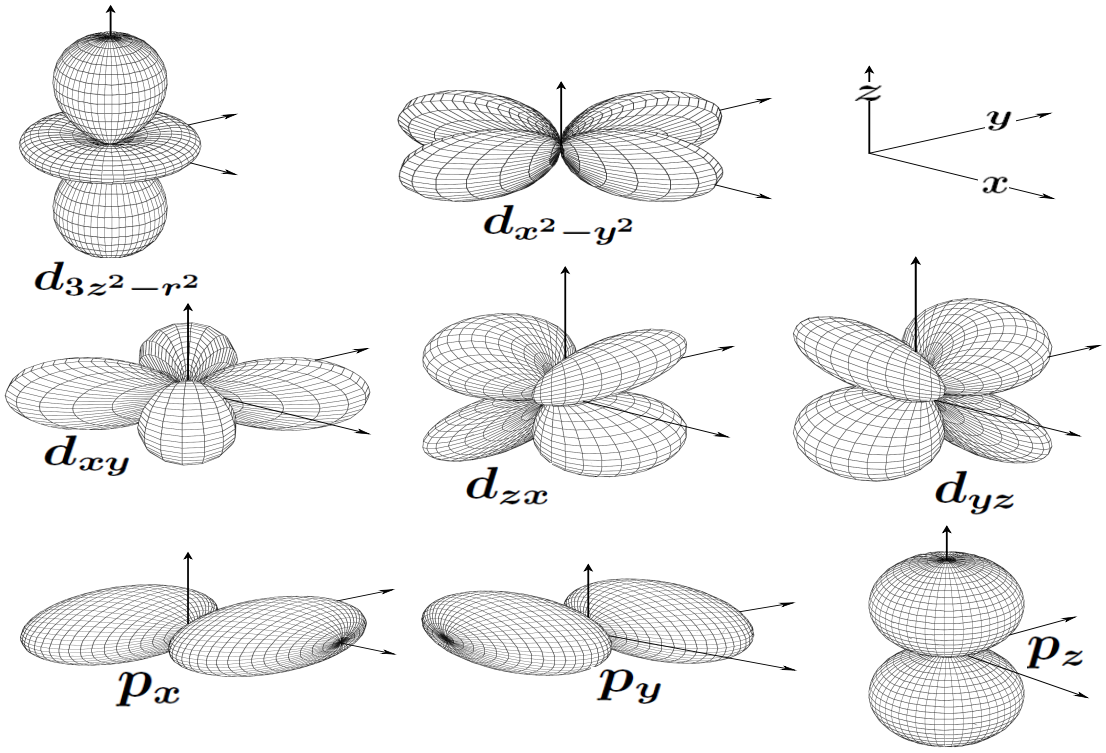

Figure 5.1: The orbitals corresponding to the transition metal e_g and t_{2g} bands, and the oxygen $2p$ band.

angular momenta. Using this expression the effective Hamiltonian matrix may be rewritten

$$\mathcal{H}_{cubic} = \frac{2Ze\langle r^4\rangle}{105}\begin{pmatrix} 1 & 0 & 0 & 0 & 5 \\ 0 & -4 & 0 & 0 & 0 \\ 0 & 0 & 6 & 0 & 0 \\ 0 & 0 & 0 & -4 & 0 \\ 5 & 0 & 0 & 0 & 1 \end{pmatrix}, \tag{5.5}$$

where the radial integral is defined

$$\langle r^4\rangle = \int_0^\infty dr r^4 X_{32}^2(r). \tag{5.6}$$

The eigenvectors of the effective Hamiltonian form the doubly degenerate e_g orbitals,

$$d_{x^2-y^2} = \sqrt{\frac{1}{2}}(Y_2^2 + Y_2^{-2}) = \frac{1}{4}\sqrt{\frac{15}{\pi}}(\hat{x}^2 - \hat{y}^2) \tag{5.7}$$

$$d_{3z^2-1} = Y_2^0 = \frac{1}{4}\sqrt{\frac{5}{\pi}}(3\hat{z}^2 - 1), \tag{5.8}$$

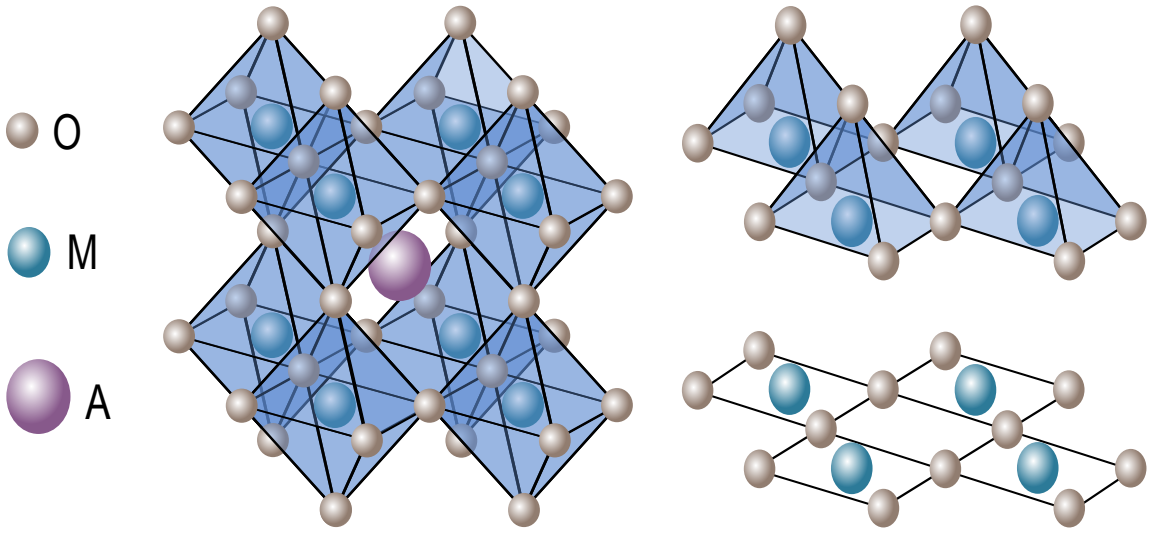

(a) The perovskite structure AMO_3 (b) layered perovskites

Figure 5.2: The perovskite structures found in transition metal oxides; M is a transition metal element such as Mn, Cu, ..., and A is a larger element such as La, Sr, Ca, ...

and the triply degenerate t_{2g} orbitals:

$$d_{xy} = i\sqrt{\frac{1}{2}}(Y_2^{-2} + Y_2^2) = \frac{1}{4}\sqrt{\frac{15}{\pi}}(\hat{x}\hat{y}) \tag{5.9}$$

$$d_{yz} = i\sqrt{\frac{1}{2}}(Y_2^{1} + Y_2^{-1}) = \frac{1}{4}\sqrt{\frac{15}{2\pi}}(\hat{y}\hat{z}) \tag{5.10}$$

$$d_{zx} = i\sqrt{\frac{1}{2}}(Y_2^{1} - Y_2^{-1}) = \frac{1}{4}\sqrt{\frac{15}{2\pi}}(\hat{z}\hat{x}). \tag{5.11}$$

The crystal field splitting between these two states is

$$\Delta E = \frac{5Zq}{3a^5}\langle r^4 \rangle = 10Dq. \tag{5.12}$$

We can understand this splitting from the shape of the orbitals; the lobes of the $d_{x^2-y^2}$ and $d_{3z^2-r^2}$ states point directly towards oxygen ions in the xy-plane and along the z-axis respectively, and so have a higher electrostatic energy than the t_{2g} orbitals whose lobes point directly between oxygen ions.

In practice, the magnitude of the energy splitting ΔE is usually obtained experimentally. The example considered involved a single $3d$ electron which feels a spherically symmetric potential from the closed shells of neighbouring oxygen ions and the on-site transition metal element. For more than one electron the situation is more complicated and the rules of addition for angular momenta and spin must be used to determine the appropriate multiplets. Fortunately, this simple calculation is also valid for an Mn^{3+} ion

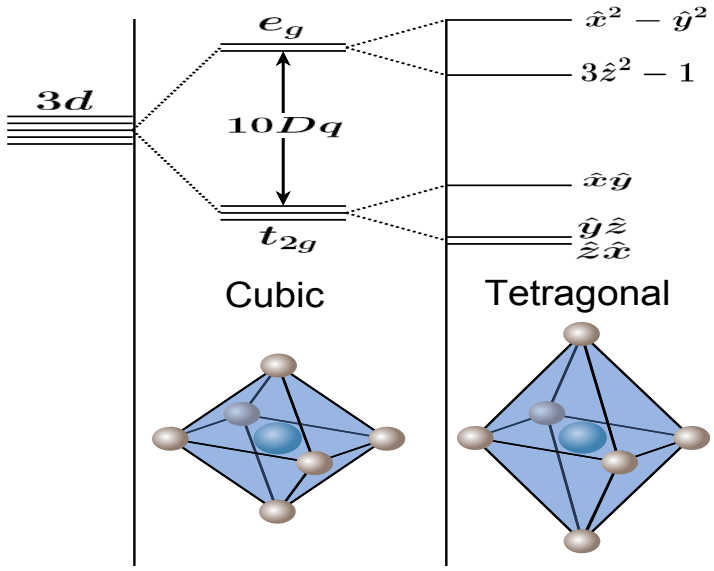

Figure 5.3: The energy level splitting of a single $3d$ electron in a crystal field of the surrounding oxygen ions. The cubic crystal field splits the five-fold degenerate $3d$ levels into the three-fold degenerate t_{2g} and doubly degenerate e_g levels. The Jahn-teller interaction further reduces the symmetry to that of a tetragonal crystal field and removes the degeneracy of the e_g energy levels.

containing a single e_g electron which, due to the large ferromagnetic coupling with the t_{2g} spins, may be treated as a single $3d$ hole. The calculation is also valid for the Cu^{2+} cation, which may also be regarded as having a single $3d$ hole, and for the Ti^{3+} cation which has a single $3d$ electron.

We have so far considered cubic symmetry, for which the lattice spacing is identical in the x, y and z directions ($a = b = c$), but if the lattice spacing in the z direction is increased ($a = b \neq c$) then the symmetry is tetragonal. In this case there is a further splitting of the energy levels as illustrated in Fig. 5.3. This energy splitting is realised in the two dimensional layered perovskites illustrated in Fig. 5.2(b), which are relevant to the HTSC cuprates. Alternatively, in most three dimensional perovskites the e_g energy levels are split due to the *Jahn-Teller* effect.

5.2 The Jahn-Teller effect

When the coordinates of the oxygen ions are treated as dynamic variables they are subject to a reaction due to the electronic states of the magnetic ions, resulting in a distortion of the lattice which removes the remaining orbital degeneracy. This removal of the orbital degeneracy due to the interaction between the electronic orbitals and the lattice distortion is known as the *Jahn-Teller effect*. This effect is present because the increase in energy is proportional to the second power of the lattice distortion, whereas the energy level splitting between the orbital states is linearly proportional to the lattice distortion.

In many of the manganites and cuprates the degeneracy of the e_g orbitals is removed by a distortion of the surrounding octahedra of oxygen anions. If we consider a single e_g electron surrounded by an oxygen octahedra and denote the displacements of the oxygen

by (X, Y, Z) and the electronic coordinates x, y and z, then the change in the potential is

$$\delta V = -\frac{1}{2}\left(\frac{9}{a^4}\right)[x^2(X_1 - X_4) + y^2(Y_2 - Y_5) + z^2(Z_3 - Z_6)]. \tag{5.13}$$

The terms of lower order, such as xX_i, do not contribute to the energy level splitting because the corresponding matrix elements are zero. There are also terms which are antisymmetric with respect to inversion through the origin, but these terms also do not contribute to the energy splitting. The remaining symmetric terms can be decomposed into the normal modes of the octahedron, six of which are symmetric (Fig. 5.4). Of these six modes only Q_1, Q_2 and Q_3, which correspond to displacements of the oxygens parallel to the Mn-O-Mn bonds, contribute to the energy level splitting. In terms of these modes the change in the potential is

$$\delta V = -\sqrt{\frac{2}{3}}\left(\frac{9}{a^4}\right)\left[\sqrt{\frac{3}{2}}(x^2 - y^2)Q_2 + \frac{1}{2}(2z^2 - x^2 - y^2)Q_3\right]. \tag{5.14}$$

The electronic coordinates can be replaced with their operator equivalents. This is simply an application of the Wigner-Eckart theorem which in its simplest form states that the matrix elements of vector operators are proportional to those of the angular momentum operators. The result is

$$\delta V = -\sqrt{\frac{2}{3}}\left(\frac{9}{a^4}\right)\alpha\langle r^2\rangle\left[\sqrt{\frac{3}{2}}(L_x^2 - L_y^2)Q_2 + \frac{1}{2}(3L_z^2 - L(L+1))Q_3\right]. \tag{5.15}$$

The matrix elements are easily evaluated in the e_g basis:

$$\delta V = -3\sqrt{\frac{2}{3}}\left(\frac{9}{a^4}\right)\alpha\langle r^2\rangle\left[Q_2\begin{pmatrix} 0 & 1 \\ 1 & 0 \end{pmatrix} + Q_3\begin{pmatrix} 1 & 0 \\ 0 & -1 \end{pmatrix}\right]. \tag{5.16}$$

Finally, the energy level splitting due to the distortion can be conveniently expressed in terms of the Pauli matrices:

$$\mathcal{H}_{JT} = -A(Q_2\sigma_x + Q_3\sigma_z) + \frac{1}{2}M\omega^2(Q_2^2 + Q_3^2), \tag{5.17}$$

where the second term is the increase in potential energy due to the distortion, the mass of the anion is M, and the frequency of the normal mode is ω. This Hamiltonian is easily solved in the polar coordinates $Q_3 = Q\cos(\theta)$ and $Q_2 = Q\sin(\theta)$, leading to the energy eigenvalues

$$E = \pm AQ + \frac{1}{2}M\omega^2Q^2. \tag{5.18}$$

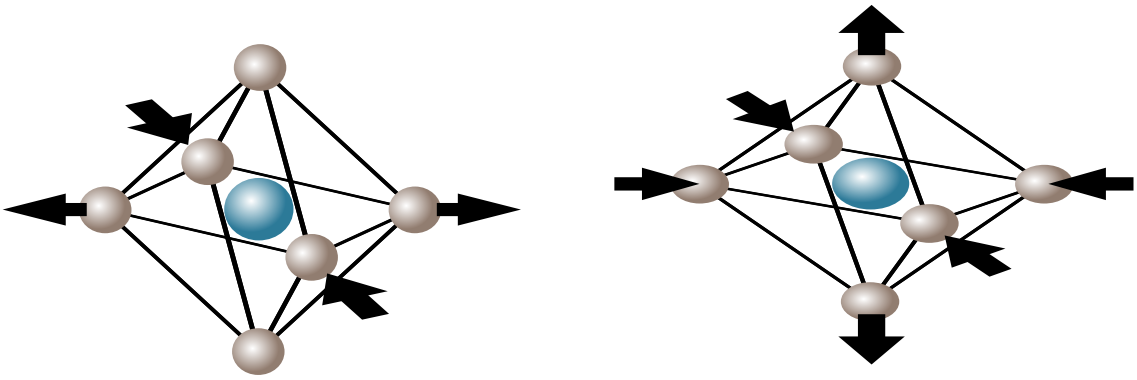

(a) The normal mode Q_2 of the oxygen ions surrounding a transition metal ion. This mode makes the $d_{x^2-y^2}$ orbital energetically favourable.

(b) The normal mode Q_3 of the oxygen ions surrounding a transition metal ion. This mode makes the $d_{3z^2-r^2}$ orbital energetically favourable.

Figure 5.4: The normal modes which lead to a Jahn-Teller splitting of the energy levels.

Then, minimising the energy with respect to Q, the optimal distortion is found to be $Q = |A|/M\omega^2$. The distortion is independent of the value of θ and and therefore stabilises an orbital of the general form

$$|\theta\rangle = \cos\left(\frac{\theta}{2}\right)|d_{3z^2-1}\rangle + \sin\left(\frac{\theta}{2}\right)|d_{x^2-y^2}\rangle. \tag{5.19}$$

This demonstrates that the linear Jahn-Teller effect splits the e_g energy levels and stabilises one of the *real* symmetry orbitals, and higher order terms are required to stabilise a unique orbital. The wavefunctions are multi-valued in the coordinate θ which results in a *Berry phase*: a geometrical phase which is acquired when a fast variable (the electron) moves adiabatically through a path in the parameter space of a slow variable (the lattice). The distortions for different values of theta are:

θ	Q
0	$3Z^2 - R^2$
$\pi/3$	$Z^2 - X^2$
$2\pi/3$	$3X^2 - R^2$
π	$X^2 - Y^2$
$4\pi/3$	$3Y^2 - R^2$
$5\pi/3$	$Y^2 - Z^2$

The Jahn-Teller distortion described above is relevant to the Mn^{3+} and Cu^{2+} configurations. The t_{2g} electrons also experience a Jahn-Teller distortion, but it is less significant because the electronic orbitals do not point directly towards the oxygen anions.

In a lattice the oxygen anions simultaneously participate in the distortions of two neighbouring octahedra, and therefore it is necessary to consider cooperative Jahn-Teller distortions[59, 60]. This results in a distribution of bond lengths that can be quantified by the ratio $\Delta d_{M-O}/\langle d_{M-O}\rangle$, which is about 0.5% in $YTiO_3$ and about 15% in $LaMnO_3$. For low hole doping these distortions tend to be *static*, whilst at higher hole doping it can be *dynamic* and the distortion moves around with the charge carriers, thus creating polarons.

5.3 Exchange interactions

The electronic properties of transition metal oxides can be quantified in terms of the exchange interactions of the electrons. These are derived from the Schrodinger equation which, when expressed in terms of field operators, may be written as[61]

$$\mathcal{H} = \int d\mathbf{r}\hat{\psi}^\dagger(\mathbf{r})\mathcal{H}_0(\mathbf{r})\hat{\psi}(\mathbf{r}) + \frac{1}{2}\int\int d\mathbf{r}d\mathbf{r}'\hat{\psi}^\dagger(\mathbf{r})\hat{\psi}^\dagger(\mathbf{r}')V(\mathbf{r},\mathbf{r}')\hat{\psi}(\mathbf{r}')\hat{\psi}(\mathbf{r}), \tag{5.20}$$

where $H_0(\mathbf{r})$ is a single particle operator including the kinetic energy term and $V(\mathbf{r},\mathbf{r}')$ is the inter-particle coulomb interaction. The single particle operator is

$$\mathcal{H}_0(\mathbf{r}) = -\frac{\hbar^2\nabla^2_{\mathbf{r}}}{2m} + \sum_i V(\mathbf{r}-\mathbf{R}_i). \tag{5.21}$$

The field operators can be expanded in terms of a complete basis of single particle states,

$$\hat{\psi}(\mathbf{r}) = \sum_{i\gamma\sigma}\psi_{i\gamma}(\mathbf{r})c_{i\gamma\sigma}, \tag{5.22}$$

where $\psi_{i\gamma}(\mathbf{r})$ is a Wannier state centred on the nucleus at $\mathbf{R}_i$, and $c_{i\gamma\sigma}$ is the corresponding spin dependent annihilation operator. For first row transition metal oxides it is convenient to use Wannier states constructed from products of $X_{32}(r)$ with the cubic harmonics[2]. In terms of creation and annihilation operators, the Hamiltonian is

$$\mathcal{H} = -\sum_{i\gamma\sigma} t^{\gamma_1\gamma_2}_{i_1 i_2} c^\dagger_{i_1\gamma_1\sigma}c_{i_2\gamma_2\sigma} + \frac{1}{2}\sum_{i\gamma\sigma}\langle i_1\gamma_1 i_2\gamma_2|\frac{e^2}{|\mathbf{r}-\mathbf{r}'|}|i_3\gamma_3 i_4\gamma_4\rangle c^\dagger_{i_1\gamma_1\sigma_1}c^\dagger_{i_2\gamma_2\sigma_2}c_{i_4\gamma_4\sigma_2}c_{i_3\gamma_3\sigma_1}, \tag{5.23}$$

where we have introduced the hopping matrix element

[2]Wannier states on different sites are constructed to be orthogonal. This involves taking a linear combination of orbitals on different sites and finding the 'most localised' orthogonal combinations.

$$t_{i_1 i_2}^{\gamma_1\gamma_2} = \int d\mathbf{r}\psi_{i_1\gamma_1}(\mathbf{r})H_0\psi_{i_2\gamma_2}(\mathbf{r}). \tag{5.24}$$

These matrix elements involve the overlap of the wavefunctions on the transition metal sites, with those on the oxygen sites, and are defined in terms of Slater-Koster parameters[62]. They therefore depend on both the length and angle of the M-O-M bonds. The electronic correlation matrix elements are defined

$$\langle i_1\gamma_1 i_2\gamma_2|\frac{e^2}{|\mathbf{r}-\mathbf{r}'|}|i_3\gamma_3 i_4\gamma_4\rangle = \int\int d\mathbf{r}d\mathbf{r}'\psi_{i_1\gamma_1}^\dagger(\mathbf{r})\psi_{i_2\gamma_2}^\dagger(\mathbf{r}')\frac{e^2}{|\mathbf{r}-\mathbf{r}'|}\psi_{i_4\gamma_4}(\mathbf{r}')\psi_{i_3\gamma_3}(\mathbf{r}). \tag{5.25}$$

Most of the terms in the expression above can be safely ignored. The most important contribution is from the *Hubbard U* term, which applies to two electrons sharing the same site i and the same orbital γ:

$$\mathcal{H}_U = \frac{1}{2}\sum_\sigma \langle i\gamma i\gamma|\frac{e^2}{|\mathbf{r}-\mathbf{r}'|}|i\gamma i\gamma\rangle c_{i\gamma\sigma}^\dagger c_{i\gamma\bar{\sigma}}^\dagger c_{i\gamma\bar{\sigma}}c_{i\gamma\sigma} = Un_{i\gamma\uparrow}n_{i\gamma\downarrow}. \tag{5.26}$$

This term is very large in free ions, but is reduced to some extent in transition metal oxides due to the mixing of the transition metal 3d and oxygen 2p orbitals. The Hubbard interaction is still the largest interaction and is responsible for the antiferromagnetic interactions between ions via the superexchange interaction. Another term which is often large is the *Hund coupling* which is the interaction between two electrons sharing the same site, but occupying different orbitals:

$$\begin{aligned}\mathcal{H}_H &= \frac{1}{2}\langle i\gamma_1 i\gamma_2|\frac{e^2}{|\mathbf{r}-\mathbf{r}'|}|i\gamma_1 i\gamma_2\rangle \sum_{\sigma_1\sigma_2} c_{i\gamma_1\sigma_1}^\dagger c_{i\gamma_1\sigma_1}c_{i\gamma_2\sigma_2}^\dagger c_{i\gamma_2\sigma_2} \\ &-\frac{1}{2}\langle i\gamma_1 i\gamma_2|\frac{e^2}{|\mathbf{r}-\mathbf{r}'|}|i\gamma_2 i\gamma_1\rangle \sum_{\sigma_1\sigma_2} c_{i\gamma_1\sigma_1}^\dagger c_{i\gamma_1\sigma_2}c_{i\gamma_2\sigma_2}^\dagger c_{i\gamma_2\sigma_1} \\ &= K_{\gamma_1\gamma_2}^0 n_{\gamma_1}n_{\gamma_2} - 2J_{\gamma_1\gamma_2}^0\left(\mathbf{S}_{\gamma_1}\cdot\mathbf{S}_{\gamma_2} + \frac{1}{4}n_{\gamma_1}n_{\gamma_2}\right),\end{aligned} \tag{5.27}$$

where the last equality makes use of the spin operators,

$$\begin{aligned}S_i^z &= \frac{1}{2}(c_{i\uparrow}^\dagger c_{i\uparrow} - c_{i\downarrow}^\dagger c_{i\downarrow}) \\ S_i^+ = c_{i\uparrow}^\dagger c_{i\downarrow} &\qquad S_i^- = c_{i\downarrow}^\dagger c_{i\uparrow}.\end{aligned} \tag{5.28}$$

J_0 is of the order 1eV in transition metal oxides and therefore the Hund coupling term favours parallel spins for electrons sharing the same site, but in different orbitals. This term is important in several transition metal oxides including the manganites, and is responsible for the ferromagnetic alignment of the spins of t_{2g} and e_g electrons. There is also

the analogous *direct exchange* interaction J which favours parallel spins on neighbouring sites, and is much smaller than U or J_0 for e_g orbitals:

$$\begin{aligned}\mathcal{H}_J &= \frac{1}{2}\langle i\gamma j\gamma|\frac{e^2}{|\mathbf{r}-\mathbf{r}'|}|i\gamma j\gamma\rangle \sum_{\sigma_1\sigma_2} c^\dagger_{i\gamma\sigma_1}c_{i\gamma\sigma_1}c^\dagger_{j\gamma\sigma_2}c_{j\gamma\sigma_2} \\ &-\frac{1}{2}\langle i\gamma j\gamma|\frac{e^2}{|\mathbf{r}-\mathbf{r}'|}|j\gamma i\gamma\rangle \sum_{\sigma_1\sigma_2} c^\dagger_{i\gamma\sigma_1}c_{i\gamma\sigma_2}c^\dagger_{j\gamma\sigma_2}c_{j\gamma\sigma_1} \\ &= K^0_{\gamma_1\gamma_2}n_{\gamma_1}n_{\gamma_2} - 2J^0_{\gamma_1\gamma_2}\left(\mathbf{S}_{\gamma_1}\cdot\mathbf{S}_{\gamma_2} + \frac{1}{4}n_{\gamma_1}n_{\gamma_2}\right). \end{aligned} \tag{5.29}$$

5.4 Charge-transfer and Mott-hubbard insulators

The electronic hopping is described by the *tight-binding* Hamiltonian,

$$\mathcal{H} = -t\sum_{\langle ij\rangle\sigma} c^\dagger_{i\sigma}c_{j\sigma}. \tag{5.30}$$

From this Hamiltonian we would expect to obtain a metal at half filling. In transition metal oxides, however, the strong electronic correlations result in a splitting of the energy band into an upper band and a lower band, and an insulator is often observed at half filling. These insulators may be classified in terms of the charge transfer energy Δ, which is the energy required for the excitation of an electron from an oxygen ligand to a transition metal ion ($d^nL \rightarrow d^{n+1}$), and the energy U required to transfer an electron from the lower Hubbard band to the upper Hubbard band ($d^nd^n \rightarrow d^{n-1}d^{n+1}$). If $U > \Delta$ the transition metal oxide is referred to as a Mott-Hubbard insulator[63], with a Mott gap of magnitude U in the density of states, whereas if $\Delta > U$ it is classified as charge transfer insulator[64], with an effective charge transfer gap Δ (Fig. 5.5). The perovskite oxides which we investigate are all charge transfer insulators, and the charge transfer gap, Δ, is an important parameter in our analysis.

5.5 Superexchange

The properties of Mott insulators can be understood by considering the *superexchange* interaction between electrons on neighbouring lattice sites. The superexchange interaction can be derived from the one-band Hubbard model[65]:

$$\mathcal{H} = -t\sum_{\langle ij\rangle\sigma}\left(c^\dagger_{i\sigma}c_{j\sigma} + h.c.\right) + U\sum_i n_{i\uparrow}n_{i\downarrow}. \tag{5.31}$$

If we consider strong electronic correlations ($U/t \gg 1$), then we can define an effective

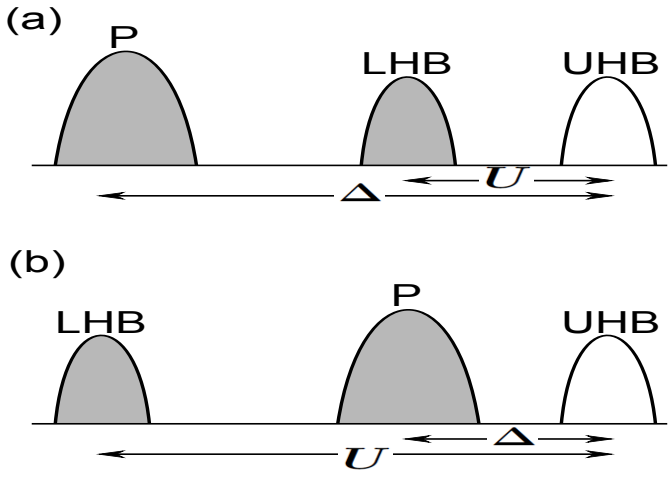

Figure 5.5: (a) The energy levels of the upper and lower Hubbard bands for a Mott-Hubbard insulator with gap U. (b) The energy levels for a charge-transfer insulator which has an effective gap equal to Δ.

Hamiltonian which acts predominantly in the singly occupied Hilbert space. The Hamiltonian may be written $\mathcal{H} = \mathcal{H}_0 + \mathcal{H}_1$, where $\mathcal{H}_1$ contains all of the terms which mix singly and doubly occupied states. We can then perform a canonical transformation, as discussed in appendix C, to eliminate $\mathcal{H}_1$ up to a specified order in perturbation theory. If we follow through with this procedure, and consider a nearly half filled band by applying the condition $1 - n \ll 1$, then we obtain the t-J model,

$$\mathcal{H}_{t-J} = -t \sum_{\langle ij \rangle \sigma} (1 - n_{i\bar{\sigma}}) c^{\dagger}_{i\sigma} c_{j\sigma} (1 - n_{j\bar{\sigma}}) + J \sum_{\langle ij \rangle} \left(\mathbf{S}_i \cdot \mathbf{S}_j - \frac{1}{4} n_i n_j \right). \tag{5.32}$$

where $J = 4t^2/U$ is the strength of the superexchange interaction[66] which favours antiparallel alignment of neighbouring spins so that electrons can exchange sites by briefly doubly occupying one of the sites. In the transition metal oxides the superexchange interaction is mediated by the oxygen atoms and is fourth order in the hopping amplitude, t, between copper and oxygen:

$$J = \frac{4t^4}{\Delta^2} \left(\frac{1}{\Delta} + \frac{1}{U} \right). \tag{5.33}$$

The t-J model is often used to describe the superconducting phase of the cuprates, and is therefore of considerable interest. When there is orbital degeneracy, such as in the manganites and the titanates, the superexchange interaction takes a very complicated form which accommodates the orbital anisotropy. When there is a single electron on each site the t-J model reduces to the *Heisenberg model*,

$$\mathcal{H} = \frac{J}{2} \sum_{\langle ij \rangle} \mathbf{S}_i \cdot \mathbf{S}_j. \tag{5.34}$$

which clearly prefers an antiferromagnetic ground state. Interestingly, according to *Nagaoka's theorem*, the motion of a single hole in the $J = 0$ limit of the t-J model is enough

to destroy the antiferromagnetism, and replace it with ferromagnetism. For non-zero values of J the motion of a finite density of holes creates a ferromagnetic interaction which can destroy the antiferromagnetism for a small enough ratio of J/t.

5.6 Interfaces

For the Perovskite oxides, the basic properties introduced in this chapter are very general, and are relevant to all of the materials we consider later in this investigation. When considering an interface between two perovskite oxides we must consider the most important interactions for each material, and how these interactions compete at the interface; deciding which interactions are dominant at the interface is a crucial step towards constructing an appropriate model. In addition, at an interface there is a discontinuity in the chemical potentials and a breaking of the translational symmetry. This can lead to all manner of complications such as: lattice distortions, polar discontinuities, charge transfer and lattice polarisation; which can drastically alter the interfacial properties. In the following chapter we focus on the broken translational symmetry and its effects on the electronic properties at an interface.

Chapter 6

Impurity theory models of interfaces

Throughout this investigation we shall employ *impurity theory* to construct simple models of perovskite oxide interfaces. The models introduced are essentially for non-interacting particles; the electronic correlations, such as the Hubbard U term, are therefore not incorporated into the models. Whilst this may seem to be a rather uncontrolled approximation, we will argue in later chapters that there is still considerable value in working in this way. In chapter 8, for the case of the cuprate-manganite interface, we argue that the non-interacting model actually provides a reasonable description of the ferromagnetic metallic phase of the manganite. In chapter 10, when we investigate the interface between $LaAlO_3$ and $SrTiO_3$, we do not attempt to model the subtleties of the electronic correlations; we are primarily interested in the charging phenomena, which has interesting consequences that are likely to be independent of the electronic correlations.

The impurity theory technique is convenient because it allows us to find exact solutions to known problems, when local impurities are added. We shall employ two types of impurity to model interfaces: electronic hopping impurities, which cancel electronic hopping between neighbouring sites thereby creating a surface, and atomic impurities, which lower the potential on specific atomic sites. The resulting analysis has a similar style to the scattering theoretical technique, which has been employed to model atomic reconstructions at semiconductor surfaces[67, 68].

We begin this chapter by introducing the *resolvent*, which is used throughout the impurity theory calculations. The resolvent, which contains information about the charge distribution in different layers, is used to analyse the electronic structure at interfaces. We then apply the techniques of impurity theory to the simplest conceivable model of an interface. Despite the simplicity of this model, it captures the basic physics which is crucial for the more detailed models considered later. Before introducing theoretical techniques we will consider some of the issues which can occur at an interface.

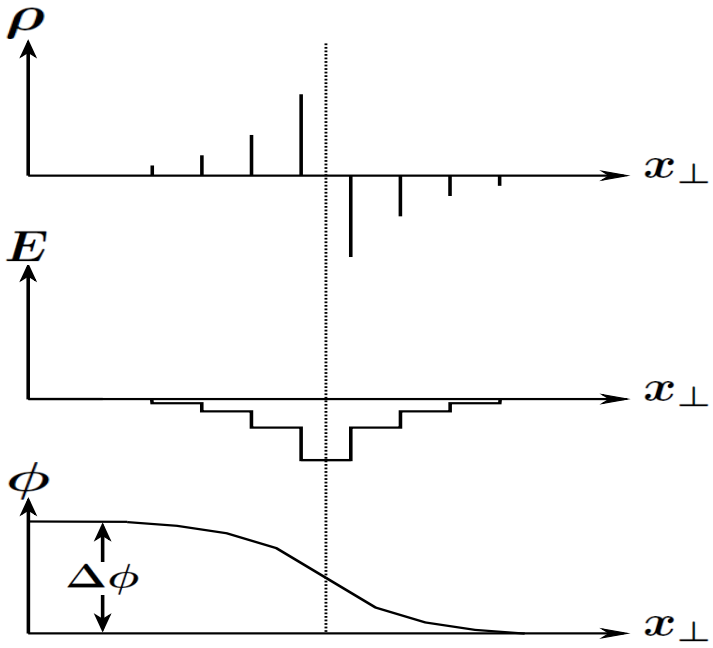

Figure 6.1: The charge transfer at an interface; the difference in chemical potentials on either side of the interface leads to a transfer of charge across the interface. At the simplest level we can imagine each atomic layer parallel to the interface to be a sheet of uniform charge ρ_j, which implies a constant electric field between adjacent layers. The electric field is determined from the relation $dE/dx = -\rho(x)$ and the electric potential is then determined from $d\phi/dx = E$. Infinitely far from the interface the electrostatic potential energy $e\Delta\phi$ exactly compensates for the difference in chemical potentials $\Delta\mu$.

6.1 Charge transfer at an interface

For semiconductor materials the physics of a simple interface can be understood in terms of *band bending*. If we consider two independent semiconductor materials, both with different chemical potentials, there will be a transfer of charge across the interface until an electric potential is built up to compensate the difference in chemical potentials. The simplest example is to consider uniformly charged atomic layers which produce a uniform electric field. This case is illustrated in Fig. 6.1.

The charge transfer can be visualised as band bending in the vicinity of the interface, as illustrated in Fig. 6.2, which often results in a doped region close to the interface[1]. A similar situation arises in the perovskite oxide interfaces which we consider in later chapters; the difference in chemical potentials can result in a doped region, next to the interface, which has different properties to the bulk. This is indeed the case for the cuprate-manganite interface investigated later. At a polar interface an additional complication arises from the sudden termination of the polar layers, which results in a diverging electric potential. When there are sufficient polar layers the electric potential can become larger than the band gap in one of the materials. In this case, the diverging electric potential can be neutralised with an 'electronic reconstruction', which dopes the interfacial layers with electrons obtained from the valence band[69]. A good example of this is the interface between $LaAlO_3$ and $SrTiO_3$, which is considered in chapter 9.

[1]This can sometimes result in a quantum well next to the interface, with discrete energy levels, creating a quasi two dimensional electron gas.

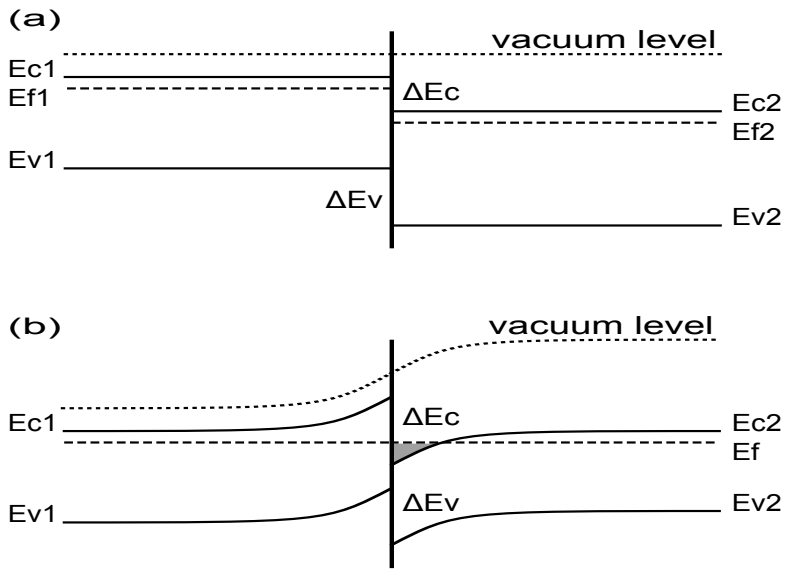

Figure 6.2: (a) The energy levels of the conduction bands (Ec), the valence bands (Ev), and the Fermi levels (Ef) of two isolated semiconductor materials. (b) At the interface the two materials must be in equilibrium; there is a transfer of charge across the interface to make the chemical potential constant throughout, which results in 'band bending'. This often leads to a small doped region next to the interface containing charge carriers.

When we consider the interface between two perovskite oxides the situation is complicated by the strong electronic correlations, which drastically alter the energy bands. It is therefore not possible to describe a generic perovskite oxide interface; each different combination of compounds must be considered independently, and it this uniqueness which makes these interfaces particularly interesting. The properties of the interface can be investigated by performing *ab initio* electronic structure calculations using *density functional theory*. Detailed electronic structure calculations are undoubtedly of considerable value; however, it is sometimes useful to have much simpler model calculations which ignore some of the finer details of the interface, but nevertheless capture the most important properties. In the following chapters we present two such models, both of which utilise impurity theory and resolvents to determine the electronic properties of the interface.

6.2 The resolvent

To model an interface using impurity theory, and to extract physically meaningful quantities from our models, we must first become familiar with resolvents. The resolvent is defined as

$$\mathcal{G}(z) = [z - \mathcal{H}]^{-1}. \tag{6.1}$$

This quantity is extremely simple in the eigenbasis of $\mathcal{H}$. The matrix elements are simply

$$\mathcal{G}(z)_{kk'} = \frac{\delta_{kk'}}{z - \epsilon_k}. \tag{6.2}$$

The unitary matrix which diagonalises $\mathcal{H}$ is constructed from the eigenvectors $a_n^{(k)}$:

$$\mathcal{U}_{nk} = a_n^{(k)} \qquad \text{where} \qquad \sum_{n'} \mathcal{H}_{n'} a_{n'}^{(k)} = \epsilon_k a_n^{(k)}. \tag{6.3}$$

Then the resolvent is represented in the original, non-diagonal, basis as

$$\mathcal{G}(z)_{nn'} = \sum_{kk'} \mathcal{U}_{nk} \mathcal{G}_{kk'} \mathcal{U}^{\dagger}_{k'n'} = \sum_k \frac{a_n^{(k)} a_{n'}^{(k)*}}{z - \epsilon_k}. \tag{6.4}$$

In our analysis, the diagonal basis will be in reciprocal space, and the non-diagonal basis will be in real space.

6.3 The density of states

The resolvent contains a lot of information about the system, including the density of states. We can take the trace of the resolvent to obtain

$$\text{Tr } \mathcal{G}(z) = \sum_k \frac{1}{z - \epsilon_k}, \tag{6.5}$$

which contains a simple pole whenever $z = \epsilon_k$. If we integrate around a closed contour containing all of these simple poles then, using the residue theorem, we deduce that the number of states is given by

$$\text{N} = \int_C \frac{dz}{2\pi i} f(z-\mu) \text{Tr } \mathcal{G}(z) = \int_C \frac{dz}{2\pi i} f(z-\mu) \sum_k \frac{1}{z - \epsilon_k} = \sum_k f(\epsilon_k - \mu), \tag{6.6}$$

provided that the contour C contains only the poles at $z = \epsilon_k$ and none of the poles of the Fermi distribution $f(z - \mu)$ (the Matsubara frequencies). We can also calculate the total energy,

$$E = \int_C \frac{dz}{2\pi i} f(z-\mu)\ z\ \text{Tr } \mathcal{G}(z) = \sum_k \epsilon_k f(\epsilon_k - \mu). \tag{6.7}$$

The appropriate contour is illustrated in Fig 8.4. For a general *real* function $g(z)$ the following relationship is easily verified:

$$\int_C \frac{dz}{2\pi i} g(z) \mapsto \int_{-\infty}^{\infty} \frac{d\epsilon}{2\pi i} [g(\epsilon - i\delta) - g(\epsilon + i\delta)] = \int_{-\infty}^{\infty} \frac{d\epsilon}{\pi} \text{Im } g(\epsilon - i\delta). \tag{6.8}$$

Applying this idea to the electron number we obtain

$$\text{N} = \int_{-\infty}^{\infty} \frac{d\epsilon}{\pi} f(\epsilon - \mu) \text{Im Tr } \mathcal{G}(\epsilon - i\delta). \tag{6.9}$$

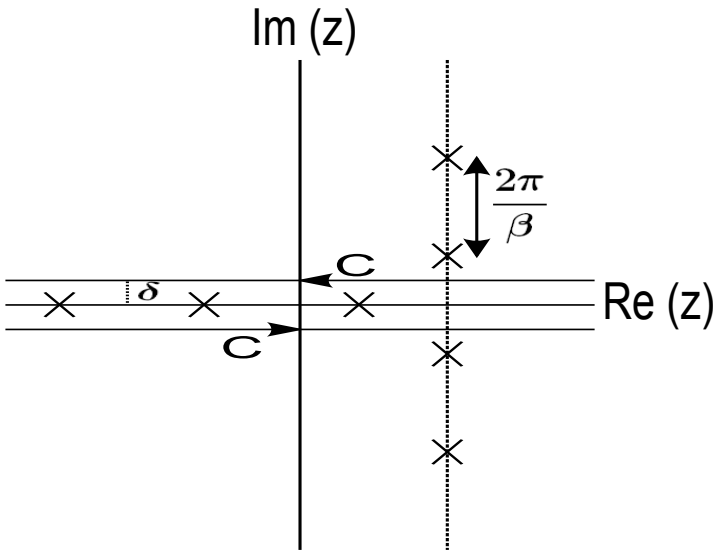

Figure 6.3: The Contour of integration, C, from which we deduce the the total occupation number, N, and the total energy, E. The poles of the resolvent, which correspond to bound states, reside on the real axis, whilst the Matsubara frequencies reside in the complex plane. The contour is chosen so that it captures all of the poles along the real axis, but none of those in the complex plane.

In the limit $\delta \to 0$, the contour collapses around the poles of the resolvent and we can then determine the density of states,

$$\rho(\epsilon) = \frac{1}{\pi} \lim_{\delta \to 0} \text{ Im Tr } \mathcal{G}(\epsilon - i\delta) = \sum_k \delta(\epsilon_k - \epsilon), \tag{6.10}$$

where we have employed an identity for the Dirac delta function:

$$\delta(\epsilon - \epsilon_k) = \lim_{\delta \to 0} \text{ Im } \frac{1}{\pi} \frac{1}{\epsilon - i\delta - \epsilon_k}. \tag{6.11}$$

Then we can write the electron number and the energy in terms of the density of states:

$$\text{N} = \int_{-\infty}^{\infty} d\epsilon \rho(\epsilon) f(\epsilon - \mu) \tag{6.12}$$

$$\text{E} = \int_{-\infty}^{\infty} d\epsilon \rho(\epsilon) \epsilon f(\epsilon - \mu). \tag{6.13}$$

6.4 Single particle correlation functions

We will often be interested in single particle correlation functions $\langle c_n^\dagger c_{n'} \rangle$, represented in the coordinate basis. In the original, non-diagonal, basis the single particle operator is

$$c_n^\dagger c_{n'} = \sum_{kk'} \mathcal{U}_{nk} c_k^\dagger c_{k'} \mathcal{U}_{k'n'}^\dagger. \tag{6.14}$$

We can evaluate the thermal average in the diagonal basis:

$$\langle c_k^\dagger c_{k'} \rangle = f(\epsilon_k - \mu) \delta_{kk'}. \tag{6.15}$$

Then the single-particle correlation is

$$\langle c_n^\dagger c_{n'} \rangle = \sum_k \mathcal{U}_{nk} f(\epsilon_k - \mu) \mathcal{U}_{kn'}^\dagger = \sum_k a_n^{(k)*} f(\epsilon_k - \mu) a_{n'}^{(k)}, \tag{6.16}$$

which is related to the resolvent,

$$\langle c_n^\dagger c_{n'} \rangle = \int_C \frac{dz}{2\pi i} f(z - \mu) \mathcal{G}(z)_{n'n}. \tag{6.17}$$

This relationship, between the correlation functions and the resolvent, is useful when require quantities such as the number of electrons occupying a particular site.

6.5 Impurity theory

Impurity theory is a useful technique for solving a reference system $\mathcal{H}_0$, for which the solution is known, with the addition of a *local* impurity $\mathcal{H}_1$:

$$\mathcal{H} = \mathcal{H}_0 + \mathcal{H}_1. \tag{6.18}$$

By local we mean that we can project $\mathcal{H}_1$ onto a finite dimensional subspace using a projection operator,

$$\mathcal{P} = \sum_{i=1}^{N} |i\rangle\langle i|, \tag{6.19}$$

where the summation is over the N basis states of the relevant subspace. Mathematically, the locality of the impurity translates into the equation $\mathcal{P}\mathcal{H}_1 = \mathcal{H}_1\mathcal{P} = \mathcal{H}_1$, which will be used to drastically simplify the problem. The impurity technique utilises the *resolvent*, which for the reference system is defined

$$\mathcal{G}_0(z) = [z - \mathcal{H}_0]^{-1}. \tag{6.20}$$

The resolvent for the system with the impurity present is defined

$$\mathcal{G}(z) = [z - \mathcal{H}_0 - \mathcal{H}_1]^{-1} = [(\mathcal{G}_0(z))^{-1} - \mathcal{H}_1]^{-1} = \mathcal{G}_0(z) + \mathcal{G}_0(z)\Sigma(z)\mathcal{G}_0(z), \tag{6.21}$$

where the matrix $\Sigma(z)$ has been defined

$$\Sigma(z) = \mathcal{H}_1 + \mathcal{H}_1\mathcal{G}_0(z)\mathcal{H}_1 + \mathcal{H}_1\mathcal{G}_0(z)\mathcal{H}_1\mathcal{G}_0(z)\mathcal{H}_1 + ... = \mathcal{H}_1[\mathcal{I} - \mathcal{G}_0(z)\mathcal{H}_1]^{-1}. \tag{6.22}$$

Any new poles appearing in the resolvent are contained in $\Sigma(z)$, which therefore contains the information about any new bound states created by the impurity. Because the impurity $\mathcal{H}_1$ is local, $\Sigma(z)$ is also local and satisfies $\mathcal{P}\Sigma(z) = \Sigma(z)\mathcal{P} = \Sigma(z)$. The matrix $\Sigma(z)$ can also be written in the form

$$\Sigma(z) = \mathcal{H}_1[\mathcal{I} - \mathcal{G}_0^{\mathcal{P}}(z)\mathcal{H}_1]^{-1} = [\mathcal{H}_1^{-1} - \mathcal{G}_0^{\mathcal{P}}(z)]^{-1}, \tag{6.23}$$

which contains the projected resolvent of the reference system,

$$\mathcal{G}_0^{\mathcal{P}}(z) = \mathcal{P}\mathcal{G}_0(z)\mathcal{P}. \tag{6.24}$$

The local matrix $\Sigma(z)$ is calculated from a finite dimensional inverse; then using $\Sigma(z)$ we can solve the impurity problem. The bound state energies are found from the poles of $\Sigma(z)$, which are solutions to the equation

$$\mathrm{Det}||\mathcal{H}_1^{-1} - \mathcal{G}_0^{\mathcal{P}}(E)|| = 0. \tag{6.25}$$

To find out detailed local information, such as the density of states on the impurity sites, we can make use of the projected resolvent,

$$\mathcal{G}^{\mathcal{P}}(z) = \mathcal{G}_0^{\mathcal{P}}(z) + \mathcal{G}_0^{\mathcal{P}}(z)\Sigma(z)\mathcal{G}_0^{\mathcal{P}}(z) = [(\mathcal{G}_0^{\mathcal{P}}(z))^{-1} - \mathcal{H}_1]^{-1}. \tag{6.26}$$

The projected resolvent is used in chapter 10, whilst investigating the interface between $SrTi_3$ and $LaAlO_3$. Alternatively, to obtain information about non-local properties[2], we can choose to calculate the matrix elements of the complete resolvent,

$$\mathcal{G}(z)_{nn'} = \mathcal{G}_0(z)_{nn'} + \sum_{i,i'} \mathcal{G}_0(z)_{ni}\Sigma(z)_{ii'}\mathcal{G}_0(z)_{i'n'}. \tag{6.27}$$

The complete resolvent is used in chapter 8, whilst investigating a cuprate-manganite interface. Depending on the nature of the problem we may wish to calculate the complete resolvent (using Eq.6.27), the projected resolvent (using Eq. 6.26), or simply the energy of any new bound states (using Eq. 6.25). We apply these techniques throughout this investigation of perovskite oxide interfaces, starting with a simple model of the one dimensional chain with a single impurity atom.

6.6 The one dimensional chain

To see how resolvents are utilised it is instructive to consider the tight-binding Hamiltonian

[2] Although the impurity is strictly local, its effects are clearly non-local.

$$\mathcal{H} = -t \sum_{<nn'>} c_n^\dagger c_{n'}. \tag{6.28}$$

We will consider the one-dimensional chain, with nearest neighbour hopping. The Hamiltonian is diagonalised by applying a Bloch transform:

$$c_k^\dagger = \frac{1}{\sqrt{N}} \sum_n e^{ikn} c_n^\dagger \qquad c_k = \frac{1}{\sqrt{N}} \sum_n e^{-ikn} c_n. \tag{6.29}$$

The Hamiltonian, in reciprocal space, is simply

$$\mathcal{H} = \sum_k \epsilon_k c_k^\dagger c_k. \tag{6.30}$$

The matrix elements of the Hamiltonian are $\mathcal{H}_{kk'} = \delta_{kk'}\epsilon_k$. Finally, we calculate the resolvent $\mathcal{G} = [z - \mathcal{H}]^{-1}$ and obtain the matrix elements

$$\mathcal{G}_{kk'} = \frac{\delta_{kk'}}{z + 2t\cos(k)}. \tag{6.31}$$

6.6.1 The density of states for the one dimensional chain

To determine the density of states on a particular lattice site we first need to transform the resolvent into coordinate space, and then make use of Eq. 6.10. We perform the inverse Bloch transform:

$$\mathcal{G}_{nn'}(z) = \frac{1}{N} \sum_{kk'} e^{ikn} \mathcal{G}_{kk'}(z) e^{-ik'n'} = \frac{1}{N} \sum_k \frac{e^{ik(n-n')}}{z + 2t\cos(k)} \to \int_{-\pi}^{\pi} \frac{dk}{2\pi} \frac{e^{ik(n-n')}}{z + 2t\cos(k)}. \tag{6.32}$$

In the last step we simply took the thermodynamic limit ($N \to \infty$). We can evaluate this integral if we introduce the complex variable $x = e^{ik}$, so that

$$\mathcal{G}(z)_{nn'} = \oint_C \frac{dx}{2\pi i x} \frac{x^{n-n'}}{z + t(x + \frac{1}{x})}. \tag{6.33}$$

The integral is to be performed around the unit circle in the complex plane, in a counter-clockwise direction. The poles are located at

$$x_\pm = \frac{-z \pm (z^2 - 4t^2)}{2t}. \tag{6.34}$$

We can see that $x_- x_+ = 1$, so in polar coordinates $x_+ = re^{i\theta}$ and $x_- = \frac{1}{r}e^{-i\theta}$, then one root lies inside and one root lies outside the unit circle. We must be particularly careful when both poles lie on the unit circle, when $r = 1$. We can also make use of the

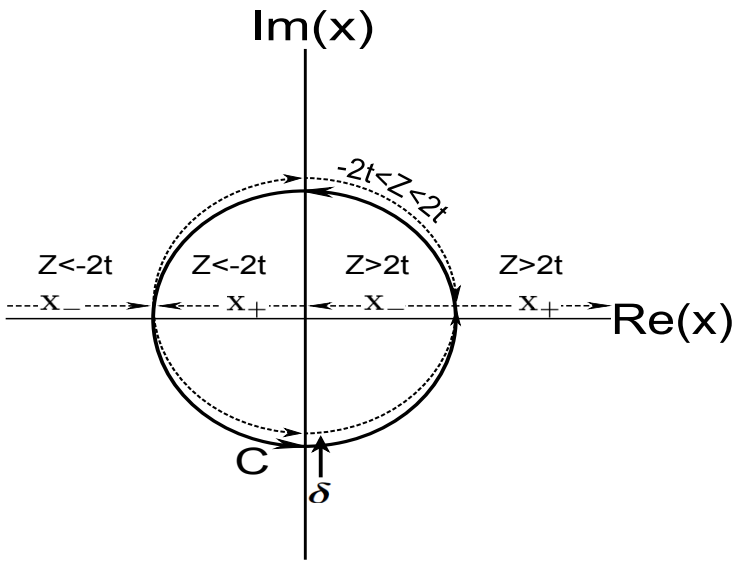

Figure 6.4: The contour of integration, C, around the unit circle, and the poles of the integrand of Eq. (6.35). The arrows indicate the motion of the poles in the complex x plane as z is increased from minus infinity to plus infinity. When $-\infty < z < -2t$, or when $2t < z < \infty$, one pole is trapped inside the contour. In the region $-2t \leq z \leq 2t$ both poles lie on the unit-circle and it is necessary to evaluate the poles for a complex argument, $z - i\delta$, which pushes the pole on the lower half-circle inside the contour. Finally, we then take the limit $\delta \to \infty$.

observation that the transformation $x \mapsto \frac{1}{x}$ leads to $\mathcal{G}_{nn'}(z) = \mathcal{G}_{n'n}(z)$. Therefore

$$\mathcal{G}(z)_{nn'} = \oint_C \frac{dx}{2\pi i} \frac{x^{|n-n'|}}{t(x-x_+)(x-x_-)}. \tag{6.35}$$

The evaluation of the integral depends on which pole is enclosed in the contour C. The possibilities are illustrated in Fig. 6.4 and it is easily verified that if $z < 2t$ the pole at x_- is enclosed, yielding

$$\mathcal{G}(z)_{nn'} = -\frac{(x_-)^{|n-n'|}}{(z^2-4t^2)^{\frac{1}{2}}}, \tag{6.36}$$

whereas if $z > 2t$ the pole at x_+ is enclosed, yielding

$$\mathcal{G}(z)_{nn'} = \frac{(x_+)^{|n-n'|}}{(z^2-4t^2)^{\frac{1}{2}}}. \tag{6.37}$$

Both of these quantities are real, which implies that the density of states is zero for energies lying outside of the main band. When $-2t < z < 2t$ the poles lie on the contour of integration and we must recall that the argument, z, of the resolvent is a complex number. Therefore, when we calculate $\mathcal{G}(\epsilon - i\delta)$ in the density of states formula, Eq. 6.10, the pole which originated on lower half of the contour is shifted inside the contour, as illustrated in Fig. 6.4. In the limit $\delta \to 0$, the resolvent just below the branch cut is

$$\mathcal{G}(z)_{nn'} = \frac{\left(-\frac{z}{2t} - i\frac{(4t^2-z^2)^{\frac{1}{2}}}{2t}\right)^{|n-n'|}}{(-i)\,(4t^2-z^2)^{\frac{1}{2}}}. \tag{6.38}$$

Finally, the density of states on the site n is

$$\rho_n(\epsilon) = \frac{1}{\pi} \lim_{\delta \to 0} \text{ Im } \mathcal{G}(\epsilon - i\delta)_{nn} = \frac{1}{\pi(4t^2 - \epsilon^2)^{\frac{1}{2}}}. \tag{6.39}$$

As expected, due to periodicity, the charge of the electrons is spread out equally over the entire chain.

6.7 A simple impurity model of an interface

At an interface, the difference in chemical potentials and the subsequent band bending can lead to states which are bound to the interface, decaying exponentially into the bulk. This scenario is directly relevant to both of the interfaces which are investigated in the following chapters, and it is therefore instructive to consider a simple example. We will consider the one dimensional Hamiltonian

$$\mathcal{H} = -t \sum_{n=1}^{\infty} \left(c_{n+1}^{\dagger} c_n + c_n^{\dagger} c_{n+1} \right) - \Delta c_1^{\dagger} c_1. \tag{6.40}$$

This Hamiltonian describes a semi-infinite chain, with an impurity atom at one end. The impurity atom lowers the energy at the site $n = 1$, causing a bound state to peel off the bottom of the bulk state energy band. Physically, the loss of hybridisation at the interface is characteristic of a metal-insulator interface, or the interface between a metal and a layered compound, whilst the impurity, which lowers the potential in the interfacial layer, reflects the difference in the chemical potentials of the two materials.

The Hamiltonian can be solved in three steps simple steps, as illustrated in Fig. 6.5, using the techniques of impurity theory: i) we calculate the dispersion relation and the resolvent for the one dimensional infinite chain ii) we use impurity theory to cut the infinite chain to form a 'semi-infinite' chain iii) we use impurity theory, again, to place the impurity atom at the end of the chain, and calculate the energy of the bound state which is formed.

Step one is straightforward; The resolvent for the one dimensional infinite chain, in real space, may me written

$$\mathcal{G}_0(z)_{nn'} = \frac{X^{|n-n'|}}{t(X - \frac{1}{X})}, \tag{6.41}$$

where

$$X = -\frac{z}{2t} + \frac{\sqrt{|z^2 - 4t^2|}}{2t}. \tag{6.42}$$

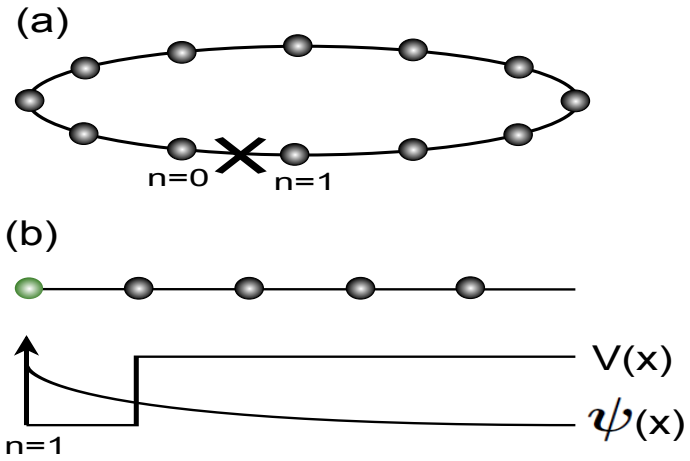

Figure 6.5: The three step impurity theory calculation, for electrons bound to an interface. (a) We calculate the resolvent for the infinite chain and use impurity theory to cut the chain and obtain the modified resolvent. (b) We place an impurity atom at the end of the chain which lowers the potential, and creates a bound state which decays exponentially into the bulk.

The parameter X is multi-valued and the phase in front of the square root is therefore dependent on the value of z. To obtain agreement with the analysis of the previous section the phases are determined as follows; when $z < -2t$ the phase is -1, when $z > 2t$ the phase is $+1$, and when z lies below the branch cut, such that $-2t < z < 2t$, the phase is $-i$. To proceed with the second step of the calculation we define the impurity

$$\mathcal{H}_1 = \begin{pmatrix} 0 & t \\ t & 0 \end{pmatrix}. \tag{6.43}$$

This impurity simply cancels the hopping between the sites $n = 0$ and $n = 1$. Since we have taken the thermodynamic limit, the two ends of the chain are infinitely far apart and therefore completely independent of each other. We will simply disregard one end of the chain and examine the effects of an impurity potential placed on the remaining end. The calculation of $\Sigma(z) = [\mathcal{H}_1^{-1} - \mathcal{G}_0^{\mathcal{P}}(z)]^{-1}$ is straightforward:

$$\Sigma(z) = \left[\begin{pmatrix} 0 & \frac{1}{t} \\ \frac{1}{t} & 0 \end{pmatrix} - \begin{pmatrix} \mathcal{G}_0(z)_{00} & \mathcal{G}_0(z)_{01} \\ \mathcal{G}_0(z)_{10} & \mathcal{G}_0(z)_{11} \end{pmatrix} \right]^{-1} = t \begin{bmatrix} -X & 1 \\ 1 & -X \end{bmatrix}. \tag{6.44}$$

The modified resolvent, using Eq. 6.27, is then

$$\mathcal{G}(z)_{nn'} = \mathcal{G}_0(z)_{nn'} + \sum_{i,i'=0}^{1} \mathcal{G}_0(z)_{ni} \Sigma_{ii'}(z) \mathcal{G}_0(z)_{in'}$$

$$= \frac{X^{|n-n'|}}{t(X - \frac{1}{X})} + \frac{1}{t(X - \frac{1}{X})^2} \left[X^{|n-1|+|n'|} + X^{|n|+|n'-1|} - X^{|n|+|n'|+1} - X^{|n-1|+|n'-1|+1} \right]. \tag{6.45}$$

The resolvent for the semi-infinite chain, which is valid when $n, n' \geq 1$, is then

$$\mathcal{G}(z)_{nn'} = \frac{X^{|n-n'|} - X^{n+n'}}{t(X - \frac{1}{X})}. \tag{6.46}$$

The matrix elements of the resolvent connecting sites at opposite ends of the chain are now identically zero. The third and final step of our calculation is to add the impurity $\mathcal{H}_1 = -\Delta$ which, by lowering the potential at the site $n = 1$, produces a bound state. If we now choose the reference system to be the semi-infinite chain, by using Eq. 6.46 for $\mathcal{G}_0$, then the modified resolvent is

$$\mathcal{G}(z)_{nn'} = \mathcal{G}_0(z)_{nn'} + \mathcal{G}_0(z)_{n1}\Sigma(z)\mathcal{G}_0(z)_{1n'}, \tag{6.47}$$

where

$$\Sigma = \frac{t}{X - \frac{t}{\Delta}}, \tag{6.48}$$

which gives

$$\mathcal{G}(z)_{nn'} = \frac{X^{|n-n'|} - X^{n+n'}}{t(X - \frac{1}{X})} + \frac{X^{n+n'}}{t(X - \frac{t}{\Delta})}. \tag{6.49}$$

The resolvent can now be used to extract information about the electronic structure of the interface. The resolvent contains a single pole, corresponding to a state which is bound to the interface. The energy of this state is the solution of $\det ||\mathcal{H}_1^{-1} - \mathcal{G}_0^{\mathcal{P}}(E)|| = 0$, which gives

$$-\frac{1}{\Delta} - \mathcal{G}_0(\epsilon)_{11} = -\frac{1}{\Delta} + \frac{X}{t} = 0, \tag{6.50}$$

resulting in the following energy for the bound state:

$$E = -\Delta - \frac{t^2}{\Delta}, \tag{6.51}$$

which is only relevant when $\Delta > t$ since

$$\sqrt{E^2 - 4t^2} = \Delta - \frac{t^2}{\Delta} > 0. \tag{6.52}$$

We find that the impurity atom produces a bound state at the surface, but only if the potential energy gained is enough to compensate for the loss of hybridisation energy. This idea is important in the real interfaces which are investigated in subsequent chapters. In all cases we find a natural competition between the impurity potential at the interface, which binds electrons to the interface, and the potential barrier created by the loss of hybridisation, which effectively repels electrons from the interface.

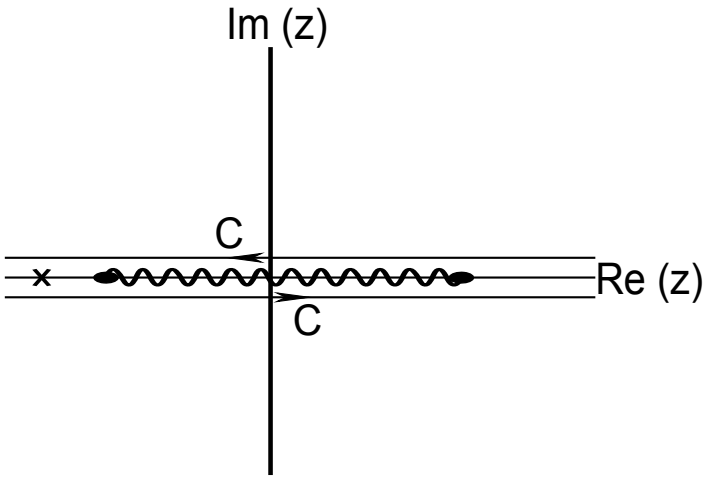

Figure 6.6: The analytical structure of the resolvent for the impurity model of the interface. The pole on the real axis corresponds to a bound state of energy $E = -\Delta - t^2/\Delta$, whilst the branch cut, running between $z = -2t$ and $z = 2t$, corresponds to the continuum of bulk states. The contour C is used to evaluate the number of electrons, and picks up the residue at $z = E$.

6.8 Extracting information from the resolvent

Typically, we will be interested in the charge, $\boldsymbol{\rho}_n$, in each layer. We use the formula

$$\boldsymbol{\rho}_n = \int_{-\infty}^{\infty} d\epsilon f(\epsilon - \mu)\rho_n(\epsilon), \tag{6.53}$$

where $f(\epsilon - \mu)$ is the Fermi-Dirac distribution. To determine the charge in each layer we integrate along the contour illustrated in Fig. 6.6. The bound state is located on the real axis at the binding energy E, and there is also a branch cut running between $z = -2t$ and $z = 2t$, which accommodates the continuum of bulk states. When there is a bound state the density of states becomes a Dirac Delta function, located at the binding energy E. The amount of charge in each layer is then proportional to the residue, evaluated at the binding energy. The charge in the n-th layer is therefore

$$\boldsymbol{\rho}_n = \operatorname*{Res}_{\epsilon=E} \mathcal{G}(\epsilon)_{nn} \propto X^{2n}(E) = \exp\left(-\frac{2n}{\xi}\right). \tag{6.54}$$

The charge (and the wavefunction) decays exponentially into the bulk, with a bound state length scale

$$\frac{1}{\xi} = \log\left(\frac{\Delta}{t}\right). \tag{6.55}$$

In later chapters we find that, even for complicated interfaces, the presence of an impurity potential in an interfacial layer often creates states which are bound to the interface and decay exponentially into the bulk. At an interface the parameters Δ and t compete with each other, and dictate the properties of the bound states.

6.9 Summary

In this chapter we have introduced the techniques of impurity theory and applied them to a simple model of an interface. Using this model we have shown how a local impurity, located at a surface or interface, can induce a bound state which decays exponentially into the bulk. In later chapters an analogous model, which displays the same characteristics, will be adopted to represent a cuprate-manganite interface. For the cuprate-manganite interface we are interested in the number of electrons present in the interfacial layers, which can be deduced using impurity theory. A second model, this time for the interface between $SrTiO_3$ and $LaAlO_3$, also exhibits bound states at the interface which decay exponentially into the bulk. For this second interface we are interested in the confinement of electrons close to the interface. In both cases it is also necessary to consider the charge transfer across the interface and the consequent screening effects, which are not included in the simple model used in this chapter.

Chapter 7

A cuprate-manganite interface

In the following two chapters we investigate the electronic properties at the interface between ferromagnetic $La_{2/3}Ca_{1/3}MnO_3$ (LCMO) and the high temperature superconductor $YBa_2Cu_3O_7$ (YBCO). Several experimental investigations, which are designed to probe the interfacial cuprate and manganite layers, have revealed unexpected properties at the YBCO-LCMO interface. The interfacial cuprate layer is observed to have two active e_g orbitals, rather than the single active orbital which is found in the cuprate superconductors, which signifies an orbital reconstruction. The magnetic properties of the interface are also intriguing, as there is some evidence of antiferromagnetic correlations between the cuprate and the manganite.

In the following two chapters we explain how the unusual properties of the YBCO-LCMO interface may be caused by *spin injection*[1] from the manganite into the cuprate[71]. In particular, we examine how the injected spins could cause an orbital reconstruction and change the magnetic properties of the interfacial cuprate layers. This explanation is found to be consistent with experimental observations. Before we consider the YBCO-LCMO interface we will give a brief overview of the rich variety of phases for each of the independent materials, and discuss the properties which make them particularly interesting.

The strongly correlated electronic motion in the cuprates leads to a variety of intriguing phenomena, such as: high temperature superconductivity, the pseudogap, an anomalous metal, and stripes. These phases are realised as the doping of the CuO_2 planes is varied, from electron doped to hole doped, and the result is an exceedingly rich phase diagram. Several different phases are relevant at a cuprate-manganite interface because, as charge is transferred from the manganite to the cuprate, the doping of the CuO_2 planes varies as a function of their proximity to the interface. To describe this rich behaviour it is necessary

[1] Spin injection is a general feature of interfaces involving a ferromagnetic material. Basically, the spin polarised electrons from the ferromagnetic material flow into the neighbouring material, and result in an accumulation of spin which can drastically alter the properties of the interface. This idea is hoped to have technological applications in *spintronic* devices[70].

to employ the three band Hubbard model, which contains the electronic interactions in the all important CuO_2 planes.

In this chapter we introduce the three band Hubbard model, and its simplifications, as a first step towards deciding on an appropriate model for the interfacial cuprate layers. We also introduce models appropriate to each of the cuprate phases, and briefly discuss the Zhang-Rice singlet[72]: the mobile charge carrier which participates in the high temperature superconductivity. It is then shown that the electron doped CuO_2 planes, which we will include in our model of a cuprate-manganite interface, can be described by the t-J model.

The orbital degeneracy in manganites, coupled with the strongly correlated motion of electrons, leads to phenomena which are as rich and diverse as those found in the cuprates. These phenomena include the Colossal magnetoresistance (CMR) effect, a ferromagnetic metallic phase, and many complicated charge ordered phases. These phases, which are activated at different levels of doping, are the result of a large number of competing interactions, which can be magnetic, electronic, or structural. It is believed that it is the complex interplay between all of these different interactions which gives rise to the CMR effect.

In this chapter, several different models are described which qualitatively reproduce most of the phases observed in the LCMO phase diagram. Although one might expect several phases to be relevant at the interface, as is the case for the cuprates, we find that only the ferromagnetic metallic phase is realised. This phase is dominated by the double exchange mechanism and the large Hund's coupling between the t_{2g} and e_g electrons. A reasonable model for the electronic structure can then be obtained by considering a simple double exchange model of the two e_g orbitals, assuming that the spin degree of freedom is removed by the strong Hund's coupling.

We conclude this chapter by looking at the two experiments which have motivated this investigation. The first experiment involves x-ray absorption spectroscopy (XAS), performed at the YBCO-LCMO interface, which indicates that both of the e_g orbitals are active in the interfacial cuprate layers. The second experiment involves polarised neutron reflectometry (PNR), performed on YBCO-LCMO superlattices, which yields, as one possible magnetic profile, antiferromagnetic correlations between the cuprate and the manganite.

Then, in Chapter 8, we propose a simple model of the interface based on the double-exchange mechanism. To solve this model, and hence determine the electronic structure at the interface, we utilise impurity theory. We are then able to provide a theoretical interpretation of the magnetic properties, and the electronic properties, which have been observed at the YBCO-LCMO interface.

7.1 The cuprates

Although we are primarily interested in the properties of YBCO, it is nevertheless possible to talk about the more general class of materials, the cuprates, which all demonstrate remarkably similar phases as the doping is changed. The literature associated with the various properties and phases of these materials is vast[2] and there are still many unresolved issues, so it is only possible to give an overview of some concepts which are relevant to the physics of the interface.

The high-T_C properties of the cuprates were first discovered in 1986 by Bednorz and Muller[54], with the discovery of $La_{2-x}Sr_xCuO_4$ which for the optimal doping $x \approx 0.15$ has a T_c of 30 K, a value sufficiently high to cast doubt on a plausible explanation from BCS theory. This was quickly followed by the subsequent discovery of $YBa_2Cu_3O_{7-x}$ (YBCO) by Wu et al[75] in the following year, with a T_c of about 93 K for the optimally doped compound with $x \approx 0.10$. Among the other compounds discovered are $Bi_2Sr_2CaCu_2O_{8+x}$ with a T_C up to 94 K, and $Ti_2Ba_2Ca_2Cu_3O_{10+x}$ with a T_C as high as 125 K. These compounds are composed of distinct layers, unlike the typical BCS compounds, and contain CuO_2 planes perpendicular to the c-axis which contain the mobile charge carriers and are believed to be responsible for the superconductivity.

These compounds form in layered perovskite structures, as illustrated in Fig. 7.1. The ideal perovskite structure AMO_3 consists of the relatively large cation A and the smaller B cation, which is surrounded by six oxygen anions forming an octahedron. The cuprates do not have this ideal perovskite structure, but are usually close to being tetragonal, or form in layered perovskite structures. The structures must be electrically neutral, which results in the individual layers being charged. The CuO_2 planes of the *parent compound* are formally composed of Cu^{2+} and O^-, and therefore have an overall negative charge, whilst the interleaved layers have a net positive charge to compensate. For doped systems the dopants normally lie in the interleaved layers, as opposed to the CuO_2 layers, and are either substitute cations such as Sr^{2+} for La^{3+}, or are additional oxygen ions (which are added to the CuO chains in YBCO).

In the parent compound we consider the electronic states to be ionic with the electrons localised around the ions, except in the CuO_2 planes and CuO chains where there is some degree of hybridisation between the Cu $3d$ states the the O $2p$ states. The formal valence configuration of Cu^{2+} consists of a single hole in the Cu crystal field split $3d$ shell, which resides in the $\hat{x}^2 - \hat{y}^2$ state. The O $2p$ states are also split by the crystal field, but have a formal valence configuration of O^{2-} which corresponds to a closed shell. Materials such as La_2CuO_4 can be doped by substituting Sr^{2+} for La^{3+} to form $La_{2-x}Sr_xCuO_4$, which

[2] See, for example, the reviews [73, 74, 58].

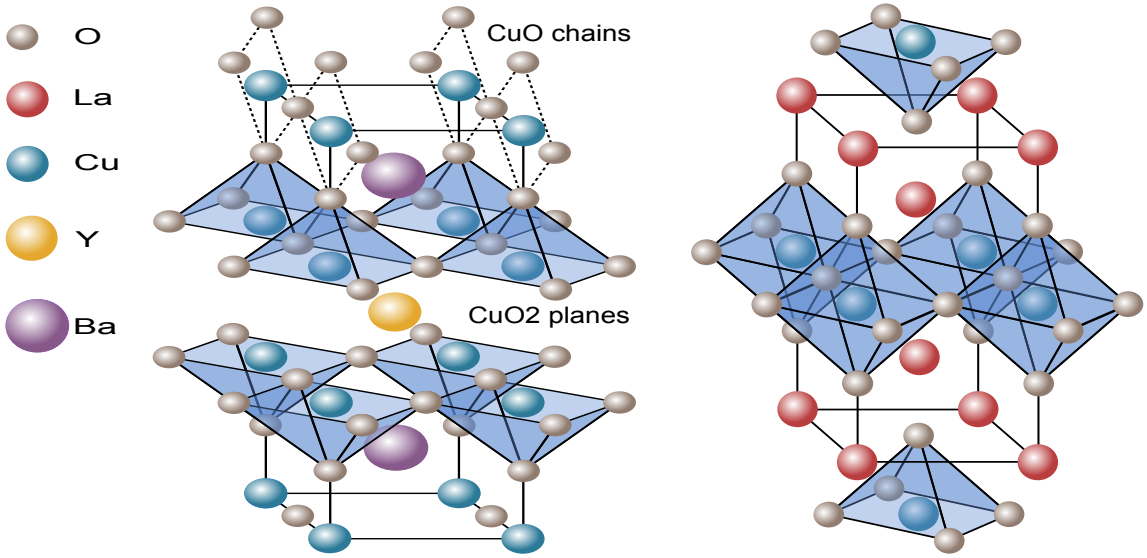

(a) $YBa_2Cu_3O_7$ (b) La_2CuO_4

Figure 7.1: The crystal structures of two cuprate superconductors

removes an electron from the CuO_2 plane and leaves it with $n = 1 + x$ holes per unit cell. In $YBa_2Cu_3O_{7-\delta}$ the doped material is obtained by adding oxygen into empty sites along the CuO chains, and although the exact doping of the CuO_2 planes is unknown, it can be approximated from an Ewald summation to be $n = 1 + \frac{1-2\delta}{3}$, if we assume that the holes are evenly distributed throughout the three Cu layers.

For comparable levels of hole doping in the CuO_2 planes the phases of the different cuprate superconductors are remarkably similar, and the generic cuprate phase diagram is illustrated in Fig. 7.2. Below approximately 300 K the parent compound corresponds to an antiferromagnetic Mott insulator, from which the superconducting state emerges as holes (or electrons) are doped into the system. The hole doped cuprate YBCO is obviously of particular interest, but the properties of the electron doped cuprates are actually more relevant at the YBCO-LCMO interface. Therefore, both the electron doped cuprates and the hole doped cuprates are of interest in this investigation.

7.1.1 The superconducting state

Despite considerable effort, and numerous reseach articles, there is still no general consensus on the form of an appropriate theory for the superconducting phase of the cuprates. In the BCS theory[76, 77] of conventional metals, the mechanism responsible for the superconductivity is well understood. The electron-phonon interaction mediates an attractive interaction between electrons near the Fermi-surface, and these electrons then form

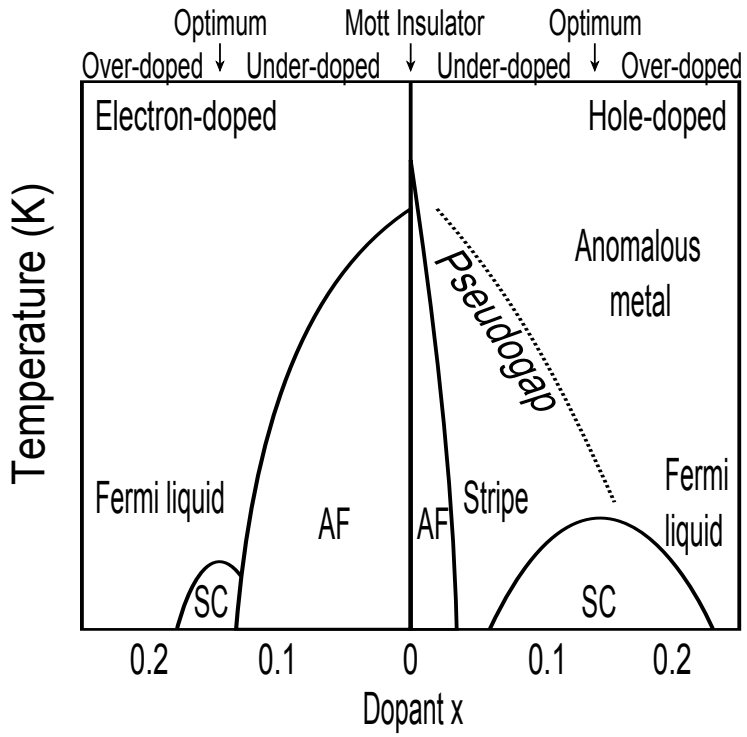

Figure 7.2: The generic phase diagram for the cuprates, for both hole doped (in this case $La_{2-x}Sr_xCuO_4$) and electron doped ($Nd_{2-x}Ce_xCuO_4$) systems. The x-axis denotes the average carrier concentration of electrons/holes found in a CuO_2 unit cell. A wide variety of phases are present including: antiferromagnetic (AF), superconducting (SC), pseudogap, anomalous metal and Fermi liquid. The asymmetry of the electron/hole phase diagrams, including the larger superconducting and smaller antiferromagnetic regions on the hole doped side, indicates that the models for the electron doped and hole doped cuprates are qualitatively different.

Cooper pair bound states which have a binding energy of 2Δ (the BCS energy gap) and carry the supercurrent. However, it is clear that the BCS theory cannot account for the high critical temperatures associated with the cuprates, and there is much experimental evidence that highlights important differences. This can be seen in the isotope effect[78], whereby T_C is only slightly affected after replacing ^{16}O with ^{18}O, and ARPES measurements which show nodes in the superconducting gap consistent with d-wave symmetry[79].

7.1.2 The pseudogap

In the underdoped compounds, at temperatures above the superconducting transition temperature, various measurements have provided evidence for the existence of a *pseudogap*, the magnitude of which appears to be maximal along the $(0, \pi)$ direction but disappears along the (π, π) direction. The pseudogap appears to be similar to the d-wave gap observed in the superconducting state, which is suggestive of a possible relationship between the two phenomena.

There is evidence of a pseudogap at a temperature $T^* > T_C$, which first appears at the crossover between the normal state and the pseudogap state. Neutron scattering measurements[80] indicate that the pseudogap is associated with a spin channel, whilst specific heat[81], ARPES[82], and tunnelling spectroscopy measurements[83] indicate that the gap also exists in the charge channel. As the temperature is reduced from the pseudo-

gap temperature T^* to below T_C, the Fermi surface contracts into *Fermi arcs*[84]. These segments of Fermi surface are holelike and several theories have been suggested to describe these phenomena: the existence of an RVB-flux phase[85], the truncation of the Fermi surface due to Umklapp scattering[86], and the existence of disordered stripe domains[87]. It has also been suggested that there exists a quantum critical point[88] where the pseudogap transition temperature T^* reaches zero for a particular level of doping, and the transition is associated with a broken symmetry. Whilst undoubtedly interesting, the pseudogap is not relevant to our investigation of the cuprate-manganite interface.

7.1.3 The electronic structure of the cuprates

On a microscopic level it is presumed that something akin to the BCS pairing theory can also be applied to the cuprates, despite the fact that the underlying pairing mechanism is still not understood. Because of the close proximity of the superconducting phase to the antiferromagnetic Mott insulating phase it is widely believed that the pairing mechanism is of magnetic origin, and therefore a lot of work focuses on the theory of highly correlated electrons in the Hubbard and t-J models.

The parent compound is an antiferromagnetic Mott insulator which can be represented by the Hubbard model for the CuO_2 planes. It is normally argued that the three band model can be reduced to a single band model. This leads to the t-J model which describes the hopping of charge carriers in the lightly hole doped system, and includes the antiferromagnetic superexchange interaction between neighbouring spins. The charge carriers in this system are the *Zhang-Rice singlets*, illustrated in Fig. 7.5, which are bound states of holes on neighbouring copper and oxygen sites. Because of the superexchange interaction the ground state of the parent compound is the Néel state, and as holes are added by doping, these holes are assumed to hop in an antiferromagnetic background of copper spins. Understanding the motion of holes in a Mott insulator is therefore considered an important step towards understanding the superconductivity.

In an ARPES experiment performed on the antiferromagnetic parent compound, a single electron is excited by the incident photon, thereby creating a *photohole* in the CuO_2 plane. This experiment is therefore a practical realisation of a hole in an antiferromagnetic background, which makes comparisons between the calculations based on the t-J model and ARPES measurements particularly meaningful.

The spectral function for a single hole in an antiferromagnetic background has been calculated theoretically, using the self consistent Born approximation[89, 90, 91]. To obtain agreement between theory and experiment it is necessary to include the parameters t' and t'' for longer range hopping. The spectral function calculated from the resulting t-t'-t''-J model is in good agreement measurements obtained using ARPES. The bandwidth

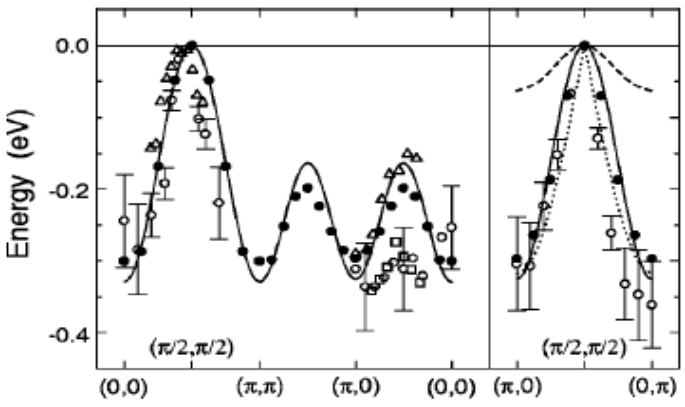

Figure 7.3: The dispersion of a single hole in the t-t′-t″-J, calculated in the self consistent Born approximation, compared with ARPES data for $Sr_2CuO_2Cl_2$. Experimental data are taken from [92] (open circles), [93] (open squares), and [94] (open triangles). The self consistent Born approximation (solid circles) is fitted to the t-t′-t″-J dsipersion (solid line).

is significantly reduced from the free electron value because of renormalisation of the quasiparticles due to interactions with the spin background. The bandwidth is even smaller than the one dimensional analogue where spin-charge separation leads to separate dispersions for *spinons* and *holons*.

Whether the single band Hubbard and t-J models reliably capture the physics of the CuO_2 planes is not entirely clear. In the next section it is shown how, by performing a canonical transformation on the three band Hubbard model, a different picture emerges for the hole doped cuprates.

7.1.4 Microscopic models of the cuprates

The appropriate model, and interaction parameters, for the cuprates can be deduced from band structure calculations and experimental observations. The accepted model, which describes the CuO_2 planes, is the three band Hubbard model. This model can be further simplified by performing canonical transformations, to yield models appropriate to the electron doped and hole doped cuprates. As can be deduced from the asymmetry of the cuprate phase diagram, these models are subtly different.

7.1.5 Band structure calculations

The antiferromagnetic insulating state observed in the parent compounds indicates that electronic correlations are very important in the cuprates. Therefore, the independent electron model, which predicts a metal at half filling, cannot be expected to predict the correct properties of the more exotic states of the cuprates. However, the normal state of the optimally doped material is metallic and band structure calculations should provide some useful information about the most important electronic configurations. The band structure calculations for YBCO incorporate the Hartree-Fock terms which account for the mean electronic correlations induced by the coulomb interaction.

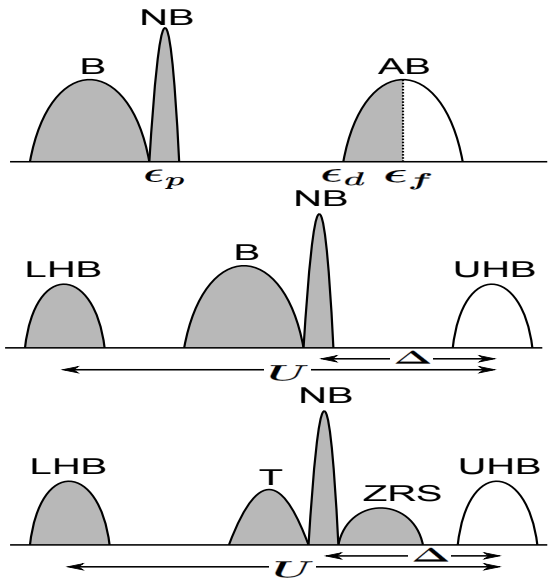

Figure 7.4: (a) The non-interacting electron band structure calculations suggests that the cuprate layer is metallic, and is described by three bands: a non-bonding band, a bonding band, and an antibonding band. (b) When electronic correlations are included the antibonding band splits into an upper and lower Hubbard band, and the cuprate layer becomes a charge transfer insulator. (c) The hybridisation of the bonding band with the upper Hubbard band creates a triplet band and a Zhang-Rice singlet band. In the hole doped compounds the holes reside in the Zhang-Rice singlet band, whilst in the electron doped compounds the electrons reside in the upper Hubbard band.

The bands associated with the CuO_2 planes involve the Cu $3d_{x^2-y^2}$ orbital hybridising with the O $2p_x$ and O $2p_y$ orbitals. The overlap between adjacent CuO_2 planes is very small and the dispersion is consequentially almost independent of k_z, which corresponds to charge carriers which are mostly confined to the individual planes. The three bands associated with the CuO_2 layers which may be thought of as bonding, antibonding and non-bonding, are illustrated in Fig. 7.4. In YBCO there are also bands which are associated with the CuO chains. Both bands are essentially one-dimensional and the dispersions are almost independent of both k_x and k_z, which corresponds to charge carriers confined to the chains.

For YBCO the calculations do not take into account the non-stoichiometric nature of the oxygen doping in the chains, which implies that the disorder present due to oxygen vacancies is not accounted for. The strong electronic correlations will also change the electronic properties substantially, but the main features of the band structure calculations, such as the approximate hybridisation parameters and the two dimensional nature of the CuO_2 planes, should remain intact. This gives a strong indication that a good model of the CuO_2 planes should contain the essential physics associated with the various phases of the cuprates[3].

[3]The superconducting transition temperature T_C varies in the presence of different types of cation disorder[95], and tends to increase as the number of cuprate layers in each unit cell is increased from $N = 1$ to $N = 3$. This variation in T_C is believed to be caused by the various distortions of the ideal CuO_2 plane in each of the HTSC materials.

7.1.6 The three band Hubbard model

Experimental considerations allow us to simplify the model of the cuprates considerably. Electron Energy Loss Spectroscopy (EELS) measurements indicate that additional holes reside on the oxygen atoms, but not the copper atoms. X-ray Photoemission Spectroscopy (XPS) indicates that the copper is essentially CuO^{2+}, and X-ray Absorption Spectroscopy (XAS) indicates that the $3\hat{z}^2 - 1$ orbital has only minor fluctuations.

A minimal model capable of describing the electronic properties of the CuO_2 planes must therefore include the oxygen p_x and p_y orbitals, and the copper $3d_{x^2-y^2}$ orbitals. The parent compound consists of Cu^{2+} which contains a single hole in the outermost shell, and O^{2-} for which the outermost shell is filled and is subsequently doped with holes. It is therefore much easier to think in terms of holes rather than electrons. The appropriate model is the three band Hubbard model:

$$\mathcal{H} = \mathcal{H}_\epsilon + \mathcal{H}_U + \mathcal{H}_T \tag{7.1}$$

$$\mathcal{H}_\epsilon = \epsilon_d \sum_{i,\sigma} n^d_{i\sigma} + (\epsilon_d + \Delta) \sum_{i,\boldsymbol{\delta},\sigma} n^p_{i+\boldsymbol{\delta}/2,\sigma} \tag{7.2}$$

$$\mathcal{H}_U = U_d \sum_i n^d_{i,\sigma} n^d_{i,\bar{\sigma}} + U_p \sum_{i,\boldsymbol{\delta}} n^p_{i+\boldsymbol{\delta}/2,\sigma} n^p_{i+\boldsymbol{\delta}/2,\bar{\sigma}} + U_{pd} \sum_{i,\boldsymbol{\delta},\sigma,\sigma'} n^d_{i,\sigma} n^p_{i+\boldsymbol{\delta}/2,\sigma'} \tag{7.3}$$

$$\begin{aligned}\mathcal{H}_T = \sum_{i,\sigma} \big[& T_{pd} d^\dagger_{i,\sigma} (p_{i+\boldsymbol{y}/2,\sigma} - p_{i+\boldsymbol{x}/2,\sigma} - p_{i-\boldsymbol{y}/2,\sigma} + p_{i-\boldsymbol{x}/2,\sigma}) \\ & + T_{pp} \left(p^\dagger_{i+\boldsymbol{y}/2,\sigma} p_{i+\boldsymbol{x}/2,\sigma} - p^\dagger_{i-\boldsymbol{x}/2,\sigma} p_{i+\boldsymbol{y}/2,\sigma} + p^\dagger_{i-\boldsymbol{y}/2,\sigma} p_{i-\boldsymbol{x}/2,\sigma} - p^\dagger_{i+\boldsymbol{x}/2,\sigma} p_{i-\boldsymbol{y}/2,\sigma} \right) + h.c. \big] ,\end{aligned} \tag{7.4}$$

where $d_{i,\sigma}$ annihilates a copper $3d_{x^2-y^2}$ hole of spin σ at site i and $p_{i\pm\boldsymbol{x}(\boldsymbol{y})/2,\sigma}$ annihilates an oxygen $2p_x(2p_y)$ hole at the neighbouring $i \pm \boldsymbol{x}(\boldsymbol{y})/2$ site. The approximate values of the interaction parameters can be obtained from band structure calculations [96], and their values are: $U_d \sim 8$, $U_p \sim 4$, $U_{pd} \sim 1$, $\Delta \sim 3$, $T_{pd} \sim 1$ and $T_{pp} \sim 0.5$.

The coulomb interactions modify the non-interacting energy bands: The coulomb interaction on the copper site splits the antibonding band into the upper and lower Hubbard bands illustrated in Fig. 7.4, and the hybridisation with the upper Hubbard band then splits the bonding band into a triplet band and the Zhang-Rice singlet band.

The three band Hubbard model is thought to contain all of the interactions which are necessary to describe the cuprate phase diagram in Fig. 7.2, but is much to complicated to work with. However, this model can be simplified considerably by performing a canonical transformation to eliminate double occupancy of the copper sites.

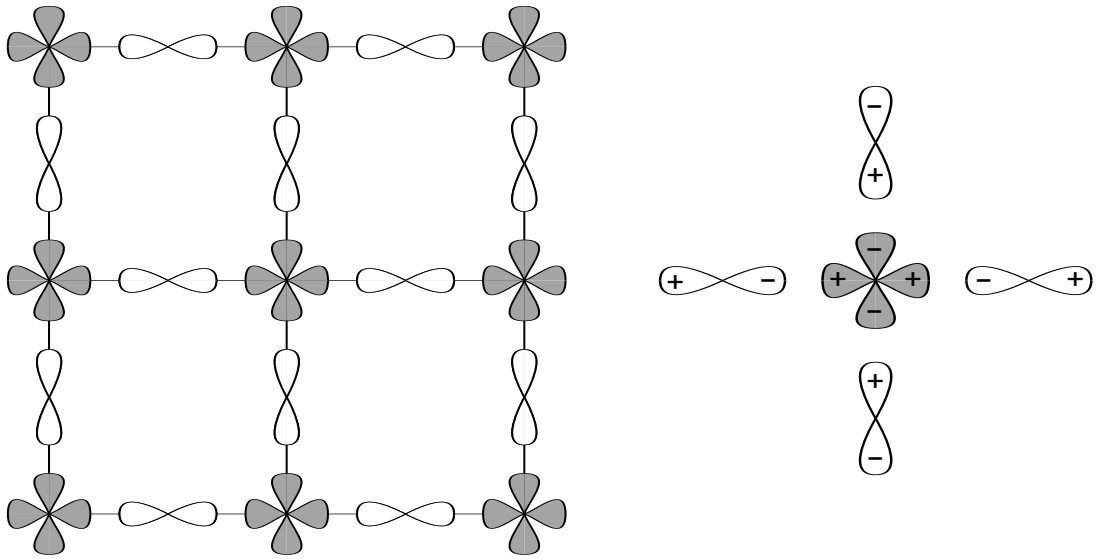

Figure 7.5: On the left is the CuO_2 plane, which is characterised by the electronic $d_{x^2-y^2}$, p_x and p_y states. On the right is the Zhang-Rice singlet, which is formed by the hybridisation between a copper $d_{x^2-y^2}$ state with the surrounding oxygen p_x and p_y states. Reciprocal space has been translated by (π, π) to give the phases depicted.

7.1.7 Hole doped cuprates

To capture the essential physics of the three band model it is necessary to retain the parameters $U \equiv U_d$, Δ and $V \equiv T_{pd}$. It is also convenient to translate reciprocal space by (π, π) to remove the awkward phases associated with the $d_{x^2-y^2}$ and O 2p orbitals. The zero of energy can be chosen to coincide with the oxygen level (so that $\epsilon_p = 0$), which eliminates the non-bonding band from consideration. The simplified Hamiltonian is then

$$\begin{aligned} \mathcal{H} &= \mathcal{H}_0 + \mathcal{H}_1 \\ \mathcal{H}_0 &= -\Delta \sum_{i\sigma} n^d_{i\sigma} + U \sum_i n^d_{i\sigma} n^d_{i\overline{\sigma}} \\ \mathcal{H}_1 &= V \sum_{i\sigma} [d^\dagger_{i\sigma} P_{i\sigma} + P^\dagger_{i\sigma} d_{i\sigma}], \end{aligned} \tag{7.5}$$

where the non-orthogonal annihilation operator $P_{i\sigma} = \sum_{\langle ij \rangle} p_j$ annihilates an electron on the oxygen site j neighbouring the copper site i. The hopping parameter V is assumed to be much smaller than both Δ and U, then a perturbation expansion in powers of V is appropriate. An effective Hamiltonian can be obtained with a canonical transformation, keeping terms up to second order in the hopping amplitude V, and including the fourth order superexchange interaction. We define an operator S which satisfies $\mathcal{H}_1 + [S, \mathcal{H}_0] = 0$, and obtain an effective Hamiltonian $\mathcal{H}_{eff} = \mathcal{H}_0 + \frac{V^2}{2}[S, \mathcal{H}_1]$. It has been observed in EELS

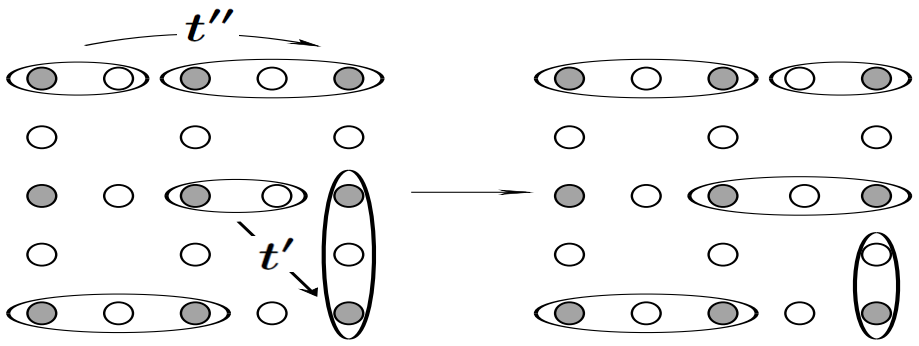

Figure 7.6: The motion of Zhang-Rice singlets, in an RVB state consisting of dimerised copper spins. The t-J-X Hamiltonian hops the singlet over several different ranges, which suggests that the t, t′ and t″ terms are already implicitly included.

experiments that the holes which are doped into the parent compound reside on the oxygen ions, and the charge on the copper is conserved. This feature can be incorporated into the effective Hamiltonian by enforcing the constraint

$$\sum_{\sigma} d^{\dagger}_{i\sigma} d_{i\sigma} = 1. \tag{7.6}$$

The model which is relevant to experiments is then found to be[97, 98]

$$\mathcal{H}_{eff} = X \sum_{\langle ij\rangle\sigma} \sum_{\langle ij'\rangle\sigma'} d^{\dagger}_{i\sigma} p^{\dagger}_{j'\sigma'} p_{j\sigma} d_{i\sigma'} - t \sum_{\langle ij\rangle\sigma} \sum_{\langle ij'\rangle} p^{\dagger}_{j\sigma} p_{j'\sigma} + \frac{J}{2} \sum_{\langle ii'\rangle} \mathbf{S}_i \cdot \mathbf{S}_{i'}, \tag{7.7}$$

where $X = \frac{UV^2}{\Delta(U-\Delta)}$, $t = \frac{V^2}{U-\Delta}$ and $J = \frac{4V^4}{\Delta^3} + \frac{4V^4}{\Delta^2 U}$. According to Nagaoka's theorem the ground state of a single hole in the infinite U Hubbard model on the square lattice is ferromagnetic, and the superexchange interaction must be included to obtain the low spin state. Interestingly, the t-J-X model does *not* have such a ground state. The motion of a single hole in the t-X-J model has been investigated numerically and it is found that even when $J = 0$ the ground state is a low spin state, but the long range order of the Néel state is not observed. This is suggestive of a resonating valence bond (RVB) state[99] which is constructed from dimers of the background copper spins. In this picture, the Zhang-Rice singlets hop in a background of dimerised copper spins, rearranging the dimers as they pass by. This also has the appeal that longer range hopping of the singlet emerges naturally from such a state, which would in principal lead to effective t′ and t″ hopping parameters in accordance with the t-t′-t″-J model.

7.1.8 Electron doped cuprates

To determine a suitable model for the electron doped cuprates we return to the Hamiltonian given by Eq. 7.5. To deal with the strong correlations induced by U it is again useful to perform a canonical transformation. The procedure works in much the same way as before, but in this case the restrictions are quite different: In the electron doped cuprates the parent compound again consists of Cu^{2+} and O^{2-} states and as electrons are doped into the system they reside on the copper sites, thereby forming some Cu^{+} states. The charge on the oxygen is therefore conserved so that $p^{\dagger}_{i\sigma}p_{i\sigma} = 0$, and the effective Hamiltonian is found to be

$$\mathcal{H}_2 = -\frac{V^2}{\Delta}\sum_{\langle ii'\rangle\sigma}(1-n_{i\bar{\sigma}})d^{\dagger}_{i\sigma}d_{i'\sigma}(n_{i'\bar{\sigma}}-1) + \frac{J}{2}\sum_{\langle ii'\rangle}\mathbf{S}_i\cdot\mathbf{S}_{i'}. \tag{7.8}$$

The effective Hamiltonian for the electron doped cuprates is the t-J model which explains the large antiferromagnetic portion of the phase diagram. The hole motion between copper sites is via intermediate oxygen sites, which gives rise to a *double exchange* mechanism similar to that observed in the manganites. This model is used to describe the CuO_2 layer at the YBCO-LCMO interface which, it is argued, is doped with electrons from the manganese. The close proximity with the manganese also introduces ferromagnetic interactions and an orbital degree of freedom into the problem, as will be explained in chapter 5.

7.2 The manganites

The manganites have been subject to intensive study in recent years[4], due largely to their remarkable colossal magnetoresistance (CMR) properties, which could potentially lead to new technological applications. The manganites have also attracted a lot of attention because of the high spin polarisation of charge carriers in the ferromagnetic metallic phase, a property which could be utilised in spin injection devices. Additionally, the manganites also have extremely rich phase diagrams which result from the complex interplay between spin, charge, orbital and lattice degrees of freedom. These phases have been identified experimentally and the phase competition at the phase boundaries leads to interesting phenomena.

The manganites are composed of trivalent cations R, divalent cations A, and MnO_6 octohedra. They can be classed in terms of the layered compounds $R_{1-x}A_{1+x}MnO_4$ and $R_{2-2x}A_{1+2x}Mn_2O_7$ which have one and two consecutive MnO_2 layers respectively, and the cubic perovskite compounds $R_{1-x}A_xMnO_3$ which have an infinite number of consecutive

[4]See, for example, [100, 101, 58].

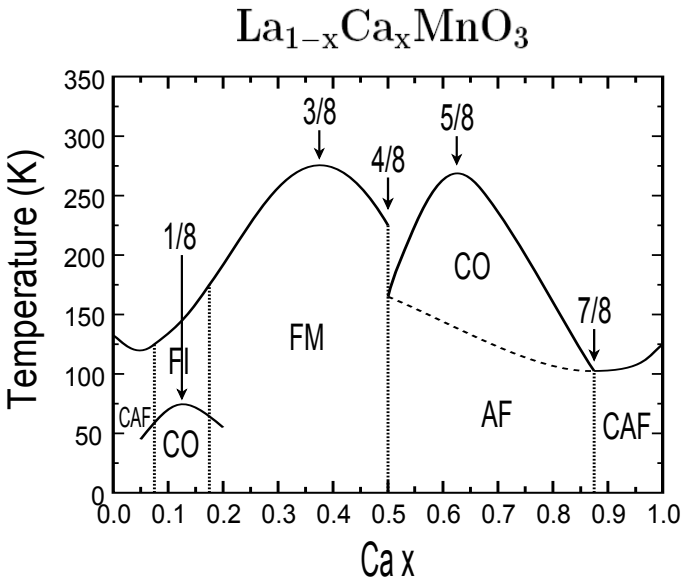

Figure 7.7: The phase diagram[102] of $La_{1-x}Ca_xMnO_3$, for $x = 0$ (Mn^{3+}) up to $x = 1$ (Mn^{4+}). As the doping and temperature are varied a rich variety of phases are observed: Canted antiferromagnetic (CAF), charge ordered (CO), ferromagnetic metal (FM), ferromagnetic insulator (FI), and antifrromagnetic (AF). The '1/8 phenomena' is also observed: Many of the transitions occur at characteristic doping levels that are, approximately, multiples of 1/8.

MnO_2 layers. The cubic perovskite structures lead to the most interesting properties, many of which are generic and appear in compounds with different cations R and A. We will discuss the basic properties of this class of manganites, but focus mainly on $La_{1-x}Ca_xMnO_3$ (LCMO) which has a very large magnetoresistance effect, and a diverse phase diagram which ranges over all Ca doping levels $0 \leq x \leq 1$.

7.2.1 Charge and orbital order

A wide variety of charge, spin and orbital order is observed in the manganites $R_{1-x}A_xMnO_3$ as the relative number of Mn^{3+} and Mn^{4+} ions is varied by changing the doping concentration x. Early studies were performed on LCMO in the 1950's which utilised neutron diffraction techniques to provide a comprehensive determination[103, 104] of the magnetic order and charge order across the whole doping range $0 < x < 1$. Probing the orbital order is more difficult and the particular orbital configurations are usually inferred from xray diffraction measurements of lattice distortions, although direct measurements have been performed[105] using resonant x-ray spectroscopy (RXS). The full phase diagram for $La_{1-x}Ca_xMnO_3$, obtained using resistivity and magnetisation data[102], is illustrated in Fig. 7.7 and the various states which occur can be classified for the different values of x as follows:

- $x = 0(RMnO_3)$: The parent compound consists of Mn^{3+} ions with one e_g electron per site, and due to the strong electronic correlations this state is a Mott insulator. Below 780K the Jahn-Teller lattice distortion appears with the concomitant staggered orbital order with $d_{3x^2-r^2}$ and $d_{3y^2-r^2}$ orbitals aligned alternately in the x-y

plane, and uniformly along the z-axis. Below 140K the structure exhibits A-type antiferromagnetic order, where the spins align ferromagnetically in the x-y plane, but antiferromagnetically along the z-axis.

- $x \sim 0.1$: As holes are doped in to $RMnO_3$ the spins align ferromagnetically but the material remains an insulator. In this region of the phase diagram some of the theoretically predicted properties are observed experimentally, such as spin canting and phase separation.

- $0.125 < x < 0.5$: The ferromagnetic metallic state is observed, for which the magnetic moment is almost perfectly polarised indicating that the Hund coupling is larger than the bandwidth. Long range charge/orbital ordering is not observed, suggesting that the orbital state may be an orbital liquid or disordered. Above the curie temperature the electrical resistivity shows insulating behaviour, and the CMR effect is also observed close to the Curie temperature.

- $x \sim 0.5$: Depending on the particular cations R and A, a charge ordered state may be observed below the charge and orbital ordering temperatures. In LCMO the CE-type antiferromagnetic order is established which has a unit cell $2\sqrt{2}a \times 2\sqrt{2}b \times 2c$. Charge order is also established with a unit cell $\sqrt{2}a \times \sqrt{2}b \times c$, and the orbital order has a unit cell $2\sqrt{2}a \times \sqrt{2}b \times c$. The charge is stacked along the z-axis, a feature which is difficult to explain theoretically.

- $0.5 < x < 0.7$: An A-type antiferrmagnetic structure is observed, but is different to that observed in $LaMnO_3$. Close to the Néel temperature there is a contraction along the z-axis corresponding to uniform $d_{x^2-y^2}$ orbital order

- $x \sim 2/3$ It is believed that in LCMO a bi-stripe arrangement may be stabilised which consists of pairs of charge stripes, separated by some distance from other pairs.

- $0.7 < x < 1$: A C-type antiferromagnetic structure is observed. The MnO_6 octahedron are elongated along the z-axis corresponding to occupation of the $d_{3z^2-r^2}$ orbitals.

- $x = 1(AMnO_3)$: There are no e_g electrons and the material is a Mott insulator. The antiferromagnetic interactions among the t_{2g} electrons stabilises the G-type antiferromagnetic order below approximately 140K.

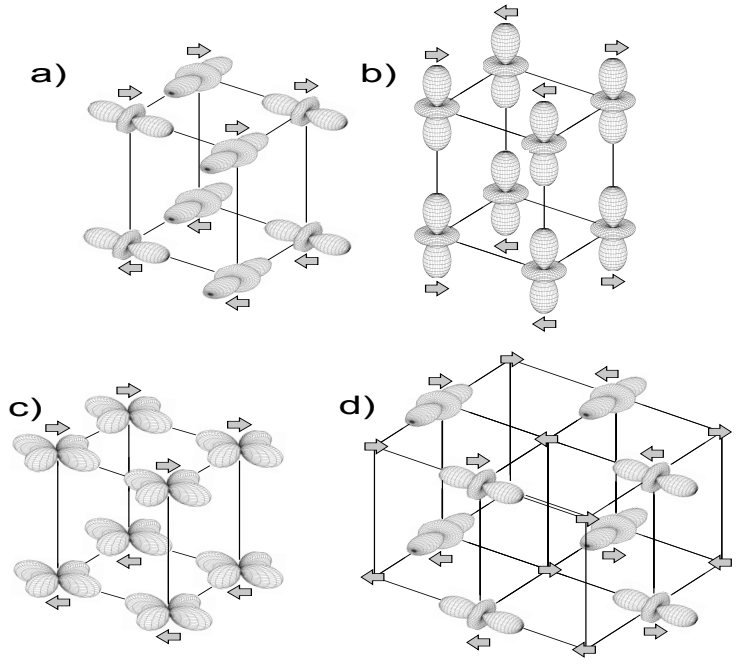

Figure 7.8: The charge and orbital ordered states found in the manganites: (a)The A-AF phase observed when $x = 0$: The spins are aligned ferromagnetically in the x-y plane, but antiferromagnetically along the z-axis with $3\hat{x}^2 - 1/3\hat{y}^2 - 1$ orbital order. (b)The CE-AF phase observed when $x = 0.5$. (c) The A-AF phase observed when $0.5 < x < 0.7$: The $\hat{x}^2 - \hat{y}^2$ orbital is energetically favourable and the spins align ferromagnetically in the x-y plane, but antiferromagnetically along the z-axis. (d) C-AF phase observed when $0.7 < x < 1$: The $3\hat{z}^2 - 1$ orbital is energetically favourable and the spins align antiferromagnetically in the x-y plane, but ferromagnetically along the z-axis.

7.2.2 Colossal magnetoresistance

Much of the interest in the manganites is due to the observation of a 'colossal' MR ratio $\Delta R/R = (R_H - R_0)/R_H$ (R_0 is the resistance without a magnetic field and R_H is the resistance in a magnetic field). This property could have technological applications, similar to those of artificially created giant magnetorestance *spintronic* devices which utilise the spin of the electron as well as the charge.

Some of the early magnetoresistance investigations are shown in Fig. 5.4(a), which contains several plots. Plot (a) contains three plots; the first plot shows the strong dependence of the magnetisation on the strength of the applied field, the second shows the effect that these fields have on the resistivity, and the final plot shows the MR ratio as a function of temperature. Below approximately 240K there is a substantial increase in the magnetisation in the presence of a relatively small magnetic field, which is not present when the field is absent. This is indicative of a ferromagnet with domains of magnetisation pointing in different directions, and it is the removal of the domain walls which leads to a finite average magnetisation. Above 240K there is a transition to the paramagnetic phase, which still exhibits a significant spin polarisation in the presence of a magnetic field. At around the same temperature there is also a sudden increase in the resistivity, which has a strong dependence on the applied field, and as the field is increased the resistivity falls dramatically: this is the MR effect. The size of the effect is shown by the MR

ratio which peaks at around 240K. From this data it can be seen that the ferromagnetic-paramagnetic transition coincides with the metal-insulator transition suggesting that the ferromagnetism is closely related to the metallic behaviour, an idea originally suggested by Zener[106] who introduced the double exchange mechanism. The fact that the MR ratio peaks close to the ferromagnetic-paramagnetic transition suggests that both phases must be important in the MR effect, and most of the recent MR work focuses on the paramagnetic phase. Plot (c) shows the CMR effect in thin films of $La_{2/3}Ca_{1/3}MnO_3$ at $200K$ which exhibits an MR ratio of about 1500%. This can be increased to over 100000% at $77K$ using a variety of optimisation techniques, whilst in thin films of $Nd_{0.7}Sr_{0.3}MnO_\delta$ at $60K$ an MR ratio of over 1000000% has been achieved.

The simple intuitive picture which qualitatively explains the MR effect is based the double exchange mechanism, which implies that e_g electrons are much more mobile when the t_{2g} spins are aligned by a magnetic field. This idea unfortunately does not give quantitative agreement with the observed metal insulator transition temperature or the observed MR ratios. Better agreement is obtained if the interplay between the double exchange mechanism and the Jahn-Teller effects is considered, which leads to the formation of Jahn-Teller *polarons* which become self trapped[107] above the Curie temperature, T_C. This is consistent with the isotope effect[108] observed in manganites, where T_C is found to be dependent on the mass of the oxygen ions. There is also evidence of phase separation[100] in the manganites, which offers an alternative explanation for the CMR effect based on the competition between the ferromagnetic metallic phase and the charge/orbital ordered phases. In this scenario one finds hole rich ferromagnetic clusters, which are dominated by the double exchange interaction, and hole depleted antiferromagnetic clusters, which are dominated by the superexchange interaction.

7.2.3 Ferromagnetic-antiferromagnetic transition

The magnetisation in an applied field is illustrated in plot (b) of Fig. 7.9. Several levels of Ca doping are investigated in the vicinity of a ferromagnetic-antiferromagnetic transition which occurs at below 160K when $x \sim 0.5$. The inset is a plot of 1/M vs T. According to the Curie-Weiss law, if there are magnetic correlations then the magnetic susceptibility obeys $\chi \propto 1/(T - \Theta_w)$; for a ferromagnetic the Weiss temperature Θ_w equals the Curie temperature T_C and is positive, whilst for an antiferromagnet Θ is negative and is related to the Neel temperature T_N so that $\Theta_w = -T_N$. Using the relationship $\chi \propto M/H$, 1/M should be proportional to $T - \Theta_w$, which is indeed the case close to room temperature indicating the existence of ferromagnetic correlations, but there are no precursors of the sharp transition to the antiferromagnetic phase which is first order and is accompanied by a change in the lattice parameters. This demonstrates that the phase transition is

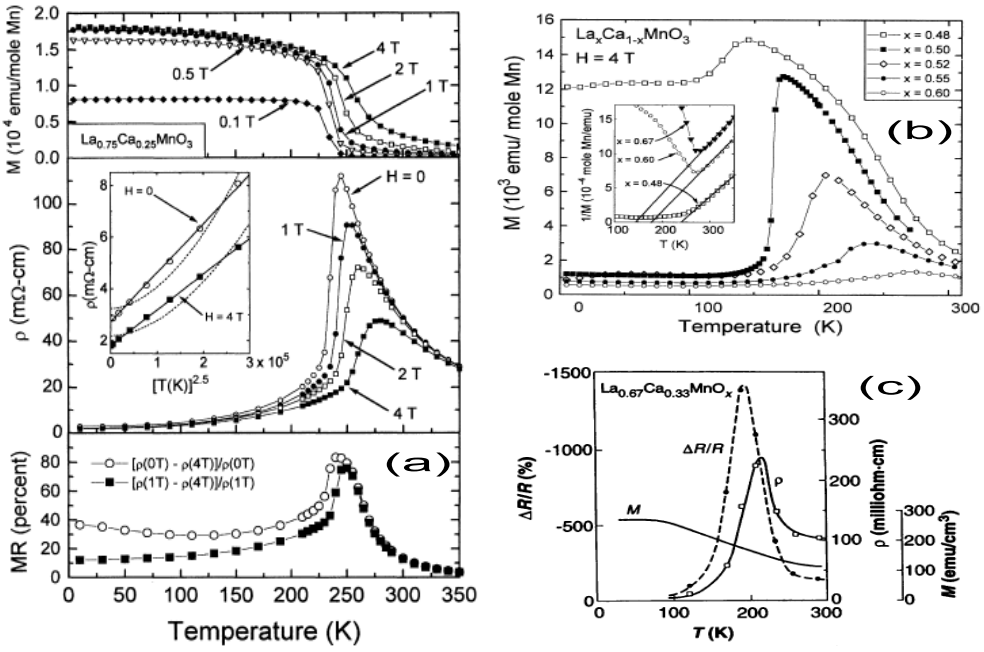

Figure 7.9: Magnetoresistance studies of LCMO. (a) Magnetisation, resistivity and magnetoresistance of $La_{0.75}Ca_0.25MnO_3$ as a function of temperature at various fields[109]. The inset shows ρ at low temperatures. (b) The magnetisation of $La_{1-x}Ca_xMnO_3$ at 4T measured on warming[109]. The inset shows $1/M$ vs T, and the straight lines indicate $\Theta_w > 0$ at each level of doping. (c) The colossal magnetoresistance of thin films of $La_{2/3}Ca_{1/3}MnO_3$ at $200K$ which reveal an MR ratio[110] of about 1500%.

simultaneously magnetic (the spin correlations change), electronic (the resistivity changes) and structural (the lattice changes). This interplay between the spin, charge and lattice degrees of freedom is responsible for the complicated phase diagram.

7.2.4 Microscopic models of the manganites

The rich assortment of the phases observed in the manganites are created by many competing interactions, involving both the electrons and the lattice, each of which becomes dominant at a different level of hole doping. The important considerations in the manganites are: the motion of the electrons via the oxygen $2p$ orbitals and the degenerate e_g orbitals, the interactions between e_g electrons and the localised t_{2g} spins, the interactions between the e_g electrons and the lattice, and the strong exchange interactions which arise from the strong local coulomb interactions between the e_g electrons. Fortunately, it is not usually necessary to model all of these interactions, particularly for the ferromagnetic metallic phase which occurs at the YBCO-LCMO interface.

7.2.5 Orbital degeneracy and pseudospin

To understand the charge and orbital order in the manganites it is useful to introduce *pseudospin* operators. This is particularly convenient for orbitally degenerate systems such as the manganites and the titanates.

The Mn^{3+} ion in $LaMnO_3$ has three electrons occupying the high spin state of the t_{2g} orbitals, whilst the remaining electron occupies one of the doubly degenerate e_g orbitals. The orbital of the e_g electron at site i may be expressed as a linear combination of the $d_{x^2-y^2}$ and $d_{3z^2-r^2}$ orbitals:

$$|\theta_i, \phi_i\rangle = \cos\left(\frac{\theta_i}{2}\right)|d_{3z^2-r^2}\rangle + e^{i\phi_i}\sin\left(\frac{\theta_i}{2}\right)|d_{x^2-y^2}\rangle, \tag{7.9}$$

where θ_i and ϕ_i are angles in the orbital space, which can be varied to change to any preferred basis. This state is an eigenstate of a pseudospin operator:

$$\boldsymbol{T}_i = \frac{1}{2}\sum_{\sigma\gamma\gamma'} d^\dagger_{i\gamma\sigma}\boldsymbol{\sigma}_{\gamma\gamma'}d_{i\gamma'\sigma}, \tag{7.10}$$

where the operator $d_{i\gamma\sigma}$ annihilates an e_g electron at site i of spin σ and orbital γ, and the $\boldsymbol{\sigma}$ are the Pauli matrices. When $\theta = 0$ and $\phi = 0$, the eigenstates of the operator T^z with eigenvalues $1/2$ and $-1/2$ are the states $|d_{3z^2-r^2}\rangle$ and $|d_{x^2-y^2}\rangle$ respectively.

The pseudospin representation allows for a systematic change of the orbital basis by varying the angles θ and ϕ. This can be a particularly useful feature when considering how the orbital degeneracy is broken by the electronic and magnetic interactions in the orbitally ordered states. When $\Phi = 0$ and $0 \leq \theta < 2\pi$ the different symmetry orbitals, which are observed in the orbitally ordered states, are obtained:

θ	$\|a\rangle$	$\|b\rangle$
0	$3\hat{z}^2 - 1$	$\hat{x}^2 - \hat{y}^2$
$\pi/3$	$\hat{z}^2 - \hat{x}^2$	$3\hat{y}^2 - 1$
$2\pi/3$	$3\hat{x}^2 - 1$	$\hat{y}^2 - \hat{z}^2$
π	$\hat{x}^2 - \hat{y}^2$	$3\hat{z}^2 - 1$
$4\pi/3$	$3\hat{y}^2 - 1$	$\hat{z}^2 - \hat{x}^2$
$5\pi/3$	$\hat{y}^2 - \hat{z}^2$	$3\hat{x}^2 - 1$

It is also possible to have more interesting choices involving complex orbitals which maintain the cubic symmetry. The particular choice of basis depends on the problem under investigation and is dictated by the symmetry. In this investigation, of the cuprate-manganite interface, it is convenient to use the $d_{x^2-y^2}$ and $d_{3z^2-r^2}$ basis, which is also relevant to the cuprate layers.

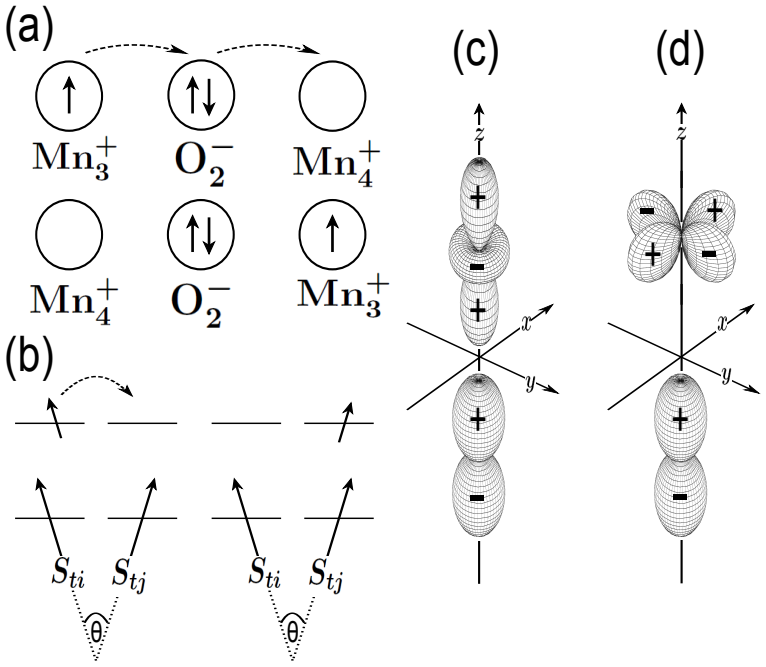

Figure 7.10: (a) In the double exchange process an electron from the oxygen hops onto an $Mn4^+$ ion, and an electron of the same spin hops from an $Mn3^+$ ion to into the vacancy on the oxygen. (b) The large Hund's rule coupling forces the e_g electron spin to be parallel to local t_{2g} spins during the double exchange process. (c) The overlap between the $d_{3z^2-r^2}$ state and and the neighbouring p_z state is equal to the Slater-Koster parameter $pd\sigma$. (d) The overlap between the $d_{x^2-y^2}$ state and and the neighbouring p_z state is zero, implying that an electron in the $d_{x^2-y^2}$ state does not hop along the z-axis.

The concept of pseudospin is particularly useful because it suggests an analogy between the superexchange interactions in orbital systems, and the superexchange interactions in spin systems. In the t-J model of the cuprates the hole motion frustrates the long range antiferromagnetic order, whilst in the analogous orbital t-J model of the manganites, the hole motion competes against local orbital order, and eventually destroys the long range orbital order.

7.2.6 Double exchange

In order to explain the ferromagnetic metallic phase occurring in the manganites Zener proposed the *double exchange* mechanism[106], which offers an intuitive explanation of the reduced resistivity observed in the ferromagnetic phase. Using LCMO as an example, the valence of the Mn ions depends on the Ca doping according to the chemical formula $La_{1-x}Ca_x(Mn^{3+}_{1-x}Mn^{4+}_x)O_3$, and the magnetic moments are almost perfectly aligned when $x = 1/3$. This corresponds to two thirds of Mn sites with one e_g electron and one third with an empty e_g band. An electron may transfer from the Mn^{3+} site to the Mn^{4+} site via the intermediate oxygen anion in a second order process proportional to t_0^2/Δ, where t_0 is the hopping matrix element between the relevant $3d_\sigma$ and O $2p_\sigma$ orbitals.

The geometrical properties of the e_g orbitals means that the hopping amplitudes between the different e_g orbitals are anisotropic. The electronic states are orthogonal Wannier states which are centred on each site, and in the nearest neighbour approximation we only count the contribution from the central site. We then need to calculate the overlap

of each e_g orbital with the neighbouring oxygen $2p$ orbitals along each of the bond directions. For simplicity we will focus on the cubic symmetric phase which is relevant to the ferromagnetic metallic phase.

The hopping amplitudes can all be expressed in terms a single *Slater-Koster*[62] parameter $pd\sigma$ which is defined as the matrix element between the manganese $d_{3z^2-r^2}$ state with the neighbouring oxygen p_z state, as illustrated in Fig. 7.10. From simple symmetry considerations it is clear that the matrix element between the $d_{x^2-y^2}$ and the oxygen p_z orbital vanishes, and so an electron in the $d_{x^2-y^2}$ does not hop along the z-axis. By analogy, the only other non-zero matrix elements involve $d_{3x^2-r^2}$ and p_x, and $d_{3y^2-r^2}$ and p_x. To determine the hopping amplitudes in the x and y directions we use the relationships

$$|d_{3x^2-r^2}\rangle = -\frac{1}{2}|d_{3z^2-r^2}\rangle + \frac{\sqrt{3}}{2}|d_{x^2-y^2}\rangle$$

$$|d_{3y^2-r^2}\rangle = -\frac{1}{2}|d_{3z^2-r^2}\rangle - \frac{\sqrt{3}}{2}|d_{x^2-y^2}\rangle. \tag{7.11}$$

We can then determine matrix elements such as

$$\langle d_{3z^2-1}|p_z\rangle = -pd\sigma. \tag{7.12}$$

The double exchange process requires two hops and is therefore proportional to $t_0 = (pd\sigma)^2/\Delta_{Mn}$, where Δ_{Mn} is the cost of transferring an electron from an oxygen site to create an additional Mn^{3+} site in the intermediate state. The matrices which represent the double exchange hopping amplitudes between the two e_g states are then

$$t_{jj'}^{\gamma\gamma'} = t_0 \begin{pmatrix} -\frac{1}{4} & \frac{\sqrt{3}}{4} \\ \frac{\sqrt{3}}{4} & -\frac{3}{4} \end{pmatrix}, \quad t_0 \begin{pmatrix} -\frac{1}{4} & -\frac{\sqrt{3}}{4} \\ -\frac{\sqrt{3}}{4} & -\frac{3}{4} \end{pmatrix}, \quad t_0 \begin{pmatrix} -1 & 0 \\ 0 & 0 \end{pmatrix}, \tag{7.13}$$

where the position of the j-th ion is $\mathbf{r}_j = \mathbf{r}_{jprime} \pm a\hat{\mathbf{x}}$, $\mathbf{r}_j = \mathbf{r}_{jprime} \pm a\hat{\mathbf{y}}$ and $\mathbf{r}_j = \mathbf{r}_{jprime} \pm a\hat{\mathbf{z}}$ respectively. The value of $pd\sigma$, and hence also t_0, obviously depends on the distance between the oxygen ion and the manganese ion. The above analysis can also be applied more generally to an arbitrary angle of the Mn-O-Mn bond, which depends on Jahn-Teller distortions and the size of the cations R and A: smaller cations lead to larger deviations from the ideal 180° Mn-O-Mn bond and to lower values of t_0.

Due to the strong Hund coupling the double exchange process is strongly suppressed if the moments of the two Mn ions are not parallel, and therefore this process favours ferromagnetism. The t_{2g} and e_g spins can occupy either an $S = 2$ or $S = 1$ state but, because J_H is much larger than the bandwidth, only the $S = 2$ state will be present and the e_g and t_{2g} spins will be therefore be parallel. The hopping amplitude will depend on the relative orientation of spins on neighbouring sites, as illustrated in Fig. 7.10. An

e_g spin has SU(2) symmetry so that two adjacent spins at sites i and j with relative orientation theta can be related through a rotation,

$$|\uparrow_i\rangle = \cos\left(\frac{\theta}{2}\right)|\uparrow_j\rangle + \sin\left(\frac{\theta}{2}\right)|\downarrow_j\rangle. \tag{7.14}$$

The energetics are controlled by the matrix elements between the initial state $|d_i\rangle|\uparrow_i\rangle$ and the final state $|d_j\rangle|\uparrow_j\rangle$:

$$\mathcal{H}_\theta = \begin{pmatrix} -J_H S & t\cos\left(\frac{\theta}{2}\right) \\ t\cos\left(\frac{\theta}{2}\right) & -J_H S \end{pmatrix}, \tag{7.15}$$

where t is the hybridisation between the two sites. The minimum energy, which is found by diagonalising the above matrix, is

$$E_0 = -J_H S - t\cos\left(\frac{\theta}{2}\right). \tag{7.16}$$

The energy is obviously minimised when $\theta = 0$, which corresponds to the spins on neighbouring sites all being parallel. Therefore, the combination of double exchange and a strong Hund's rule coupling induces ferromagnetism in the manganites.

The superexchange interaction between neighbouring t_{2g} orbitals favours antiparallel spins on neighbouring sites, and it has been shown by De Gennes[111] that the competition between double exchange and superexchange between the orbitals can cause a canting of the spins in $La_{1-x}Ca_xMnO_3$ when the carrier concentration is small.

7.2.7 Constructing a Hamiltonian

A complete model of the manganites would incorporate all of the interactions among the Mn $3d$ and O $2p$ states. Constructing an appropriate model which captures the most important interactions, but is simple enough to investigate, is a difficult task. A single Mn^{3+} ion in a $3d^4$ state has a degeneracy of 210. This degeneracy is reduced through the formation of LS multiplets, the lowest of which has a degeneracy of 25. This degeneracy is further reduced by the crystal field splitting due to the surrounding oxygen anions, resulting in the cubic symmetric e_g and t_{2g} states. The lowest energy states are then the high spin $t_{2g}^3 e_g^1$ configurations which have a degeneracy of 10. In addition, to obtain quantitatively accurate results would require the inclusion of the three O 2p states which hybridise with the Mn 3d states. To simplify matters the standard procedure is to assume that the O sites can be integrated out and replaced with effective interactions between neighbouring Mn sites. This idea is similar to that of replacing the Cu and O orbitals in the cuprates with the symmetric Zhang-Rice singlets, thereby producing an effective Hamiltonian for only the Cu sites. To further simplify the model it is also useful to

concentrate on the e_g orbitals and treat the t_{2g} orbitals as localised spins.

A very general model of the manganites includes the interactions between the itinerant e_g electrons, the nearest neighbour interactions between localised t_{2g} electrons, the interaction between e_g and t_{2g} electrons and the electronic coupling with Jahn-Teller phonons:

$$\mathcal{H} = \mathcal{H}_{e_g} + \mathcal{H}_{t_{2g}} + \mathcal{H}_{e_g - t_{2g}} + \mathcal{H}_{el-ph}, \tag{7.17}$$

where the interactions among the e_g electrons are controlled by

$$\mathcal{H}_{e_g} = \epsilon_d \sum_{i\gamma\sigma} d^\dagger_{i\gamma\sigma} d_{i\gamma\sigma} + \sum_{\langle ij\rangle\gamma\gamma'\sigma} \left(t^{\gamma\gamma'}_{ij} d^\dagger_{i\gamma\sigma} d_{j\gamma'\sigma} + h.c. \right) + \mathcal{H}_{el-el}. \tag{7.18}$$

The creation operator $d^\dagger_{i\gamma\sigma}$ is for an electron at site i, with spin σ, and orbital label γ ($d_{3z^2-r^2}$ or $d_{x^2-y^2}$ in our chosen basis). The most important electronic interactions which arise in $\mathcal{H}_{el-el}$ are U and U' which represent the intra orbital and inter orbital coulomb repulsions respectively. The other large energy J is associated with the Hund' coupling:

$$\mathcal{H}_{el-el} = U \sum_{i\gamma} n_{i\gamma\uparrow} n_{i\gamma\downarrow} + U' \sum_{i} n_{ia} n_{ib} + J \sum_{i\sigma\sigma'} d^\dagger_{i\gamma\sigma} d^\dagger_{i\bar{\gamma}\sigma'} d_{i\gamma\sigma'} d_{i\bar{\gamma}\sigma}. \tag{7.19}$$

The interactions among the t_{2g} electrons are controlled by

$$\mathcal{H}_{t_{2g}} = J_{AF} \sum_{\langle ij\rangle} \mathbf{S}_{ti} \cdot \mathbf{S}_{tj}. \tag{7.20}$$

The interaction between nearest neighbour t_{2g} electrons is proportional to J_{AF}, which is positive. The spin on each site is $S = 3/2$, so the spins are treated classically and result in an antiferromagnetic interaction. The final term controls the interactions between e_g electrons and t_{2g} electrons:

$$\mathcal{H}_{e_g - t_{2g}} = J_H \sum_{i} \mathbf{S}_{ti} \cdot \mathbf{S}_{i}. \tag{7.21}$$

The interaction parameters for $LaMNO_3$ have been estimated from photoemission spectroscopy (PES) and x-ray absorption spectroscopy (XAS) experiments to be[112] $U = 7.8$eV, $\Delta = 4.5$eV and $t = -1.8$eV for $LaMnO_3$, and $U = 7.5$eV, $\Delta = 2$eV and $t = -1.5$eV for $CaMnO_3$. In $La_{1-x}Sr_xMnO_3$ the Hund' coupling between e_g and t_{2g} spins is estimated from optical spectra[113, 114] to be $3J_H/2 \sim$ 2-3.5eV. The antiferromagnetic interactions between t_{2g} spins is estimated from mean field calculations of the Néel temperature $T_N = 120$K in $CaMnO_3$ to be $J_{AF} \sim 1$meV. The Hund coupling parameter J_H is negative and therefore leads to a ferromagnetic on-site interaction between e_g and t_{2g} spins: it is larger than the crystal field induced energy gap and the spins are therefore parallel. The large Hund coupling also enforces single occupancy of each orbital, thereby performing

the role of the coulomb repulsion U.

The interactions between the e_g electrons and the Jahn-Teller phonons is described by

$$\mathcal{H}_{el-ph} = -2g\sum_i (Q_{2i}T_i^x + Q_{3i}T_i^z) + \frac{k_{JT}}{2}\sum_i (Q_{2i}^2 + Q_{3i}^2). \tag{7.22}$$

There are two alternative approaches which have been followed in the literature to model the various orbital/charge ordered states which are observed experimentally as a function of electron doping. The first approach incorporates the Jahn-Teller phonons in a two orbital model, whilst the second approach focuses on the superexchange interactions among the e_g electrons.

7.2.8 The two orbital model

The first approach is to incorporate the two e_g orbitals, together with their interactions with the t_{2g} spins and the Jahn-Teller phonons, but excludes the Coulomb terms $\mathcal{H}_{el-el}$ with the justification that the large Hund coupling prohibits double occupancy. The resulting Hamiltonian is then

$$\mathcal{H} = \epsilon_d \sum_{i\gamma\sigma} d^\dagger_{i\gamma\sigma} d_{i\gamma\sigma} + \sum_{\langle ij\rangle\gamma\gamma'\sigma} \left(t_{ij}^{\gamma\gamma'} d^\dagger_{i\gamma\sigma} d_{j\gamma'\sigma} + h.c. \right) + J_{AF} \sum_{\langle ij\rangle} \mathbf{S}_{ti} \cdot \mathbf{S}_{tj} - J_H \sum_i \mathbf{S}_{ti} \cdot \mathbf{S}_i$$

$$-2g\sum_i (Q_{2i}T_i^x + Q_{3i}T_i^z) + \frac{k_{JT}}{2}\sum_i (Q_{2i}^2 + Q_{3i}^2). \tag{7.23}$$

This model reproduces[115] the A-type AF state for $x = 0$ and the G-type AF state for $x = 1$. It also produces C-type AF, ferromagnetic metallic and A-type ($d_{x^2-y^2}$) states for some region of the parameter space, and the charge ordered state for large Jahn-Teller coupling.

7.2.9 The orbital t-J model

An alternative approach is to incorporate the coulomb terms into the Hamiltonian, but excludes the Jahn-Teller interactions. An effective Hamiltonian can then be obtained via a canonical transformation which eliminates double occupancy on the Mn sites, thus defining an effective Hamiltonian which contains all of the superexchange interactions[116]. This is analogous to the derivation of the t-J model from the Hubbard model, and the reduction of the three band Hubbard model of the cuprates. The resulting Hamiltonian contains a large number of terms and can be most conveniently represented using pseudospin. The Hamiltonian takes the form

$$\mathcal{H}_{e_g} = \mathcal{H}_t + \mathcal{H}_J. \tag{7.24}$$

The first term simply hops the electrons in the singly occupied subspace:

$$\mathcal{H}_t = \sum_{\langle ij\rangle\sigma\gamma\gamma'} t_{ij}^{\gamma\gamma'} \left(\tilde{d}^{\dagger}_{i\gamma\sigma}\tilde{d}_{j\gamma'\sigma} + h.c.\right), \tag{7.25}$$

with

$$\tilde{d}_{i\gamma\sigma} = d_{i\gamma\sigma}(1 - n_{i\gamma\sigma})(1 - n_{i\gamma\overline{\sigma}})(1 - n_{i\overline{\gamma}\overline{\sigma}}) \tag{7.26}$$

The second term can be written

$$\begin{aligned}\mathcal{H}_J = -2J_1 \sum_{\langle ij\rangle} \left(\frac{3}{4}n_i n_j + \mathbf{S}_i \cdot \mathbf{S}_j\right)\left(\frac{1}{4}n_i n_j - \tau_i^l \tau_j^l\right) \\ -2J_2 \sum_{\langle ij\rangle} \left(\frac{1}{4}n_i n_j - \mathbf{S}_i \cdot \mathbf{S}_j\right)\left(\frac{3}{4}n_i n_j + \tau_i^l \tau_j^l + \tau_i^l + \tau_j^l\right),\end{aligned} \tag{7.27}$$

with

$$\tau_i^l = \cos\left(\frac{2\pi n_l}{3}\right) T_i^z - \sin\left(\frac{2\pi n_l}{3}\right) T_i^x. \tag{7.28}$$

with $(n_x, n_y, n_z) = (1, 2, 3)$. The effects of the t_{2g} spins can be taken into account in a mean field sense by redefining the energies. The J_1 term describes the interaction involving two parallel spins occupying the same site in the intermediate state, whilst the J_2 term describes the interaction with two antiparallel spins in the intermediate state. The orbital t-J model produces many of the observed magnetic and orbital structures[116], with the exception of the charge ordered CE state.

7.2.10 Superexchange

The superexchange interaction in the orbitally degenerate manganites is complicated by the pseudospin interactions, which leads to a rich variety of ordered states . The superechange tends to be dominated by the interactions among the e_g states. This is because the O $2p_\sigma$ orbitals, which point directly towards the Mn ions, have vanishing matrix elements with the t_{2g} orbitals due to their symmetry properties. The only contribution comes the O $2p_\pi$ orbitals which point away from the Mn ions and consequentially have a very small matrix element. This results in a very weak antiferromagnetic interaction between neighbouring t_{2g} electrons which is only significant for the G-type antiferromagnetic phase close to $x = 1$, when there are no e_g electrons. The other ordered states

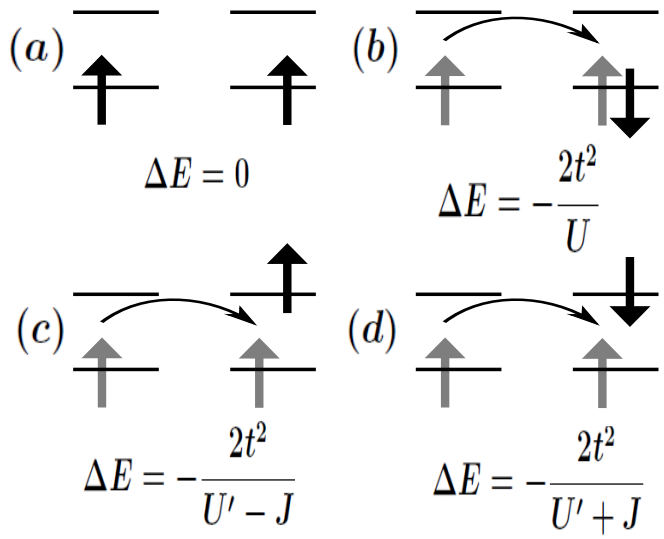

Figure 7.11: The exchange interactions between neighbouring Mn sites, assuming diagonal hopping ($t_{ij}^{\gamma\gamma'} = \delta_{\gamma\gamma'} t_0$): (a) If both spins are aligned then coulomb repulsion prevents hopping and leads to no energy gain. (b) This antiferromagnetic spin configuration pays the coulomb repulsion in the intermediate state and leads to a moderate energy gain. (c) The ferromagnetic spin configuration with staggered orbital order benefits from the Hund coupling and obtains the greatest energy gain. (d) This antiferromagnetic spin configuration pays the Hund coupling in the intermediate state and leads to a moderate energy gain.

are controlled by the complicated spin/pseudospin interactions among the e_g electrons, which are described by the orbital t-J model. The largest energy gain J_1 arises when two electrons briefly occupy the same site in the intermediate state, with parallel spins and therefore different orbitals; this interaction clearly favours staggered orbital order and parallel spins. When this term is absent the J_2 term favours uniform orbital order and antiferromagnetic spins.

Both the two orbital model, and the orbital t-J model produce orbitally ordered states which are similar to those observed experimentally, and it would therefore appear that the Jahn-Teller coupling and the superexchange interactions are cooperative mechanisms which both favour orbitally ordered ground states.

7.2.11 Ferromagnetic metallic phase

In the region $0.125 < x < 0.5$ $La_{1-x}Ca_xMnO_3$ is in the ferromagnetic metallic state. The nature of this state was originally explained by Zener using the double exchange mechanism[106]. As a consequence of the large Hund' coupling combining with the double exchange mechanism, as illustrated in Fig. 7.11, a gap is opened between the bands of opposite spin polarisation. The charge carriers close to the Fermi energy are therefore almost fully spin polarised, resulting in a *half metal* (which conducts spins of only one spin polarisation). When the magnetic moments of the t_{2g} ions are perfectly aligned, such as in a high magnetic field, the e_g electrons are fully spin polarised due to the large Hund' coupling and the spin degree of freedom is eliminated.

The absence of any Jahn-Teller distortion indicates that there is no clear orbital ordering, and hence both orbitals can be considered to be active. In this regime the long

range orbital order is destroyed by the motion of charge carriers and it is assumed that an orbitally disordered state, possibly an orbital liquid[117], is formed. This phase may arise due to geometrical frustration, or due to large quantum fluctuations which prevent the formation of the orbitally ordered states observed in the rest of the phase diagram. A relatively large concentration of charge carriers is required for the system to become metallic due to the tendency for holes to become localised in orbital polarons. The simplest model one can construct for the ferromagnetic metallic phase captures the motion of spin polarised charge carriers, which hop via the double exchange mechanism:

$$\mathcal{H} = \sum_{\langle jj' \rangle \gamma\gamma'} \left(t_{jj'}^{\gamma\gamma'} d_{j\gamma}^{\dagger} d_{j'\gamma'} + h.c. \right) = \sum_{\mathbf{k}\gamma\gamma'} \epsilon_{\mathbf{k}}^{\gamma\gamma'} d_{\mathbf{k}\gamma}^{\dagger} d_{\mathbf{k}\gamma'}, \tag{7.29}$$

where $\hat{\epsilon}_{\mathbf{k}}$ is a 2×2 matrix in the e_g orbital subspace:

$$\hat{\epsilon}_{\mathbf{k}} = \frac{t_0}{2} \begin{pmatrix} -\left(C_x + C_y + 4C_z\right) & \sqrt{3}\left(C_x - C_y\right) \\ \sqrt{3}\left(C_x - C_y\right) & -3\left(C_x + C_y\right) \end{pmatrix}, \tag{7.30}$$

where $C_\alpha = \cos(k_\alpha)$. The hopping matrices are

$$t_{ij}^{\gamma\gamma'} = t_0 \begin{pmatrix} -\frac{1}{4} & \frac{\sqrt{3}}{4} \\ \frac{\sqrt{3}}{4} & -\frac{3}{4} \end{pmatrix}, \quad t_0 \begin{pmatrix} -\frac{1}{4} & -\frac{\sqrt{3}}{4} \\ -\frac{\sqrt{3}}{4} & -\frac{3}{4} \end{pmatrix}, \quad t_0 \begin{pmatrix} -1 & 0 \\ 0 & 0 \end{pmatrix}. \tag{7.31}$$

where the position of the j-th ion is $\mathbf{r}_j = \mathbf{r}_i \pm a\hat{\mathbf{x}}$, $\mathbf{r}_j = \mathbf{r}_i \pm a\hat{\mathbf{y}}$ and $\mathbf{r}_j = \mathbf{r}_i \pm a\hat{\mathbf{z}}$ respectively. The dispersion is found by diagonalising $\hat{\epsilon}_{\mathbf{k}}$:

$$E_{\mathbf{k}}^{\pm} = -t_0 \left(C_x + C_y + C_z \pm \sqrt{C_x^2 + C_y^2 + C_z^2 - C_x C_y - C_x C_z - C_y C_z} \right). \tag{7.32}$$

The large Hund coupling enforces single occupancy of each orbital, thereby performing the role of the coulomb repulsion U, which can therefore be safely ignored. The inter orbital coulomb repulsion parameter U' is too large to be ignored and will have an effect on the simple double exchange model mentioned above. A possible resolution to this problem can be found if we consider the ground state to be a *Gutzwiller projection* of the non-interacting ground state, which involves projecting out the states with two electrons in the e_g orbitals. The Gutzwiller projection operator is defined $\mathcal{P}_{Gutz} = \prod_j (1 - \eta n_j n_j)$, and the Gutzwiller projected state is obtained by applying the projection operator to the Fermi sea, $|FS\rangle$, obtained for the ground state of the non-interacting model. Therefore

$$|\Psi\rangle = \prod_j (1 - \eta n_j n_j) |FS\rangle = \mathcal{P}_{Gutz} |FS\rangle, \tag{7.33}$$

where η is a variational parameter chosen to minimise the expectation value for the energy:

$$E(\Psi) = \frac{\langle\Psi|\mathcal{H}|\Psi\rangle}{\langle\Psi|\Psi\rangle}. \tag{7.34}$$

Physically, the Gutzwiller projection restricts the motion of the electrons to avoid double occupancy of any particular atom, so that most of the hopping energy can be gained without incurring the large energy penalty U'. The hybridisation matrix element t is renormalised by an amount which is dependent on the number of electrons[5]. For $x = 1/3$ each manganese atom has 2/3 electrons on average and consequentially the electronic motion would be substantially reduced by the Gutzwiller projection, leading to an increase in the effective electronic mass and a significant renormalisation of the hopping parameter t.

In the next chapter we examine the cuprate-manganite interface, with the manganite $La_{2/3}Ca_{1/3}MnO_3$ in the ferromagnetic metallic phase. We therefore make use of the double exchange model, and use it to determine the electronic structure on the manganite side of the interface.

7.3 The YBCO-LCMO interface

Atomically sharp interfaces between LCMO and YBCO can be created using techniques such as pulsed laser deposition and high pressure oxygen sputtering. The interfaces are formed in superlattices which comprise of alternating YBCO-LCMO layers of varying thicknesses. The properties of very thin layers vary drastically from the properties of the bulk, with suppression of the Curie temperature in LCMO, and suppression of the superconductivity transition temperature T_C in YBCO.

The quality of these structures can be investigated using a variety of experimental probes. The atomic positions can be visualised with scanning transmission electron microscopy (STEM) in a Z-contrast image, whereby the intensity of the signal is related to the atomic number of the target atom and is proportional to Z^2. Z-contrast images at the YBCO-LCMO interface[118] are illustrated in Fig. 7.12(a). The brightest points on the YBCO side of the interface therefore correspond to Ba atoms, followed by Y atoms, and on the LCMO side, the La atoms show up the brightest. From these images two different types of interface structure can be observed. By far the most common structure is illustrated in Fig. 7.12(b), where the interfacial layers are BaO-MnO_2-LaO and the last CuO layer is not present on the YBCO. Less common is the slightly irregular structure where the last CuO layer is present and the interfacial layers are BaO-CuO-LaO-MnO_2.

[5]At half filling t is renormalised by a factor $2Zd(1-2d)$, where Z is the number of nearest neighbours and d is the fraction of sites that are doubly occupied. This is, essentially, the probability that an electron is able to hop from a doubly occupied site to a neighbouring singly occupied site.

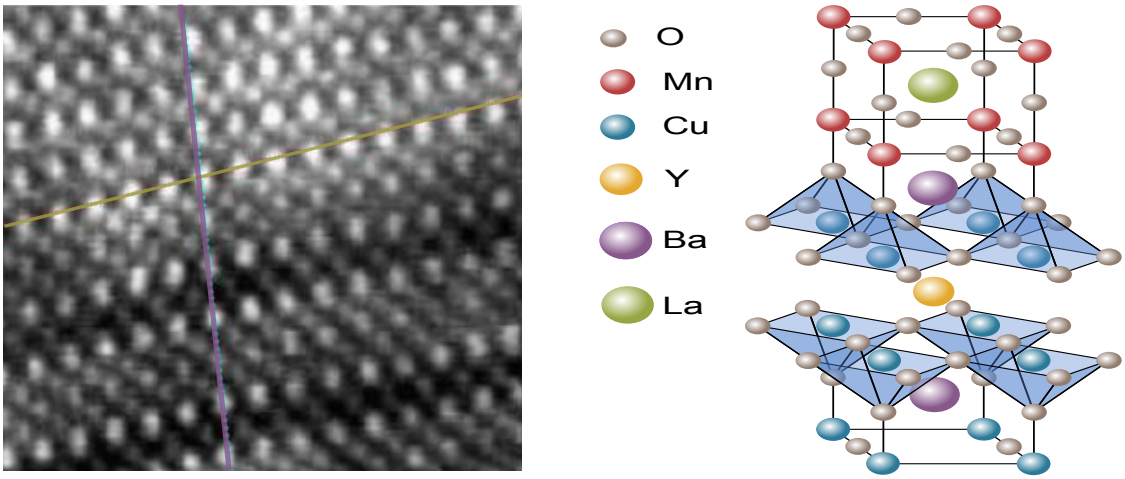

(a) STEM Z-contrast image of an YBCO-LCMO interface[118]. The dark rows correspond to the CuO chains, and the first LaO layer and a column of Ba/Y are highlighted for clarity.

(b) The most common crystal structure found at the interface, with the interfacial layers BaO-MnO_2-LaO

Figure 7.12: Structural characterisation of an YBCO-LCMO interface.

There are three main concerns when creating an interface: the effects of lattice strain due to the different lattice parameters of the two materials, the magnitude of the surface roughness which breaks the translational symmetry, and interdiffusion of the different chemical elements which leads to chemical disorder. The effects of lattice strain are small due to the well matched lattice parameters of LCMO, with a cubic lattice parameter of 3.86 Å, and YBCO with lattice parameters $a = 3.82$ Åand $b = 3.89$ Å. The surface roughness is also relatively small as illustrated in the Z-contrast images. A useful method for analysing the extent of interdiffusion is to perform high spatial resolution electron energy loss spectroscopy (EELS) in conjunction with scanning transmission electron microscopy (STEM) measurements[118]. Using this method it is possible to characterise the elemental constituents of each atomic layer. The proportion of each different element as a function of distance from the interface is illustrated in Fig. 7.13(b), and it can be seen that the interface is indeed very sharp and the elemental composition reaches the bulk composition within a couple of atomic layers.

7.4 Experimental investigations of the YBCO-LCMO interface

There are various experimental techniques which have been employed to probe the interface between cuprates and manganites, and we will focus on two which have been

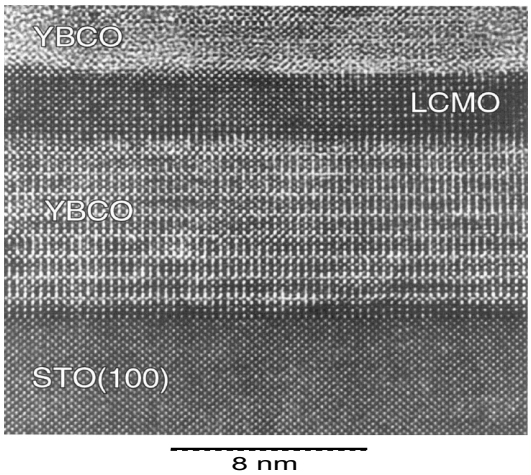

(a) STEM Z-contrast image of an YBCO-LCMO superlattice[119]

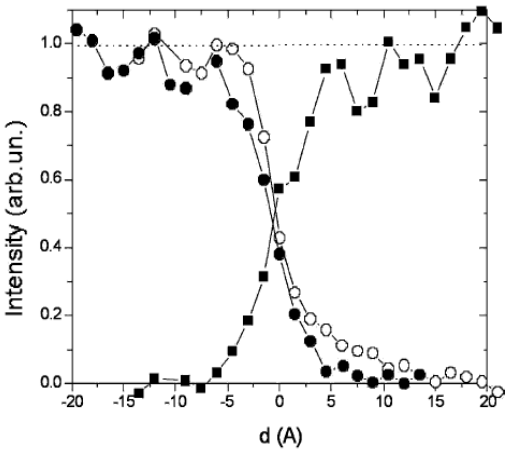

(b) EELS performed at an YBCO-LCMO interface[118]. The integrated intensity, after normalisation, for La (open circles), Ba (solid squares) and Mn (solid circles) as a function of distance from the interface.

Figure 7.13: STEM and EELS measurements at an YBCO-LCMO interface.

particularly important to our investigation of the electronic structure at the interface between $La_{2/3}Ca_{1/3}MnO_3$ (LCMO) and $YBa_2Cu_3O_7$ (YBCO). The first technique is x-ray absorption spectroscopy (XAS) which is a particulary useful probe of the occupation of different orbitals in the $3d$ bands of both materials. Using this technique it is believed that a change in the electronic valence states has been observed in the interfacial YBCO layers. The second technique is polarised neutron reflectometry which is sensitive to periodic magnetic profiles and has been applied to YBCO-LCMO superlattices. The reflectivity curves exhibit a structurally forbidden Bragg peak, and the reconstructed magnetic profiles are suggestive of a magnetic moment in the interfacial YBCO layers. A brief introduction to these techniques will be given, followed by an explanation of what has been learnt from their application to the YBCO-LCMO interface.

7.4.1 X-ray absorption spectroscopy at the YBCO-LCMO interface

We will summarise the results obtained, by Chakhalian et al, for x-ray absorption spectroscopy (XAS) and x-ray linear dichroism (XLD) measurements at an YBCO-LCMO interface[53]. The application of XAS to probe orbital occupancies is discussed in appendix E. The experiments were performed on epitaxial trilayers and superlattices of the optimally doped high temperature superconductor $YBa_2Cu_3O_7$, combined with the ferromagnetic $La_{1-x}Ca_xMnO_3$ at a doping level $x = 1/3$. To separate the interfacial elec-

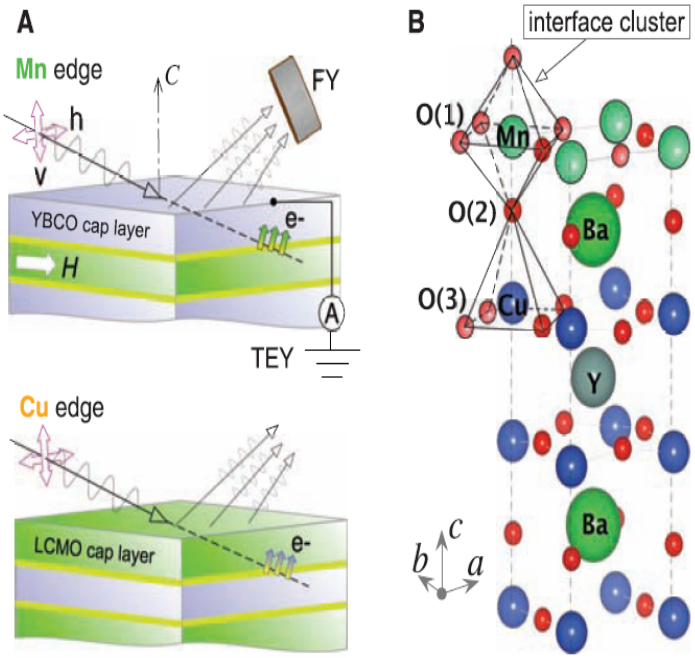

Figure 7.14: From [53].(A)Schematic of the experimental setup used in to obtain the XAS and XLD data in TEY and FY modes. Data sensitive to interfacial Cu (Mn) atoms were taken in TEY mode with photon energies near the Cu (Mn) edge, on samples with LCMO (YBCO) capping layers. C indicates the axis of the film, H is the applied field; h and v denote the linear polarisation state of the incident x-ray. (B)Atomic positions near the YBCO-LCMO inerface, and the $MnCuO_{10}$ cluster used for exact diagonalisation calculations[53].

tronic structure from surface and bulk contributions, the experiments were performed on heterostructures with different capping layers, making use of the shallow probing depth of XAS and XLD in total electron yield (TEY) mode to ensure that only layers directly beneath the capping layers contributed to the signal (Fig. 7.14). The photon energies were tuned to the appropriate absorption edge, so that the capping layers would not effect the signal apart from an overall attenuation factor.

Measurements were performed at the Cu L_3 edge in bulk-sensitive fluorescence yield (FY) mode and interface-sensitive TEY mode; the absorption spectra for YBCO are illustrated in Fig. 7.15(a), and the absorption spectra for LCMO are illustrated in Fig. 7.15(b). The bulk-sensitive absorption spectra show agreement with previous XAS data at the Cu L_3 edge of optimally doped YBCO. The main absorption peak at around 931eV is associated with the intra-ionic transition $2p^6 3d^9 \rightarrow 2p^5 3d^{10}$. The shoulder on the right hand side of main peak is attributed to the inter-ionic transition $2p^6 3d^9 L \rightarrow 2p^5 3d^{10} L$, where L denotes a hole on the oxygen ligand[6]. This is a signature of the *Zhang-Rice singlet*, a bound state consisting of a localised hole on a copper ion, hybridised with holes on the neighbouring oxygen ions: the higher energy of this transition is due to the hybridisation energy lost from destroying the Zhang-Rice singlet with the excited electron. The high absorption of x-rays polarised in the plane parallel to the CuO_2 sheets also demonstrates that the majority of the holes occupy the $d_{x^2-y^2}$ orbital. This is a generic feature of the

[6]The energy of this transition is higher because the Cu-O hybridisation energy of the Zhang-Rice singlet state is relinquished in the final state: this hybridisation energy corresponds, approximately, to the gap between the main peak and the right hand shoulder.

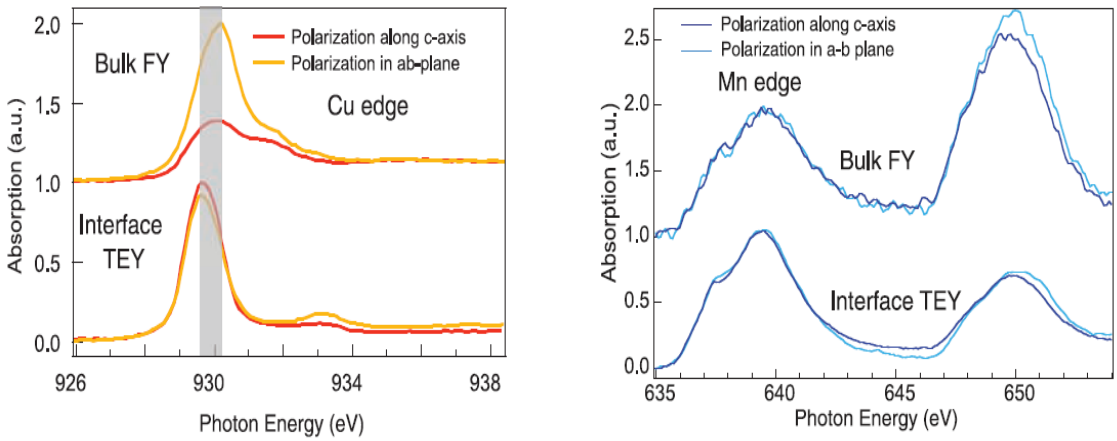

(a) XAS from YBCO

(b) XAS from LCMO

Figure 7.15: From [53]: XAS spectra from either side of the YBCO-LCMO interface.

cuprate superconductors.

The interface-sensitive data show a shift of the main absorption peak with respect to the bulk by ~ 0.4eV, and the disappearance of the high-energy shoulder. The shift in the absorption peak indicates a change in the Cu valence state, which is caused by a transfer of charge across the interface, forming a charged double layer. This is characteristic for heterostructures of materials with different work functions. A comparison with reference materials containing Cu^{+} and Cu^{2+} yields a rough estimate for this charge transfer of $0.2e$ per copper ion. Since numerous XAS measurements of YBCO and other high temperature superconductors demonstrate that the peak position is independent of doping, the shift cannot be attributed to a change in the hole density alone and indicates a significant change in the electronic states at the interface.

The absorption is almost equal for polarisation parallel and perpendicular to the CuO_2 layers. This is an indication that the number of holes occupying $d_{3z^2-r^2}$ and $d_{x^2-y^2}$ states is comparable at the interface, whereas in the bulk the holes are predominantly found in the $d_{x^2-y^2}$ state. This can be interpreted as an 'orbital reconstruction'. Measurements were repeated over a range of temperatures from 30K to 300K, and in the over-doped regime by Ca substitution, and the peak position and polarisation dependence were found to be unaffected. The charge transfer and 'orbital reconstruction' can therefore be considered as robust characteristics of the YBCO-LCMO interface.

The XAS spectra near the Mn L_2 and L_3 edges on the LCMO side of the interface are also shown in Fig. 7.15(b). The spectra are much broader than those taken near the Cu L_3 edge, because the five Mn d orbitals are all partially occupied and result in a complicated multiplet splitting of the absorption peak. The peak intensity is independent

of polarisation dependence, and is interpreted as evidence of roughly equal numbers of holes in the $d_{3z^2-r^2}$ and $d_{x^2-y^2}$ states in bulk metallic LCMO. A change in the valence state is also expected on the LCMO side of the interface to compensate for the charge transfer to the YBCO side, but due to the broad spectra, a corresponding shift in the absorption peak is difficult to determine.

7.4.2 Orbital reconstruction

One interpretation of these results involves an orbital reconstruction of the electronic states at the interface. The calculation is performed on the $MnCuO_{10}$ cluster illustrated in Fig. 7.14 using the full set of Cu d orbitals and interaction parameters from the literature. The Mn ion is represented by a single $d_{3z^2-r^2}$ orbital with a classical Hund's rule coupling to the t_{2g} spins. To simulate the difference in LCMO and YBCO work functions the on-site energy of the Mn hole was tuned, and the number of holes on the copper sites is plotted against the energy of the Mn site in Fig. 7.16. For a large on-site energy of the Mn hole, the hole resides mainly on the Cu site, and as the on-site energy is reduced the hole moves to the Mn site. The orbital reconstruction is viewed as being *static*, and hence the hybridisation between the Cu site and the Mn site is of the order t_0^2, where t_0 is related to the Slater-Koster intergrals[62] such that $t_0 = (pd\sigma)^2$. This causes a very sharp transition between the two configurations, and the intermediate state where the hole is delocalised between the Cu site and the Mn site only occurs at a very specific energy.

In the next chapter we offer an explanation based on the double exchange mechanism. The resulting orbital reconstruction is *dynamic* and is a consequence of the metallicity in the manganite 'spilling' into the cuprate. The double exchange between the cuprate and the manganite necessarily utilises the $d_{3z^2-r^2}$ states in the cuprate to enhance the mobility of the electrons across the interface. The occupancy of the two orbitals is determined by tuning the chemical potential in the manganite. Because the energy scale of this process is of the order of t_0, we find a robust orbital reconstruction at the interface, with partial occupation of the $d_{3z^2-r^2}$ states in the cuprate.

7.4.3 Polarised neutron reflectometry at the YBCO-LCMO interface

We will now summarise the results obtained, by Stahn et al, for polarised neutron reflectometry (PNR) measurements on superlattices composed of alternating layers of YBCO and LCMO[120]. The technique, and its application to the YBCO-LCMO interface, is introduced in the appendix. PNR is used to probe the magnetic potential V_m and the nu-

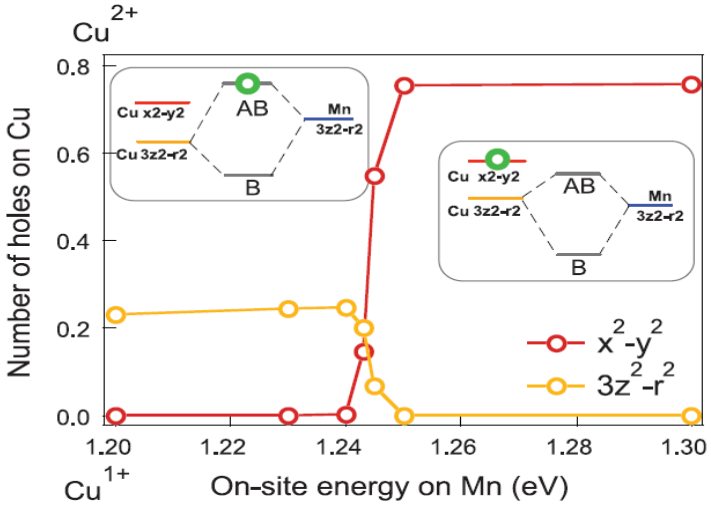

Figure 7.16: Calculation performed on a $CuMnO_{10}$ cluster by J. Chalhalian et al[53]. The total number of holes, as measured from the full $3d^{10}$ shell, calculated as a function of the on-site Mn hole energy. The insets show the orbital level scheme at the interface, including bonding (B) and antibonding (AB) 'molecular orbitals' formed by hybridised Cu and Mn $d_{3\hat{z}^2-1}$ orbitals.

clear potential V_n in the direction normal to the surface to deduce possible depth profiles.

Reflection occurs at the interfaces of a multilayer, so Bragg's law for a one dimensional crystal can be applied to obtain the conditions for constructive and destructive interference. Because the magnetic potential is expected to be spatially uniform and confined to the LCMO layers, an extinction rule disallows all even order Bragg peaks.

The experiments were performed on superlattices of [LCMO(98 Å)/YBCO(98 Å)] and [LCMO(160 Å)/YBCO(160 Å)]. Resistivity and superconducting quantum interference device (SQUID) magnetisation measurements revealed a ferromagnetic transition temperature $T_{mag} \approx 165K$ and a superconducting transition temperature $T_{SC} \approx 75K$, both of which are substantially reduced from their bulk values of $T_{mag}^{LCMO} \approx 270K$ and $T_{SC}^{YBCO} \approx 93K$ respectively.

The results for the specular reflectivity are shown in Fig. 7.17(a), together with the integrated intensities for the first two Bragg peaks which are shown in Fig. 7.17(b). Above T_{mag} the second Bragg peak is absent, in accordance with the extinction rule, but as T is reduced below T_{mag} the second, structurally forbidden, Bragg peak appears. This peak is associated with the magnetic interactions at the interface caused by the onset of the ferromagnetic phase in the LCMO layers, and indicates that the magnetic profile is no longer confined to the LCMO layers, but has extended into the YBCO layers. Below T_{SC} weight is transferred from the specular to the off-specular reflectivity, which is an indication of SC induced in-plane magnetic roughness.

The polarised specular reflectivities are also measured and the results are shown in Fig. 7.17(c), together with the simulated results in Fig. 7.17(d). To determine the magnetic profile, the unit cell is broken down into 96 sublayers, and the iterative scheme is used to reproduce the observed reflectivities at the surface of the superlattice. Of the many magnetic profiles implemented, only two reproduced the observed spectra. The first

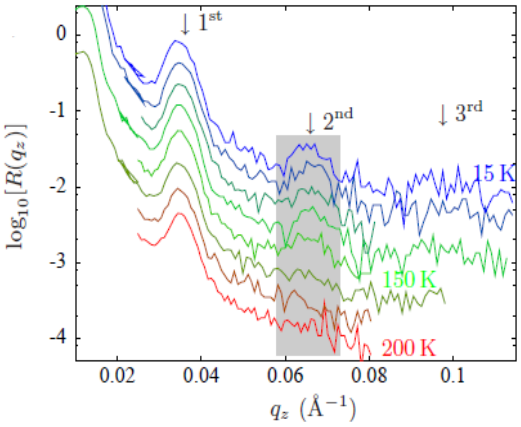

(a) Unpolarised specular refectivity from an YBCO-LCMO superlattice in an external field $H = 100Oe$ (field cooled).

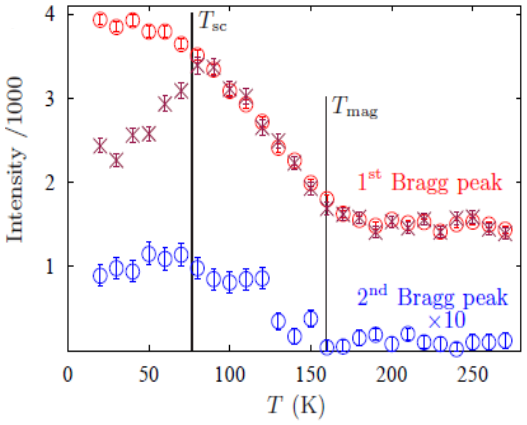

(b) T dependence of the first (red) and second (blue) Bragg-peak intensities, integrated over $q_x(\bigcirc)$ and at $q_x = 0(\times$, scaled by 6).

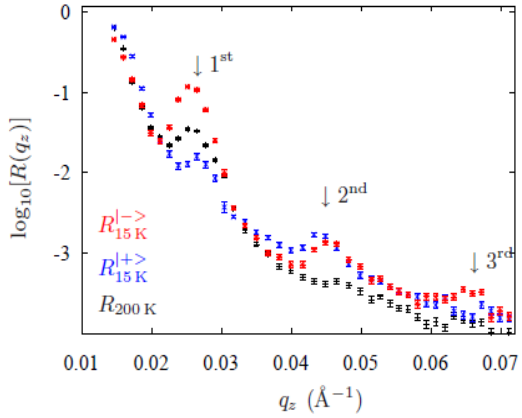

(c) The measured polarised specular reflectivity at 15K and 200K in an external field $H = 100Oe$ (field cooled)

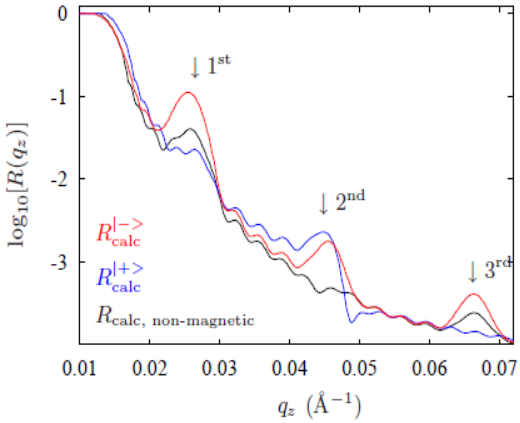

(d) The simulated specular reflectivity

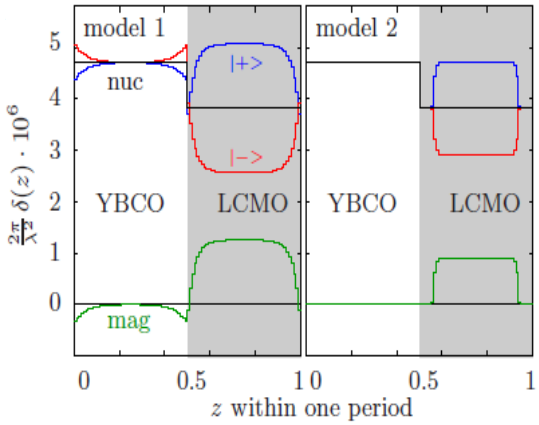

(e) The two magnetic profiles which are consistent with the measured reflectivity. Model 1 exhibits antiferromagnetic correlations across the interface, whilst model 2 exhibits a magnetic dead layer.

Figure 7.17: from [120]Polarised neutron reflectometry (from [120]) performed on an YBCO-LCMO superlattice.

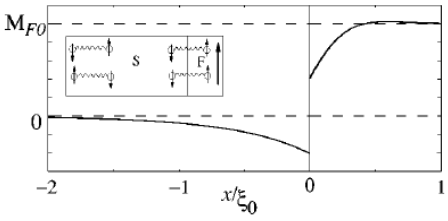

Figure 7.18: The inverse proximity effect at a superconductor-ferromagnet interface, obtained from [123]. The magnetic moment is plotted against the distance, in units of the correlation length ξ, from the interface.

profile displays antiferromagnetic correlations across the interface, with a sizeable moment on the YBCO side of the interface. The second possibility is a magnetic 'dead layer' on the LCMO side of the interface, where there is no magnetic moment in the LCMO layers close to the interface. These magnetic profiles are illustrated in Fig. 7.17(e). Several physically meaningful profiles are excluded, such as a conventional magnetic proximity effect[121] where the magnetisation decays exponentially into the SC layer.

The second profile consisting of a magnetic 'dead layer', a feature which has previously been observed in interfaces with manganites, is not easy to justify in this case. The cause of the magnetic dead layer is usually attributed to chemical interdiffusion[122] but, as the EELS measurements at the interface demonstrate, the interfaces are atomically sharp and the extent of the interdiffusion is therefore small and is limited to the first few atomic layers.

The first profile which corresponds to antiferromagnetic correlations across the interface is the one we pursue in this investigation. The presence of antiferromagnetic correlations at a superconductor-ferromagnet interface is not unreasonable and is often explained by the *inverse proximity effect*[123], which creates the magnetic profile illustrated in Fig. 7.18. The antiferromagnetic correlations arise from the formation of Cooper pairs which involve one electron in the superconductor and one electron from the ferromagnet. The length scale of the Cooper pairs, and hence of the antiferromagnetic correlations, is about one coherence length.

However, the inverse proximity effect can be ruled out at the YBCO-LCMO interface, due to the very short pair coherence length perpendicular to the interface, which for YBCO is $\xi_c \approx 0.24$nm[124] and is less than the Cu-Mn separation. In the next Chapter we propose an explanation for the antiferromagnetic correlations, which is based on the idea that the metallicity of the manganite spreads into the cuprate layer at the interface and spin polarises the holes.

Chapter 8

Model of a cuprate-manganite interface

After examining the experimental evidence for an orbital reconstruction[53] and antiferromagnetic correlations[120] at the interface, in this chapter we propose an explanation. The central idea is that the spin polarised metallicity of the manganite 'spills' out into the interfacial cuprate layer and polarises the spin of the holes. Through this process the electrons are able to maximise their kinetic energy by delocalising, both into the bulk manganite, and into the interfacial cuprate layer.

The microscopic details of this theory are worked out first, and justified on the basis that the difference in chemical potentials between the two materials leads to a flow of charge across the interface from the manganite into the cuprate. It is then argued that the hybridisation energy is sufficient to overcome the crystal field splitting between the two styles of orbital in the cuprates, which therefore leads to an orbitally disordered state in the interfacial cuprate layer.

To put this theory on a more solid foundation we introduce a simple model which captures the electronic structure of the bulk manganite with a single cuprate capping layer. We employ impurity theory to deal with the broken spatial symmetry caused by the presence of the interface, and to implement the crystal field splitting and charge transfer in the cuprate layer. The impurity method is also useful for determining the occupation of the two styles of orbital, and qualitative agreement with the XLD experiments is obtained.

In addition, the solution to our model reveals some unexpected bound states in the interfacial layers. These states reside in the interfacial cuprate and manganite layers, but become degenerate with the bulk states from the manganite and decay into the bulk. As a consequence, the coherent peaks in the spectral function are seen to 'disappear' at the Fermi energy. Finally, it is proposed that this last feature may be observed in ARPES performed on cuprate-manganite interfaces.

8.1 Charge transfer across the interface

To predict the anticipated behaviour we first need to characterise the two materials, and then analyse the likely changes at the interface. This is slightly complicated by the fact that it is easier to understand the cuprate using holes and the manganite using particles (electrons).

The cuprate involves a doped parent compound: this parent involves an active Cu^{2+} ion which is one hole away from the passive closed shell Cu^{+} configuration, with the hole residing in the e_g orbitals. The crystal field energy of having four close negative oxygen neighbours in the x-y plane and only one more distant oxygen neighbour in the z direction stabilises the hole in the $d_{x^2-y^2}$ orbital with an energy saving of about half an electron-volt (eV), which can be inferred from polarised XAS measurements[125]. The interesting observation of the XAS experiments is that this crystal field appears to be overcome at the interface, where roughly equal amounts of both $d_{x^2-y^2}$ and $d_{3z^2-r^2}$ are observed. Where does this half an eV come from? $YBa_2Cu_3O_7$ is doped with holes, stoichiometrically 1/3 of a hole per copper atom. Most of these holes are thought to reside on oxygen atoms, forming Zhang-Rice singlets in the important CuO_2 planes.

The manganites also have a parent compound: This compound, $LaMnO_3$, has an active Mn^{3+} ion. In terms of electrons, there are four in the d-shell which, due to the strong Hund's coupling, have parallel spins. Three fill the crystal field preferred t_{2g} shell and the fourth is in the doubly degenerate e_g shell, analogous to the cuprates. It is the lifting of the orbital degeneracy and the choice of magnetism which are the relevant physical issues. In the parent compound the degeneracy is lifted by a Jahn-Teller distortion, with a subsequent A-type antiferromagnetic order. In the doped compound the double exchange phenomena is dominant, and the experimentally relevant material is a saturated ferromagnet at low temperatures, with all spins aligned. About 1/3 of the e_g electrons have been removed and the motion of the remaining electrons, via double-exchange, stabilises the ferromagnetism. It is the electronic motion which provides an energy scale of one eV or more.

Initial considerations of the interface involve trying to establish how to mesh the two pictures of the different materials energetically: At the most trivial level, we can compare the work functions. As one might naively guess from the chemistry, there is a flow of electrons from the manganite into the cuprate until an electric field builds up to compensate the difference in isolated chemical potentials.

There is good evidence that in the spatially accessible region of the cuprates all the Zhang-Rice singlets have disappeared and naively one might consider the cuprates to have reverted to their parent compound. However, things might not be so simple: The energy gap in the cuprates is less than one eV and so the difference in chemical potential

might also overcome this gap and further dope the cuprates with electrons. Such an eventuality would convert some of the Cu^{2+} into passive Cu^{+}, which would be analogous to the electron doped systems, $Nd_{2-x}Ce_xCuO_4$. An energy shift is indeed observed in the interfacial XAS spectra, and this could be explained quite naturally using this idea and its consequences.

To analyse the interface system more carefully we can resort to the atomic limit to quantify the relevant interactions and their energy scales. If we accept the irrelevance of the Zhang-Rice singlets, then there are two important electronic energies: for the cuprates the cost of converting Cu^{2+} into Cu^{+} with an electron is one energy, denoted ECu, and for the manganites the cost of converting Mn^{4+} into Mn^{3+} with an electron is the other, denoted E_{Mn}. Ignoring all chemical bonding we would start out with the chemical potential at E_{Mn} and if $\Delta\mu = E_{Mn} - E_{Cu} > 0$ then we would expect charge flow at the interface and the cuprates would metallise until a charge balance is achieved. This flow of charge would also provide an electric field which reduces E_{Mn} and raises E_{Cu}, making the subsequent doping less likely.

The largest chemical bonding phenomenon to incorporate into the atomic picture is *double-exchange*: originating in the manganites, this term refers to the motion of an e_g orbital across an intermediate oxygen atom, exchanging the relative positions of Mn^{3+} and Mn^{4+} ions. The intermediate state finds both ions in an Mn^{3+} configuration and the intrinsic energy scale is t_{Mn}^2/Δ_{Mn} where t_{Mn} is the hopping matrix element between oxygen p-states and Manganese e_g-d-states, and Δ_{Mn} is the energy cost of transferring an electron from the oxygen to the manganese. This interaction is strong, being a sizeable fraction of an eV, and metallises the manganites, driving the system into a saturated ferromagnet. Interestingly, there is an analogous interaction in the electron doped cuprates. A Cu^{2+} and Cu^{+} ion can also exchange with a transfer of an electron. The intermediate state now finds both ions in the Cu^{+} configuration and the intrinsic energy scale is t_{Cu}^2/Δ_{Cu} where t_{Cu} is the hopping matrix element between oxygen p states and copper e_g states, and Δ_{Cu} is the energy cost of transferring an electron from the oxygen site to the copper. Unlike manganese, this interaction only weakly influences the spin state of the copper system through the Nagaoka interaction which can safely be ignored. Although one might expect $t_{Mn} \geq t_{Cu}$ since the copper d-shell is marginally smaller, the facts that $\Delta_{Mn} \neq \Delta_{Cu}$, and the oxygen electrons are more strongly bound in manganites, makes the two energy scales different. Still we expect the double-exchange in both systems to be similar and a sizeable fraction of an eV.

At the interface there are essentially two possibilities; either the energy gap $E_{Mn} - E_{Cu}$ is larger than the double-exchange induced bandwidth, or it is not. If the gap is retained then the copper remains an insulator and if not the whole system metallises. It is this

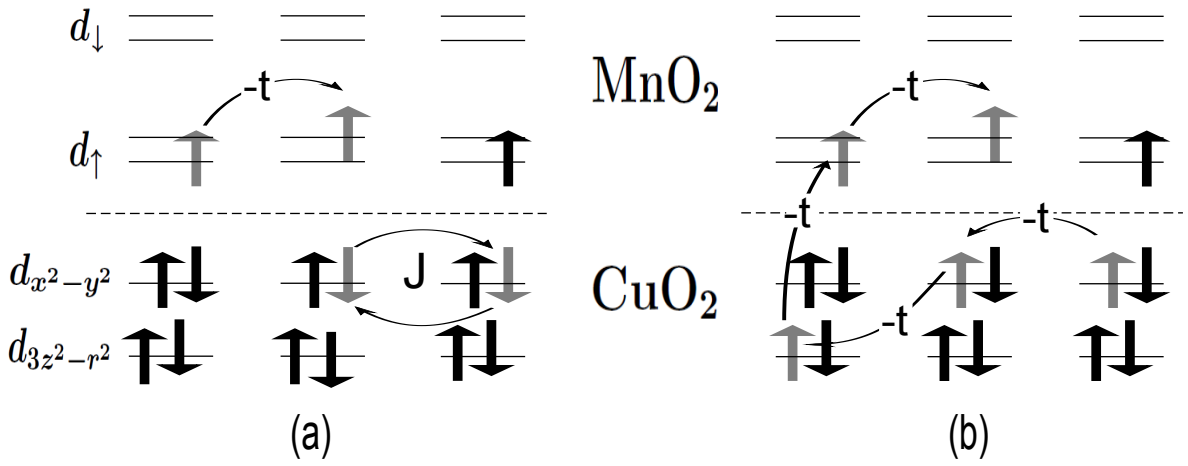

Figure 8.1: Metallisation of the cuprate layer. (a) In the electron doped cuprates the superexchange interaction is dominant in the cuprate layers. (b) At the cuprate-manganite interface, the mobile charge carriers maximise their kinetic energy by delocalising in both the cuprate layer, and in the bulk manganite. The antiferromagnetic superexchange interaction is then overcome by the ferromagnetic double exchange interaction.

second case that appears the most likely experimentally. There is a strong double exchange interaction between the interfacial manganese and copper ions, which utilises the $d_{3z^2-r^2}$ orbital, and the spin polarised electrons from the manganite can therefore pass into the cuprate. Since we expect the charge carriers to be spin polarised, the physical picture simplifies: in the manganites the e_g electrons all have spins parallel to the ferromagnetic t_{2g} background and in the interfacial cuprate layer all the holes are expected to have parallel spins to this background. Electrons from the manganite can cross seamlessly into the cuprates annihilating a hole, and the resulting Cu^+ can readily either hop back or move around in the cuprate using double-exchange, as illustrated in Fig. **??**. At its simplest one can consider the ferromagnetic metal in the manganites to 'spill' out onto the cuprate with the only complication that the local energy difference, $\Delta\mu$, exists and decides relative electron densities. In the manganites the cubic symmetry, manifested in the occupancies of $d_{x^2-y^2}$ and $d_{3z^2-r^2}$ orbitals, is maintained and one might assume that this property is weakened in the cuprates but not eradicated, leading to the next issue of the effects which control this occupancy.

The crucial experimental observation which requires to be understood is why the orbital occupancy in the cuprate interface is essentially random and not heavily biased as it is in the parent compound and the superconducting systems. The crystal field, stemming from the four oxygens in the x-y plane and only one along the z-axis, is retained and offers an energy of half an eV or so and this energy must be overcome. The double-exchange provides a compensatory bias; double exchange within the cuprate layers employs $d_{3x^2-r^2}$

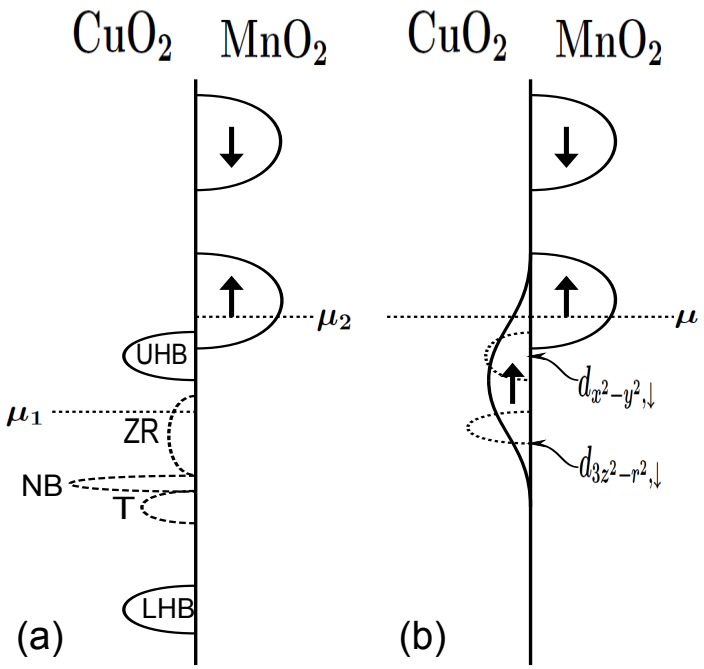

Figure 8.2: A schematic illustration of the density of states in the manganite and the cuprate. (a) away from the interface the manganite is a half metal and the cuprate layer consists of the oxygen non-bonding (NB), Zhang-Rice singlet (ZR) and triplet (T) bands, and the copper $d_{x^2-y^2}$ upper Hubbard (UHB) and lower Hubbard (LHB) bands. (b) At the interface the difference in chemical potentials is compensated by charge transfer across the interface, which raises the chemical potential in the cuprate up to the upper Hubbard band. Only the electrons with parallel spin to the manganite hybridise with the bulk manganite states.

and $d_{3y^2-r^2}$ orbitals which 'average' to form the $d_{x^2-y^2}$ symmetry, whereas the inter copper-manganese double-exchange employs the $d_{3z^2-r^2}$ orbital. The energy scale of the double exchange is competitive with the cuprate crystal-field and, to overcome both the crystal field and antiferromagnetic superexchange correlations, we require a *sizeable* fraction of Cu^+ ions. This would lead to a reconstruction of the density of states at the interface, as is shown in Fig. 8.2.

The physical picture that we are offering should now be clear: we expect the inequality $\Delta\mu > 0$ to be satisfied, so that charge is forced into the cuprates at a level where it can compete and hopefully dominate the crystal-field energy and antiferromagnetic correlations. In accordance with experimental observations, this would require the use of both types of orbital, and would also require there to be an antiferromagnetic moment across the interface.

8.2 Double exchange model of the interface

To analyse the interface we propose a simple Hamiltonian based on the double-exchange interaction. To capture the metallic behaviour in both materials we include a single cuprate capping layer attached to a semi-infinite lattice representing the bulk manganite. In principle the double-exchange interactions may spread to the second CuO_2 layer due to direct exchange between two Cu sites, but the energy gained is small because there is no oxygen ion to facilitate double exchange between the first and second layers, so that a

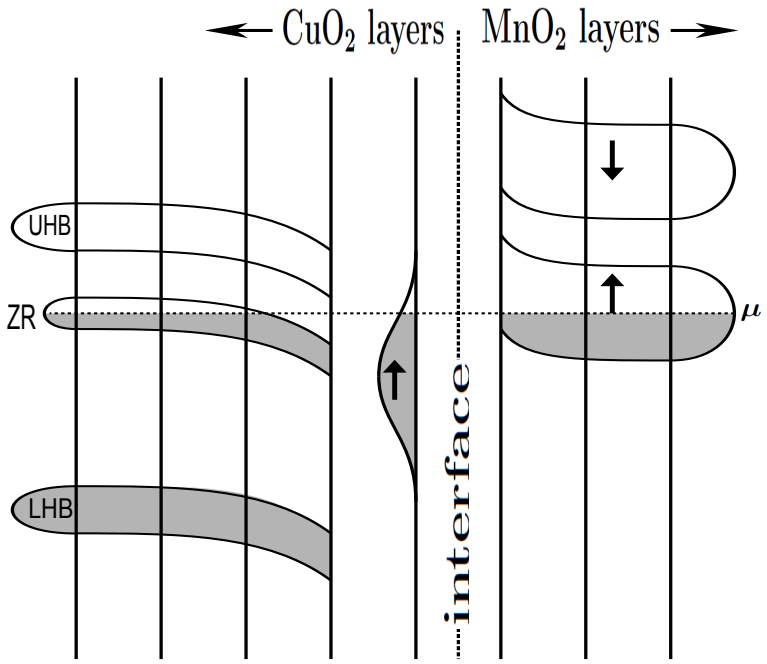

Figure 8.3: The doping of the CuO_2 layers as a function of their distance from the interface. Close to the interface the charge transfer results in CuO_2 layers with variable levels of doping. Far from the interface the chemical potential lies in the Zhang-Rice singlet band and the associated cuprate layers are superconducting. As we move closer to the interface the cuprate layers change from being optimally hole doped, to underdoped, to a Mott insulator. Finally, in the interfacial cuprate layer we find the orbitally reconstructed state, which is observed experimentally.

description involving a single CuO_2 layer should be reasonable. In the first cuprate layer we investigate the idea that the crystal field energy is overcome by the double exchange mechanism which allows the ferromagnetic spins from the manganite into the cuprate layer. In further layers we expect the antiferromagnetic interaction to induce an antiferromagnetic phase analogous to the parent compound, whilst the bulk superconductivity is only expected to be recovered in further layers once the Zhang-Rice singlets reappear. This idea is in Fig. 8.3 using a simple band-bending picture.

The length scale over which the cuprate layers are affected by the manganite is controlled by the difference in chemical potentials of the two materials; electrons flow from the manganite until a compensatory electric potential is created to balance the difference in isolated chemical potentials. In principle one should use Poisson's equation to determine when the potentials balance, but we opt for a simpler approach and introduce the parameter Γ to control both the electrostatic potential and the difference in chemical potentials. The value that Γ will take is not simply the difference between the isolated chemical potentials: it must also incorporate the electrostatic potential in the first layer due to the charge flow from the manganite which electron dopes the cuprate, and should therefore be determined self consistently.

In the manganites we assume that the orbitally degenerate double exchange model is valid: this seems reasonable because the absence of Jahn-Teller distortions and orbital ordering suggests that the electronic motion is the dominant interaction. The model for the manganites is therefore

$$\mathcal{H}_{Mn} = \sum_{\langle jj'\rangle\gamma\gamma'} \left(t_{jj'}^{\gamma\gamma'} d_{j\gamma}^{\dagger} d_{j'\gamma'} + h.c. \right) = \sum_{\mathbf{k}\gamma\gamma'} \epsilon_{\mathbf{k}}^{\gamma\gamma'} d_{\mathbf{k}\gamma}^{\dagger} d_{\mathbf{k}\gamma'}, \tag{8.1}$$

where $\hat{\epsilon}_{\mathbf{k}}$ and the hopping matrices $\hat{t}_{jj'}$ are defined in Chapter 7. We know that there are 2/3 electrons per site on average, which will result in a significant renormalisation of the bare bandwidth $t_{Mn} = t_0$. We assume that the renormalisation can be represented by a Gutzwiller projection, whereby the electrons avoid each other to avoid the intra-orbital coulomb energy U'.

In the cuprate layer, the kinetic energy of spin polarised electrons from the manganite is assumed to overcome both the crystal field energy splitting, and the antiferromagnetic correlations induced by superexchange interactions. The model of the cuprate layer must therefore describe the double exchange mechanism of the spin polarised electrons in the crystal field split e_g states. This model is analogous to that used for the manganites, but with the energy splitting Δ between the $d_{3z^2-r^2}$ and $d_{x^2-y^2}$ states, which we know from photoemission experiments to be about half an eV. The relevant Hamiltonian for a single cuprate layer is

$$\mathcal{H}_{Cu} = \sum_{j\gamma} \epsilon_0^{\gamma\gamma} d_{j\gamma}^{\dagger} d_{j\gamma} + \sum_{\langle jj'\rangle\gamma\gamma'} \left(t_{jj'}^{\gamma\gamma'} d_{j\gamma}^{\dagger} d_{j'\gamma'} + h.c. \right), \tag{8.2}$$

where the hopping is restricted to nearest neighbours in the x-y plane. The energy level splitting is represented by the matrix

$$\hat{\epsilon}_0 = \begin{pmatrix} -\Gamma & 0 \\ 0 & \Delta - \Gamma \end{pmatrix}. \tag{8.3}$$

The parameter Γ has also been included to account for the lower chemical potential relative to the manganite. In the electron doped cuprates the value of t_{Cu} is reduced from its bare value, as the electrons avoid each other to avoid the strong local coulomb interaction U. However, when the cuprate layer becomes ferromagnetic at the cuprate-manganite interface, the electrons avoid each other more effectively, and t_{Cu} should be comparable in size to t_{Mn}.

The parameters Γ, t_M and t_C depend on the amount of charge transferred into the cuprate layer, and should in principal be determined self consistently. Since we are only intending to make qualitative comparisons with experiment this would introduce an unnecessary complication, and would only obscure the simple physical picture that we are offering. We therefore make some reasonable simplifications; we assume that the hopping amplitude is roughly equal in the cuprate layer and in the manganite, and can be represented by the single parameter t. We also elect to choose 'by hand' some reasonable values

for both t and Γ. We choose $\Gamma > t$, which implies that the loss of hybridisation at the interface is compensated by the gain in potential energy. This ensures that a significant amount of charge is transferred across the interface, possibly into states which are bound to the interfacial cuprate layers. We also choose $\Delta < t$, so that the crystal field splitting is overcome by the double exchange mechanism.

We require a model for a single cuprate layer in metallic contact with the bulk manganite. To do this we make use of impurity theory (which in this context is also referred to as the scattering theoretical method[67, 68]), which is a very convenient method for solving a known Hamiltonian $\mathcal{H}_0$ with a local impurity $\mathcal{H}_1$.

8.2.1 Representing the interface as an impurity

To apply impurity theory to the cuprate manganite interface we take the bulk manganese as the reference system and treat the cuprate layer as a local impurity which changes the energies of occupying either orbital. The calculation is a three step process: i) We calculate the resolvent associated with the bulk manganite, ii) We use impurity theory to modify this resolvent to describe a semi-infinite lattice, iii) We use impurity theory to modify the surface layer to represent a CuO_2 layer with the introduction of Γ and Δ. The resolvent can then be used to calculate the density of states for each orbital in any layer parallel to the surface. Step one: the reference Hamiltonian which describes the bulk manganite is

$$\mathcal{H}_0 = \sum_{\langle jj' \rangle} \left(t_{jj'}^{\gamma\gamma'} d_{j\gamma}^{\dagger} d_{j'\gamma'} + h.c. \right) = \sum_{\mathbf{k}\gamma\gamma'} \epsilon_{\mathbf{k}}^{\gamma\gamma'} d_{\mathbf{k}\gamma}^{\dagger} d_{\mathbf{k}\gamma'}, \tag{8.4}$$

with

$$\hat{\epsilon}_{\mathbf{k}} = \frac{t_0}{2} \begin{pmatrix} -\left(C_x + C_y + 4C_z\right) & \sqrt{3}\left(C_x - C_y\right) \\ \sqrt{3}\left(C_x - C_y\right) & -3\left(C_x + C_y\right) \end{pmatrix}. \tag{8.5}$$

The dispersion relations for the two bulk bands are given by

$$E_{\mathbf{k}}^{\pm} = -t\left(C_x + C_y + C_z \pm \sqrt{C_x^2 + C_y^2 + C_z^2 - C_xC_y - C_xC_z - C_yC_z}\right), \tag{8.6}$$

where C_x, C_y and C_z represent $\cos(k_x)$, $\cos(k_y)$ and $\cos(k_z)$ respectively. The resolvent for the bulk manganite may be represented as a 2×2 matrix,

$$\begin{aligned} \hat{\mathcal{G}}_0(z)_{\mathbf{k}\mathbf{k}'} &= \delta_{\mathbf{k}\mathbf{k}'} \left[z - \hat{\epsilon}_{\mathbf{k}} \right]^{-1} \\ &= \frac{\delta_{\mathbf{k}\mathbf{k}'}}{\mathrm{Det}||z - \hat{\epsilon}_{\mathbf{k}}||} \begin{pmatrix} z + \frac{3}{2}(C_x + C_y) & -\frac{\sqrt{3}}{2}(C_x - C_y) \\ -\frac{\sqrt{3}}{2}(C_x - C_y) & z + \frac{1}{2}(C_x + C_y + 4C_z) \end{pmatrix}, \end{aligned} \tag{8.7}$$

where, for convenience, the energy has been represented in units of t. The expression for the resolvent in reciprocal space may be very simple, but to add localised impurities we need to represent it in real space. This turns out to be relatively straightforward for this system because the impurities are independent of x and y, which means that the problem is quasi one dimensional. Therefore, in analogy with the one dimensional case, we express the resolvent in the form

$$\hat{\mathcal{G}}_0(z)_{\mathbf{k}\mathbf{k}'} = \frac{\delta_{\mathbf{k}\mathbf{k}'}}{A + 2BC_z} \begin{pmatrix} B & -C \\ -C & \frac{1}{B}\left(A + 2B + C^2\right) + 2C_z \end{pmatrix}, \tag{8.8}$$

where we have introduced the parameters

$$A = z^2 + 2z(C_x + C_y) + 3C_xC_y \tag{8.9}$$

$$B = z + \frac{3}{2}(C_x + C_y) \tag{8.10}$$

$$C = \frac{\sqrt{3}}{2}(C_x - C_y). \tag{8.11}$$

We elect to represent only the z coordinate in real space so that we may manipulate and analyse individual layers parallel to the interface. This is accomplished by performing the one dimensional Bloch transform of Eq. 8.8:

$$\hat{\mathcal{G}}_0(z)_{\mathbf{k}_\parallel \mathbf{k}'_\parallel nn'} = \sum_{k_z k'_z} e^{ik_z n} \hat{\mathcal{G}}_0(z)_{\mathbf{k}\mathbf{k}'} e^{-ik'_z n'}$$

$$= \delta_{\mathbf{k}_\parallel \mathbf{k}'_\parallel} \int_{-\pi}^{\pi} \frac{dk_z}{2\pi} \frac{e^{ik_z(n-n')}}{A + 2BC_z} \begin{pmatrix} B & -C \\ -C & \frac{1}{B}\left(A + 2B + C^2\right) + 2C_z \end{pmatrix}, \tag{8.12}$$

which is a function of the two dimensional Bloch wave vector $\mathbf{k}_\parallel = (k_x, k_y)$ and the layer index n. The label $\mathbf{k}_\parallel$ will henceforth be dropped to simplify the notation. The integrals involved can be determined using complex analysis and are of an identical form to those encountered when calculating the resolvent for the one dimensional chain (which reflects the one dimensional nature of this problem). After performing these integrals we obtain the layer representation of the resolvent

$$\hat{\mathcal{G}}_0(z)_{nn'} = \begin{pmatrix} 0 & 0 \\ 0 & 1 \end{pmatrix} \frac{\delta_{nn'}}{B} + \begin{pmatrix} 1 & \frac{C}{B} \\ \frac{C}{B} & \frac{C^2}{B^2} \end{pmatrix} \frac{R^{|n-n'|}}{R - \frac{1}{R}} \tag{8.13}$$

$$R = \left(-\frac{A}{2B} + \frac{\sqrt{|A^2 - 4B^2|}}{2B} \right). \tag{8.14}$$

The two branch cuts of the resolvent correspond to the two z-projected bulk bands of

the manganite, which merge into a single band whenever $k_x = k_y$. The parameter R is multi-valued and the phase in front of the square root is therefore dependent on the value of z. When z is real and to the left of the lower band or to the right of the upper band the phase is $+1$, when z is in the band gap the phase is -1, and when $z - i\delta$ is just below the lower(upper) band the phase is $+i(-i)$.

The resolvent of the bulk manganite, Eq 8.13, contains a single pole when $B = 0$. This is actually a pathological point where the eigenstate is composed of only the $\hat{x}^2 - \hat{y}^2$ orbital which, because it does not hybridise with the $3\hat{z}^2 - 1$ orbital, is bound to a single layer in the x-y plane (other layer bound states will appear once we incorporate the cuprate layer). This state appears throughout the analysis, but is not really relevant to our investigation.

To produce a surface we apply impurity theory to cancel the hopping between two adjacent layers in the z direction. This is equivalent to replacing the periodic boundary conditions along the z-axis with open boundary conditions, thus breaking the translational symmetry.

Step two: we use impurity theory to modify the resolvent to represent a semi-infinite crystal lattice. The impurity required for this step is represented as a 2×2 matrix which cancels the hopping between the $3\hat{z}^2 - 1$ orbitals in the first two layers:

$$\mathcal{H}_1 = \begin{pmatrix} 0 & 1 \\ 1 & 0 \end{pmatrix}. \tag{8.15}$$

The basis states for this impurity are the $3\hat{z}^2 - 1$ orbitals in the first two layers. To modify the resolvent we then require the local matrix $\Sigma(z)$, which is given by

$$\Sigma(z) = \begin{pmatrix} -\mathcal{G}_0(z)^{00}_{00} & 1 - \mathcal{G}_0(z)^{00}_{01} \\ 1 - \mathcal{G}_0(z)^{00}_{10} & -\mathcal{G}_0(z)^{00}_{11} \end{pmatrix}^{-1} = \begin{pmatrix} -R & 1 \\ 1 & -R \end{pmatrix}. \tag{8.16}$$

In the resolvent $\mathcal{G}_0(z)^{\gamma\gamma'}_{nn'}$ the superscript γ refers to the orbital, the subscript n is a layer index. The modified resolvent is then

$$\mathcal{G}(z)^{\gamma\gamma'}_{nn'} = \mathcal{G}_0(z)^{\gamma\gamma'}_{nn'} + \sum_{i,i'=0}^{1} \mathcal{G}_0(z)^{\gamma 0}_{ni} \Sigma(z)_{ii'} \mathcal{G}_0(z)^{0\gamma'}_{i'n'}. \tag{8.17}$$

After a fair amount of algebra the resolvent can be written in a compact form,

$$\hat{\mathcal{G}}_0(z)_{nn'} = \begin{pmatrix} 0 & 0 \\ 0 & 1 \end{pmatrix} \frac{\delta_{nn'}}{B} + \begin{pmatrix} 1 & \frac{C}{B} \\ \frac{C}{B} & \frac{C^2}{B^2} \end{pmatrix} \frac{R^{|n-n'|} - R^{n+n'+2}}{R - \frac{1}{R}}. \tag{8.18}$$

The resolvent for the semi-infinite lattice contains no new poles, implying that the presence of the surface simply modifies the amplitudes of the three dimensional $\mathbf{k}$ states.

Step three: we use impurity theory to modify the surface (which has been translated

from $n = 1$ to $n = 0$ for simplicity) so that it resembles a cuprate layer. The electrons reduce their energy by visiting the cuprate layer where the reduced chemical/electrostatic potential is represented by Γ and the crystal field splitting between the $\hat{x}^2 - \hat{y}^2$ and $3\hat{z}^2 - 1$ orbitals is represented by Δ. We make the resolvent of the semi-infinite crystal lattice (Eq 8.18) our reference, and then the impurity which modifies the surface layer is represented by a simple 2×2 matrix:

$$\mathcal{H}_1 = \begin{pmatrix} -\Gamma & 0 \\ 0 & \Delta - \Gamma \end{pmatrix}. \tag{8.19}$$

We should note that the basis states for this second impurity are the $\hat{x}^2 - \hat{y}^2$ and $3\hat{z}^2 - 1$ orbitals in the surface layer. For the second impurity the matrix $\Sigma(z)$ is

$$\begin{aligned} \Sigma(z) &= \begin{pmatrix} -\Gamma - \mathcal{G}_0(z)^{00}_{00} & -\mathcal{G}_0(z)^{01}_{00} \\ -\mathcal{G}_0(z)^{10}_{00} & \Delta - \Gamma - \mathcal{G}_0(z)^{11}_{00} \end{pmatrix}^{-1} \\ &= \frac{1}{D} \begin{pmatrix} B(\Delta - \Gamma)\left(\Gamma - \frac{B}{R}\right) & -\Gamma(\Delta - \Gamma)C \\ -\Gamma(\Delta - \Gamma)C & \Gamma\left(\frac{B}{R} - \frac{(\Delta - \Gamma)}{R} + \frac{(\Delta - \Gamma)C^2}{B}\right) \end{pmatrix}, \end{aligned} \tag{8.20}$$

where $D = \det||\mathcal{I} - \mathcal{G}_0\mathcal{H}_1||$ and is defined by Eq. 8.31. We then modify the resolvent a second time:

$$\mathcal{G}(z)^{\gamma\gamma'}_{nn'} = \mathcal{G}_0(z)^{\gamma\gamma'}_{nn'} + \sum_{i,i'=0}^{1} \mathcal{G}_0(z)^{\gamma i}_{n0} \Sigma(z)_{ii'} \mathcal{G}_0(z)^{i'\gamma'}_{0n'}. \tag{8.21}$$

After a fair amount of algebra the resolvent of the bulk manganite with a CuO_2 capping layer may be written compactly as

$$\hat{\mathcal{G}}_0(z)_{nn'} = \begin{pmatrix} 0 & 0 \\ 0 & 1 \end{pmatrix} \frac{\delta_{nn'}}{B_n} + \begin{pmatrix} 1 & \frac{C}{B_n} \\ \frac{C}{B_{n'}} & \frac{C^2}{B_n B_{n'}} \end{pmatrix} \left(\frac{R^{|n-n'|} - R^{n+n'}}{R - \frac{1}{R}} + \frac{R^{n+n'}}{\lambda - \frac{1}{R}} \right) \tag{8.22}$$

$$B_n = B + \delta_{n0}(\Gamma - \Delta) \tag{8.23}$$

$$\lambda = \frac{(\Gamma - \Delta)C^2}{BB_0} + \Gamma. \tag{8.24}$$

By introducing the second impurity a new term has appeared in the resolvent. This term, which contains the $\lambda - 1/R$ in the denominator, contains a single pole for each state which is bound to the interface. This concludes the calculation of the resolvent. This simple analytical function provides a great deal of information about our model of the interface. In fact, our task now is simply to extract the information we require from this resolvent.

8.2.2 Extracting information from the resolvent

The resolvent can be used to determine the layer resolved partial density of states for each of the orbitals, and will provide exactly the information we require to make deductions about the relative occupations of $d_{x^2-y^2}$ and $d_{3z^2-r^2}$ states in the cuprate layer. For the orbital γ in the j-th layer, the partial density of states is

$$\rho_n^\gamma(\epsilon, \mathbf{k}_\parallel) = \frac{1}{\pi} \lim_{\delta \to 0} \mathrm{Im}\ \mathcal{G}(\epsilon - i\delta)_{nn}^{\gamma\gamma}. \tag{8.25}$$

The cuprate layer breaks the translational symmetry along the z-axis, which therefore implies that the density of states will contain both a coherent part, which arises because some of the electrons bind to the cuprate layer to reduce their energy, and an incoherent part which appears as a consequence of the three dimensional nature of the bulk manganite. The distinction between these two contributions can occasionally become blurred when a bound state becomes degenerate with a bulk state, thereby creating a clear resonance in the density of states.

The coherent contribution to the density of states appears at energies for which the resolvent has a simple pole. At these points the density of states becomes a Dirac delta function, with a weight Z that can be determined by calculating the residue at the binding energy E:

$$\rho_n^\gamma(\epsilon, \mathbf{k}_\parallel) = Z_n^\gamma(E, \mathbf{k}_\parallel)\delta(\epsilon - E), \tag{8.26}$$

with

$$Z_n^\gamma(E, \mathbf{k}_\parallel) = \operatorname*{Res}_{\epsilon=E}\ \mathcal{G}(\epsilon)_{nn}^{\gamma\gamma}. \tag{8.27}$$

The coherent states are two dimensional bound states which are quantised along the z-axis and are therefore localised at the interface, decaying exponentially into the bulk. The incoherent part of the density of states is only nonzero when the energy sits on a branch cut in the complex plane. The density of states then forms a continuous distribution between the branch points. The incoherent states are three dimensional bulk states which are not quantised along the z-axis, and are therefore not normalisable. At the interface these states have an enhanced amplitude, because of the impurity, which becomes especially pronounced when there is a resonance.

To extract information about the cuprate manganite interface we need to examine the analytic structure of the resolvent (Eq 8.22), and understand how this structure relates to the states of the system. The poles in the resolvent occur at the points where $\lambda = 1/R$, which can be cast into an equivalent fourth order polynomial equation:

$$\left(z+\frac{3}{2}\left(C_x+C_y\right)\right)\left(z+\frac{3}{2}\left(C_x+C_y\right)+\Gamma-\Delta\right)^2\left(z+\frac{1}{2}\left(C_x+C_y\right)+\Gamma+\frac{1}{\Gamma}\right)$$
$$-\frac{3}{4}\left(C_x-C_y\right)^2\frac{\Delta}{\Gamma}\left(z+\frac{3}{2}\left(C_x+C_y\right)+\Gamma-\Delta\right)\left(z+\left(\frac{\Gamma}{\Delta}+\frac{1}{2}\right)\left(C_x+C_y\right)+\Gamma-\frac{\Gamma^2}{\Delta}\right)$$
$$-\left(\frac{3}{4}\left(C_x-C_y\right)^2\right)^2\left(1-\frac{\Delta}{\Gamma}\right)=0, \tag{8.28}$$

which obviously has four solutions corresponding to possible bound states. Further analysis of the resolvent also reveals branch cuts and branch points which arise because of the multi-valued nature of R. The branch cuts represent the continuum of bulk states emanating from the manganite. The four branch points defining the edge of the continuum states are located at

$$z_1^{\pm}=-(C_x+C_y+1)\pm\sqrt{C_x^2+C_y^2-C_xC_y-C_x-C_y+1}$$
$$z_2^{\pm}=-(C_x+C_y-1)\pm\sqrt{C_x^2+C_y^2-C_xC_y+C_x+C_y+1}. \tag{8.29}$$

The poles of the resolvent move around the complex z-plane as k_x and k_y are varied, but can never sit directly on a the branch cut. Instead, they may acquire complex values and lead to a resonance in the continuum of bulk states. We can track these resonances by calculating the change in the density of states caused by the impurity[126]. The method for determining the resonances is outlined in appendix D. The change in the density of states is

$$\Delta\rho_n^{\gamma}(\epsilon,\mathbf{k}_{\parallel})=\frac{1}{\pi}\frac{\mathrm{d}\delta}{\mathrm{d}\epsilon}, \tag{8.30}$$

where the phase shift of the scattered waves is defined by $\delta(\epsilon)=\arg(D(\epsilon))$. To find the resonances at the cuprate-manganite interface we can look at the change in the density of states caused by replacing the surface layer of the semi-infinite crystal lattice with the cuprate layer. We then obtain

$$D(\epsilon)=\det||\mathcal{I}-\mathcal{G}_0\mathcal{H}_1||=\frac{B_0(1-R\lambda)}{B}, \tag{8.31}$$

and therefore

$$\tan\delta=\pm\frac{\sqrt{4B^2-A^2}}{A+2B/\lambda}, \tag{8.32}$$

where the positive and negative signs correspond to the upper and lower bands respectively. If we define an energy ϵ_0 such that Re $D(\epsilon_0)=0$, and expand $D(\epsilon)$ in the vicinity

of this point, we obtain a Lorentzian form centered at ϵ_0:

$$\Delta\rho(\epsilon, \mathbf{k}_\parallel) \approx \frac{\Gamma_0}{2\pi} \frac{1}{(\epsilon - \epsilon_0)^2 + \Gamma_0^2/4}. \tag{8.33}$$

The half width Γ_0, which is related to the inverse lifetime of an electron in the cuprate layer, is defined

$$\Gamma_0 = \frac{2\text{Im } D(\epsilon_0)}{\text{Re } D'(\epsilon_0)}, \tag{8.34}$$

where the prime denotes differentiation with respect to ϵ. The sign of Γ_0 is positive for a resonance, and negative for an antiresonance. There are two situations where the resonances at the cuprate-manganite interface become large. Firstly, when a pole sits on one of the branch points there is a square root divergence in the density of states. The points where these resonances occur are solutions of the equation

$$\left(\frac{\frac{1}{2}(\Delta \pm 1)(C_x + C_y) + 1 + \Gamma(\Gamma - \Delta \pm 1)}{2\Gamma - \Delta \pm 1} \right)^2 = \frac{3}{4}(C_x - C_y)^2 + \left(1 \pm \frac{1}{2}(C_x + C_y)\right)^2, \tag{8.35}$$

where the $\pm$ sign corresponds to a resonance on the branch point $z_1^\pm$ or $z_2^\pm$. The second type of resonance occurs along the symmetry axis $k_x = k_y$, for which there is no hybridisation between the two orbitals, and is associated with an electron of $d_{x^2-y^2}$ character becoming trapped in a layer.

8.2.3 The spectral function

To understand the properties of the interface we must choose appropriate values of the crystal field splitting Δ and the potential difference Γ; we choose $\Delta = 0.5t$ and $\Gamma = 2.5t$, in accordance with our requirements that $\Gamma > t$ and $\Delta < t$. We can then examine the locations of the poles in the complex z-plane, as k_x and k_y are traced along the path $(k_x = 0, k_y = 0) \rightarrow (k_x = \pi, k_y = 0) \rightarrow (k_x = \pi, k_y = \pi)$, as is illustrated in Fig. 8.4. Only the poles which lie on the first Riemann sheet correspond to bound states and, as can be seen from the illustration, there are initially three bounds states, one of which exists in the band gap. Further along the path the poles collide with the branch points and move to the second Riemann sheet, creating clear resonances in the density of states. The resonances can be visualised by plotting the *spectral function*, $A(\epsilon, \mathbf{k}_\parallel)$, which is related to the density of states:

$$\rho_n^\gamma(\epsilon, \mathbf{k}_\parallel) = \frac{1}{2\pi} A_n^\gamma(\epsilon, \mathbf{k}_\parallel). \tag{8.36}$$

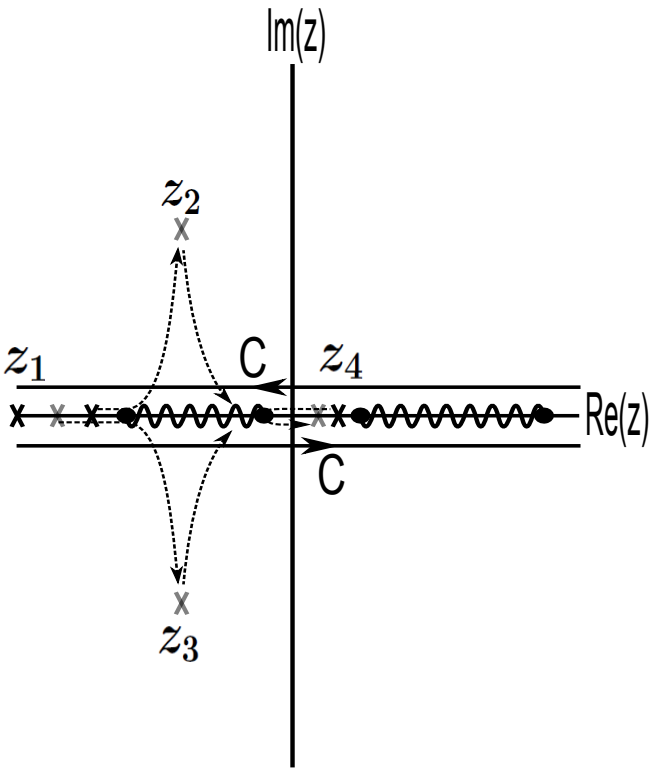

Figure 8.4: A schematic illustration of the locations of the poles (of the resolvent) in the complex plane, along the path $(k_x = 0, k_y = 0) \rightarrow (k_x = \pi, k_y = 0) \rightarrow (k_x = \pi, k_y = \pi)$. z_1 always lies on the real axis and corresponds to a bound state. Initially, z_2 corresponds to another bound state, whilst z_3 lies on the second Riemann sheet and is irrelavant. As k_x is increased both z_2 and z_3 become degenerate at the branch point and create a resonance in the density of states, which decays as the poles pass onto the second Riemann sheet. When $k_x = \pi$ and k_y is increased these poles move towards the branch cut and create a perfect resonance when $(k_x = \pi, k_y = \pi)$. Initially, z_4 corresponds to a bound state in the band gap. As k_x is increased this pole moves into the branch point, creating a resonance, and finally passes through to the second Riemann sheet where it becomes irrelevant.

This quantity is approximately determined in an ARPES experiment and provides a means of comparing experimental data with theory. The first thing we notice when observing the spectral function is the presence of three distinct bound states. The two low lying states clearly reside in the cuprate layer (Fig. 8.5(a)), benefitting from the lower potential energy, and decay rapidly into the bulk. Because of orthogonality, the third bound state (Fig. 8.5(c)), which exists in the band gap, must be associated with the manganite. This is indeed verified by the large spectral weight which is present in the manganite, penetrating more than five layers into the bulk. The origin of this state is a little more subtle: the band gap appears because of the hybridisation between the $3\hat{z}^2 - 1$ and $\hat{x}^2 - \hat{y}^2$ orbitals, and the loss of this hybridisation energy at the surface induces a bound state in the band gap.

In the cuprate layer resonances are observed in the spectral function at the edges of the lower band, close to $(\pi/2, 0)$, as illustrated in Fig. 8.5(a). The resonance at the bottom edge is caused by the degeneracy of the bulk states with a state bound to the cuprate layer, whilst the resonance at top edge is caused by the degeneracy of the bulk states with a state bound to the manganite layer. Whenever $k_x = k_y$ there is a resonance in the cuprate layer which corresponds to a simple pole in the spectral function (Fig. 8.5(b)). This resonance is not associated with any impurity, but is simply a consequence of the two dimensional nature of electrons occupying the $\hat{x}^2 - \hat{y}^2$ orbitals which become

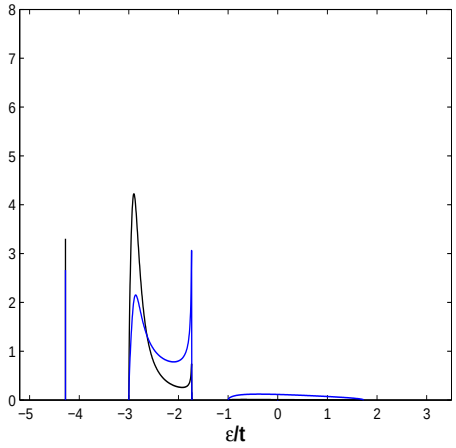

(a) Resonances at the edges of the lower band, in the interfacial cuprate layer, appearing close to $(\pi/2, 0)$. Also visible are the low energy states, which are bound to the cuprate layer.

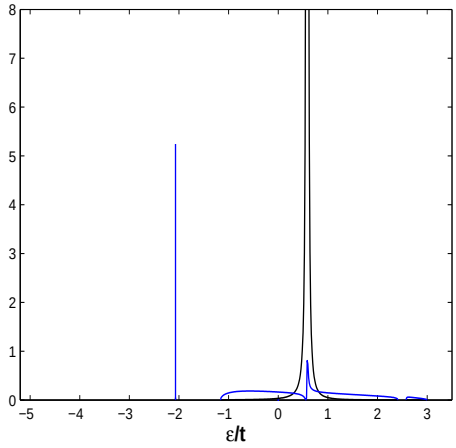

(b) The resonance at the point $(\pi, 3\pi/2)$, which is close to the perfect resonance appearing whenever $k_x = k_y$.

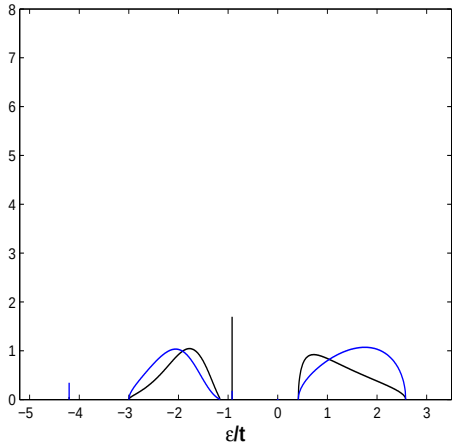

(c) The state which is bound to the interfacial manganite layer, appearing in the band gap close to $(\pi, \pi/2)$

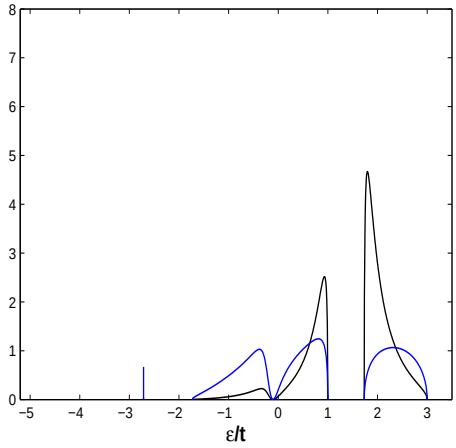

(d) An antiresonance in the middle of the lower band, appearing in the interfacial manganite layer close to $(3\pi/2, 0)$

Figure 8.5: Resonances and bound states, appearing in the spectral function $A_n^\gamma(\epsilon, \mathbf{k}_\parallel)$, in the interfacial layers.

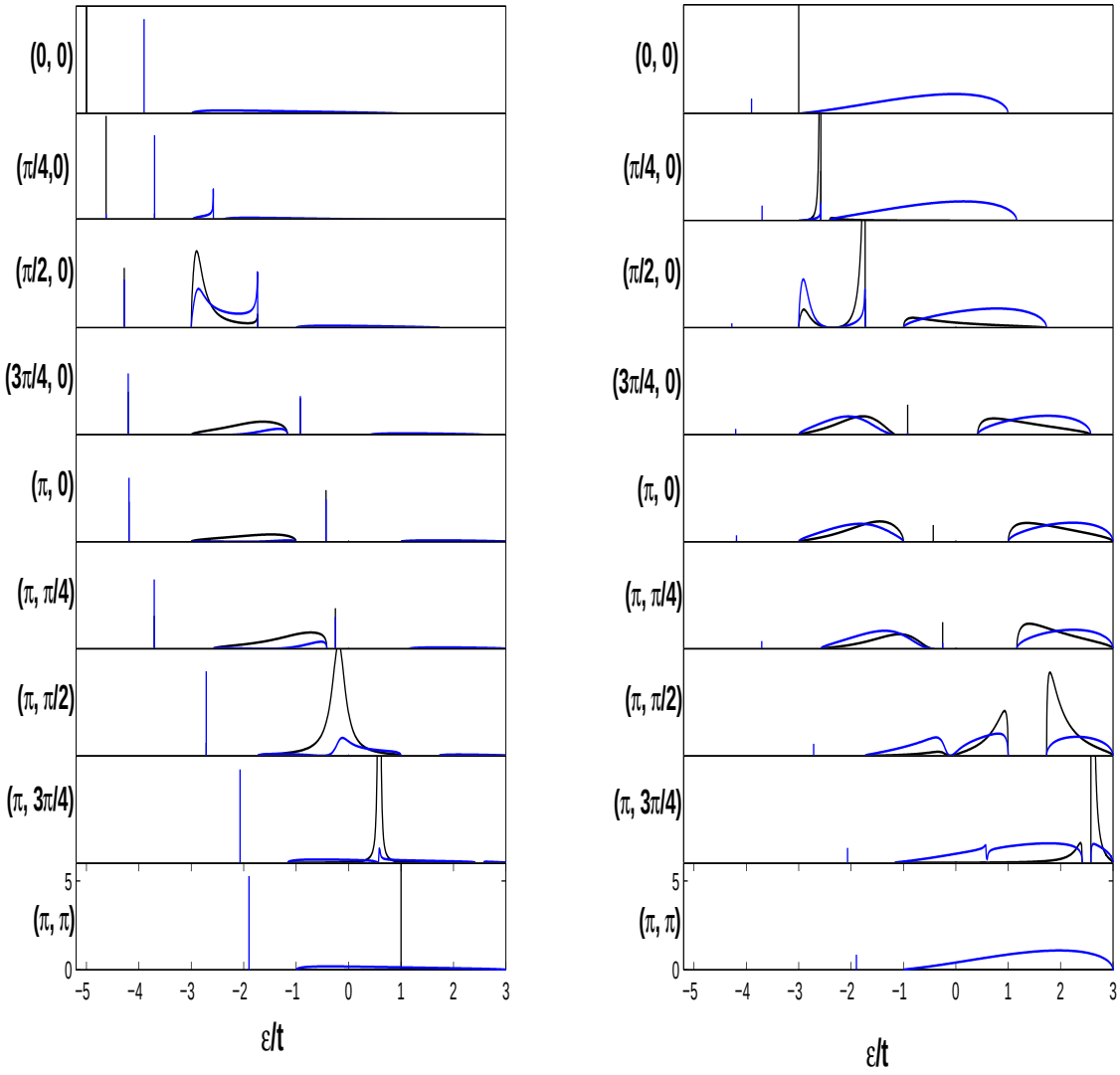

(a) The spectral function $A_n^\gamma(\epsilon, \mathbf{k}_\parallel)$ of the $d_{x^2-y^2}$ state (black line) and the $d_{3z^2-r^2}$ state (blue line), in the cuprate layer.

(b) The spectral function $A_n^\gamma(\epsilon, \mathbf{k}_\parallel)$ of the $d_{x^2-y^2}$ state (black line) and the $d_{3z^2-r^2}$ state (blue line), in the interfacial manganite layer.

Figure 8.6: The spectral functions of the interfacial cuprate and manganite layers along the path $(0,0) \rightarrow (\pi,0) \rightarrow (\pi,\pi)$. Resonances are observed in the cuprate layer in the vicinity of $(\pi/2,0)$ and (π,π), whilst antiresonances are observed in the manganite layer close to $(\pi,\pi,\pi/2)$.

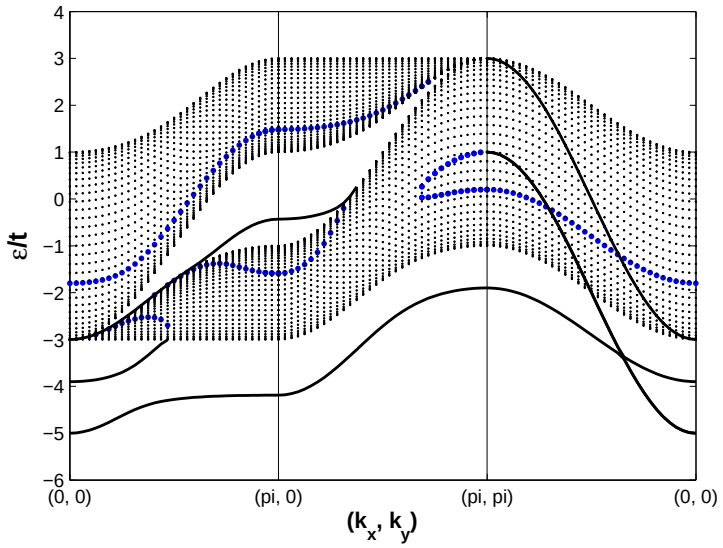

Figure 8.7: Energy bands and resonances, along the path $(0,0) \rightarrow (\pi,0) \rightarrow (\pi,\pi)$, in the interfacial cuprate and manganite layers (with $\Gamma = 2.5$ and $\Delta = 0.5$). The plot shows the two dimensional states bound to the interface (solid lines), the resonances (blue circles) in the bulk density of states, and the incoherent background of z-projected bulk bands (dotted lines).

trapped in individual layers. We can solve the equations exactly in this case and find one pole of $d_{3z^2-r^2}$ character with energy $\epsilon = -(C_x + \Gamma + 1/\Gamma)$ and an occupation of $Z_0^{x^2-y^2} = 1 - 1/\Gamma^2$ (for $\Gamma > 1$). The other pole corresponds to a fully occupied state of $d_{x^2-y^2}$ character, which has an energy $\epsilon = -(3Cx + \Gamma - \Delta)$. Finally, the restructuring of the density of states in the cuprate layer also leads to antiresonances in the manganite layers (Fig. 8.5(d)).

The spectral function is mapped out, along the path $(k_x = 0, k_y = 0) \rightarrow (k_x = \pi, k_y = 0) \rightarrow (k_x = \pi, k_y = \pi)$, in Fig. 8.6. Fig. 8.6(a) displays the formation of bound states and resonances which dominate the electronic properties of the cuprate layer, whilst Fig. 8.6(b) shows how these resonances interfere with the bulk manganite bands, drastically altering the density of states. We can also identify the emergence and subsequent disappearance, as k_x and k_y are varied, of the bound state in the manganite band gap.

A more complete picture of the bound states, resonances and anti-resonances can be seen by looking at the energy bands which are mapped out in Fig. 8.7. The z-projected density of states (for which the density of states with specific values for k_x and k_y, but arbitrary k_z, is proportional to the density of points) associated with the bulk manganite is also illustrated.

8.3 Comparing theory with experiment

Having analysed this simple model of the cuprate-manganite interface in some detail, we can now consider what this model has to say about the interfacial magnetic profile and the orbital reconstruction in the cuprate layer. Experimentally, the occupation of $d_{x^2-y^2}$

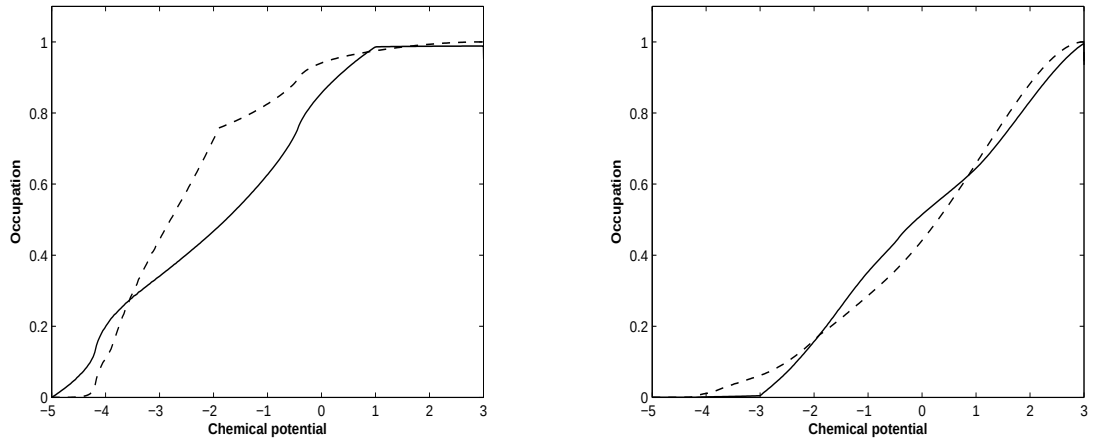

(a) Interfacial CuO_2 layer

(b) Interfacial MnO_2 layer

Figure 8.8: Charges, $\boldsymbol{\rho}^{x^2-y^2}$ (solid line) and $\boldsymbol{\rho}^{3z^2-r^2}$ (dashed line), occupying the interfacial cuprate and manganite layers. In these calculations $\Gamma = 2.5t$ and $\Delta = 0.5t$

states and $d_{3z^2-r^2}$ states was found to be roughly equal in the interfacial cuprate layer. We can easily find out if our model agrees with these observations by determining the charge, $\boldsymbol{\rho}_n^\gamma$, in each orbital, in each layer:

$$\boldsymbol{\rho}_n^\gamma = \int_{-\infty}^{\infty} d\epsilon \int \frac{d\mathbf{k}_\parallel}{4\pi^2} f\left(\frac{\epsilon}{t} - \frac{\mu}{t}\right) \rho_n^\gamma\left(\frac{\epsilon}{t}, \mathbf{k}_\parallel\right), \tag{8.37}$$

where we have introduced the Fermi-Dirac distribution $f(\epsilon - \mu)$, which we evaluate at zero temperature. The plots in Fig. F.1 shows the results for the occupation of $d_{x^2-y^2}$ and $d_{3z^2-r^2}$ states in the interfacial cuprate and manganite layers.

At low doping the electrons in the cuprate layer bind to the interface using the two dimensional $\hat{x}^2 - \hat{y}^2$ orbital, thereby benefitting from the lower potential energy without losing any hybridisation energy. As the doping is increased electrons start to bind to the interface using the $3\hat{z}^2 - 1$ orbital. Because of the narrow bandwidth of the $d_{3z^2-r^2}$ states in the two dimensional cuprate layer, these states are filled faster than the $d_{x^2-y^2}$ states at intermediate energies.

For the experimental system, there are $2/3$ e_g electrons per site in the bulk manganite, which corresponds to a chemical potential of $\mu = -1$. From this we can immediately determine that the occupation numbers in the CuO_2 layer are $\boldsymbol{\rho}_0^{x^2-y^2} \approx 0.63$ and $\boldsymbol{\rho}_0^{3z^2-r^2} \approx 0.83$. This corresponds to about $1/3$ of the holes occupying the $3\hat{z}^2-1$ orbital and $2/3$ occupying the $\hat{x}^2 - y^2$ orbital, which is not too far off the ratio inferred from XLD measurements[53]. The fraction of Cu^+ can also be estimated to be approximately 0.46, which is slightly larger than the rough approximation of 0.2, determined experimentally. In practice, the amount of charge in the cuprate layer can be tuned by varying Γ, but the relative occu-

pation of the two orbitals remains approximately the same. An important observation from our calculations is that the reduction in charge in the interfacial manganite layer is very small, at about 0.02e per manganese ion, and the manganite therefore remains relatively unaffected by the presence of the interface. This validates the assumption that the manganite is still in the ferromagnetic metallic phase close the interface.

The magnetic moment on each copper site is proportional to the number of holes, per copper site, in the CuO_2 layer; from the double exchange model we find that $\mu_{\rm Cu} \approx -0.54\mu_B$: where μ_B is the Bohr magneton. The experimental magnetic profile exhibits a magnetic moment on the YBCO side of the interface, which penetrates several layers ($\approx$ 20Å) from the interface; a crude estimate of the total magnetic moment is $\mu_{\rm Cu} \approx -2{\rm N}\mu_B$, which is not unreasonably different from our prediction. However, the double exchange model, which is based upon the assumption that the magnetic moment is limited to a single cuprate layer, cannot accommodate the spread of the magnetic moment throughout multiple cuprate layers.

the magnetic moment per manganese ion in the interfacial MnO_2 layer consists of contributions from the three parallel t_{2g} spins and the itinerant e_g spins: for the double exchange model we find that $\mu_{\rm Mn} \approx 3.64\mu_B$, which is very close to the bulk magnetic moment of $3.66\mu_B$. On the LCMO side of the interface, the experimental magnetic profile exhibits a reduction in the magnetic moment, relative to the bulk value, which penetrates several layers ($\approx$ 20Å) from the interface. The total reduction is roughly $\delta\mu_{\rm Mn} \approx 3\mu_B$ which is not in accordance with our prediction.

Although we cannot obtain good quantitative agreement with the neutron reflectometry experiments, it is nevertheless clear that our model does provide a rationale for there being antiferromagnetic correlations across the interface. It also demonstrates that the charge in the interfacial manganite layers is close to the bulk value; the properties of the manganite should therefore be unaffected by the interface.

8.4 Fermi surfaces at the cuprate-manganite interface

By analysing the analytic properties of the resolvent we found that our model predicted a rich variety of bound states and resonances in the interfacial cuprate and manganite layers. The Lorentz broadened spectral weight, evaluated at the Fermi energy, is illustrated in Fig. 8.9. The plots are almost identical apart from a slight redistribution of spectral weight, and a small signal from the $k_x = k_y$ resonance which occurs at different points in the cuprate and manganite layers. Interestingly, if we were to consider measuring the layer resolved spectral weight using two dimensional ARPES, then the spectral weight would

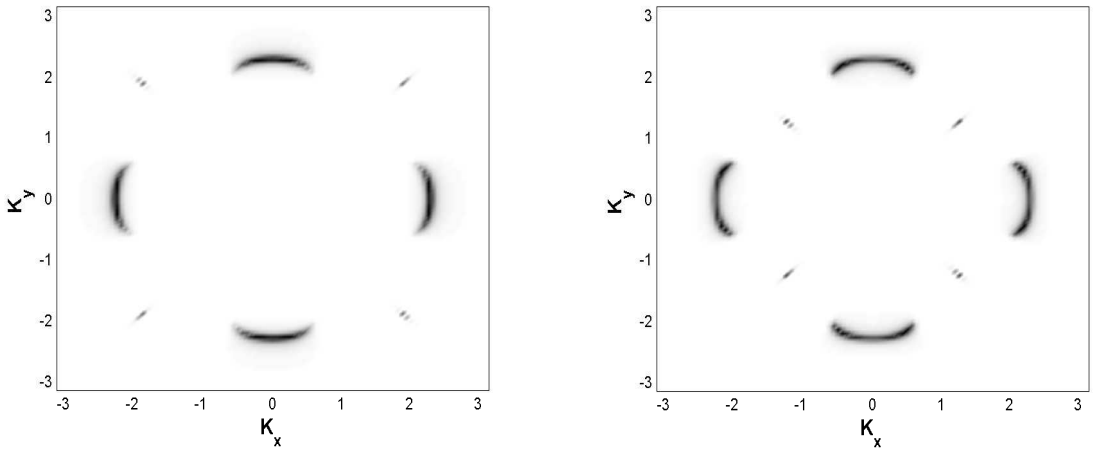

(a) Interfacial CuO_2 layer

(b) Interfacial MnO_2 layer

Figure 8.9: The Lorentz broadened spectral functions of the interfacial cuprate and manganite layers, evaluated at the Fermi energy.

decay rapidly when the bound states become degenerate with the three dimensional bulk states. We could therefore choose to interpret this result as a two dimensional, but *discontinuous*, Fermi surface.

Because of the nature of the charge transfer, we would expect the interfacial cuprate layers to be doped, to varying degrees, with electrons. This would lead to a distinct change in the Fermi surface topology in each layer, until the bulk properties are recovered several layers from the interface. The basic picture that we suggest, in cuprate layers close to the interface, is as follows:

- Far from the interface the bulk properties of YBCO are recovered and the cuprate layers are optimally doped with holes. The Fermi surface of the hole doped compound is fitted to the t-t′-t''-J model to agree with high resolution ARPES performed on untwinned samples.

- Closer to the interface the layers are doped with electrons, bringing them into the underdoped regime. A contraction of the hole-like Fermi surface would be expected, with a reduced spectral weight due to the reduction in the number of mobile charge carriers.

- Next to the interface the Mott insulating parent compound should be recovered, and therefore the Fermi surface should be absent. There may also be an electron doped cuprate layer with a hole-like Fermi surface corresponding to that of the square lattice above half filling.

- The interfacial cuprate layer is heavily doped with electrons and displays the coherent peaks associated with the bound state in the band gap. These peaks have the appearance of a disappearing Fermi surface as they interact with the bulk states emanating form the manganese and decay into the bulk.

- On the manganite side of the interface the three dimensional nature of the electronic states would give rise to an incoherent background. The weight of the incoherent background should be largest at the band edges due to the Van-Hove singularities.

We have superimposed these Fermi surfaces in Fig. 8.10 to give a clearer idea of what we are envisioning. In theory, one could perform ARPES on a thin layer of YBCO superimposed on LCMO and attempt to observe the superposition of Fermi surfaces in the interfacial layers. This simple idea would, unfortunately, be extremely difficult to realise.

The preparation of high quality YBCO samples is complicated by the natural *twinning* (domains orthogonal to each other with respect to the CuO chain orientations) of YBCO crystals, and by the difficulty associated with creating a high quality cleaved surface. These problems would be even more severe if a high quality surface is required close to an interface. Reliable ARPES measurements have been performed on YBCO[127], but the situation is complicated by the presence of an intense peak from a surface state which dominates over the bulk signal. Putting aside these important issues, we would expect that for a thin YBCO layer superimposed on LCMO there would be a discernible signal from the interfacial layers, and an incoherent background from the bulk manganite states. The strength of the signal from each layer is dictated by the electron escape depth, which means that the signal from subsequent layers reduces rapidly as a function of the depth from the YBCO surface. We would therefore expect the signals from each layer to be superimposed with an appropriate weight.

8.5 Summary

In this chapter we have formulated a simple model of a cuprate-manganite interface. This model is based on just two parameters: the crystal field splitting Δ/t and the potential difference Γ/t. The main prediction of this model is that under the condition $\Gamma > t$, there is a significant flow of charge carriers into the interfacial cuprate layer. Then, when $\Delta < t$, the double exchange mechanism overcomes the crystal field splitting, leading to a partial occupation of the $3\hat{z}^2 - 1$ orbital, which is consistent with XAS data. In addition, the spin polarisation of the charge carriers leads to a small magnetic moment in the cuprate layer, which is consistent with PNR data. The model also predicts states which are bound to

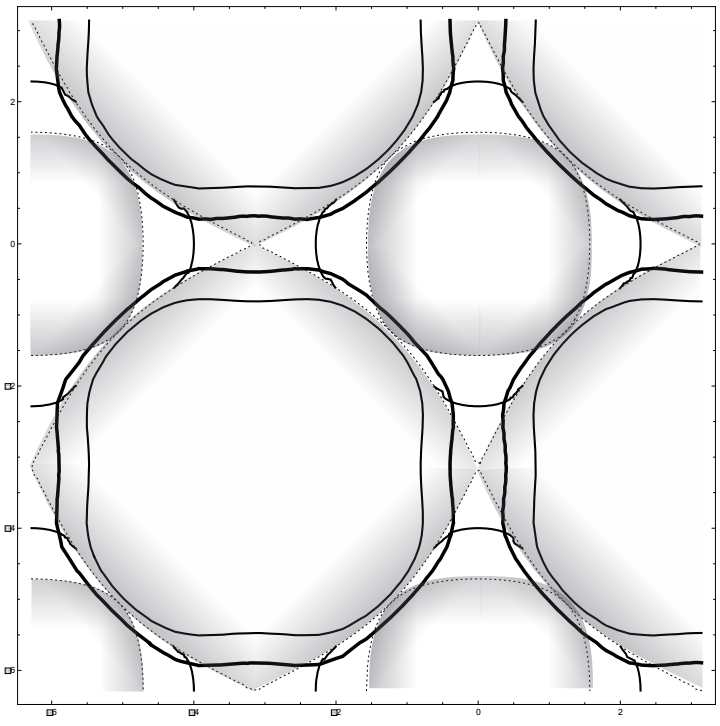

Figure 8.10: A schematic of the superposition of Fermi surfaces from different layers, which may result from ARPES performed at a cuprate-manganite interface. The continuous solid lines represent the Fermi surfaces of the hole doped layers at 30% and 20% hole doping, whilst the discontinuous solid lines represent the coherent states, residing in the band gaps of the manganite, which are bound to the interfacial layers. The shaded regions contain the incoherent background, which is caused by the three dimensional bulk states emanating from the manganite.

the interface and lie in the three dimensional band gap. These states form a distinct, but discontinuous, two dimensional Fermi surface. We have also indicated that, *if* we were able to perform ARPES at the interface, the distribution of charge in the cuprate would lead to an interesting superposition of Fermi surfaces, although the practical realisation of this experiment would probably be prohibitively difficult.

Chapter 9

The interface between STO and LAO

The interface between $SrTiO_3$ (STO) and $LaAlO_3$ (LAO) has been subject to several intriguing experiments which probe the electronic and magnetic properties of the interface on the nanoscale. As a result, a lot of interest has been generated by the discovery of a high mobility two dimensional electron gas, magnetism, and superconductivity. These properties demonstrate that the STO-LAO interface displays exotic properties, which are unique to the interface, and are not found in either of the bulk materials which are both non-magnetic and insulating. In addition, it is also possible to control the doping of the STO by applying electric fields across the interface, so that the STO can be tuned through phase transitions[1]. This ability, to control the diverse physical properties of the STO-LAO interface, clearly illustrates the huge potential of perovskite oxide interfaces in general.

Both STO and LAO are band insulators and are well understood. However, at the interface there is a polar discontinuity, and this is thought to cause an electronic reconstruction. The STO is therefore doped with electrons which partially occupy the titanium t_{2g} orbitals, leading to to a variety of different phases.

In this chapter we give a very brief introduction to the titanates and the three-fold degeneracy of the t_{2g} orbitals. It is the two dimensional nature of the electronic orbitals, and the strong local coulomb repulsion between electrons occupying the same site, which are the most important considerations at the interface. We also examine the chemical and electronic properties of the interface, obtained from EELS measurements, and we look at the experimental evidence for a two dimensional electron gas, superconductivity, and magnetism.

In the final chapter we introduce a simple model of the STO-LAO interface. This model includes the effects of electronic screening, which stabilises the interfacial electronic

[1]This property can been exploited in field effect devices. In these devices charge is forced into the interfacial STO layers, from the LAO, by varying the applied field.

reconstruction, and the two dimensional orbital physics, which governs the electronic motion. To solve this model, and therefore obtain information about the nature of the electronic reconstruction at the interface, we again utilise impurity theory. We find that our model strongly supports the experimental evidence for a two dimensional electron gas, and predicts a threshold for photoemission for two electronic states bound to the interface.

9.1 The titanates

At the STO-LAO interface the interfacial STO layers are doped with electrons and the resulting electronic interactions can be understood by considering the titanates. The titanates are a class of light transition metal oxide which forms in the perovskite crystal structure $R_{1-x}A_xTiO_3$, where R is a trivalent cation, A is a divalent cation, and consequentially Ti is in the mixed valence state Ti^{3+}/Ti^{4+}. The parent compound is a Mott-Hubbard insulator which passes through a metal-insulator transition as holes are added through substition of R cations with A cations[128]. In the titanates the orbital degree of freedom, which has a three-fold degeneracy, is responsible for a variety of anomalous electrical, magnetic and optical properties.

In the series $RTiO_3$, as the radius of R decreases the octahedra rotate, bending the Ti-O-Ti bond and resulting in a smaller hopping matrix element t. This effects the properties of the respective compounds; the ground state of $YTiO_3$ is a ferromagnet with a Curie temperature $T_C = 30K$, whilst for $LaTiO_3$ the ground state is the G-type antiferromagnetic order with a Neél temperature $T_N = 145K$.

In the titanates the electronic motion, which is essentially two dimensional, involves the three-fold degenerate t_{2g} states and the oxygen $2p$ states. Due to symmetry considerations, which are illustrated in Fig. 9.1, there is no hybridisation between the t_{2g} orbitals and the $2p_\sigma$ orbitals. Therefore, if we consider the d_{xy} orbital, then the hybridisation along the x-direction is with the p_y orbital, and the hybridisation along the y-direction is with the p_x orbital. The transfer matrix element involves $t_{pd\pi}$, which is significantly smaller than $t_{pd\sigma}$. Along the z-axis there is no hybridisation between d_{xy} and p_z, and the only non-zero hybridisation involves higher energy oxygen states which can safely be ignored. The hopping between the t_{2g} and the oxygen $2p$ orbitals is illustrated in Fig. 9.1. The Hamiltonian for the titanates may be written in the general form

$$\mathcal{H} = \varepsilon_d \sum_{i\gamma\sigma} d^\dagger_{i\gamma\sigma} d_{i\gamma\sigma} + \sum_{\langle ij\rangle\gamma\gamma'\sigma} \left(t^{\gamma\gamma'}_{ij} d^\dagger_{i\gamma\sigma} d_{j\gamma'\sigma} + h.c. \right) + \mathcal{H}_{el-el}, \tag{9.1}$$

where the electronic correlations are represented by $\mathcal{H}_{el-el}$. These correlations lead to a

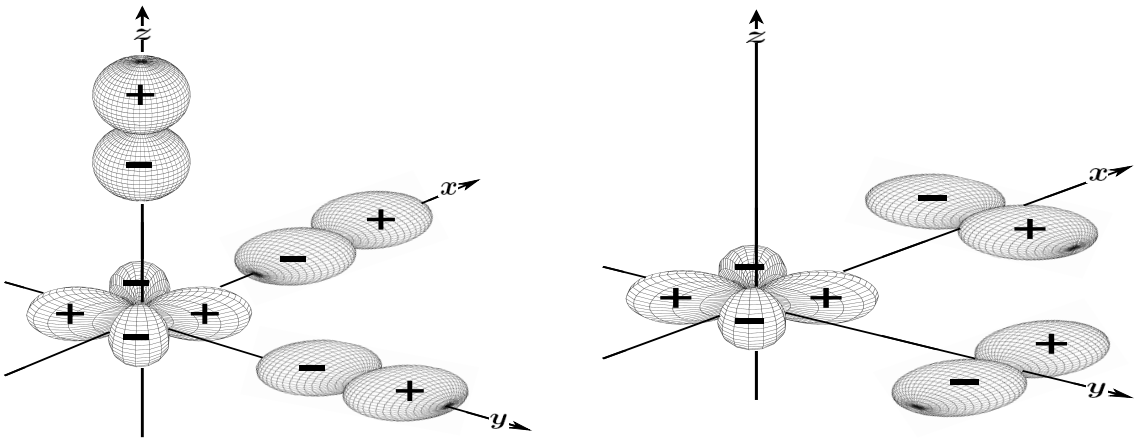

(a) The hybridisation between the t_{2_g} orbitals and the oxygen $2p_\sigma$ orbitals. Due to the symmetry of the orbitals the d_{xy} orbital does not hybridise with any of the $2p_\sigma$ orbitals in the x-y plane, or along the z-axis.

(b) The hybridisation between the t_{2_g} orbitals and the oxygen $2p_\pi$ orbitals. The d_{xy} orbital hybridises with both the $2p_\pi$ orbitals in the x-y plane, but, because of symmetry, does not hybridise with the $2p_\pi$ orbitals along the z-axis.

Figure 9.1: Hybridisation in the titanates.

complicated set of superexchange interactions[129] which, in analogy to the manganites, encourage orbitally ordered states. In reality, the degeneracy of the t_{2g} states is removed by both the spin-orbit coupling, and a weak Jahn-Teller distortion. The size of the energy level splitting is believed to be larger than the energy gained from quantum fluctuations of the orbital states, which suggests that the ground state should be orbitally ordered, rather than an orbital liquid. Orbital order has indeed been observed using resonant x-ray spectroscopy (RXS)[130] and polarised neutron scattering[131].

9.2 $LaAlO_3$ and $SrTiO_3$

$LaAlO_3$ ($La^{3+}Al^{3+}O_3^{2-}$) is a conventional band insulator with a gap of about 5.6eV between the filled O $2p$ bands hybridised with Al p bands and and unfilled Al $3s$, $3p$ and La $5d$ conduction bands. $SrTiO_3$ ($Sr^{2+}Ti^{4+}O_3^{2-}$) is also a band insulator with a band gap of 3.2eV between filled O $2p$ bands and unfilled Ti $3d$ conduction bands[132]. The lattice constant for $LaAlO_3$ is estimated to be $a = 3.79$Å, whilst for $SrTiO_3$ it is estimated to be $a = 3.92$Å, which implies a lattice parameter mismatch of about 4%.

Despite the fact that $SrTiO_3$ is a paraelectric, the crystal lattice of $SrTiO_3$ makes it susceptible to a ferroelectric transition. In fact, the transition can be realised under a variety of circumstances: under tensile or compressive strain[133, 134], under an external electric field[135], at a surface[136], or with isotope substitution[137]. In addition, upon doping with oxygen vacancies, $SrTiO_3$ becomes a high mobility metal, or even a

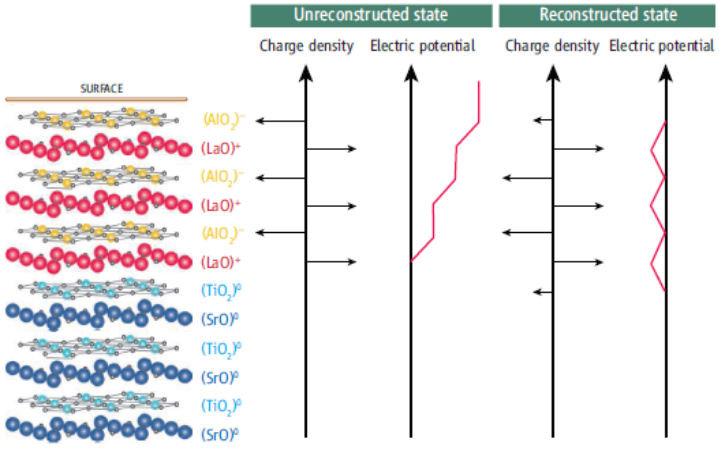

Figure 9.2: From [138](left) The ideal n-type STO-LAO interface. (middle) The charge distribution of the unreconstructed interface leads to a diverging electric potential. (right) Above a threshold thickness the charge distribution reconstructs, removing the diverging potential. The divergence can be removed by transferring half the charge from the surface to the interfacial TiO_2 layer.

superconductor at low temperatures.

9.3 The $LaAlO_3$-$SrTiO_3$ interface

LAO consists of alternating layers of $(LaO)^{-1}$, which is negatively charged, and $(AlO_2)^{+1}$, which is positively charged. The situation in STO is quite different, with alternating layers of SrO and TiO_2, both of which are charge neutral. If, when considering the STO-LAO interface, we treat the individual layers as flat sheets of charge, then the result is a *polar catastrophe*[138]: a divergent electric potential on the LAO side of the interface, as illustrated in Fig. 9.2. This situation, which is a general feature of a polar interface, quickly becomes energetically unfavourable as the number of LAO layers increases. To avoid a polar catastrophe there must be a redistribution of charge to remove the divergence in the electric potential. In a conventional semiconductor this redistribution is achieved through an *atomic* reconstruction, which changes the interface stoichiometry and usually leads to interface roughening and diffusion. However, in perovskite oxide interfaces, it is possible to achieve a suitable redistribution of charge with an *electronic* reconstruction: in this case the necessary charge is accommodated by the mixed valence states, such as Ti^{3+} and Ti^{4+}, of the transition metal ions. Whether the redistribution of charge is actually achieved via an electronic reconstruction, as opposed to an atomic reconstruction, is thought to depend on the sample preparation. In non-annealed samples oxygen vacancies diffuse across the interface, resulting in very high mobilities in the interfacial layers. In annealed samples, without the oxygen vacancies, the charge transfer is believed to occur above a threshold thickness of the LAO layer. This is consistent with an electronic reconstruction, whereby the diverging electric potential eventually forces the doping of the STO. The mobilities achieved in annealed samples are significantly less impressive than in the non-annealed samples.

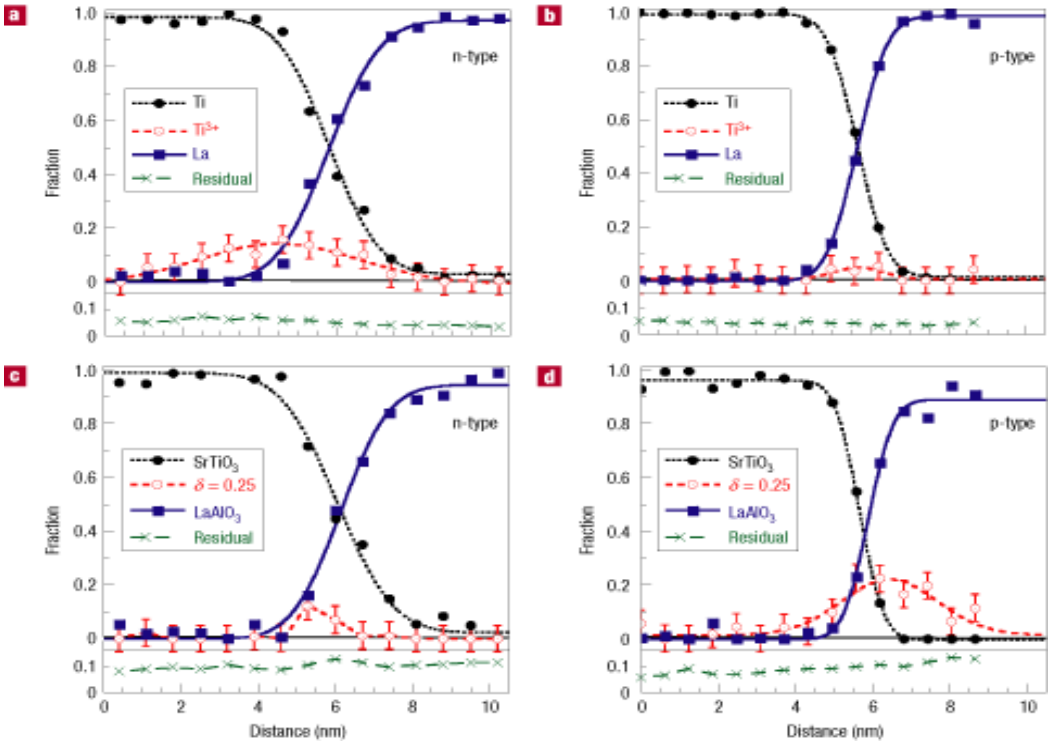

Figure 9.3: From [139]. EELS performed at the STO-LAO interface. (a) $AlO_2/LaO/TiO_2$ interface showing the fraction of Ti^{3+}. (b) $AlO_2/SrO/TiO_2$ interface showing the fraction of Ti^{3+}. (c) $AlO_2/LaO/TiO_2$ interface showing the fraction of oxygen vacancies. (d) $AlO_2/SrO/TiO_2$ interface showing the fraction of oxygen vacancies.

The nature of the STO-LAO interface depends on the terminating layer of STO; the interface is expected to be p-type, when the terminating layer is SrO, or n-type, when the terminating layer is TiO_2. The p-type interface, which is believed to be dominated by the oxygen vacancies arising from an atomic reconstruction, is an insulator. The n-type interface is reported to be conducting[49], with electrons residing in the Ti dominated $3d$ conduction band. Atomic resolution EELS measurements[139] on annealed samples show the chemical compositions of the n-type and p-type interfaces. The fraction of Ti^{3+} and the fraction of oxygen vacancies are also determined, by comparing with appropriate reference materials. Significantly, the measurements reveal a significant density of Ti^{3+} states, confined to within a few nanometres of the n-type interface, but a relatively low density of oxygen vacancies. This can be contrasted with the p-type interface which shows only a small fraction of Ti^{3+}, but has a larger fraction of oxygen vacancies. The properties of the n-type interface are therefore consistent with an electronic reconstruction.

9.3.1 The two dimensional electron gas

The resistance profile of the n-type STO-LAO interface has been determined[140] using a conducting tip atomic force electron microscope (CT-AFM). In samples prepared without annealing (Fig. 9.4(a)) the resistance profile consists of two parts: the bulk STO substrate, which is conducting due to the high diffusion coefficient of oxygen vacancies which extend into the bulk, and the interface, which has much lower resistance than the bulk. The non-annealed samples are estimated to have a remarkably high sheet carrier density $n_{sheet} = 3\times 10^{17}$ cm^{-2} at room temperature. In annealed samples (Fig. 9.4(b)) the oxygen vacancies are eliminated and the result is a high mobility electron gas confined to within about 7nm of the interface. The sheet carrier density of the annealed sample is substantially reduced, and estimated to be $n_{sheet} = 5 \times 10^{14}$ cm^{-2} which is consistent with an electronic reconstruction ($n_{sheet} = 3 \times 10^{14}$ cm^{-2}).

9.3.2 Magnetism at the interface

A large negative magnetoresistance has been observed at the STO-LAO interface[51], at temperatures below 1K. It has been speculated that the negative magnetoresistance is an artefact of the *Kondo effect*[141] arising from interactions between itinerant electrons and localised magnetic moments; as a consequence of the finite Zeeman splitting between spin up and spin down energy levels, under an applied field, the spin-flip scattering with localised moments is suppressed at the Fermi level. The large negative magnetoresistance can therefore be attributed to an enhancement of the coherent motion of electrons due to the ferromagnetic alignment of the spins.

It has been pointed out that, to account for the large magnetoresistance, the Kondo effect would require a large fraction of localised magnetic moments: approximately 10%, as observed in interfaces doped with magnetic ions such as Cr^{3+}[142]. These moments are thought to arise as a result of the charge transfer associated with the polar discontinuity. However, this result is still unexpected since electrons doped into STO typically occupy hybridised *spd* bands, rather than localised $3d$ orbitals with a spin-1/2 localised moment. Theoretical calculations[132] predict that the doped electrons occupy $3d$ dominated conduction bands and make the interfacial TiO_2 layer a ferromagnetic metal.

The mobility of STO-LAO interfaces delta-doped with magnetic cations such as Mn and Co has also been reported[143]. Interestingly, the insertion of a single 2% Mn doped unit cell of STO (STO/Mn-STO/LAO) radically alters the carrier density and mobility of charge carriers. This observation not only suggests that the electron gas is confined to within about one unit cell of the interface, but also indicates that the insertion of a small number of magnetic impurities can drastically alter the scattering between electrons and

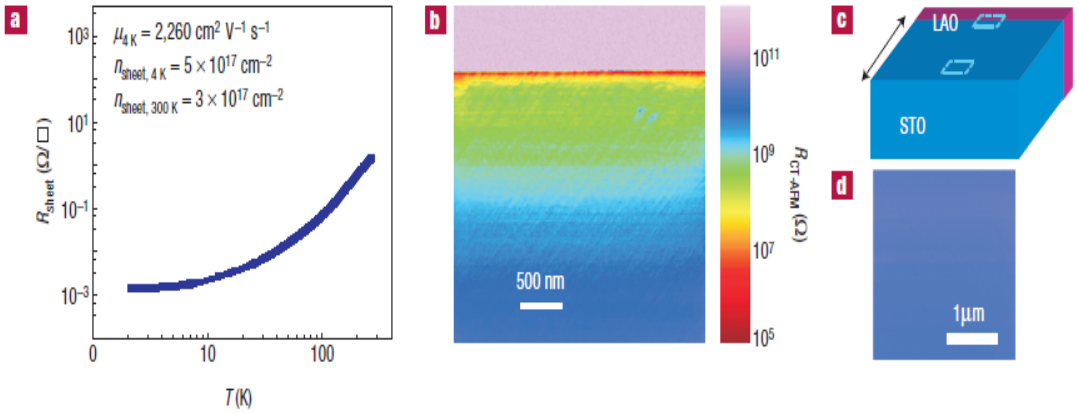

(a) Non-annealed interface[140] (a) Temperature dependence of the sheet resistance R_{sheet}. (b) CT-AFM resistance mapping around the interface. (c) Schematic illustration of the sample and CT-AFM scans. (d) CT-AFM scan $\sim 500\mu$m away from the interface.

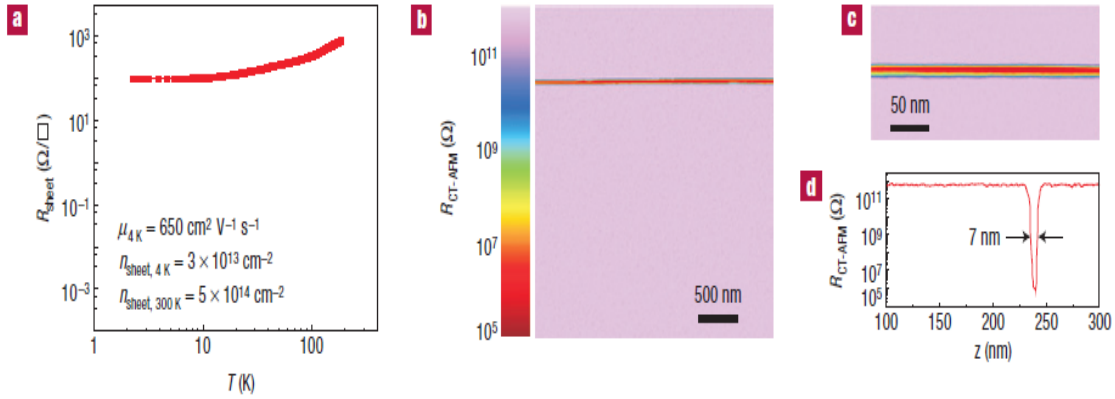

(b) Annealed interface[140] (a) Temperature dependence of the sheet resistance R_{sheet}. (b) CT-AFM resistance mapping around the interface. (c) High resolution CT-AFM scan. (d) Resistance profile across the interface.

Figure 9.4: Resistance profiles of the STO-LAO interface.

localised moments in the interfacial layers.

9.3.3 Electronic phase diagram of the interface

The superconductivity observed at the STO-LAO interface[145] indicates that the ground state is sensitive to small changes in the carrier concentration. This property has since been utilised in field effect devices[144], constructed from $SrTiO_3$ and $LaAlO_3$, for which the concentration of charge carriers is modulated by applying an electric field. The resulting phase diagram is illustrated in Fig. 9.5.

As the gate voltage is varied between -300V and 320V the system transits from an insulating ground state to a superconducting ground state, with a maximum critical tem-

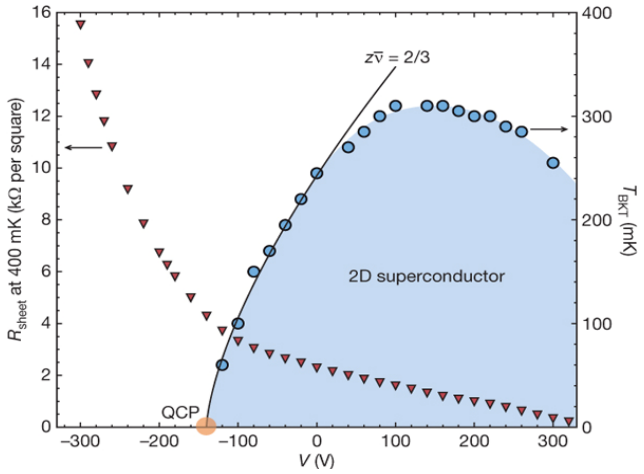

Figure 9.5: Electronic phase diagram of the STO-LAO interface[144]. The critical temperature T_{BKT} is plotted against gate voltage, revealing the superconducting region of the phase diagram. The solid line approaches the quantum critical point using the scaling relation $T_{BKT} \propto (V - V_c)^{z\nu}$, with $z\nu = 2/3$. Also plotted is the normal sheet resistance, measured at 400K, as a function of gate voltage.

perature of ∼310mK. Close to the quantum critical point the dependence of the transition temperature on the applied field, which is itself proportional to the carrier density, is consistent with a *Kosterlitz-Thouless*[146] transition for a thin film superconductor.

Chapter 10

Model of the interface between STO and LAO

In this chapter we investigate the charge bound to an interface between $SrTiO_3$ and $LaAlO_3$. We employ an elementary model which incorporates just two pieces of physics: We include the charging energy of the surface, which compensates the long range coulomb interactions caused by the polar discontinuity, and we include the three t_{2g} orbitals. The strong local Coulomb interactions are omitted, in spite of their obvious importance, but we find that the model still displays rich behaviour which must be considered when more sophisticated models are developed.

We find three different types of behaviour, depending on the doping of the t_{2g} orbitals. At very low doping we find a phase where only the orbital which delocalises in the plane parallel to the interface is occupied. The state extends exponentially into the bulk and the chemical potential tends to the bottom of the band. At intermediate doping we find a phase in which all of the orbitals are occupied and the previously occupied orbitals become *trapped*, next to the interface, in a *finite* number of layers. This coincides with the opening of a *gap* between the energy of the interface electrons and the energy of the bulk states. Finally, at higher doping the gap closes and all orbitals extend exponentially into the bulk.

10.1 Modelling the interface

The early first row transition metal oxides are dominated by t_{2g} electrons which occupy the $\hat{x}\hat{y}$, $\hat{y}\hat{z}$ and $\hat{z}\hat{x}$ orbitals. These states have the lowest crystal-field energy and are therefore the only states which justify consideration. The electrons move via the hybridisation with the intermediate oxygen ions, but have only a weak effective hopping energy of less than 0.1eV. The orbitals are essentially two dimensional and the hopping is therefore very

anisotropic, with electrons of each type delocalising in an appropriate two dimensional plane of the crystal. This property has some consequences at the interface; the $\hat{x}\hat{y}$ orbitals move in the plane parallel to the interface and do not notice it, whereas the $\hat{y}\hat{z}$ and $\hat{z}\hat{x}$ orbitals move in planes perpendicular to the interface, and crash into it.

10.1.1 Screening

The *classical* coulomb problem amounts to solving Poisson's equation:

$$\frac{d^2}{dx^2}\frac{\partial E}{\partial \rho(x)} = \rho(x). \tag{10.1}$$

The energy, $E(\rho(x))$, is a local density approximation for the energy of the electrons as a function of their density, $\rho(x)$:

$$E = \int \rho(x)\phi(x)dx. \tag{10.2}$$

If there is a small perturbation away from an otherwise uniform density, then the problem linearises and we find an exponential screening length. However, at an interface the energy dependence is dictated by the behaviour of $E(\rho)$ at the bottom of the energy band. At the bottom of the band, in d dimensions, we may expand the energy as

$$\epsilon_{\mathbf{k}} = \sum_{i=1}^{d} \alpha_i k_i^2 + \cdots \tag{10.3}$$

The corresponding charge density is

$$\rho(\epsilon) \approx \int \frac{d\mathbf{k}}{(2\pi)^d}\delta\left(\epsilon - \sum_{i=1}^{d}\alpha_i k_i^2\right) = \prod_{i=1}^{d}\alpha_i^{-1/2}\int \frac{d\mathbf{q}}{(2\pi)^d}\delta(\epsilon - q^2)$$

$$\propto \int q^{d-1}dq\delta(\epsilon - q^2) \propto \epsilon^{\frac{d}{2}-1}. \tag{10.4}$$

We therefore find that

$$E(\rho) \sim \rho^{1+\frac{2}{d}} \Rightarrow \frac{\partial E}{\partial \rho} \sim \rho^{\frac{2}{d}}. \tag{10.5}$$

In two dimensions the screening leads to an exponential decay of the charge density, whilst in three dimensions the screening is far less effective, such that $\rho(x) \sim 1/x^6$. In the STO we employ two dimensional orbitals and would therefore expect to find an exponential decay of the charge density on the STO side of the interface. However, we find that the inequivalent screening from electrons in the different orbitals results in a charge distribution which differs from this simple result.

10.1.2 Mean field Hamiltonian for the interface

We place the interface perpendicular to the z-axis and restrict attention to the t_{2g} orbitals. The largest electronic hopping terms are between equivalent orbitals, so we include only the diagonal hopping elements in our model. The local coulomb interactions between electrons occupying the same atom are the largest energies, and they must be expected to lead to strong coupling physics. In this investigation we ignore the local coulomb interactions, but deal with the hopping and charging actively. We employ the following tight-binding Hamiltonian for the electronic hopping:

$$\mathcal{H}_0 = -t \sum_{\langle jj' \rangle_x \sigma} x^\dagger_{j\sigma} x_{j'\sigma} - t \sum_{\langle jj' \rangle_y \sigma} y^\dagger_{j\sigma} y_{j'\sigma} - t \sum_{\langle jj' \rangle_z \sigma} z^\dagger_{j\sigma} z_{j'\sigma}, \tag{10.6}$$

where $x_{j\sigma}$ annihilates a d_{yz} electron with spin σ, $y_{j\sigma}$ annihilates a d_{zx} electron with spin σ and $z_{j\sigma}$ annihilates a d_{xy} electron with spin σ. The notation $\langle jj' \rangle_x$ denotes nearest neighbours perpendicular to the x-axis, $\langle jj' \rangle_y$ denotes nearest neighbours perpendicular to the y-axis and $\langle jj' \rangle_z$ denotes nearest neighbours perpendicular to the z-axis. The z electrons are constrained to lie in planes parallel to the interface and are oblivious to it, whilst y and z electrons lose hybridisation at the surface and consequentially avoid it to some extent, treating it as a potential barrier. However, if their is sufficient charging to compensate for the loss of hybridisation, electrons will be bound to the interface.

We assume that the system retains both spin and charge symmetry and consequentially that the most important variation is in the charge densities per layer. Therefore

$$\boldsymbol{\rho}^{\parallel}_n = 2\langle z^\dagger_{j_n\sigma} z_{j_n\sigma} \rangle \qquad \boldsymbol{\rho}^{\perp}_n = 2\langle x^\dagger_{j_n\sigma} x_{j_n\sigma} \rangle = 2\langle y^\dagger_{j_n\sigma} y_{j_n\sigma} \rangle, \tag{10.7}$$

where n labels the layer and j_n is any site in the n-th layer. The total density is therefore

$$\boldsymbol{\rho}_n = \boldsymbol{\rho}^{\parallel}_n + 2\boldsymbol{\rho}^{\perp}_n. \tag{10.8}$$

To model the long range coulomb interactions we adopt a capacitor-like view of layers of uniformly distributed charge. The polar nature of the LAO side of the interface can be accommodated with a single residual positive charge $\boldsymbol{\rho}_0$, which lowers the potential for the charge carriers on the STO side of the interface. Using this model for the polar interface, which is illustrated in Fig. 10.1, the charging energy per atom in a layer is found to be

$$E_1 = \frac{\Delta}{2} \left(\sum_{n=1}^{\infty} \boldsymbol{\rho}_0 \boldsymbol{\rho}_n (n - \lambda) - \sum_{n=1}^{\infty} \boldsymbol{\rho}_n \sum_{m=n+1}^{\infty} \boldsymbol{\rho}_m (m - n) \right), \tag{10.9}$$

where Δ sets the scale for the coulomb interaction, $\boldsymbol{\rho}_0$ is the positive charge density in the $LaAlO_3$ and λ is the effective position of the positive charge. The appropriate value for Δ

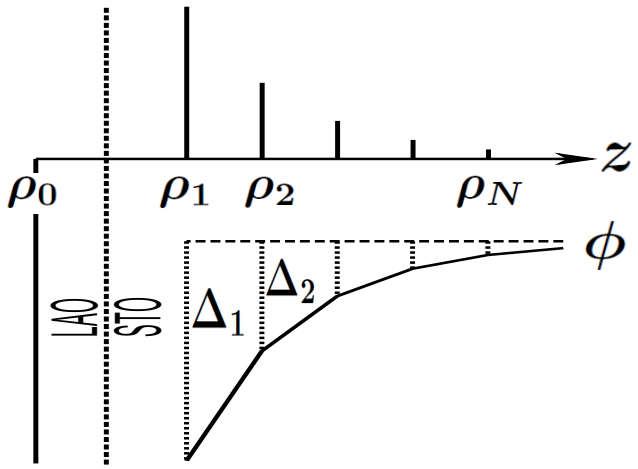

Figure 10.1: Model of an electronic reconstruction at the polar STO-LAO interface. The positive charge, $\boldsymbol{\rho}_0$, from the LAO is screened by the exponentially decaying electronic charges, $\boldsymbol{\rho}_1 \cdots \boldsymbol{\rho}_N$, in the TiO_2 layers of the STO. The result, is a lowering of the potentials in the TiO_2 layers by $\Delta_1 \cdots \Delta_N$. In the limit $N \to \infty$, the charge, $\boldsymbol{\rho}_N$, tends to zero, whilst the potential, ϕ, tends to the bulk value.

is subtle and can be chosen to include the screening effects of lattice polarisation, which are known to be quite large[147], by incorporating an effective dielectric constant[148]. The Coulomb energy will be treated in mean field theory. We write the energy as a functional of the charge densities, $E \equiv E(\boldsymbol{\rho}_n)$, and minimise the energy with a unitary transformation. The effective mean field Hamiltonian is then

$$\mathcal{H}_{mf} = \sum_n \frac{\partial E_1}{\partial \boldsymbol{\rho}_n} \hat{\boldsymbol{\rho}}_n + E_1 - \sum_n \frac{\partial E_1}{\partial \boldsymbol{\rho}_n} \boldsymbol{\rho}_n. \tag{10.10}$$

Each layer feels an effective potential of the form

$$\frac{\partial E_1}{\partial \boldsymbol{\rho}_n} = \frac{\Delta}{2} \left(\boldsymbol{\rho}_0 (n - \lambda) - \sum_{m=n+1}^{\infty} \boldsymbol{\rho}_m (m - n) - \sum_{m=1}^{n-1} \boldsymbol{\rho}_m (n - m) \right). \tag{10.11}$$

In the limit that the number of layers becomes infinite, the potential is only physical if

$$\boldsymbol{\rho}_0 = \sum_{m=1}^{\infty} \boldsymbol{\rho}_m, \tag{10.12}$$

so that the charge bound to the interface exactly compensates the associated positive trapping charge. Defining

$$\Delta_n = \Delta \sum_{m=n+1}^{\infty} \boldsymbol{\rho}_m (m - n) \tag{10.13}$$

we can then rewrite the effective potential as

$$\frac{\partial E_1}{\partial \boldsymbol{\rho}_n} = -\frac{\Delta}{2} \lambda \boldsymbol{\rho}_0 + \frac{\Delta_0}{2} - \Delta_n. \tag{10.14}$$

Finally, we find that the Hamiltonian is

$$\mathcal{H}_{mf} = -\frac{\Delta}{2}\lambda\boldsymbol{\rho}_0^2 + \frac{1}{2}\Delta_0\boldsymbol{\rho}_0 + \frac{1}{2}\sum_{n=1}^{\infty}\Delta_n\boldsymbol{\rho}_n + \mathcal{H}_{eff}, \tag{10.15}$$

where

$$\mathcal{H}_{eff} = \mathcal{H}_0 - \sum_{n=1}^{\infty}\Delta_n\sum_{j_n\sigma}\left(x^\dagger_{j_n\sigma}x_{j_n\sigma} + y^\dagger_{j_n\sigma}y_{j_n\sigma} + z^\dagger_{j_n\sigma}z_{j_n\sigma}\right). \tag{10.16}$$

The above Hamiltonian must be solved, subject to the constraint that the total charge in a layer perpendicular to the interface is ρ_0, self consistently for all layer densities $\boldsymbol{\rho}_n$. There are essentially two parameters in the model: the relative strength of the coulomb interaction, $\frac{\Delta}{t}$, and $\boldsymbol{\rho}_0$, the charge density. In this investigation we study the phase diagram over both of these quantities.

10.1.3 The z-electrons

The analysis of the z-electrons is straightforward, since each layer has its own local potential. The dispersion of the z-electrons therefore corresponds to that of the square lattice, so we simply fill up all of the states in each layer, up to a global chemical potential. The formulae for the occupation number and the total energy for the square lattice may be written in the form

$$N_2(\epsilon) = 1 - \frac{2}{\pi}\int_0^1\frac{dx}{s}\ln\left(\frac{1+s}{1-[1-\frac{\epsilon}{4}]\frac{s^2}{2}+s\left[\frac{\epsilon}{4}+[1-\frac{\epsilon}{4}]^2\frac{s^2}{4}\right]^{\frac{1}{2}}}\right) \tag{10.17}$$

$$E_2(\epsilon) = -\frac{16}{\pi}\int_0^1\frac{dx}{s^2}\left(1-\left[\frac{\epsilon}{4}+[1-\frac{\epsilon}{4}]^2\frac{s^2}{4}\right]^{\frac{1}{2}}\right)$$

$$+\frac{16}{\pi}\int_0^1\frac{dx}{s^2}\left[\frac{1}{s}-\frac{s}{2}\right]\ln\left(\frac{1+s}{1-[1-\frac{\epsilon}{4}]\frac{s^2}{2}+s\left[\frac{\epsilon}{4}+[1-\frac{\epsilon}{4}]^2\frac{s^2}{4}\right]^{\frac{1}{2}}}\right), \tag{10.18}$$

with

$$s = \sin\left(\frac{\pi x}{2}\right). \tag{10.19}$$

The occupation number and the total energy are depicted in Fig. 10.2. These formulae are valid for $\epsilon \geq 0$, but for negative energies we use the symmetries $N_2(-\epsilon) = \frac{1}{2} - N_2(\epsilon)$ and $E_2(-\epsilon) = E_2(\epsilon)$. The charge on each layer is

$$\boldsymbol{\rho}_n^{\|} = 2N_2\left(\frac{\mu}{t}+\frac{\Delta_n}{t}\right) \tag{10.20}$$

and the energy from a single plane is

$$\epsilon_n^{\parallel} = 2\left(tE_2\left(\frac{\mu}{t}+\frac{\Delta_n}{t}\right)+\Delta_n N_2\left(\frac{\mu}{t}+\frac{\Delta_n}{t}\right)\right). \tag{10.21}$$

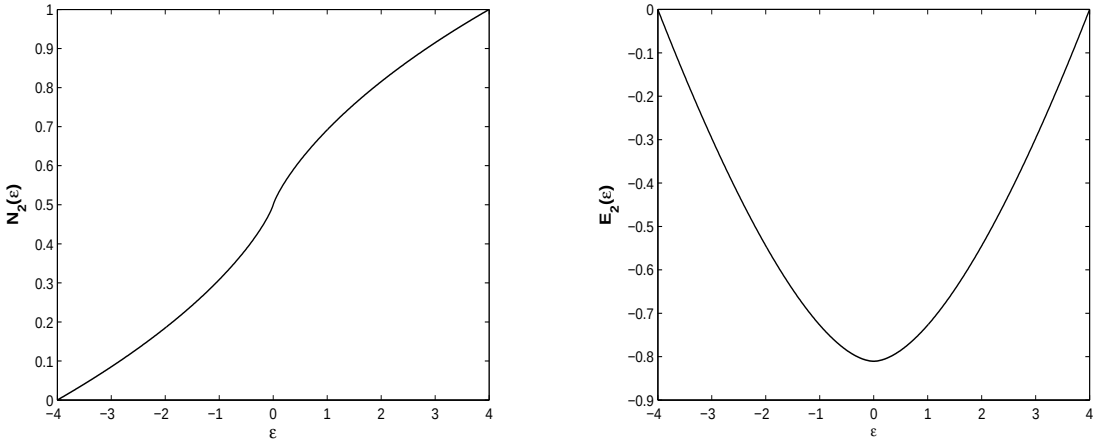

(a) The occupation number for the square lattice.

(b) The total energy for all of the electronic states in the square lattice.

Figure 10.2: Occupation number and total energy for the square lattice.

10.1.4 The x- and y-electrons

The calculation for the number of x and y electrons, moving in the planes perpendicular to the interface, is more involved. The symmetry remains parallel to the interface and can be incorporated using a one dimensional dispersion. The number and total energy formulae for the one dimensional chain are

$$N_1(\epsilon) = 1 - \frac{1}{\pi}\cos^{-1}\left(\frac{\epsilon}{2}\right) \tag{10.22}$$

$$E_1(\epsilon) = -\frac{1}{\pi}[4-\epsilon^2]^{\frac{1}{2}}. \tag{10.23}$$

The occupation number and the total energy are depicted in Fig. 10.3. These formulae are valid for $\epsilon \geq 0$, but for negative energies we use the symmetries $N_1(-\epsilon) = \frac{1}{2} - N_1(\epsilon)$ and $E_1(-\epsilon) = E_1(\epsilon)$.

The symmetry perpendicular to the interface is broken, by both the interface and by the lowering of the effective potentials in each layer by Δ_n, and bound states are created close to the interface. To obtain the energies of these bound states we first require the resolvent for the semi-infinite plane. This is similar to the resolvent for the semi-infinite

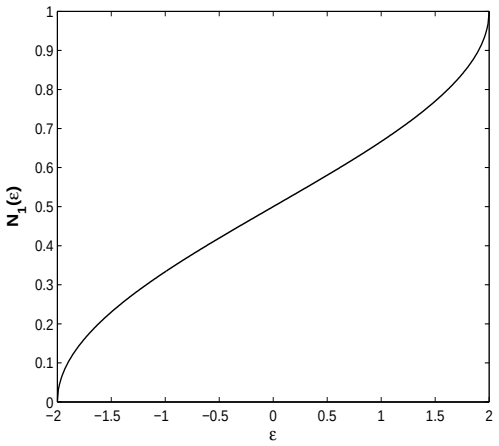

(a) The occupation number for the one dimensional chain.

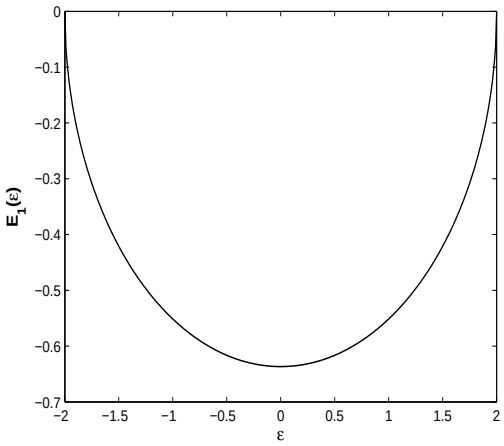

(b) The total energy for all of the electronic states in the one dimensional chain.

Figure 10.3: Occupation number and total energy for the one dimensional chain.

chain, which was derived in chapter 6, but with the dependence on the momentum parallel to the interface, $k_{\|}$, implicitly included. We find

$$\mathcal{G}_0(\tilde{z})_{nn'} = \frac{X^{|n-n'|} - X^{n+n'}}{X - \frac{1}{X}}, \tag{10.24}$$

where we have suppressed the label $k_{\|}$ to simplify the notation. In analogy with the one dimensional case, X is given by

$$X = -\frac{\tilde{z}}{2} + \frac{\sqrt{|\tilde{z}^2 - 4|}}{2}. \tag{10.25}$$

The energy is measured in units of t and, because of the electronic motion parallel to the interface, is also renormalised to $\tilde{z} = z - 2\cos(k_{\|})$. The positive charge on the LAO side of the interface lowers the potential in the n-th layer by Δ_n. We can model this effect by employing impurity theory, which can be used to place a unique impurity on each layer to lower the potential by the appropriate amount. The lowering of the potentials also leads to electronic states which are bound to the interface, and impurity theory will also be used to investigate these states.

We begin by considering N TiO_2 layers, next to the interface, which are effected by the positive charge in the LAO. To calculate the electronic properties around the interface we only require the *projected* resolvent, which will provide us with the *local* charge and orbital character of each of the N layers. The projected resolvent for the modified system, i.e the semi-infinite plane in the presence of the impurity potential $\mathcal{H}_1$, is given (from chapter 6) by

$$\mathcal{G}^{\mathcal{P}}(\tilde{z}) = [(\mathcal{G}_0^{\mathcal{P}}(\tilde{z}))^{-1} - \mathcal{H}_1]^{-1}. \tag{10.26}$$

The impurity potential lowers the potential in each layer by the appropriate amount:

$$\mathcal{H}_1 = \begin{pmatrix} -\Delta_1 & 0 & 0 & \cdots & 0 & 0 \\ 0 & -\Delta_2 & 0 & \cdots & 0 & 0 \\ \vdots & \vdots & \vdots & \ddots & \vdots & \vdots \\ 0 & 0 & 0 & \cdots & -\Delta_{N-1} & 0 \\ 0 & 0 & 0 & \cdots & 0 & -\Delta_N \end{pmatrix}. \tag{10.27}$$

To determine the projected resolvent for the complete system, using Eq. 10.26, we first require the projected resolvent for the reference system, $\mathcal{G}_0^{\mathcal{P}}$. When we invert this, we obtain

$$(\mathcal{G}_0^{\mathcal{P}}(\tilde{z}))^{-1} = \begin{pmatrix} \tilde{z} & 1 & 0 & \cdots & 0 & 0 \\ 1 & \tilde{z} & 1 & \cdots & 0 & 0 \\ \vdots & \vdots & \vdots & \ddots & \vdots & \vdots \\ 0 & 0 & 0 & \cdots & \tilde{z} & 1 \\ 0 & 0 & 0 & \cdots & 1 & \frac{1}{2}\left(\tilde{z} + \sqrt{\tilde{z}^2 - 4}\right) \end{pmatrix}, \tag{10.28}$$

where the energy is measured in units of t. Except for the last term, this resolvent is of a simple form that corresponds to an open chain consisting of N sites. The fact that the N-th layer is connected to the bulk simply means that the last term is changed from $\tilde{z}$ to $\frac{1}{2}\left(\tilde{z} + \sqrt{\tilde{z}^2 - 4}\right)$, and when a large number of layers are included this change obviously becomes insignificant. The projected resolvent for the modified system, in the presence of the impurity, is

$$\mathcal{G}^{\mathcal{P}}(\tilde{z}) = \begin{pmatrix} \tilde{z} + \Delta_1 & 1 & 0 & \cdots & 0 & 0 \\ 1 & \tilde{z} + \Delta_2 & 1 & \cdots & 0 & 0 \\ \vdots & \vdots & \vdots & \ddots & \vdots & \vdots \\ 0 & 0 & 0 & \cdots & \tilde{z} + \Delta_{N-1} & 1 \\ 0 & 0 & 0 & \cdots & 1 & \frac{1}{2}\left(\tilde{z} + \sqrt{\tilde{z}^2 - 4}\right) + \Delta_N \end{pmatrix}^{-1}. \tag{10.29}$$

To obtain $\mathcal{G}^{\mathcal{P}}(\tilde{z})$ we need to invert this tri-diagonal matrix. Fortunately, because of the simple form of this matrix, we can conveniently perform the inversion using the formula[1]

$$\mathcal{G}^{\mathcal{P}}(\tilde{z}) = \frac{\mathrm{Adj}((\mathcal{G}_0^{\mathcal{P}}(\tilde{z}))^{-1} - \mathcal{H}_1)}{\mathrm{Det}||(\mathcal{G}_0^{\mathcal{P}}(\tilde{z}))^{-1} - \mathcal{H}_1||}. \tag{10.30}$$

[1]We are simply utilising the general formula $\mathcal{A}^{-1} = \mathrm{Adj}(\mathcal{A})/\mathrm{Det}||\mathcal{A}||$.

We can use this formula to calculate the diagonal matrix elements, $\mathcal{G}^{\mathcal{P}}(\tilde{z})_{nn}$, which will provide the necessary information necessary for calculating the charge and orbital character in each of the N layers. We obtain

$$\mathcal{G}^{\mathcal{P}}(\tilde{z})_{nn} = \frac{1}{\tilde{z} + \Delta_n - s_n - r_n}, \tag{10.31}$$

where we have introduced the parameters s_n and r_n. The values of these parameters for a particular n are determined using following recurrence relations

$$s_n(\tilde{z}) = \tilde{z} + \Delta_N - \frac{1}{s_{n+1}(\tilde{z})} \qquad \text{with} \qquad s_N(\tilde{z}) = \frac{1}{2}\left(\tilde{z} + \sqrt{\tilde{z}^2 - 4}\right) + \Delta_N \tag{10.32}$$

$$r_n(\tilde{z}) = \tilde{z} + \Delta_N - \frac{1}{r_{n-1}(\tilde{z})} \qquad \text{with} \qquad r_1(\tilde{z}) = \tilde{z} + \Delta_1. \tag{10.33}$$

So s_n is determined iteratively, starting from s_N, whilst r_n is determined iteratively, starting from r_1. Incorporating an arbitrarily large number of impurity potentials using this method is straightforward and we can therefore approach the limit $N \to \infty$. The energies, E, of the bound states correspond to the poles of $\mathcal{G}^{\mathcal{P}}(\tilde{z})$, which appear whenever

$$\mathrm{Det}||(\mathcal{G}_0^{\mathcal{P}}(E))^{-1} - \mathcal{H}_1|| = s_1 s_2 \cdots s_N = 0. \tag{10.34}$$

Equivalently, but more conveniently, we can instead solve

$$s_1(E) = 0. \tag{10.35}$$

Once we have determined the energies, we then need to find the number of x- and y-electrons occupying each layer. The resulting charge, $\boldsymbol{\rho}_n^{\perp}$, can determined from the diagonal components of the resolvent. The charge in the n-th layer is

$$\begin{aligned}
\boldsymbol{\rho}_n^{\perp} &= \int_{-\pi}^{\pi} \frac{dk_{\parallel}}{2\pi} \int_{-\infty}^{\infty} d\epsilon f\left(\frac{\epsilon}{t} - \frac{\mu}{t}\right) \rho_n\left(\frac{\epsilon}{t} - 2\cos(k_{\parallel})\right) \\
&= \int_{-\pi}^{\pi} \frac{dk_{\parallel}}{2\pi} H\left(\frac{E}{t} + 2\cos(k_{\parallel}) - \frac{\mu}{t}\right) \left(\operatorname*{Res}_{\frac{\epsilon}{t}=E} \mathcal{G}_{nn}^{\mathcal{P}}\left(\frac{\epsilon}{t}\right)\right) \\
&= 2N_1 \left(\frac{\mu}{t} - \frac{E}{t}\right) \frac{1}{\frac{ds_n}{d\tilde{z}}\left(\frac{E}{t}\right) + \frac{dr_n}{d\tilde{z}}\left(\frac{E}{t}\right) - 1},
\end{aligned} \tag{10.36}$$

where $f(\epsilon - \mu)$ is the Fermi-Dirac distribution, which is evaluated at zero temperature, and E is the energy of the state bound to the interface. In principle there could be several poles in the resolvent, each corresponding to a bound state, but we find that only one such state exists in our calculations. If we sum up the contributions from all of the layers,

taking the limit $N \to \infty$, then the total energy of the $\hat{y}\hat{z}$ and $\hat{z}\hat{x}$ orbitals combined is

$$\epsilon^{\perp} = 4\left(tE_1\left(\frac{\mu}{t} - \frac{E}{t}\right) + EN_1\left(\frac{\mu}{t} - \frac{E}{t}\right)\right). \tag{10.37}$$

10.1.5 Self consistent determination of the charge distribution

To determine the charge distribution on the STO side of the interface, we must determine the self consistent charge distribution of the x-, y- and z-electrons, subject to the constraint that the total charge is conserved. In practice we must therefore self consistently solve Eqs. 10.20, 10.36, 10.35 and 10.13. The chemical potential is tuned so that the total charge, given by Eq. 10.12, is conserved. We then determine μ, E, $\boldsymbol{\rho}_n^{\parallel}$ and $\boldsymbol{\rho}_n^{\perp}$, as $\boldsymbol{\rho}_0$ and $\frac{\Delta}{t}$ are allowed to vary. We place all of the residual charge on the layer at $N+1$ and use the approximation that there is zero charge on layers farther from the interface. We self consistently solve the charge distribution for a few hundred layers, which ensures that the approximation is reasonable.

The chemical potential is plotted against the total charge, for $\Delta = 0.5t$, in Fig. 10.4(a). For a wide range of doping a gap opens between the energy of the electrons at the interface and the chemical potential of the bulk. At both low and high doping the chemical potential reduces to the bulk value of -4t. In the low doping region there are only z-electrons which exhibit the classical exponential decay into the bulk, as illustrated in Fig. 10.4(b). Physically the electrons provide a balance between the coulombic attraction to the interface and Pauli exclusion which repels them from the higher density regions. As the doping is increased a transition occurs; when the gain in potential energy , Δ_n, is sufficient to compensate for the loss of hybridisation energy, then a bound state is formed at the interface (Fig. 10.4(c)). Initially, this bound state is much longer range than the cloud of z-electrons,and therefore replaces the z-electrons at long distances. As the doping is increased further the number of z-electrons in more distant layers falls rapidly to zero, and the z-electrons are then confined to a *finite* number of layers (Fig. 10.4(d)). Finally, a second transition occurs at high doping: the x- and y-electrons are no longer extended enough to screen the z-electrons, which again decay exponentially into the bulk (Fig. 10.4(e)). The complete dependence of the charge in each layer, plotted as a function of total charge, $\boldsymbol{\rho}_0$, is illustrated in Fig. 10.5.

10.2 Relevance to experimental systems

To make deductions about the experimental systems we choose the parameters to be $\boldsymbol{\rho}_0 = 0.5$ and $\Delta = 20t$. The charge distribution is illustrated in Fig. 10.6; we find that the x- and y-electrons hold in place a *single* layer of z-electrons! From the electronic

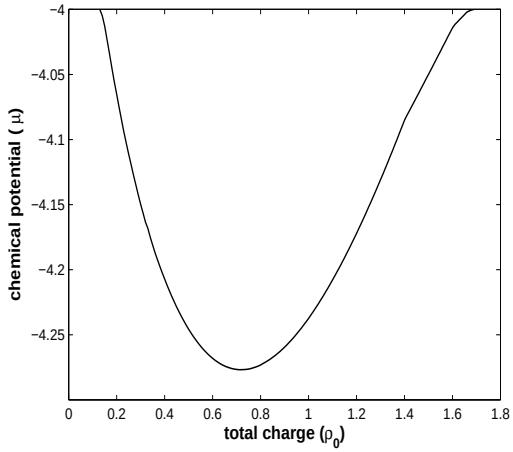

(a) The chemical potential μ plotted against the total charge $\boldsymbol{\rho}_0$, for $\Delta = 5t$.

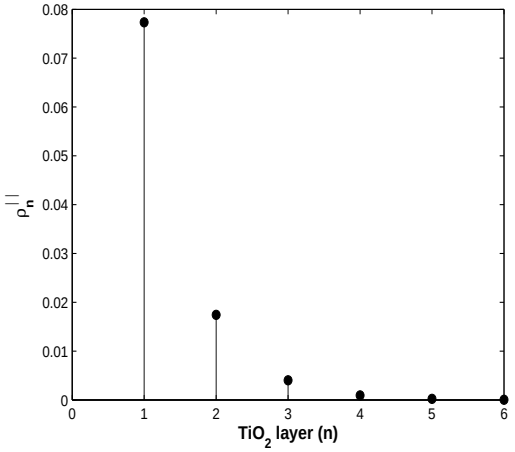

(b) $\boldsymbol{\rho}_0 = 0.1$: When only the z-electrons (black circles) are active, the charge distribution decays exponentially into the bulk.

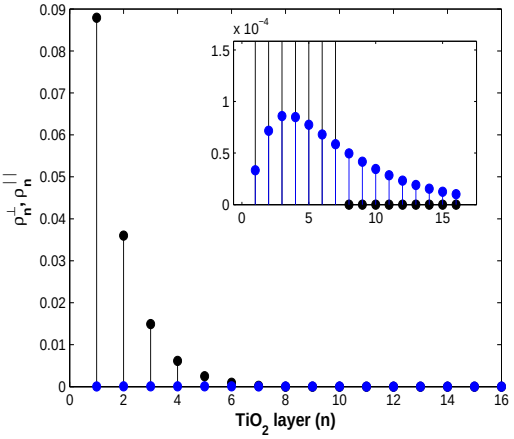

(c) $\boldsymbol{\rho}_0 = 0.15$: When the x-electrons and y-electrons (blue circles) are active, they form a very long range bound state.

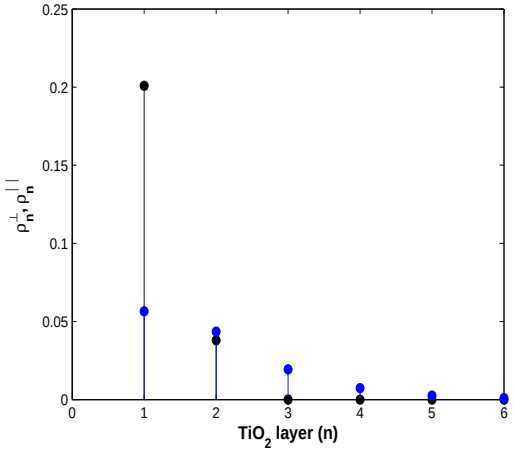

(d) $\boldsymbol{\rho}_0 = 0.5$: The long range bound state holds the z-electrons in place, next to the interface, in just two layers.

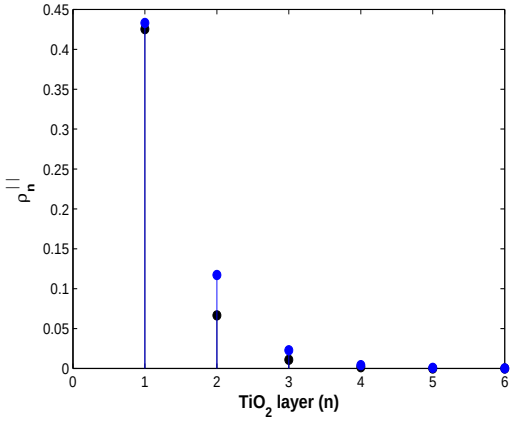

(e) $\boldsymbol{\rho}_0 = 1.66$: When the x- and y-electrons can no longer screen the z-electrons, the z-electrons again extend past the first two layers.

Figure 10.4: Electronic transition at the STO-LAO interface.

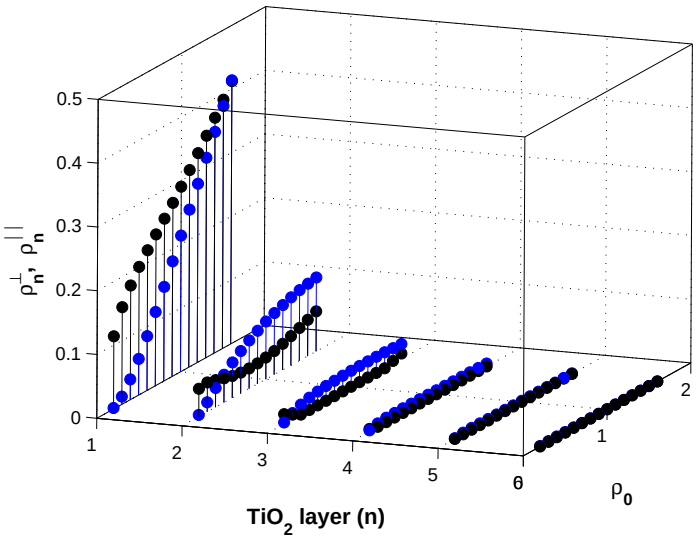

Figure 10.5: The charge distribution in interfacial TiO_2 layers, calculated for $\Delta = 5t$, and plotted as a function of the total charge $\boldsymbol{\rho}_0$. The number of z-electrons, $\boldsymbol{\rho}_n^{||}$ (black circles), and the number of x-electrons (or y-electrons), $\boldsymbol{\rho}_n^{\perp}$ (blue circles), are shown for each layer.

reconstruction there are approximately 0.25 electrons, per titanium atom, in the $\hat{x}\hat{y}$ orbitals, whilst the remaining 0.25 electrons are found to occupy the $\hat{y}\hat{z}$ and $\hat{z}\hat{x}$ orbitals. The sheet conductivity depends solely on the z-electrons, and our results would therefore be consistent with a two dimensional electron gas, confined to within one unit cell of the interface. Interestingly, density functional theory calculations have also revealed a similar feature[149].

Also of possible relevance to experiments is the intriguing region where the chemical potential drops below the energy of the bulk states; electrons are bound to the interface by a finite energy, which amounts to the analogue of a work function: it costs a finite amount of energy to release these electrons into the bulk, and there should be a corresponding threshold for photoemission.

With regards to the magnetism, the fact that $U \gg t$ would lead us to expect itinerant magnetism close to the interface. We are therefore unable to make deductions about the effect of electronic correlations on the conductivity of the interfacial layer, and an investigation of these effects would require the inclusion of electronic correlation terms. Such models have been used to investigate similar polar interfaces, and yield a variety of magnetic and orbitally ordered phases[150, 148].

10.3 Summary

We have self-consistently determined the effects of the competition between the coulomb attraction to the STO-LAO interface, and the Pauli exclusion of electrons from high density regions. By explicitly incorporating the planar t_{2g} orbitals and the braking of translational symmetry caused by the interface, we have captured the interaction between

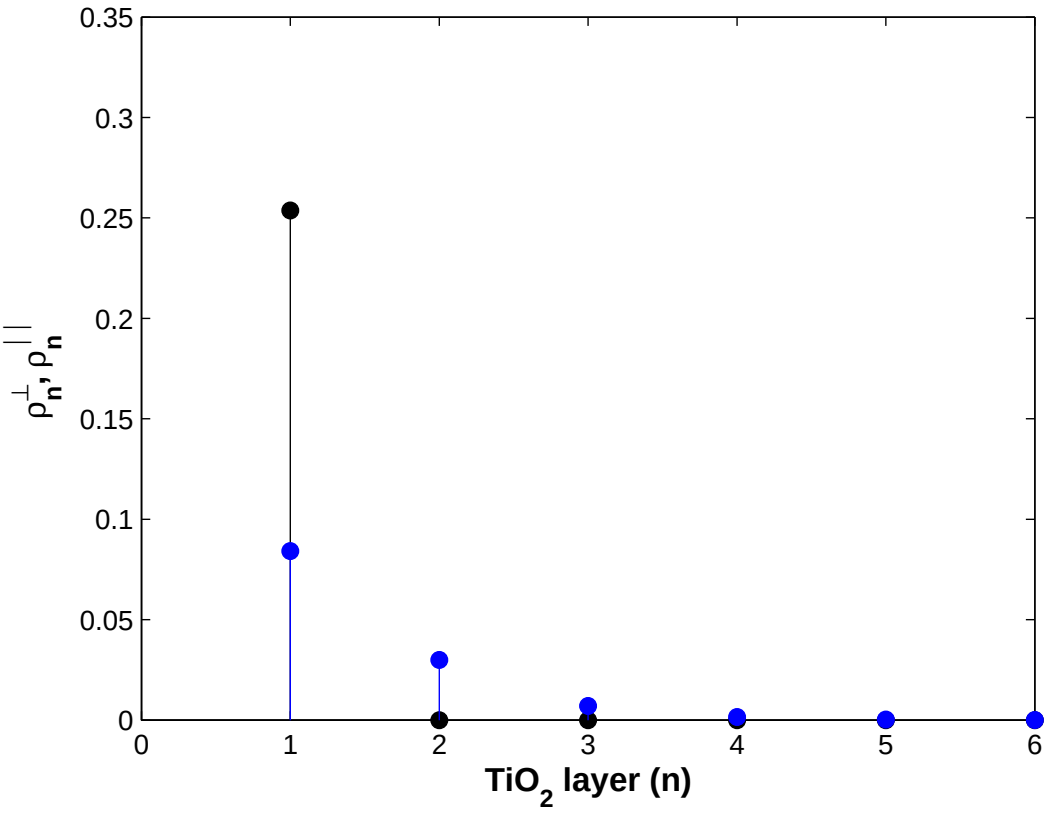

Figure 10.6: When $\boldsymbol{\rho}_0 = 0.5$ and $\Delta = 20t$ the z-electrons are confined to a single interfacial layer, whilst the x- and y-electrons decay exponentially into the bulk.

the bound states of x- and y-electrons and the interfacial z-electrons. We find that the x- and y-electrons screen the residual charge at longer distances, whilst the z-electrons are confined to the interfacial layer and account for half of the total transferred charge. This is particularly interesting because it suggests that conductivity measurements would be probing a single layer of electrons in the $\hat{x}\hat{y}$ orbitals.

Chapter 11

Conclusions

In this thesis we have performed detailed investigations of two different topics: neutron Compton scattering from hydrogen and Perovskite oxide interfaces.

In part one of this thesis we have investigated the anomalous measurements of the hydrogen cross section: which were obtained with the VESUVIO neutron spectrometer, at the ISIS pulsed neutron source, in neutron Compton scattering experiments. We have briefly reviewed some of the possible explanations for these anomalous measurements, including the main theoretical and experimental issues surrounding the results.

In our attempt to explain the anomalous measurements we have performed a focused theoretical investigation: to determine whether electronic excitation could be responsible for the unexpected results. To gain a detailed understanding of the mechanisms which facilitate electronic excitation, in neutron-nucleus collisions, the excitation spectra have been calculated for several simple systems. We have examined separable systems, which are straightforward to understand because analytic solutions are readily obtainable. The response function of the four body problem, which is intended to be analogous to the H_2 molecule, is an original result that clearly demonstrates the convolution of probabilities occurring in separable systems. This system also demonstrates the weakness of the CMR effect at realistic energy transfers. For the hydrogen atom, the probability that the electron remains in its ground state, at energy transfers of 100eV, is found to be less than one percent; this is in agreement with previous results. The calculation of the probabilities associated with electronic dissociation, in a high energy neutron-nucleus collision, is an original result. However, to excite these high lying modes requires incident neutrons with energies far in excess of those which are relevant to the experiments on VESUVIO. Finally, we have investigated the non-adiabatic effects in H_2^+. These effects have been studied previously, but our approach is differentiated by the fact that we employ a non-perturbative method to obtain the molecular wavefunctions. We have carefully extracted the translational and rotational degrees of freedom from the shape coordinates, so that we

could attempt accurate numerical solutions. We found that the adiabatic approximation is reliable, at the energies of the experiments, and we also find that the non-adiabatic effects, which facilitate electronic excitation during nuclear dissociation, are very small.

From this investigation we conclude that electronic excitations are very unlikely to be responsible for the anomalous experimental results. At present, there are no other theoretical arguments that offer a satisfactory explanation for the results and an alternative line of investigation may be required. There are still experimental issues which need to be resolved and it may, therefore, be important to consider the limitations of the experiment when acquiring data at large scattering angles.

In the second part of this thesis we have looked at two Perovskite oxide interfaces: the interface between the high temperature superconductor $YBa_2Ca_3O_7$ and ferromagnetic $La_{2/3}Ca_{1/3}MnO_3$, and the interface between the band insulators $LaAlO_3$ and $SrTiO_3$. We have used impurity theory to construct simple models of these interfaces.

We have carefully examined two particularly intriguing experiments performed on the cuprate-manganite interface. Using the knowledge gained from these experiments we have proposed an explanation for the orbital reconstruction and the magnetic moment observed in the interfacial layers, and we have constructed a simple model to illustrate the consequences of our theory. Using our model we predict a sizeable orbital reconstruction, which is in reasonable agreement with experiment, and a magnetic moment in the interfacial cuprate layer, which is comparable but slightly less than would naively be inferred from experiment. Whilst studying our model of the cuprate-manganite interface we also discovered states which bind to the interface and reside in the gap between the two bulk manganite bands. These states become degenerate with the bulk bands to form resonances, which gives the appearance of a discontinuous two dimensional Fermi surface; we have indicated how this distinctive feature might show up in ARPES performed at the interface.

Finally, we have looked at the novel properties of the interface between $LaAlO_3$ and $SrTiO_3$, paying particular attention to the two dimensional electron gas which is confined to within a few atomic layers of the interface. This state is believed to result from the avoidance of the polar catastrophe via a transfer of charge across the interface. We have constructed a simple model of the charging phenomena at the interface, which we have self consistently solved for the charge distribution in the titanate layers. Into our model, we have incorporated the two dimensional orbital physics of the titanates, and we have found that the model displays interesting physics: at low doping the electrons move exclusively in the plane parallel to the interface; for intermediate doping the electrons moving parallel to the interface screen the residual charge at short distances, and are therefore trapped in a finite number of layers, whilst the charges moving perpendicular to the interface screen

the charge at longer distances; at high doping the electrons moving parallel to the interface again screen the charge at longer distances. The STO-LAO interface corresponds to the case of intermediate doping and, as a result, we find that the electrons moving parallel to the interface are trapped in a finite number of layers. We have therefore shown that the effect of charging at the interface is to reduce the width of the conducting region at the interface. This is consistent with the experiments that reveal a narrow two dimensional electron gas at the interface.

The effects of the local coulomb interactions between electrons are not considered in our model oft the STO-LAO interface, and we would expect these to lead to interesting magnetic properties. To investigate these properties would require a more complicated model which incorporates the local coulomb interactions. The results obtained from our model could therefore provide useful intuition when more sophisticated models are developed.

Appendices

Appendix A

The method of integral representations

The solution of ordinary differential equations by obtaining an integral representation is often useful, as these representations are often easier to manipulate and have a larger radius of convergence. For the solution of the equation

$$\hat{L}_z u(z) = 0, \tag{A.1}$$

where $\hat{L}_z$ is a linear differential operator, we seek a solution of the form

$$u(z) = \int_C K(z,t)v(t)dt, \tag{A.2}$$

where C is an arbitrary contour in the complex plane, and $K(z,t)$ is the required integral Kernel. To find a solution we require that there exists an operator M_t such that

$$\hat{L}_z K(z,t) = \hat{M}_t K(z,t), \tag{A.3}$$

so that we may write

$$\hat{L}_z u(z) = \int_C [\hat{L}_z K(z,t)]v(t)dt = \int_C [\hat{M}_t K(z,t)]v(t)dt. \tag{A.4}$$

We also require that $\hat{M}_t$ has an *adjoint* operator $\hat{M}^\dagger$ so that we may perform an integration by parts, and transfer the operator onto the function $v(t)$:

$$\hat{L}_z u(z) = \int_C K(z,t)\hat{M}_t^\dagger v(t)dt + [Q(K,v)]_{\partial C}. \tag{A.5}$$

The contribution from the boundary after performing the integration by parts is a function of z and t which must be evaluated at the end points of the contour ∂C. The solution to Eq. A.1 is then found by choosing the contour such that the boundary term vanishes,

and then solving the differential equation

$$\hat{M}_t^\dagger v(t) = 0, \tag{A.6}$$

so that the integrand also vanishes. The technique is useful when Eq. A.6 is easier to solve than Eq. A.1. The success of this method depends on choosing a suitable integral kernel, and some of the most useful examples are:

i) When the coefficients of the differential operator $\hat{L}_z$ are linear functions of z, the solution can be found by using the *Laplace kernel*:

$$K(z,t) = e^{zt}. \tag{A.7}$$

This is useful for solving equations such as the *confluent hypergeometric* differential equation.

ii) When the coefficients of the derivatives d^n/dz^n is a polynomial of degree n the solution may be found by using the *Euler kernel*:

$$K(z,t) = K(z-t) = (z-t)^\beta, \tag{A.8}$$

where β is a complex number. This technique is useful for functions such as the *hypergeometric* differential equation.

iii) When the differential equation is of the form

$$\hat{L}_z = z^n H_1\left(z\frac{d}{dz}\right) + H_2\left(z\frac{d}{dz}\right) \tag{A.9}$$

the *Mellin kernel* can be used to obtain a solution

$$K(z,t) = K(z^t). \tag{A.10}$$

iv) For *Bessel's* equation it is often useful to employ the kernel

$$K(z,t) = \left(\frac{z}{2}\right) e^{t-\frac{z^2}{4t}}. \tag{A.11}$$

Appendix B

The exact nuclear and electronic wavefunctions

The standard method for separating the nuclear motion from the electronic motion is the Born-Oppenheimer approximation. In this scheme it is assumed that an adiabatic separation can be made, resulting in a molecular wavefunction of the form

$$\Psi_{mol}(\mathbf{R}, \mathbf{r}) \approx X(\mathbf{R})\Phi_{\mathbf{R}}(\mathbf{r}), \tag{B.1}$$

which is simply the product of a nuclear wavefunction $X(\mathbf{R})$ and an electronic wavefunction $\Phi_{\mathbf{R}}(\mathbf{r})$ which depends parametrically on the nuclear coordinates. The normalisation is such that

$$\langle \Phi_{\mathbf{R}} | \Phi_{\mathbf{R}} \rangle = 1 \tag{B.2}$$

$$\int d\mathbf{R} |X(\mathbf{R})|^2 = 1. \tag{B.3}$$

The wavefunction can be associated with a marginal probability density amplitude,

$$|\Psi_{mol}(\mathbf{R}, \mathbf{r})|^2 \approx |X(\mathbf{R})|^2 |\Phi_{\mathbf{R}}(\mathbf{r})|^2 \mapsto P(\mathbf{R})P(\mathbf{r}|\mathbf{R}). \tag{B.4}$$

This interpretation of the nuclear and electronic wavefunctions suggests that it should be possible to obtain the *exact* marginal probability density amplitude. The equations for the exact nuclear and electronic wavefunctions can be determined by variationally minimising the expectation value of the energy of the molecular Hamiltonian with respect to both $\Phi_{\mathbf{R}}$ and $X(\mathbf{R})$. The molecular Hamiltonian is defined

$$H_{mol} = H_{BO} - \sum_{\alpha=1}^{N} \frac{\hbar^2 \nabla_\alpha^2}{2M_\alpha}. \tag{B.5}$$

The Born-Oppenheimer Hamiltonian for the electronic states is defined

$$H_{BO} = \sum_{i=1}^{N_e} \frac{\hbar^2 \nabla^2_{\mathbf{r}_i}}{2m_e} + \sum_{i>j=1}^{N_e} \frac{1}{|\mathbf{r}_i - \mathbf{r}_j|} + \sum_{\alpha>\beta=1}^{N} \frac{Z_\alpha Z_\beta}{|\mathbf{R}_\alpha - \mathbf{R}_\beta|} - \sum_{i=1}^{N_e}\sum_{\alpha=1}^{N} \frac{Z_\alpha}{|\mathbf{R}_\alpha - \mathbf{r}_i|}. \tag{B.6}$$

The expectation value for the energy is then minimised under the normalisation constraints on the nuclear and electronic wavefunctions[151]. The constraints are managed by introducing the Lagrange multipliers E and $\Lambda(\mathbf{R})$:

$$\int d\mathbf{R} \langle \Phi_{\mathbf{R}}(\mathbf{r}) | H_{mol} | \Phi_{\mathbf{R}}(\mathbf{r}) \rangle - E \int d\mathbf{R} (|X(\mathbf{R})|^2 - 1) - \int d\mathbf{R} \Lambda(\mathbf{R}) (\langle \Phi_{\mathbf{R}} | \Phi_{\mathbf{R}} \rangle - 1). \tag{B.7}$$

When the above expression is minimised variationally, first with respect to $\Phi_{\mathbf{R}}(\mathbf{r})$ and then with respect to $X(\mathbf{R})$, the following set of coupled equations are found for the exact nuclear and electronic wavefunctions

$$\left[H_{BO} - \sum_{\alpha=1}^{N} \frac{\hbar^2 \nabla^2_\alpha}{2M_\alpha} + \sum_{\alpha=1}^{N} \frac{X^*(\mathbf{R})(-i\hbar\nabla_\alpha X(\mathbf{R}))}{M_\alpha |X(\mathbf{R})|^2} \cdot (-i\hbar\nabla_{\mathbf{R}}) \right] \Phi_{\mathbf{R}}(\mathbf{r}) = \Lambda(\mathbf{R}) \Phi_{\mathbf{R}}(\mathbf{r}) \tag{B.8}$$

$$\left[\sum_{\alpha=1}^{N} \frac{[-i\hbar\nabla_{\mathbf{R}} + \mathbf{A}_\alpha(\mathbf{R})]^2}{2M_\alpha} + \langle \Phi_{\mathbf{R}} | H_{BO} | \Phi_{\mathbf{R}} \rangle + \sum_{\alpha=1}^{N} \frac{\hbar^2 \langle \nabla_\alpha \Phi_{\mathbf{R}} | \nabla_\alpha \Phi_{\mathbf{R}} \rangle}{2M_\alpha} - \sum_{\alpha=1}^{N} \frac{A^2_\alpha(\mathbf{R})}{2M_\alpha} \right] X(\mathbf{R}) = E X(\mathbf{R}). \tag{B.9}$$

The term $\mathbf{A}_\alpha(\mathbf{R})$ is like a vector potential, and is defined

$$\mathbf{A}_\alpha(\mathbf{R}) = \langle \Phi_{\mathbf{R}} | \nabla_\alpha | \Phi_{\mathbf{R}} \rangle. \tag{B.10}$$

The solution to the coupled equations results in an exact molecular wavefunction of the form

$$\Psi_{mol}(\mathbf{R}, \mathbf{r}) = X(\mathbf{R}) \Phi_{\mathbf{R}}(\mathbf{r}), \tag{B.11}$$

which is uniquely defined up to an $\mathbf{R}$ dependent phase:

$$X(\mathbf{R}) \mapsto e^{i\theta(\mathbf{R})} X(\mathbf{R}) \qquad \Phi_{\mathbf{R}}(\mathbf{r}) \mapsto e^{-i\theta(\mathbf{R})} X(\mathbf{R}). \tag{B.12}$$

The term $\mathbf{A}_\alpha$ can usually be made to disappear through an appropriate choice of the phase, except when there is a degeneracy in the electronic energy surfaces. In this case a

geometric phase is introduced into the nuclear Hamiltonian.

Appendix C

Operator perturbation theory

Operator perturbation theory is a technique which is used extensively in problems involving strongly correlated electrons, for which the Hamiltonain is often of the form

$$\mathcal{H} = \mathcal{H}_0 + \lambda \mathcal{H}_1, \tag{C.1}$$

where $\mathcal{H}_0$ is the reference Hamiltonian, and $\mathcal{H}_1$ is an interaction term which is proportional to a small parameter λ. The idea is to use perturbation theory to derive an effective Hamiltonian $\tilde{\mathcal{H}}$ that lifts the degeneracy of the reference Hamiltonian $\mathcal{H}_0$, and obtain a simpler model which still includes the interesting physics of the full Hamiltonian. A Unitary transformation is applied to the eigenstates, which creates the effective Hamiltonian $\tilde{\mathcal{H}}$ in the new basis:

$$\tilde{\mathcal{H}} = e^{\lambda S} \mathcal{H} e^{-\lambda S}, \tag{C.2}$$

where $e^{\lambda S}$ is has the general form of a unitary transformation, which is defined by the anti-Hermitian operator S. This transformation transforms the eigenstates, whilst leaving the eigenvalues unchanged:

$$\tilde{\mathcal{H}} e^{\lambda S} |\psi\rangle = E e^{\lambda S} |\psi\rangle. \tag{C.3}$$

The effective Hamiltonian can be expanded as a Taylor series in λ:

$$\frac{d\tilde{\mathcal{H}}}{d\lambda} = e^{\lambda s} [S, \mathcal{H}] e^{-\lambda S} \tag{C.4}$$

$$\frac{d^2\tilde{\mathcal{H}}}{d\lambda^2} = e^{\lambda s} [S, [S, \mathcal{H}]] e^{-\lambda S}, \tag{C.5}$$

which leads to the expansion

$$\tilde{\mathcal{H}} = \mathcal{H} + \lambda[S, \mathcal{H}] + \frac{\lambda^2}{2}[S, [S, \mathcal{H}]] + ... \tag{C.6}$$

Then we group together the terms in powers of λ:

$$\tilde{\mathcal{H}} = \mathcal{H}_0 + \lambda(\mathcal{H}_1 + [S, \mathcal{H}_0]) + \frac{\lambda^2}{2}(2[S, \mathcal{H}_1] + [S, [S, \mathcal{H}_0]]) + ... \tag{C.7}$$

We now look for an operator S which satisfies the equation

$$\mathcal{H}_1 + [S, \mathcal{H}_0] = 0 \tag{C.8}$$

which eliminates the first order term in λ. The effective Hamiltonian in the new basis is then

$$\tilde{\mathcal{H}} = \mathcal{H}_0 + \frac{\lambda^2}{2}[S, \mathcal{H}_1] + ... \tag{C.9}$$

which is second order in the parameter λ. The interpretation of the operators in the new basis is subtle, as the original operators are mixed by the transformation

$$\tilde{d}^\dagger_{i\sigma} = e^{-\lambda S} d^\dagger_{i\sigma} e^{\lambda S} = d^\dagger_{i\sigma} - \lambda[S, d^\dagger_{i\sigma}] + ... \tag{C.10}$$

which can lead to hybridisation effects being included in the new operators.

Appendix D

Resonances

Apart from creating new bound states, an impurity can also lead to *resonances* and *antiresonances* in the density of states. These often appear when a new state induced by the impurity becomes degenerate with the bulk states and leads to a Lorentzian shaped peak in the density of states. These resonances can be derived from the density of states formula[126]:

$$\rho(\epsilon) = \frac{1}{\pi}\text{Im Tr } [\epsilon^- - \mathcal{H}]^{-1} = \frac{1}{\pi}\text{Im Tr } \frac{d\log(\epsilon^- - \mathcal{H})}{d\epsilon}, \tag{D.1}$$

where we have used the abbreviation $\epsilon^- = \epsilon - i\delta$. Then, using the matrix identity $\det|A| = \exp(\text{Tr } \log(A))$ we can rewrite the density of states as

$$\rho(\epsilon) = \frac{1}{\pi}\text{Im } \frac{d\log(\det|\epsilon^- - \mathcal{H}|)}{d\epsilon}. \tag{D.2}$$

We can separate the impurity part of this matrix equation by rewriting the term $[\epsilon^- - \mathcal{H}] = [\epsilon^- - \mathcal{H}_0][\mathcal{I} - [\epsilon^- - \mathcal{H}_0]^{-1}\mathcal{H}_1]$, so that

$$\rho(\epsilon) = \frac{1}{\pi}\text{Im } \frac{d}{d\epsilon}\left(\log(\det|\epsilon^- - \mathcal{H}_0|) + \log(\det|\mathcal{I} - [\epsilon^- - \mathcal{H}_0]^{-1}\mathcal{H}_1|)\right). \tag{D.3}$$

The change in the density of states caused by the impurity is then

$$\Delta\rho(\epsilon) = \rho(\epsilon) - \rho_0(\epsilon) = \frac{1}{\pi}\text{Im } \frac{d\log(\det|\mathcal{I} - [\epsilon^- - \mathcal{H}_0]^{-1}\mathcal{H}_1|)}{d\epsilon} = \frac{1}{\pi}\text{Im } \frac{d\log(D)}{d\epsilon}, \tag{D.4}$$

where we have written the determinant $D = \det|\mathcal{I} - [\epsilon^- - \mathcal{H}_0]^{-1}\mathcal{H}_1|$. We now introduce the phase shift, δ, of the scattered wave:

$$\tan(\delta) = \frac{\text{Im } D}{\text{Re } D}, \tag{D.5}$$

so that $\delta = \text{Arg}(D)$. Then using the identity $\log(D) = \log|D| + i\text{arg}(D)$, we obtain

$$\Delta\rho(\epsilon) = \frac{1}{\pi}\frac{d\delta}{d\epsilon}. \tag{D.6}$$

In the vicinity of a point for which Re $D(\epsilon_0) = 0$, we may write $D(\epsilon) \approx i\text{Im } D + (\epsilon - \epsilon_0)\text{Re } D' + i(\epsilon - \epsilon_0)\text{Im } D'$. Then we can approximate the size of the resonance/antiresonance to be

$$\Delta\rho(\epsilon) \approx \frac{\Gamma}{2\pi}\frac{1}{(\epsilon - \epsilon_0)^2 + \frac{\Gamma^2}{4}}. \tag{D.7}$$

The resonance/antiresonance is a Lorentzian with half width $\Gamma = 2\text{Im } D(\epsilon_0)/\text{Re } D'(\epsilon_0)$. If Γ is positive we find a resonance, and if Γ is negative we find an antiresonance. Resonances appear when we investigate the cuprate-manganite interface.

Appendix E

X-ray absorption spectroscopy

X-ray absorption spectroscopy (XAS) is extensively used to probe the unoccupied states of specific elements in materials; by tuning the incident photon energy to an absorption edge of a particular element it is possible to extract a great deal of information about the absorbing atom, such as its local geometry and bonding characteristics, its dependence on oxidation state, and the density of unoccupied electronic states. With the use of high energy synchrotron radiation sources even more refined measurements are possible. These make use of linearly polarised and circularly polarised soft x-rays to uncover properties related to charge, spin and orbital states of the absorbing atom. This technique is particularly effective in the transition metal oxides because the interaction between the core hole created by the x-ray and the valence electrons is much larger than the bandwidth, which means that the absorption process is *excitonic* and may be understood in terms of simple atomic-like transitions. The allowed transitions are then highly constrained by the dipole selection rules which decide the transition probabilities between states, and the resulting spectra are therefore greatly simplified.

The *transmission mode* of XAS, which measures the number of incident photons and the number of transmitted photons, is not always practical because the absorption of x-rays by matter is very strong, and consequentially the technique can only be applied to very thin samples. There are however two other modes of operation illustrated in Fig. E.1, which measure the decay products of the absorption process. In *fluorescence yield mode* the incident x-ray excites a core electron to an unoccupied state above the Fermi surface, leaving behind a core hole which interacts strongly with the valence electrons. This strong interaction can cause the decay of a valence electron, which fills the hole and releases its excess energy by emitting a photon, which is then detected. The number of photons detected is proportional to the number of core holes created. The advantage of fluorescence yield (FY) mode is that there is no limitation on the thickness of the sample, and the probing depth is ~ 2000Åwhich makes FY mode bulk sensitive. The final, and

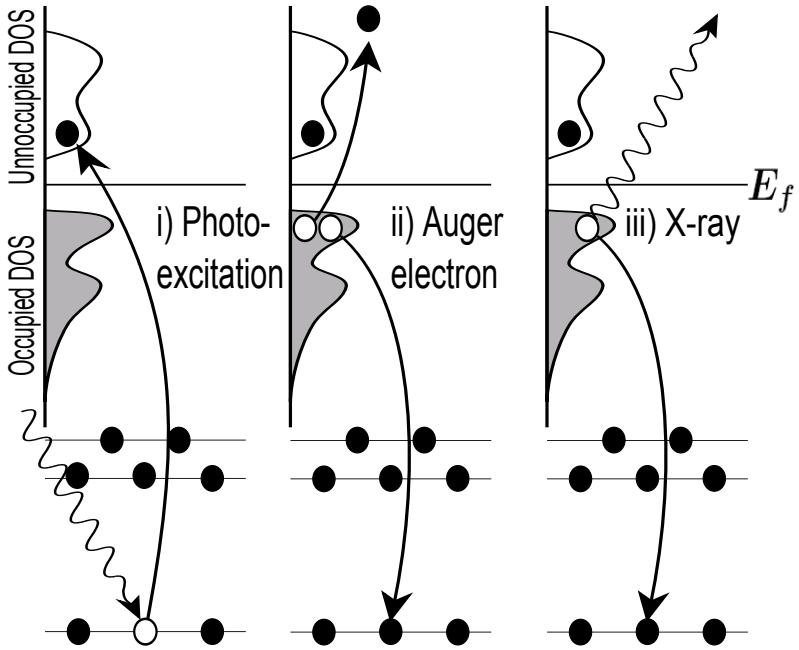

Figure E.1: A schematic illustration of the two different modes used in XAS. i) The incident x-ray excites an electron from below the fermi surface into an unoccupied state. The hole left behind is later filled by an electron, which can give up its extra energy through two possible processes: (ii) through the transfer of some of its energy to an *Auger electron* which leaves the sample and is detected as a loss of charge in TEY mode, (iii) through the emission of an x-ray which is detected in FY mode.

most common mode of detection is *total electron yield mode*. In total electron yield (TEY) mode, when the core hole is filled by a valence electron, the excess energy is transferred to an *Auger electron* which is excited from an occupied state and can escape the sample. The sample is grounded through a pico-amperemeter, which measures the current required to neutralise the sample after the absorption process. Only electrons which are close to the surface will escape from the sample without suffering inelastic collisions, and electrons further away will usually transfer some of their energy to *secondary electrons*. The number of secondary electrons is much larger than the original number of Auger electrons, which amplifies the signal, which is proportional to the absorption coofficient. The penetration of TEY mode is only in the range $\sim$ 40Å$-$100Åwhich makes it more sensitive to the surface.

The absorption amplitude of incident x-rays, with polarisation $\hat{\boldsymbol{\epsilon}}$, is given by Fermi's golden rule:

$$\mu(\omega) \sim \sum_f |\langle\psi_i|e^{-i\boldsymbol{k}\cdot\boldsymbol{r}}\hat{\boldsymbol{\epsilon}}\cdot\boldsymbol{p}|\psi_f\rangle|^2\delta(\hbar\omega + E_i - E_f). \tag{E.1}$$

This is simplified by using the dipole approximation ($\boldsymbol{k}\cdot\boldsymbol{r} \ll 1$), which is accurate because the wavelength of the incident x-rays is much larger than the size of the atom. The momentum operator can be replaced by using the commutator relation $\boldsymbol{p} = m/i\hbar[\boldsymbol{r}, \hat{H}]$, so that the absorption amplitude may be written

$$\mu(\omega) \sim \omega \sum_f |\langle\psi_i|\hat{\boldsymbol{\epsilon}}\cdot\boldsymbol{r}|\psi_f\rangle|^2\delta(\hbar\omega + E_i - E_f). \tag{E.2}$$

If we consider the simplest case of a single electron in an unclosed shell of an atom, the initial and final states may be written as the product of a radial wavefunction and an angular wavefunction, so that the transition matrix element in the above expression is

$$\langle\psi_i|\hat{\boldsymbol{\epsilon}}\cdot\boldsymbol{r}|\psi_f\rangle = \int_0^\infty dr r^3 R_{n,l}R_{n',l'}\int d\Omega Y_l^m \hat{\boldsymbol{\epsilon}}\cdot\hat{\boldsymbol{r}}Y_{l'}^{m'} \tag{E.3}$$

$$= \int_0^\infty dr r^3 R_{n,l}R_{n',l'}\int d\Omega Y_l^m \left(\epsilon_z Y_1^0 + \frac{-\epsilon_x + i\epsilon_y}{\sqrt{2}}Y_1^1 + \frac{\epsilon_x + i\epsilon_y}{\sqrt{2}}Y_1^{-1}\right) Y_{l'}^{m'}. \tag{E.4}$$

For circularly polarised x-rays the polarisation vector is $\hat{\boldsymbol{\epsilon}}_{\pm1} = (\mp1/\sqrt{2}, -i/\sqrt{2}, 0)$, whilst for linearly polarised x-rays $\hat{\boldsymbol{\epsilon}}_0 = (0,0,1)$. Then denoting the dipole operator as $\hat{P}_q = \hat{\boldsymbol{\epsilon}}_q\cdot\hat{\boldsymbol{r}}$, the angular part of the matrix element can be expressed in terms of Clebsch-Gordan coefficients:

$$\langle lm|\hat{P}_q|lm\rangle = \int d\Omega Y_l^m Y_1^q Y_{l'}^{m'} = \sqrt{\frac{3(2l+1)}{4\pi(2l'+1)}}\langle l100|l'0\rangle\langle l1mq|l'm'\rangle. \tag{E.5}$$

The Clebsch-Gordan coefficients vanish unless the angular momentum addition criteria are satisfied, which enforces the *selection rules* for x-ray induced dipole transitions: $\Delta m = q$ and $\Delta l = \pm1$. Obviously spin is also conserved in the transition. We will consider a situation which is of relevance for the XAS experiment on an YBCO-LCMO interface. If we consider the transition $2p^6 3d^9 \rightarrow 2p^5 3d^{10}$ in the cubic crystal field environment, then in the initial state there is a single hole in an e_g state, whilst in the final state there is a single hole in a $2p$ state. The determinantal wavefunctions differ by just two orbitals, and the matrix element is proportional to the matrix element between these two orbitals. The correct symmetry orbitals are just linear combinations of the spherical harmonics so, using the selection rules we have just derived, we can deduce the dipole transition matrix elements for linearly polarised x-rays with polarizaton vector $\hat{\epsilon}_0 = \hat{\boldsymbol{e}}_z$:

$$|\langle p_z|\hat{P}_0|d_{x^2-y^2}\rangle|^2 = 0 \qquad |\langle p_z|\hat{P}_0|d_{3z^2-r^2}\rangle|^2 = \frac{1}{5\pi}. \tag{E.6}$$

All other matrix elements are zero. We can see from these simple (and very approximate) results that for x-rays polarised along the z-axis, the transition to the $d_{x^2-y^2}$ state is strongly suppressed. Alternatively, for polarization along the x-axis, i.e, $\hat{\epsilon}_0 = \hat{\boldsymbol{e}}_x$, we find

$$|\langle p_x|\hat{P}_0|d_{x^2-y^2}\rangle|^2 = \frac{3}{20\pi} \qquad |\langle p_x|\hat{P}_0|d_{3z^2-r^2}\rangle|^2 = \frac{1}{20\pi}. \tag{E.7}$$

The transition to the $d_{x^2-y^2}$ state is then no longer suppressed, and accounts for most of the absorption.

Appendix F

Polarised neutron reflectometry

Polarised neutron reflectometry (PNR) is a powerful technique for probing the magnetic and nuclear potentials of surfaces and interfaces, and is now a widely used technique for studying magnetism. Similar information about the structure can be obtained in x-ray reflectivity, but because the neutron spin interacts with the magnetic field, the reflectivity of polarised neutrons can also be used to create depth profiles of the magnetism.

In neutron optical processes the scattered waves interfere with the incident wave, resulting in both constructive and destructive interference. In general, waves can only interfere if they have the same frequency, so that the coherent scattering only involves elastic processes. Because the state of the sample remains unchanged in these elastic processes, the coherent state wavefunction is (rigorously[18]) represented by a single particle Schrodinger equation:

$$\left[-\frac{\hbar^2\nabla^2_{\mathbf{r}_n}}{2m_n} + v(\mathbf{r}_n)\right]\psi(\mathbf{r}_n) = E\psi(\mathbf{r}_n) \tag{F.1}$$

The interaction between the neutrons, and the material through which they propagate, is composed of a nuclear interaction V_n involving the scattering length b, and a magnetic interaction V_m between the neutron spin and the magnetic field created by the electrons:

$$V = V_n + V_m = \frac{2\pi\hbar^2}{m_n}Nb - \boldsymbol{\mu}_n \cdot \boldsymbol{B}. \tag{F.2}$$

The nuclear interaction described is an average interaction: the number of atoms per unit volume is N and their mean scattering length is b. The term $\boldsymbol{B}$ is the magnetic field induced by the orbital current density and the spin current density of the electrons, in addition to the applied field B_0.

The neutron refractive index of a medium can be defined in the usual way, i.e, as the ratio of the wave vectors k and k', inside and outside of the medium respectively:

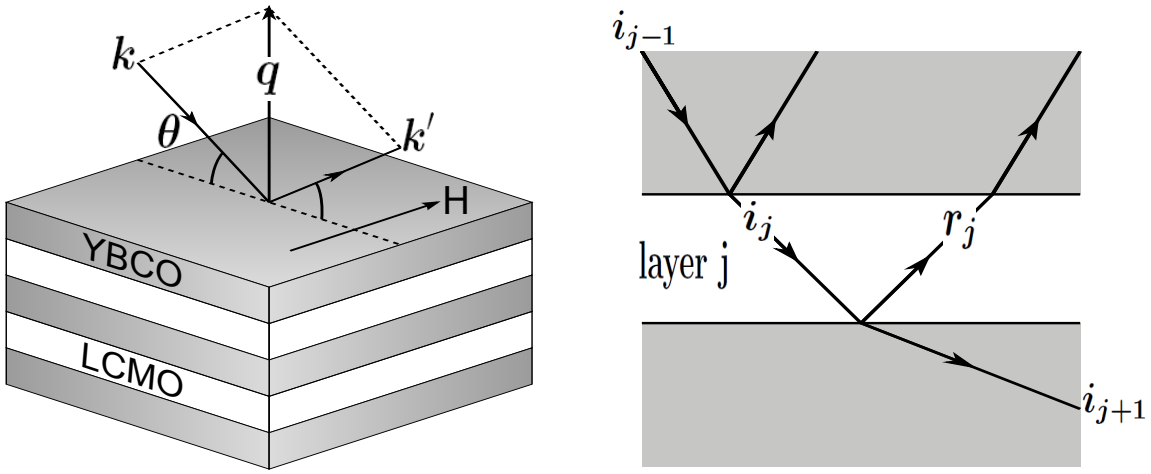

(a) Polarised specular reflectivity from an YBCO/LCMO superlattice. The momentum transferred to the neutron is $\boldsymbol{q}$

(b) The coherent wavefunction accounts for both reflection and refraction of the neutron at each layer in the medium.

Figure F.1: Polarised neutron spectrometry from a YBCO/LCMO superlattice.

$$n = \frac{k'}{k} = \sqrt{1 - \frac{\lambda^2}{\pi}\rho b}, \tag{F.3}$$

where the scattering length density is defined $\rho = Nb$ and $\lambda = 2\pi/k$ is the wavevector of the incident neutron. There is also a critical angle given by $\theta_c \approx \sqrt{\frac{\rho}{\pi}}$, below which the neutrons are totally reflected. In practice the refractive index is slightly less than one, such that $(1 - n) \sim 10^{-6}$, and consequentially the critical angle is very small and is typically measured in terms of milli-radians per *Å*ngstrom.

In this investigation we consider possible magnetic profiles of an YBCO-LCMO superlattice, which are obtained using PNR. For a medium with translational symmetry in the x-y plane, we can determine the coherent wavefunction by dividing the medium into thin layers, and then calculating the reflection and refraction at the interface between each of these layers. As the number of layers increases we approach the exact solution for the coherent wavefunction, from which we can self consistently determine the reflectivity and magnetic depth profiles of the medium.

The neutron wave function, which satisfies the single particle Schrodinger equation with translational invariance in the x-y plane, is simply

$$\Psi(\boldsymbol{r}) = \psi(z) e^{i\boldsymbol{k}_\parallel \cdot \boldsymbol{r}_\parallel}, \tag{F.4}$$

where $\psi(z)$ satisfies a one dimensional equation

$$\left(\frac{d^2}{dz^2} + \frac{2m_n}{\hbar^2}(E - V) - k_\parallel^2\right)\psi(z) = 0. \tag{F.5}$$

We next divide the medium into thin layers of thickness d_j, and with a constant potential V_j:

$$V_j = \frac{2\pi\hbar^2}{m} N_j(b_j + p_j), \tag{F.6}$$

where a magnetic scattering length p_j has been defined so that the average value of $-\boldsymbol{\mu}_n \cdot \boldsymbol{B}_{eff}$, in the j-th layer, is equal to $(2\pi\hbar^2/m)N_j p_j$. Then the neutron can be represented as a plane wave with a layer dependent wave vector. If we focus on an arbitrary layer j, as depicted in Fig. F.1(b), the general solution is

$$\psi(z) = i_j e^{ik_{zj}(z-\frac{d_j}{2})} + r_j e^{-ik_{zj}(z-\frac{d_j}{2})}. \tag{F.7}$$

Here we have used i_j and r_j to denote the coefficients of the incident and reflected waves respectively, evaluated midway through layer j, and their values must be chosen so that both $\psi(z)$ and $d\psi(z)/dz$ are continuous at the layer boundaries. The wave vector in layer j is

$$k_{zj} = \left(\frac{2m_n}{\hbar^2}(E - V_j) - k_\parallel^2\right)^{\frac{1}{2}}. \tag{F.8}$$

The first layer ($j = 1$) is the region above the free surface (i.e the vacuum), and the last layer ($j = N$) is the region below the last layer of the sample. There is no reflectance from this end layer since $d_N = \infty$, which implies that the reflectance r_N is zero. Then the reflectance r_1 associated with the first layer can be found by iterating backwards, starting from the last layer.

The measured quantity is the reflectivity $R = |r_1/i_1|^2$. The reflectivity is conveniently characterised in terms of the momentum transfer $q = k'_z - k_z = 4\pi\sin(\theta)/\lambda$, which is conjugate to the coordinate z normal to the surface. Then the reflectivity $R(q)$ is related to the depth profile of the superlattice, which can be reconstructed using the iterative method. The calculation of the reflectivity does however involve a loss of phase information, and as a consequence this method must be used in conjunction with additional knowledge of the materials under investigation to look for consistent depth profiles.

With polarised neutrons it is possible to extract more detailed information about the magnetic properties of the sample by separately measuring the *spin-flip* and *non spin-flip* scattering. The reflectivities for non spin-flip scattering are denoted R^{++} and R^{--}, and the reflectivities for spin-flip scattering are denoted R^{+-} and R^{-+}. The interaction between the neutron and the sample depends on the orientation of the neutrons spin

relative to the magnetic field; if the spin polarisation is parallel to the magnetic field it will be unaffected, if spin polarisation is not parallel to the magnetic field it will precess around $\boldsymbol{B}$, and if there are magnetic domains the spin polarisation will be quenched. A simple consequence of this dependence on polarisation can be seen if we consider the case when the spin polarisation is parallel to the magnetic field. The potential for the up and down spin configurations becomes $V^{\pm} = (2\pi\hbar^2/m)Nb \pm \mu B$, and the corresponding refractive indexes are $n^{\pm}$; this implies that the magnetic medium is birefringent and the reflectivity is different for each spin configuration. The reflectivity curves obtained for each of these processes can be reproduced using the iterative technique to deduce the appropriate magnetic depth profile.

The methods discussed are concerned with the specular reflectivity, but it is also useful to make measurements of the off-specular reflectivity. The off-specular beam is a consequence of broken translational symmetry in the $x - y$ plane, which may be caused by diffusion, roughness or the formation of magnetic domains. The direction of the off-specular beam relates to the repeat distances in the x and y directions.

Appendix G

Numerical solution of the exact Hamiltonian

The molecular wavefunctions representing the $L = 0$ states of H_2^+ can be calculated directly from the exact Hamiltonian using the *finite difference* technique. To obtain a numerical solution it is first necessary to transform to a more practical system of coordinates, and to redefine the wavefunction in a manner which simplifies the boundary conditions. Once this is done, the next step is to devise a scheme which uses the orthogonality and normalisation of the wavefunctions to obtain a spectrum of solutions with different energies. Finally, the Hamiltonian is represented on a discrete grid using finite difference equations for the derivatives, and a self consistent solution is found which satisfies the boundary conditions. The Hamiltonian to be solved is given in spheroidal coordinates as

$$\mathcal{H}_0 = -\mathcal{A}_0 - \alpha\mathcal{B}_0 + V, \tag{G.1}$$

where $\mathcal{A}_0$ is the operator representing the $L = 0$ electronic Hamiltonian and $\mathcal{B}_0$ is the operator representing the motion of the nuclei in the $L = 0$ state. These terms are defined

$$\mathcal{A}_0 = \frac{4}{w^2(u^2 - v^2)} \left(\frac{\partial}{\partial u} \left((u^2 - 1) \frac{\partial}{\partial u} \right) + \frac{\partial}{\partial v} \left((1 - v^2) \frac{\partial}{\partial v} \right) \right) \tag{G.2}$$

$$\begin{aligned} \mathcal{B}_0 = {} & \frac{2}{w^2} \frac{\partial}{\partial w} \left(w^2 \frac{\partial}{\partial w} \right) - \frac{4}{w^2(u^2 - v^2)} \left(w \frac{\partial}{\partial w} + 1 \right) \left(-u(u^2 - 1) \frac{\partial}{\partial u} + v(1 - v^2) \frac{\partial}{\partial v} \right) \\ & + \frac{2(u^2 + v^2)}{w^2(u^2 - v^2)} \left(\frac{\partial}{\partial u} \left((u^2 - 1) \frac{\partial}{\partial u} \right) + \frac{\partial}{\partial v} \left((1 - v^2) \frac{\partial}{\partial v} \right) \right) \end{aligned} \tag{G.3}$$

$$V = \left(\frac{2}{w} - \frac{8u}{(u^2 - v^2)w} \right). \tag{G.4}$$

The boundary conditions require careful consideration. The domain of Ψ is defined to be

$$1 \leq u \leq \infty \qquad -1 \leq v \leq 1 \qquad 0 \leq w \leq \infty. \tag{G.5}$$

The boundary conditions for the electronic coordinates require a regular solution which satisfies $\Psi \sim \alpha + \beta u$ when $u \to 1$, $\Psi \sim \exp(i\sqrt{E}wu/2)$ when $u \to \infty$, and $\Psi \sim \alpha' + \beta' v$ when $v \to \pm 1$. These conditions can be satisfied with a sensible parameterisation of the coordinates: we choose $u = \cosh(\theta)$ and $v = \cos(\phi)$, which results in the following domain for Ψ:

$$0 \leq \theta \leq \infty \qquad 0 \leq \phi \leq \pi \qquad 0 \leq w \leq \infty. \tag{G.6}$$

The boundary conditions therefore require that $\Psi \sim \alpha + \beta(1 + \theta^2/2)$ when $\theta \to 0$. We also choose $\Psi \to 0$ when $\theta \to \infty$, which is approximately satisfied for sufficiently large θ because the electronic wavefunction decays exponentially far from the nuclei. These boundary conditions can then enforced by imposing the symmetric boundary condition $\Psi(\theta) = \Psi(-\theta)$ when $\theta \to 0$, and the antisymmetric boundary condition $\Psi(\theta_{max} - \theta) = -\Psi(\theta - \theta_{max})$ when $\theta \to \infty$.

The analysis of the ϕ dependence is similar, and the regular solution corresponds to $\Psi \sim \alpha' + \beta'(1 - \phi^2/2)$ when $\phi \to \pm 1$. Symmetric boundary conditions would also be applicable in this case, but there is still the remaining degeneracy of the bonding and antibonding solutions. The two styles of solution can be separated by recognising that the bonding solution can be obtained by imposing antisymmetric boundary conditions at the midpoint of the two nuclei ($\phi = \pi/2$), and the antibonding solution is obtained by imposing antisymmetric boundary conditions at the midpoint.

The boundary condition for the nuclear coordinate when $w = 0$ becomes trivial if we define a new wavefunction $\tilde{\Psi} = w^2\Psi$, which effectively changes the measure to be used in the normalisation of the wavefunction. The wavefunction $\tilde{\Psi}$ clearly vanishes when $w = 0$, which implies that antisymmetric boundary conditions are appropriate.

At infinite internuclear separation the boundary conditions must be appropriate for both the bound states and the dissociated states of the molecule. There are a finite number of bound states which form a discrete spectrum and decay exponentially for large values of w, and a continuum of dissociated states which oscillate when w is large. To calculate the wavefunctions we elect to quantise the system in a finite box, so that each subsequent state of increasing energy has an additional node within the box. Both the bound states and the dissociated states can be found by imposing antisymmetric boundary conditions when $w \to \infty$. For the dissociated states, this boundary condition enforces a node in the

nuclear wavefunction at the edge of the finite box[1].

The only way of obtaining the high energy states using the finite difference method is to ensure orthogonality, with all states of lower energy, at each step. This imposes a severe constraint on our ability to calculate high energy states, especially when the mass ratio, α, is very small and the number of states within a set energy range is very large. For this reason we choose $\alpha \geq 0.005$, which is an order of magnitude larger than is appropriate to the real system.

After applying the parameterisation $u = \cosh(\theta)$ and $v = \cos(\theta)$ and defining $\tilde{\Psi} = w^2\Psi$, we obtain

$$\mathcal{A}_0 = \frac{4}{w^2(\sinh^2(\theta)+\sin^2(\phi))}\left(\frac{1}{\sinh(\theta)}\frac{\partial}{\partial\theta}\left(\sinh(\theta)\frac{\partial}{\partial\theta}\right)+\frac{1}{\sin(\phi)}\frac{\partial}{\partial\phi}\left(\sin(\phi)\frac{\partial}{\partial\phi}\right)\right) \quad \text{(G.7)}$$

$$\begin{aligned}\mathcal{B}_0 &= \frac{2}{w}\frac{\partial}{\partial w}\left(w\frac{\partial}{\partial w}\right)-\frac{6}{w}\frac{\partial}{\partial w}+\frac{4}{w^2}\\ &-\frac{4}{w^2(\sinh^2(\theta)+\sin^2(\phi))}\left(w\frac{\partial}{\partial w}+1\right)\left(\cosh(\theta)\sinh(\theta)\frac{\partial}{\partial\theta}-\cos(\phi)\sin(\phi)\frac{\partial}{\partial\phi}\right)\\ &+\frac{2(\sinh^2(\theta)-\sin^2(\phi))}{w^2(\sinh^2(\theta)+\sin^2(\phi))}\left(\frac{1}{\sinh(\theta)}\frac{\partial}{\partial\theta}\left(\sinh(\theta)\frac{\partial}{\partial\theta}\right)+\frac{1}{\sin(\phi)}\frac{\partial}{\partial\phi}\left(\sin(\phi)\frac{\partial}{\partial\phi}\right)\right) \quad \text{(G.8)}\end{aligned}$$

$$V = \left(\frac{2}{w}-\frac{8\cosh(\theta)}{(\sinh^2(\theta)+\sin^2(\phi))w}\right), \quad \text{(G.9)}$$

where it is understood that the operators now act on $\tilde{\Psi}$. We must then solve the eigenvalue problem

$$\mathcal{H}_0\tilde{\Psi}_n = E_n\tilde{\Psi}_n. \quad \text{(G.10)}$$

The eigenvalues can be determined by requiring that the solutions are normalised. To illustrate this idea it is best to use a simple example: suppose we wish to use the finite difference technique to find the excitation spectrum of the equation

$$\frac{d^2y(x)}{dx^2} = Ey(x). \quad \text{(G.11)}$$

This equation can be represented on a finite grid by the (second order) finite difference equation

$$\frac{y(x+h)-2y(x)+y(x-h)}{h^2} = Ey(x), \quad \text{(G.12)}$$

[1]Whilst this boundary condition is only approximate, i.e the exact nuclear wavefunction is known to be nodeless, the error is small and of the order of α.

which can be rearranged to give

$$y(x) = \frac{y(x+h) + y(x-h)}{2 + h^2 E}. \tag{G.13}$$

If we assume that we have an approximate value for the energy $E' \approx E + \Delta E$, and expand the normalisation condition $\langle y|y\rangle = 1$ about the exact energy E we obtain

$$\langle y|y\rangle \approx \int \left(\frac{\left(y(x+h) + y(x-h)\right)^2}{\left(2 + h^2\left(E + \Delta E\right)\right)^2} \right) dx$$

$$\approx \int \left(\frac{\left(y(x+h) + y(x-h)\right)^2}{\left(2 + h^2 E\right)^2} \right) dx - 2\Delta E h^2 \int \left(\frac{\left(y(x+h) + y(x-h)\right)^2}{\left(2 + h^2 E\right)^3} \right) dx = 1. \tag{G.14}$$

This allows us to predict the energy step required to find the correct energy:

$$\Delta E \approx \frac{\int \left(\frac{(y(x+h)+y(x-h))^2}{(2+h^2E)^2} \right) dx - 1}{2h^2 \int \left(\frac{(y(x+h)+y(x-h))^2}{(2+h^2E)^3} \right) dx}. \tag{G.15}$$

If this method is used to solve Eq G.11 iteratively, then the ground state (which has no nodes) will be obtained. This is because the finite difference method converges to the solution with low frequency components. In order to find the excitations we must ensure that a particular solution y_n with energy E_n is orthogonal to any states of lower energy, which means that we must first find the $n-1$ states of lower energy. Then, at each iteration step, we perform the *Gram-Schmidt* process to remove the $n-1$ lower energy components from the wavefunction y_n.

The solutions to Eq G.10 are found using the method just described, using the correct measure for $\tilde{\Psi}$:

$$J(w, \theta, \phi) = \frac{w}{8}(\sinh^2(\theta) + \sin^2(\phi)) \sinh(\theta) \sin(\phi). \tag{G.16}$$

The normalisation is therefore

$$\langle \tilde{\Psi} | \tilde{\Psi} \rangle = \int_0^\infty dw \int_1^\infty d\theta \int_0^{\frac{\pi}{2}} d\phi |J(w, \theta, \phi)| |\tilde{\Psi}(\theta, \phi, w)|^2. \tag{G.17}$$

The solutions presented in section 4.6 are for $\alpha = 0.005$. They are performed on a grid of size $N_w \times N_\theta \times N_\phi$, where $N_w = 200$, $N_\theta = 20$ and $N_\phi = 12$. The grid spacing used is $h_w = 0.1$, $h_\theta = 0.1$ and $h_\phi = \pi/24$, and the finite difference equations used are sixth order in these parameters.

Appendix H

Numerical solution of the Born-Huang equations

The Born-Huang matrix equations for the $L = 0$ states of H_2^+, obtained from the expansion of the molecular wavefunctions into the basis of electronic states, leads to a set of coupled ordinary differential equations; these can be solved using the *Runge-Kutta* technique. The matrix equation for the non-adiabatic states is

$$\hat{\boldsymbol{\mathcal{H}}}\tilde{\boldsymbol{X}}^m_n = E^m_n \tilde{\boldsymbol{X}}^m_n \tag{H.1}$$

with the matrix elements

$$\hat{\boldsymbol{\mathcal{H}}}_{n'n''} = -\widehat{\langle \Phi_{n'} | \alpha \mathcal{B}_0 | \Phi^{m''} \rangle} + \delta_{m'm''}\varepsilon_{m'}(w), \tag{H.2}$$

where the first tem is an operator which may be expanded as

$$\widehat{\langle \Phi_{n'} | \alpha \mathcal{B}_0 | \Phi^{m''} \rangle} = \delta_{n'n''}\left(-\alpha\frac{2}{w}\frac{d}{dw}\left(w\frac{d}{dw}\right)\right) + \mu_{n'n''}\frac{d}{dw} + \nu_{n'n''}. \tag{H.3}$$

The diagonal terms represent the standard Born-Oppenheimer approximation, but with minor corrections to the electronic energy surfaces, whilst the off-diagonal matrix elements give rise to the non-adiabatic coupling between electronic states:

$$\mu_{n'n''} = \left\langle \Phi_{n'} \left| \mathcal{B}_3 + \frac{\partial}{\partial w} \right| \Phi_{n''} \right\rangle = \mu_{n''n'} \tag{H.4}$$

$$\nu_{n'n''} = \left\langle \Phi_{n'} \left| -\mathcal{B}_1 - \mathcal{B}_2 + \mathcal{B}_3\frac{\partial}{\partial w} \right| \Phi_{n''} \right\rangle = \nu_{n''n'}. \tag{H.5}$$

The operators $\mathcal{B}_1$ and $\mathcal{B}_2$ are Hermitian, and $\mathcal{B}_3$ is anti-Hermitian:

$$\mathcal{B}_1 = \frac{2}{w}\frac{\partial}{\partial w}\left(w\frac{\partial}{\partial w}\right) \tag{H.6}$$

$$\mathcal{B}_2 = \frac{2}{w^2(\sinh^2(\theta)+\sin^2(\phi))\sinh(\theta)\sin(\phi)}\left[\frac{\partial}{\partial\theta}\left((\sinh^2(\theta)-\sin^2(\phi))\sinh(\theta)\sin(\phi)\frac{\partial}{\partial\theta}\right)\right.$$
$$\left. + \frac{\partial}{\partial\phi}\left((\sinh^2(\theta)-\sin^2(\phi))\sinh(\theta)\sin(\phi)\frac{\partial}{\partial\phi}\right)\right] + \frac{4}{w^2} \tag{H.7}$$

$$\mathcal{B}_3 = \frac{4}{w(\sinh^2(\theta)+\sin^2(\phi))}\left(\cosh(\theta)\sinh(\theta)\frac{\partial}{\partial\theta} - \cos(\phi)\sin(\phi)\frac{\partial}{\partial\phi} + \frac{3}{2}\right)\frac{\partial}{\partial w}. \tag{H.8}$$

The non-adiabatic matrix equation (Eq. H.1) defines a set of coupled ordinary differential equations which can be solved using the Runge-Kutta method. To illustrate how this method is applied it is helpful to use a simple example: suppose we wish to solve the equation

$$\frac{d^2y(x)}{dx^2} = Ey(x). \tag{H.9}$$

If we write $y_1 = y$ and $y_2 = dy/dx$ as components of a vector the above equation can be transformed into a system of first order differential equations:

$$\frac{dy_1(x)}{dx} = y_2(x) \qquad \frac{dy_2(x)}{dx} = Ey_1(x). \tag{H.10}$$

Then the problem is reduced to that of solving the following generic style of equation:

$$\frac{dy(x)}{dx} = f(x,y). \tag{H.11}$$

To obtain an accurate solution in a small number of steps the Runge-Kutta method uses the derivatives at intermediate points to calculate the next step. The intermediate points are chosen to give agreement with Taylors theorem up to a specified order. We define the quantities

$$\begin{aligned} k_1 &= hf(x+a_1h, y(x)) \\ k_2 &= hf(x+a_2h, y(x)+b_{21}k_1) \\ k_3 &= hf(x+a_3h, y(x)+b_{31}k_1+b_{32}k_2) \\ &... \end{aligned} \tag{H.12}$$

and express the next step as linear combination of these quantities:

$$y(x+h) = y(x) + w_1 k_1 + w_2 k_2 + w_3 k_3 + ... \tag{H.13}$$

The parameters $a_1, a_2, a_3, ...$ and $b_{21}, b_{31}, b_{32}, ...$ and $w_1, w_2, w_3, ...$ are chosen so that Eq. H.13 agrees with Taylors theorem. At second order the next step requires two terms:

$$y(x+h) = y(x) + hw_1 f(x + a_1 h, y(x)) + hw_2 f(x + a_2 h, y(x) + b_{21} h f(x + a_1 h, y(x))) \tag{H.14}$$

$$\begin{aligned} &= y(x) + hw_1 f(x,y) + hw_2 f(x,y) + h^2 w_1 a_1 f_x(x,y) + h^2 w_2 a_2 f_x(x,y) \\ &\quad + h^2 w_2 b_{21} f(x,y) f_y(x,y) + O(h^3), \end{aligned} \tag{H.15}$$

where f_x and f_y denote the partial derivatives of f. The corresponding Taylor series is

$$\begin{aligned} y(x+h) &= y(x) + hy^1(x) + \frac{h^2}{2} y^2(x) + O(h^3) \\ &= y(x) + hf(x,y) + \frac{h^2}{2}(f_x(x,y) + f(x,y) f_y(x,y)) + O(h^3), \end{aligned} \tag{H.16}$$

where y^n represents the nth derivative of y. Equating the two expressions for $y(x+h)$ gives

$$\begin{aligned} w_1 + w_2 &= 1 \\ w_1 a_1 + w_2 a_2 &= \tfrac{1}{2} \\ w_2 b_{21} &= \tfrac{1}{2} \end{aligned} \quad . \tag{H.17}$$

One particular solution is $w_1 = 0$, $w_2 = 1$, $a_1 = 1$, $a_2 = 1/2$ and $b_{21} = 1/2$, which results in the *midpoint* method

$$\begin{aligned} k_1 &= hf(x+h, y) \\ k_2 &= hf(x + \tfrac{h}{2}, y + \tfrac{k_1}{2}) \\ y(x+h) &= y(x) + k_2 \end{aligned} \quad . \tag{H.18}$$

This method simply uses the derivative at the midpoint to integrate the solution forwards, using the initial conditions for $y_1(0)$ and $y_2(0)$. Returning to Eq. H.1, the simplest calculation involves just the $1\sigma_g$ and $2\sigma_g$ states:

$$\hat{\boldsymbol{\mathcal{H}}} = \begin{pmatrix} -\alpha \frac{2}{w} \frac{d}{dw} \left(w \frac{d}{dw} \right) + \varepsilon_1 + \mu_{11} \frac{d}{dw} + \nu_{11} & \mu_{12} \frac{d}{dw} + \nu_{12} \\ \mu_{21} \frac{d}{w} + \nu_{21} & -\alpha \frac{2}{w} \frac{d}{dw} \left(w \frac{d}{dw} \right) + \varepsilon_2 + \mu_{22} \frac{d}{dw} + \nu_{22} \end{pmatrix} \tag{H.19}$$

$$\tilde{\boldsymbol{X}}_n^m = (\tilde{X}_n^{m1}, \tilde{X}_n^{m2}). \tag{H.20}$$

This can be written as a set of first order coupled differential equations:

$$\begin{aligned}
\frac{dy_1}{dx} &= y_3 \\
\frac{dy_2}{dx} &= y_4 \\
\frac{dy_3}{dx} &= \frac{1}{2\alpha - \mu_{12}} \left((\varepsilon_1 - E_{n,m} + \nu_{11}) y_1 + \left(\mu_{11} + \nu_{12} - \frac{2\alpha}{w} \right) y_3 \right) \\
\frac{dy_4}{dx} &= \frac{1}{2\alpha - \mu_{21}} \left((\varepsilon_2 - E_{n,m} + \nu_{22}) y_2 + \left(\mu_{22} + \nu_{21} - \frac{2\alpha}{w} \right) y_4 \right)
\end{aligned} \tag{H.21}$$

$$\boldsymbol{y} = \left(\tilde{X}_n^{m1}, \tilde{X}_n^{m2}, \frac{d\tilde{X}_n^{m1}}{dw}, \frac{d\tilde{X}_n^{m2}}{dw} \right). \tag{H.22}$$

All that is required to run the Runge-Kutta algorithm are the initial conditions $y_1(0) = 0$, $y_2(0) = 0$, $y_3(0) = a$ and $y_4(0) = b$. There exist two linearly independent solutions, and the constants a and b determine both the particular linear combination and the normalisation. However, a simple WKB analysis shows that the two solutions are associated with the two electronic energy surfaces and both increase exponentially at the origin, but with different exponents. Thus, numerical errors stabilise the solution with the largest exponent for almost all values of a and b. To circumvent this problem it is also necessary to employ a *Newton-Raphson* root finder to tune the initial conditions for the second solution.

The solutions to the non-adiabatic equations with the $1\sigma_g$ and $2\sigma_g$ electronic states are presented in section 4.6, where a sixth order Runge-Kutta algorithm was used.

Bibliography

[1] V. F. Sears, E. C. Svensson, P. Martel, and A. B. D. Woods, Phys. Rev. Lett. **49**, 279 (1982)

[2] T. R. Sosnick, W. M. Snow, and P. E. Sokol, Phys. Rev. B **41**, 16 (1990)

[3] G. F. Reiter, J. Mayers, and P. Platzmann, Phys. Rev. Lett. **89**, 135505 (2002)

[4] G. I. Watson, J. Phys.: Condens. Matter **8**, 5955 (1996)

[5] C. A. Chatzidimitriou-Dreismann, T. Abdul-Redah, R. M. F. Streffer, and J. Mayers, Phys. Rev. Lett. **79**, 2839 (1997)

[6] E. B. Karlsson, C.A.Chatzidimitriou-Dreismann, T. Abdul-Redah, R. M. F. Streffer, B. Hj*ö*rvarsson, J. *Ö*hrmalm, and J. Mayers, Europhys. Lett. **46**, 617 (1999)

[7] T. Abdul-Redah, R. M. F. Streffer, C. A. Chatzidimitriou-Dreismann, B. Hj*ö*rvarsson, E. B. Karlsson, and J. Mayers, Physica B **824**, 276 (2000)

[8] E. B. Karlsson, T. Abdul-Redah, R. M. F. Streffer, B. Hj*ö*rvarsson, J. Mayers, and C. A. Chatzidimitriou-Dreismann, Phys. Rev. B **67**, 184108 (2003)

[9] C. A. Chatzidimitriou-Dreismann and T. Abdul-Redah, J. Chem. Phys. **113**, 2784 (2000)

[10] C. A. Chatzidimitriou-Dreismann, T. Abdul-Redah, and R. M. F. Streffer, J. Chem. Phys. **116**

[11] C. A. Chatzidimitriou-Dreismann, C. K. M. Vos, and T. Abdul-Redah, Phys. Rev. Lett. **91**, 057403 (2003)

[12] E. B. Karlsson and S. W. Lovesey, Phys. Rev. A **61**, 062714 (2000)

[13] J. Mayers and T. Abdul-Redah, J. Phys.: Condens. Matter **16**, 4811 (2004)

[14] R. A. Cowley, J. Phys.: Condens. Matter **15**, 4143 (2003)

[15] R. A. Cowley and J. Mayers, J. Phys.:Condens. Matter **18**, 5291 (2006)

[16] S. W. Lovesey, C. D. Bowman, and R. G. Johnson, Z. Phys. B - Condens. Matter **47**, 137 (1982)

[17] L. D. Landau and E. M. Lifshitz, *Quantum Mechanics*, 3rd ed., Course of theoretical physics, Vol. 3 (Butterworth-Heinemann, 1977)

[18] V. F. Sears, *Neutron Optics* (Oxford University Press, Oxford, 1989)

[19] E. Amaldi, O. D'Agostino, E. Fermi, B. Pontecorvo, F. Rasetti, and E. Segrè, Proc. Roy. Soc. **A 149**, 522 (1935)

[20] R. S. et al, Phys. Rev. Lett. **86**, 4584 (2001)

[21] E. Fermi, Ric. Sci. **7**, 13 (1936)

[22] E. Fermi and L. Marshall, Phys. Rev. **71**, 666 (1947)

[23] S. W. Lovesey, *Theory of Neutron Scattering from Condensed Matter* (Clarendon, Oxford, 1984)

[24] C. A. et al, Phys. Rev. B **50**, 12744 (1994)

[25] V. F. Sears, Phys. Rev. B **30**, 44 (1984)

[26] J. D. Bjorken, Phys. Rev. **179**, 1547 (1969)

[27] J. Mayers, C. Andreani, and D. Colegnesi, J. Phys.: Condens. Matter **9**, 10639 (1997)

[28] L. V. Hove, Phys. Rev. **95**, 249 (1954)

[29] C. G. Windsor, *Pulsed Neutron Scattering* (Taylor and Francis, London, 1981)

[30] H. Sugimoto, H. Yiiki, and A. Okumura, Phys. Rev. Lett. **94**, 165506 (2005)

[31] D. Colognesi, Physica B **344**, 73 (2004)

[32] R. G. Littlejohn and M. Reinsch, Re. Mod. Phys. **69**, 213 (1997)

[33] V. Aquilanti and S. Cavalli, J. Chem. Phys. **85**, 1355 (1986)

[34] J. Makarevicz, Am. J. Phys. **54**, 178 (1986)

[35] N. Bohr, Philos. Mag. **26**, 1 (1913)

[36] N. Gidopoulos, Phys. Rev. B **71**, 054106 (2005)

[37] M. Born and R. Oppenheimer, Annaln Phys. **84**, 457 (1927)

[38] M. Born and K. Huang, *Dynamical theory of crystal lattices* (Oxford University Press, Oxford, 1955)

[39] I. A. Howard, C. Amovilli, N. Gidopoulos, and N. H. March, J. Math. Chem **42**, 3 (2007)

[40] F. T. Smith, Phys. Rev. **179**, 111 (1969)

[41] M. V. Berry, Proc. R. Soc. **A392**, 45 (1984)

[42] C. Eckart, Phys. Rev. **47**, 552 (1935)

[43] J. Tennyson and B. T. Sutcliffe, J. Chem. Phys. **77**, 4061 (1982)

[44] J. C. Slater, *Quantum theory of molecules and solids* (McGraw-Hill, 1963)

[45] J. Czub and L. Wolniewicz, Molecular Physics **1978**, 1301 (1978)

[46] D. Colognesi, Physica B **358**, 114 (2005)

[47] G. Hunter, Int. J. Quant. Chem. **9**, 237 (1975)

[48] D. Colognesi, E. Degiorgi, and E. pace, Physica B **293**, 317 (2001)

[49] A. Ohtomo and H. Y. Hwang, Nature **427**, 423 (2004)

[50] A. Ohtomo and H. Y. Hwang, Nature **441**, 120 (2006)

[51] A. B. et al, Nature Mater. **6**, 493 (2007)

[52] A. Ohtomo, D. A. Muller, J. L. Grazul, and H. Y. Hwang, Nature **419**, 378 (2002)

[53] J. Chakhalian, J. W. Freeland, H. U. Habermeier, G. Cristiani, G. Khaliullin, M. van Veenendaal, and B. Keimer, Science **318**, 1114 (2007)

[54] J. G. Bednorz and K. A. Muller, Z. Phys. **64**, 189 (1986)

[55] S. J. et al, Science **264**, 413 (1994)

[56] I. Terasaki, Y. Sasago, and K. Uchinokura, Phys. Rev. B **56**, R12685 (1997)

[57] M. Imada, A. Fujimori, and Y. Tokura, Rev. Mod. Phys. **70**, 1039 (1998)

[58] S. Maekawa, T. Tohyama, S. E. Barnes, S. Ishihara, W. Koshibae, and G. Khaliullin, *Physics of Transtion Metal Oxides* (Springer-Verlag, New York, 2004)

[59] G. A. Gehring and K. A. Gehring, Rep. Prog. Phys. **38**, 1 (1975)

[60] M. D. Kaplan, *Cooperative phenomena in Jahn-Teller crystals* (Plenum Press, New York, 1995)

[61] A. L. Fetter and J. D. Walecka, *Quantum Theory of Many-Particle Systems* (Dover Publications, New York, 1971)

[62] J. C. Slater and G. F. Koster, Phys. Rev. B **94**, 1498 (1954)

[63] N. F. Mott, Proc. Phys. Roy. Soc. **62**, 416 (1949)

[64] J. Zaanen, G. A. Sawatzky, and J. W. Allen, Phys. Rev. Lett. **55**, 418 (1985)

[65] J. Hubbard, Proc. Roy. Soc. **A276**, 238 (1963)

[66] P. W. Anderson, Phys. Rev. **115**, 2 (1959)

[67] J. Pollmann and S. T. Pantelides, Phys. Rev. B **18**, 10 (1978)

[68] M. Schmeits, A. Mazur, and J. Pollmann, Phys. Rev. B **27**, 8 (1983)

[69] A. R. et al, J. Vac. Sci. Technol. B **17**, 1674 (1999)

[70] I. Žutić, J. Fabian, and S. D. Sarma, Rev. Mod. Phys **76**, 323 (2004)

[71] P. Kraus, A. Bhattacharya, K. Nikolaev, and A. M. Goldman, Mater. Sci. Eng. B **84**, 63 (2001)

[72] F. C. Zhang and T. M. Rice, Phys. Rev. B **37**, 7 (1988)

[73] E. dagotto, Rev. Mod. Phys **66**, 3 (1994)

[74] P. A. Lee, N. Nagaosa, and X. Wen, Rev. Mod. Phys **78**, 1 (2006)

[75] M. K. W. et al, Phys. Rev. Lett. **58**, 908 (1987)

[76] J. Bardeen and L. N. Cooper, Phys. Rev. **108**, 1175 (1957)

[77] M. Tinkham, *Introduction to Superconductivity* (McGraw-Hill, New York, 1975)

[78] J. P. Franck, *Physical Properties of High Temperature Superconductors*, Vol. 4 (Singapore: World Scientific, 1994)

[79] H. D. et al, Phys. Rev. B **54**, 9678 (1996)

[80] J. R.-M. et al, Physica C **86**, 185 (1991)

[81] J. W. Loram, K. A. Mirza, and J. R. Cooper, Phys. Rev. Lett. **71**, 1740 (1993)

[82] A. G. L. et al, Science **273**, 325 (1996)

[83] C. Renner, B. Revaz, J. Y. Genoud, K. Kadowaki, and Ø. Fischer, Phys. Rev. Lett. **80**, 149 (1998)

[84] M. R. N. et al, Nature **392**, 157 (1998)

[85] X. G. Wen and P. A. Lee, Phys. Rev. Lett. **76**, 503 (1996)

[86] N. Furukawa and T. M. Rice, Phys. Rev. Lett. **10**, L381 (1998)

[87] M. I. Salkola, V. J. Emery, and S. A. Kivelson, Phys. Rev. Lett. **77**, 155 (1996)

[88] J. L. Tallon and J. W. Loram, Physica C **349**, 53 (2001)

[89] S. Schmitt-Rink, C. M. Varma, and A. E. Ruckenstein, Phys. Rev. Lett. **60**, 2793 (1988)

[90] C. L. Kane, P. A. Lee, and N. Read, Phys. Rev. B **39**, 6880 (1989)

[91] G. Martinez and P. Horsh, Phys. Rev. B **44**, 317 (1991)

[92] B. O. W. et al, Phys. Rev. Lett. **74**, 964 (1995)

[93] C. K. et al, Phys. Rev. Lett. **80**, 4245 (1998)

[94] S. L. et al, Phys. Rev. B **56**, R525 (1997)

[95] P. W. Anderson, Phys. Rev. B **69**, 064512 (2004)

[96] A. K. McMahan, R. M. Martin, and S. Satpathy, Phys. Rev. B **38**, 6650 (1988)

[97] I. B. Styles and M. W. Long, J. Phys. A: Math. Gen. **36**, 9361 (2003)

[98] M. W. Long and I. B. Styles, Phys. Rev. B **70**, 205119 (2004)

[99] P. W. Anderson, Science **235**, 1196 (1987)

[100] E. Dagotto, *Nanoscale Phase Separation and Colossal Magnetoresistance* (Spring-Verlag, New York, 2003)

[101] M. B. Salamon and M. Jaime, Rev. Mod. Phys **73**, 3 (2001)

[102] S. W. Cheong and H. Y. Hwang, *Colossal magnetoresistance oxides* (Gordon and Breach, London, 1999)

[103] E. O. Wollan and W. C. Koehler, Phys. Rev. **100**, 545 (1955)

[104] J. B. Goodenough, Phys. Rev. **100**, 564 (1955)

[105] Y. M. et al, Phys. Rev. Lett. **80**, 1932 (1998)

[106] C. Zener, Phys. Rev. **82**, 403 (1951)

[107] A. J. Millis, B. I. Shraiman, and R. Mueller, Phys. Rev. Lett. **77**, 1 (1996)

[108] N. A. B. et al, Nature **391**, 159 (1998)

[109] P. Schiffer, A. P. Ramirez, W. Bao, and S. W. Cheong, Phys. Rev. Lett. **75**, 3336 (1995)

[110] S. J. et al, Science **264**, 413 (1994)

[111] P. G. de Gennes, Phys. Rev. **118**, 141 (1960)

[112] T. S. et al, Phys. Rev. B **51**, 13942 (1995)

[113] A. Chainani, M. Mathew, and D. D. Sarma, Phys. Rev. B **47**, 15397 (1993)

[114] J. H. P. et al, Phys. Rev. Lett. **76**, 4215 (1996)

[115] T. Hotta, S. Yunoki, M. Mayr, and E. Dagotto, Phys. Rev. B **60**, R15009 (1999)

[116] S. Ishihara, J. Inoue, and S. Maekawa, Phys. Rev. B **55**, 8280 (1997)

[117] S. Ishihara, M. Yamanaka, and N. Nagaosa, Phys. Rev. B **56**, 686 (1997)

[118] H. U. H. et al, Physica C **364**, 298 (2001)

[119] M. V. et al, Solid-state Electronics **47**, 2245 (2003)

[120] J. Stahn, J. Chakhalian, C. Niedermayer, J. Hoppler, T. Gutberlet, J. Voigt, F. Treubel, H. U. Habermeier, G. Cristiani, B. Keimer, and C. Bernhard, Phys. Rev. B **71**, 140509 (2005)

[121] H. Meissner, Phys. Rev. **117**, 672 (1960)

[122] W. Luo, S. J. Pennycook, and S. T. Pantelides, Phys. Rev. Lett. **101**, 247204 (2008)

[123] F. S. Bergeret, A. F. Volkov, and K. B. Efetov, Phys. Rev. B **69**, 174504 (2004)

[124] D. L. Z. et al, Phys. Rev. B **49**, 1417 (1994)

[125] A. Bianconi, P. Castrucci, A. Fabrizzi, M.Pompa, A. M. Flank, P. Lagarde, H. Katayama-Yoshida, and G. Calestani **162-164**, 209 (1989)

[126] J. Callaway, J. Math. Phys **5**, 6 (1963)

[127] H. D. L. et al, Phys. Rev. Lett. **86**, 4370 (2001)

[128] D. A. MacLean, H. N. Ng, and J. E. Greedan, Jour. Sol. Stat. Chem. **30**, 35 (1979)

[129] S. Ishihara, T. Hatakeyama, and S. Maekawa, Phys. Rev. B **65**, 064442 (2002)

[130] H. N. et al, Phys. Rev. B **66**, 184419 (2002)

[131] H. Ichikawa, J. Akimitsu, M. Nishi, and K. Kakurai, Physica B **281**, 482 (2000)

[132] R. Pentcheva and W. E. Pickett, Phys. Rev. B **74**, 035112 (2006)

[133] J. H. H. et al, Nature **430**, 758 (2004)

[134] A. V. et al, Phys. Rev. Lett. **97**, 257602 (2006)

[135] Y. Fujii and T. Sakudo, Phys. Rev. B **13**, 1161 (1976)

[136] E. D. M. et al, Phys. Rev. Lett. **85**, 3664 (2000)

[137] M. I. et al, Phys. Rev. Lett. **82**, 17 (1999)

[138] H. Y. Hwang, Science **313**, 1895 (2006)

[139] N. Nakagawa, H. Y. Hwang, and D. A. Muller, Nature **5**, 204 (2006)

[140] M. B. et al, Nature Mater. **7**, 621 (2008)

[141] A. C. Hewson, *The Kondo Problem to Heavy fermions* (Cambridge Univ. Press, Cambridge, 1993)

[142] J. Inaba and T. Katsufuji, Phys. Rev. B **72**, 052408 (2005)

[143] T. Fix, J. L. MacManus-Driscoll, and M. G. Blamire, Appl. Phys. Lett. **94**, 172101 (2009)

[144] A. D. C. et al, Nature **456**, 624 (2008)

[145] N. R. et al, Science **317**, 1196 (2007)

[146] J. M. Kosterlitz and D. J. Thouless, J. Phys. C **5**, L124 (1972)

[147] N. O. et al, Phys. Rev. B **80**, 081106 (2009)

[148] S. Okamota, A. J. Millis, and N. A. . Spaldin, Phys. Rev. Lett. **97**, 056802 (2006)

[149] Z. S. Popović, S. Satpathy, and R. M. Martin, Phys. Rev. Lett. **101**, 256801 (2008)

[150] S. Okamota and A. J. Millis, Phys. Rev. B **70**, 075101 (2004)

[151] N. I. Gidopoulos and E. K. U. Gross, cond. mat., 0502433(2005)